MICROCOPY RESOLUTION TEST CHART

NATIONAL BUREAU OF STANDARDS-1963-A

PREDICTION OF CRUCIFORM ALL–MOVABLE CONTROL
CHARACTERISTICS AT TRANSONIC SPEEDS

by

Jack N. Nielsen, Frederick K. Goodwin,
and Marnix F. E. Dillenius

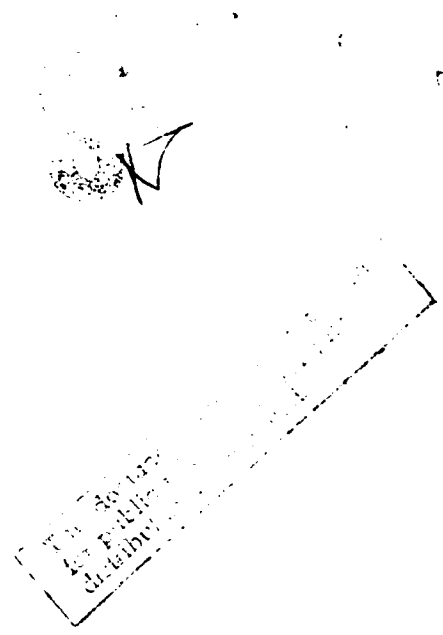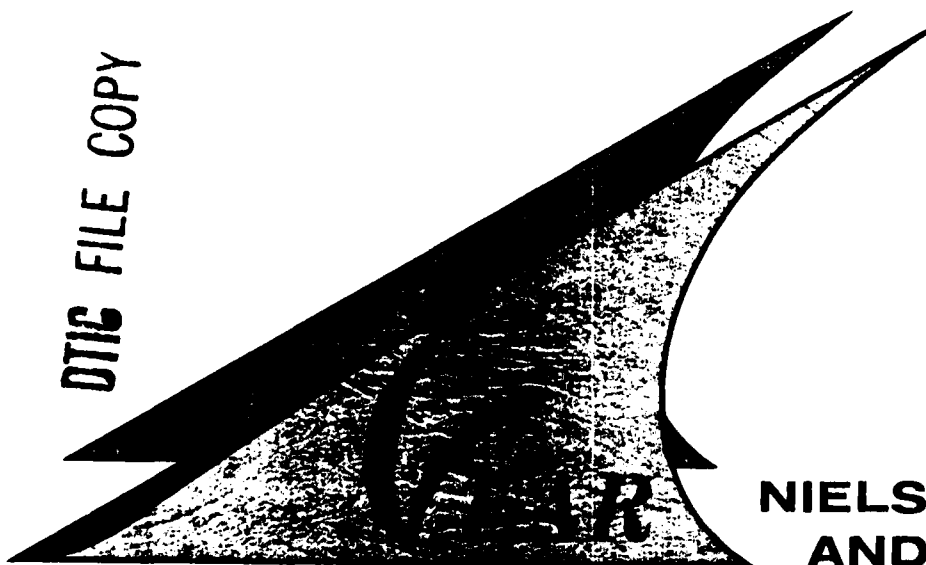NEAR TR 321

**NIELSEN ENGINEERING
AND RESEARCH, INC.**

PREDICTION OF CRUCIFORM ALL-MOVABLE CONTROL
CHARACTERISTICS AT TRANSONIC SPEEDS

by

Jack N. Nielsen, Frederick K. Goodwin,
and Marnix F. E. Dillenius

NEAR TR 321

February, 1984

NOV 7 1984

A

SECURITY CLASSIFICATION OF THIS PAGE (When Data Entered)

REPORT DOCUMENTATION PAGE		READ INSTRUCTIONS BEFORE COMPLETING FORM
1 REPORT NUMBER NEAR TR 321	2 GOVT ACCESSION NO.	3 RECIPIENT'S CATALOG NUMBER
4 TITLE (and Subtitle) PREDICTION OF CRUCIFORM ALL-MOVABLE CONTROL CHARACTERISTICS AT TRANSONIC SPEEDS		5 TYPE OF REPORT & PERIOD COVERED FINAL REPORT 1/1/83 to 3/31/84
		6 PERFORMING ORG. REPORT NUMBER NEAR TR 321
7 AUTHOR(s) Jack N. Nielsen, Frederick K. Goodwin, and Marnix F. E. Dillenius		8 CONTRACT OR GRANT NUMBER(s) N00014-81-C-0267
9 PERFORMING ORGANIZATION NAME AND ADDRESS Nielsen Engineering & Research, Inc. 510 Clyde Avenue Mountain View, CA 94043		10 PROGRAM ELEMENT, PROJECT, TASK AREA & WORK UNIT NUMBERS 62241N RF41-411-801 NR212-269
11 CONTROLLING OFFICE NAME AND ADDRESS Office of Naval Research Code 432 800 N. Quincy Street Arlington, VA 22217		12 REPORT DATE MARCH 1984
		13 NUMBER OF PAGES 254
14 MONITORING AGENCY NAME & ADDRESS(if different from Controlling Office)		15 SECURITY CLASS. (of this report) Unclassified
		15a DECLASSIFICATION DOWNGRADING SCHEDULE

16 DISTRIBUTION STATEMENT (of this Report)

Approved for public release; distribution unlimited

17 DISTRIBUTION STATEMENT (of the abstract entered in Block 20, if different from Report)

18 SUPPLEMENTARY NOTES

19 KEY WORDS (Continue on reverse side if necessary and identify by block number)

Missile Airframes	Aerodynamic Forces
All-Movable Controls	Transonic Characteristics
Hinge Moments	Control Surfaces

20 ABSTRACT (Continue on reverse side if necessary and identify by block number)

A study has been made of the feasibility of developing a transonic hinge-moment prediction method for cruciform all-movable controls by correlating an extensive data base using the equivalent angle of attack concept. Body vortex effects have been handled using a simplified vortex model. Existing data from the Army generalized missile have been studied to examine transonic nonlinearities including pitch-yaw coupling

DD FORM 1473 EDITION OF 1 NOV 65 IS OBSOLETE
1 JAN 73

SECURITY CLASSIFICATION OF THIS PAGE (When Data Entered)

20.   ABSTRACT   (concluded)

and fin-fin control interference. Data for an aspect ratio
3.53, taper ratio 0.06 canard fin have been successfully
correlated on the basis of the equivalent angle-of-attack
concept. Data for an aspect ratio 2 delta fin mounted aft
on the triservice missile have also been studied for angle
of attack to 20° for Mach numbers of 0.8 and 12. Methods of
extending the range of applicability of a previous hinge-
moment prediction method have been developed. Desirable
future extensions have been pointed out.

PREFACE

This technical report covers the work performed under
Contract N00014-81-C0276 from January 1, 1983 to March 31, 1984.
The program is sponsored by the Office of Naval Research,
Arlington, Virgina. Dr. Robert E. Whitehead is the Scientific
Officer.

Support for the program was provided by Air Force Wright
Aeronautical Laboratory (AFWAL), under the leadership of
Mr. Vernon O. Hoehne.

A-1

SUMMARY

A study has been made of the feasibility of developing a transonic hinge-moment prediction method for cruciform all-movable controls by correlating an extensive data base using the equivalent angle of attack concept. Body vortex effects have been handled using a simplified vortex model. Existing data from the Army generalized missile have been studied to examine transonic nonlinearities including pitch-yaw coupling and fin-fin control interference. Data for an aspect ratio 3.53, taper ratio 0.06 canard fin have been successfully correlated on the basis of the equivalent angle-of-attack concept. Data for an aspect ratio 2 delta fin mounted aft on the triservice missile have also been studied for angle of attack to 20° for Mach numbers of 0.8 and 1.2. Methods of extending the range of applicability of a previous hinge-moment prediction method have been developed. Desirable future extensions have been pointed out.

TABLE OF CONTENTS

LIST OF ILLUSTRATIONS

6

8

LIST OF SYMBOLS

a	body radius
$\cancel{R}$	fin aspect ratio
c_r	fin root chord
CHM	hinge-moment coefficient based on ℓ_r and S_R
CHMi	hinge-moment coefficient of fin i
$(CHM)_p$	part of CHM due to nonvortical flow
$(CHM)_t$	total CHM
$(CHM)_{max}$	maximum hinge-moment coefficient
$(CHM)_v$	part of CHM due to body vortices
$(CHM)_\alpha$	value of CHM due to α_c
$(CHM)_\delta$	value of CHM due to control deflection
C_N, C_{N_W}	wing-alone normal-force coefficient based on wing planform area
CNF	fin normal-force coefficient based on S_R
CNFi	value of CNF for fin i
$(CNF)_o$	value of CNF for $\delta = 0$
$(CNF)_p$	part of CNF due to nonvortical flow
$(CNF)_t$	total CNF
$(CNF)_v$	value of CNF due to vortex loading
$(CNF)_\alpha$	value of CNF for $\delta = 0$ and no vortex effects
$(CNF)_\delta$	value of CNF due to control deflection
$\Delta(CNF)_i$	change in fin i normal-force coefficient due to control deflection δ_j of fin j
k_w	control interference factor, eq. (2)
K_W	wing-body interference factor, eq (1)
K_ϕ	roll interference factor, eq. (5)
ℓ_r	reference length; body diameter for Army generalized missile, fin root chord for triservice missile
M_∞	free-steam Mach number
s_m	maximum span of fin measured from body axis
S_R	reference area; body cross-sectional area for Army generalized missile, fin planform for triservice missile

10

x	axial distance measured behind leading edge of root chord
$\bar{x}$	axial center-of-pressure location of wing alone
x_{HL}	value of x of hinge line
$\bar{x}_\alpha$	axial center-of-pressure position of fin loading due to α
$\bar{x}_\delta$	axial center-of-pressure position of fin loading due to δ
$\bar{x}_p$	center-of-pressure of $(CNF)_p$
$\bar{x}_v$	axial center-of-pressure position of fin loading due to body vortices
$\bar{y}_v$	lateral position of fin loading due to body vortices measured from body axis
V_∞	free-stream velocity
α	angle of attack of fin, eq. (3)
α_c	body angle of attack
α_{eq}	equivalent angle of attack, eq. (6)
$\alpha_{eq,o}$	value of α_{eq} for $\delta = 0$
$\alpha_{eq,\delta}$	value of α_{eq} with control deflection
$(\Delta\alpha_{eq})_{ij}$	change in equivalent angle of attack of fin i due to deflection of fin j
$(\Delta\alpha_{eq})_v$	change in equivalent angle of attack due to body vortices
β	angle of sideslip of fin, eq. (3)
δ	fin deflection angle (degs.), see note 1
δ_p	pitch control deflection angle for both horizontal fins, deflected trailing edge down
δ_i	value of δ for fin i, see note 2
λ	fin taper ratio
Λ_{ij}	change in α_{eq} for fin i due to deflection δ_j of fin j, eq. (13)
$\Lambda_{\ell e}$	sweep of leading edge of horizontal (unrolled) fin
ϕ	roll position of fin
ϕ_i	roll position of fin i

Note 1. With respect to positive control deflections, the convention for the Army generalized missile is different from that for the triservice missile. For the Army generalized missile, positive pitch deflections of the horizontal fins corresponds to trailing edge down. Positive yaw deflection of the vertical fins is trailing edge to the right looking forward. For the triservice missile, positive fin deflection for all fins corresponds to trailing-edge deflection in the clockwise direction looking forward.

Note 2. For the Army generalized missile the fins are numbered counterclockwise starting with fin 1 at the leeward meridian. For the triservice missile the numbering is clockwise starting with fin 1 at the leeward meridian.

1. INTRODUCTION

All-movable controls are extensively used in missiles, and it has been traditional to obtain the control effectiveness and hinge moments from extensive wind-tunnel testing over the operating range. Only then can the maximum hinge moments be determined, and thereby the weight and size of the control actuator. In reference 1, a preliminary method for estimating hinge moments of all-movable controls is advanced, but several significant limitations of the method are noted. Probably the principal limitations are due to transonic nonlinearities in the Mach number range 0.6 to 1.2 It is the propose of this study to investigate further these transonic nonlinearities with a view to extending the range of applicability of the method.

One way of predicting hinge moment is to assemble a systematic data base and to interpolate in the base. A systematic triservice data base is being assembled under a joint effort by NASA-Langley Research Center and NEAR Inc. The NEAR Inc. work is being accomplished under Office of Naval Research Contract N00014-81-C-0267, jointly sponsored by the Army, Navy, and Air Force. The resulting data base covers fin planforms of aspect ratio 1 to 4, taper ratio 0 to 1, and Mach numbers 0.6 to 4.5 to high angles of attack and control deflections. If a rational aerodynamic model for estimating hinge moments can be established based on these data, then it can be generalized to apply to configurations with fins mounted at different longitudinal positions on the body, to configurations having different ratios of body diameter to fin span, and to configurations with all-movable controls influenced by forward fixed or movable fins. In this way the purely emperical results can be generalized to a configuration space of three more parameters. Because of the extensive testing needed to establish the primary data base, it would be impossible to extend the data base to such a broad configuration space experimentally.

The rational modelling required to extend the data base is described in reference 1. It consists of several parts, the first

part of which is correlation curves of the data constructed on the basis of the equivalent angle-of-attack concept, subsequently to be described. The second part consists of a vortex model used to estimate the effect of body vortices or other vortices on the all-movable fin characteristics. We will apply these two tools to systematic transonic data to determine the limitations of the method, to identify phenomena not accounted for by the method, and to investigate means for modelling these phenomena in the method.

In what follows the report describes relevant background material including the equivalent angle-of-attack concept and its application to the Army generalized missile. Experimental results on pitch-yaw control coupling and interference between a deflected and undeflected fins are analyzed. Next, a systematic analysis is made of the experimental results for an aspect ratio 2 delta control mounted on a triservice missile using the hinge-moment prediction method and a supersonic missile program.

2. BACKGROUND; ARMY GENERALIZED MISSILE RESULTS

2.1 Introductory Remarks

In references 1 and 2 special effects exhibited by transonic all-movable controls have been described. It is the purpose of this section to summarize these effects. There is at this time no published data base on all-movable control effectiveness and hinge moments for systematic planform variations. However, available data will be analyzed. Generally speaking, the state of the art will be summarized.

Hinge moment is the product of the fin normal force and the normal distance from the center of pressure to the hinge line. The fin normal force is a measure of the fin effectiveness so that anything affecting fin effectiveness influences hinge moment.

2.2 Nonlinear Wing Section Effects
on Transonic Hinge Moments

There are relatively few studies in the general literature concerning the transonic characteristics of all-movable controls. Many measurements of the effectiveness and hinge moments of all-movable controls in the transonic range have been made on particular missiles, but these data are unpublished and reside in the archives of the missile manufacturers.

In reference 1, a general preliminary method of predicting all-movable control fin hinge moments was presented based on the equivalent angle-of-attack method (later to be described). It was concluded "the method is not accurate at transonic speeds principally because no method exists to account for wing section effects on axial center-of-pressure location."

It is possible to illustrate the effects of wing section on the axial center-of-pressure location by comparison of two different data sets differing in wing section. The first data set is that of references 3 and 4 which includes the systematic set of fins shown in figure 1. Reference 4 presents figures of the tabulated data of reference 3. The fin-alone characteristics were determined by force measurement on a reflection plate. The second set of data is that of references 5 and 6 which include the systematic set of wings shown in figure 2. These wings were tested as pressure models supported by a dog-leg sting with the orifices on the surface opposite the sting to minimize sting interference.

It is of interest to compare the normal-force curves and axial center-of-pressure locations for the wings of both sets for $R = 2$, $\lambda = 0.5$. These wings correspond to fin P_8 of the Stallings-Lamb-Briggs set (fig. 2) and fin T23 of the Baker set (fig. 1). It is noted that fin P_8 has a root-chord thickness ratio of 0.088, which increased linearly toward 0.166 at the tip, but does not attain this value at the tip because of the bevel. Fin T23 has a thickness ratio of 0.049 at the root chord and appears to change slowly (if at all) as the section moves

15

spanwise toward the tip. Both fins show varying thickness
distributions with changes in spanwise position.

The normal-force comparisons for the fins are shown in
figures 3(a) and 3(b), respectively, for Mach numbers of 0.8
and 1.2. Note that the thicker wing, P_8, shows a stall near
$\alpha = 20°$ while the thinner wing does not. The stall of wing P_8
makes it difficult to apply the equivalent angle-of-attack
concept to this wing above the stall.

The wing axial center-of-pressure positions are shown in
figure 4. There are significant differences between the axial
center-of-pressure locations of the two wings. These and the
results from the foregoing figure exhibit the differences that
wing section can make on the quantities influencing hinge-moment
coefficients for wings alone. These differences can be expected
to appear also in fins attached to circular bodies. Admittedly
the P_8 wing is fairly thick and accentuates differences due to
wing section. However, wings P_2 and T31 of aspect ratio 0.5 and
taper ratio 0.5 which are both fairly thin, also show pronounced
stall differences at $M_\infty = 0.8$ and some significant center-of-
pressure differences at $M_\infty = 0.8$. The differences at $M_\infty = 1.2$
are not large.

The points to be learned from these observations are that
a high angle-of-attack hinge-moment predictive method at transonic
speeds should be able to account for effects of wing section on
stall characteristics and center-of-pressure location. Also,
any systematic data base to obtain transonic hinge moment data
should not have different airfoil sections from fin to fin.

2.3 Linear Equivalent Angle-of-Attack Method

The nonlinear equivalent angle-of-attack method is described
in reference 7 in full mathematical detail, and here we will
briefly describe the linear form of the concept preparatory to
exhibiting some transonic nonlinearities in existing data. The
first notion to be considered is the so-called "wing alone." If
two fins, which are mirror images of one another, are present on

16

a body at different ends of a diameter, then the wing alone
consists of the wing formed by joining the fins at a common
root chord. The equivalent angle of attack of a fin on a body
with normal-force coefficient CNF is the angle of attack of the
wing alone at which its normal-force coefficient CNW is equal
to CNF. The normal-force coefficients CNF and CNW should be
based on the fin planform area and the wing planform area,
respectively, to avoid a complicating factor of two.

Anything that can influence the normal force on a fin will
affect its equivalent angle of attack. We will consider the fol-
lowing four influences.

    (1)   Body angle of attack

    (2)   Fin deflection angle

    (3)   Fin roll angle

    (4)   Induced vortex effects

Let us now consider the first influence; namely body angle of
attack. If the fins are horizontally mounted on a body of revo-
lution at angle of attack, there will be additional upwash at
the positions the fins would occupy due to speed up of the cross
flow to get around the body. As a result the average angle of
attack of the fins is greater than α_c, the body angle of attack.
If CNF is the normal-force coefficient of the fin and α_{eq} its
equivalent angle of attack, then a fin interference factor for
angle of attack can be defined as follows.

$$K_W = \frac{\alpha_{eq}}{\alpha_c}; \quad \delta = 0 \tag{1}$$

In other words, the equivalent angle of attack is $K_W \alpha_c$ for the
horizontal fins. The factor K_W is given by the ratio of the
fin normal-force coefficient to that for the wing alone at α_c
only in the case of a linear normal-force curve, which will not
be the case for high angles of attack. Based on slender-body
theory, K_W, is a function only of $a/s_m{}^*$.

---

 *See "Missile Aerodynamics" by Jack N. Nielsen

17

Let us now consider the effect of all-movable control deflection on equivalent angle of attack. For this purpose, consider the following sketch, giving the fin numbering system for a cruciform fin-body combination, and establishing the roll angle ϕ of the combination. Let $\phi = 0$, and let the horizontal fins develop

rear view
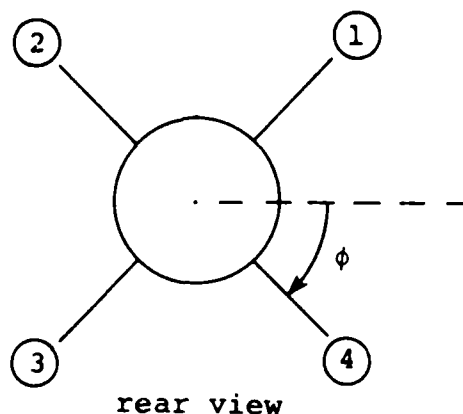
a normal-force coefficient $(CNF)_o$ at $\delta = 0$ and CNF at $\delta \neq 0$. Let the corresponding equivalent angles of attack be $\alpha_{eq,o}$ and $\alpha_{eq,\delta}$. Then let a control-effectiveness factor k_w be defined as

$$k_w = \frac{\alpha_{eq,\delta} - \alpha_{eq,o}}{\delta} \qquad (2)$$

The contribution of the fin deflection δ to fin equivalent angle of attack is thus $k_w \delta$. If the fins were mounted on an infinite reflection plane, then k_w would be unity. However, a circular body is not a perfect reflection plane so that k_w is usually less than unity. What is interesting, however, is that k_w is not much less than unity on the basis of slender-body theory, having a minimum value of about 0.94.[*]

_____
[*] See "Missile Aerodynamics" by Jack N. Nielsen

18

The roll position of the fin has an influence on the sweep angle of its leading edge relative to the free-stream direction. If $\Lambda_{\ell e}$ is the sweep angle of the leading edge for $\phi = 0°$, then it is $(\Lambda_{\ell e} + \alpha_c)$ for $\phi = -90°$ and $(\Lambda_{\ell e} - \alpha_c)$ for $\phi = +90°$. As a result the fin in the first quadrant, $-90° \leq \phi \leq 0$, loses normal force and the fin in the fourth quadrant gains normal force. The angle of attack of the fin, α, and its sideslip angle, β, are related to α_c and ϕ in accordance with the pitch-roll sequence.*

$$\sin \alpha = \sin \alpha_c \cos \phi$$
$$\sin \beta = \sin \alpha_c \sin \phi \tag{3}$$

The change in normal force due to roll angle (other than the direct effect on α) is proportional to the product $\alpha\beta$. The same holds true for the corresponding change in the equivalent angle of attack. Thus

$$\Delta\alpha_{eq} \sim \alpha\beta \tag{4}$$

The constant of proportionality, K_ϕ, is normalized by $4/\mathbb{R}$ since slender-body theory yields this scaling for the aspect ratio of delta wings. We thus have

$$\Delta\alpha_{eq} = \frac{4}{\mathbb{R}} K_\phi \, \alpha\beta = \frac{4}{\mathbb{R}} K_\phi \, \alpha_c |\alpha_c| \, \sin \phi \cos \phi \tag{5}$$

The vortical effect on equivalent angle of attack is the angle of attack induced normal to the fin by the vortices in the field together with their images in the body. Without explaining how this quantity is calculated, we simply designate it by $(\Delta\alpha_{eq})_v$. The equivalent angle of attack for a fin at roll angle ϕ accounting for all four effects and allowing for negative angle of attack is

---

*See "Missile Aerodynamics" by Jack N. Nielsen

19

$$\alpha_{eq} = K_W \alpha_c \cos \phi + k_w \delta$$

$$+ \frac{4}{R} K_\phi \, \alpha_c |\alpha_c| \, \sin \phi \cos \phi + (\Delta \alpha_{eq})_v \qquad (6)$$

Having established the equation for the equivalent angle of attack on the basis of linearity, it is seen that we have linearily superimposed the four components of the equivalent angle of attack. How nonlinearities can still be treated on this basis will now be explained, and will then be demonstrated in the next section. The basic assumption underlying the equivalent angle-of-attack concept is that the nonlinear behavior of the fin attached to the body is in one-to-one correspondence with that of the wing alone. Specifically if we determine α_{eq} from equation (6), we can then determine CNF as the value of the wing alone C_N at an angle of attack equal to α_{eq}. Further consequences of the concept, neglecting vortex effects, are that the axial and lateral center-of-pressure locations should also similarly be obtained. It also follows that the hinge-moment coefficient without vortex effects should also similarly be obtained. Body vortex effects influence fin center-of-pressure position in a way which does not correlate with α_{eq}. It is best to have data on the wing alone which exhibits its nonlinear behavior, although a wing-alone curve can be simulated by correlation as will be shown.

The equivalent angle-of-attack concept also suggests means for correlating fin data. For instance, when the fin normal-force coefficient is plotted against α_{eq}, all the data should fall on a single curve for variable α, δ, and ϕ for a given Mach number. It is now our purpose to investigate, using data, how far we can go with these notions.

2.4 Some Transonic Correlations Based on Equivalent Angle of Attack at $\phi = 0$, Case I

A basic set of data exists for a canard all-movable control on the Army generalized missile, references 8 and 9. It is quite suitable for checking out the equivalent angle-of-attack concept. The missile and canard fin (C_6) are shown in figure 5, as well

20

as the triservice missile, later to be considered. These data are particularly suitable for the program because nose vortex effects are minimal for these canard fins due to the nose shape and short forebody length. If strong vortex effects occurred, it would be necessary to estimate $(\Delta\alpha_{eq})_v$ in equation (6) in order to check out the equivalent angle-of-attack concept. Thus, the α_{eq} comparisons would be influenced by inaccuracies in the approximate methods now used to estimate $(\Delta\alpha_{eq})_v$.

For the Army generalized missile, three cases will be considered as follows:

Case I: $\phi = 0$; $\delta_p = 0°$, $5°$, $10°$, $15°$
Case II: $-90° \leq \phi \leq 90°$; $\delta_p = 0$
Case III: $-90° \leq \phi \leq 90°$; $\delta_p = 15°$

The first correlations will be of CNF for fin C_6 at $\phi = 0$ for the combined effect of α_c and δ. The correlations have been made for an angle-of-attack range $0 \leq \alpha_c \leq 20°$ and $\delta = 0°$, $5°$, $10°$, and $15°$ for $M_\infty = 0.8$ and 1.3 in figure 6. Correlations are given using both the linear and nonlinear definitions of α_{eq} (ref. 7).

Examining first figure 6(a) we note that the CNF data for $M_\infty = 0.8$ using the linear α_{eq} are quite well correlated for the range of α and δ quoted above. Some scatter at the higher angles of attack is seen but does not cause larger percentage errors in CNF for a given α_{eq}. What is interesting is that a linear α_{eq} correlates the data into a nonlinear normal-force curve. The question arises how the nonlinear α_{eq} correlates the same data. This result is shown in figure 6(b). Note that the correlation is no better, but if anything it exhibits more scatter at high α_{eq}. The same nonlinear behavior of the CNF curve is exhibited. Another difference is exhibited; namely that the maximum α_{eq} is less for the nonlinear α_{eq} correlation. The reason for this is that the nonlinear α_{eq} method utilizes a tangent addition theorem rather than a linear addition theorem, although the effect of δ is linearly additive for both the linear and nonlinear (ref. 1) forms of α_{eq}.

21

Figures 6(c) and 6(d) show correlations for $M_\infty = 1.3$ based on the linear and nonlinear definitions of α_{eq}, respectively. These figures exhibit the same general results as figures 6(a) and 6(b). One notable difference, however, is that the $M_\infty = 1.3$ data exhibit less scatter than the $M_\infty = 0.8$ data. This result is probably associated with the tendency of transonic flow to be more nonlinear if subsonic.

According to the equivalent angle-of-attack concept, the correlation curves should correspond to the normal-force curves of the wing alone. However, we have different correlation curves for the linear and nonlinear definitions of α_{eq}. From the theoretical point of view, the correlation curve for the nonlinear α_{eq} should more closely approximate the wing-alone normal-force curve. We do not have an experimental wing-alone curve in this instance to verify this conjecture. However, we will take a different point of view in the following work. Since it is easier to use the linear α_{eq} definition, we will use the correlation curve for the linear correlation as a "simulated wing-alone curve." If we have CNF versus α_c for $\delta = 0$, we can then determine CNF for various δ.

One final point is made in connection with the correlation curves. Slender-body values of K_W and k_w have been used in calculating α_{eq}, and these values should be used with the correlation curves.

In addition to the fin normal-force coefficients associated with α and δ, we need the corresponding center-of-pressure positions of these normal-force components to determine hinge-moment coefficients in accordance with the following formula. In this equation the

$$
CHM = (CNF)_\alpha \left[\left(\frac{\bar{x}}{c_r} \right)_\alpha - \left(\frac{x}{c_r} \right)_{HL} \right]
$$
$$
+ (CNF)_\delta \left[\left(\frac{\bar{x}}{c_r} \right)_\delta - \left(\frac{x}{c_r} \right)_{HL} \right] \tag{7}
$$

22

reference area is assumed to be the same for CNF and CHM, and the reference length is the root chord. Let us now examine first $(\bar{x}/c_r)_\alpha$ and then $(\bar{x}/c_r)_\delta$.

The values of $(\bar{x}/c_r)_\alpha$ are given in figures 7(a) and 7(b) for $M_\infty = 0.8$ and 1.3, respectively. Results are given for both the left fin (No. 2) and right fin (No. 4) to give an idea of the accuracy of the measurements. As seen in both figures, the measured values for both fins are well within 0.01 of each other. The $M_\infty = 0.8$ data exhibit nonlinear travel of $\bar{x}_\alpha$ which amounts to about 0.07 c_r. The data for $M_\infty = 1.3$ show almost uniform center-of-pressure locations from $\alpha_{eq} = 0°$ to $\alpha_{eq} = 20°$. How roll angle ϕ affects these results will be discussed in the next section.

Values of $(\bar{x}/c_r)_\delta$ are shown as a function of α_c for $M_\infty = 1.3$ and $\delta = 5°$, 10°, and 15° in figure 8 for both fin 2 and fin 4. It is noted that the fin 4 results show generally more rearward center-of-pressure positions than fin 2. A slight difference in hinge-line position could account for the difference. The scatter of the data definitely decreases as δ increases as might be expected. The data for all three δ's has been plotted versus α_c in figure 8(d) for fin 4, exhibiting a correlation with generally less than ±0.01 scatter. Note the differences between the $(\bar{x}/c_r)_\alpha$ results of figure 7(b) and the $(\bar{x}/c_r)_\delta$ results of figure 8(d). Slender-body theory predicts a more rearward position of $(\bar{x}/c_r)_\delta$ than $(\bar{x}/c_r)_\alpha$ of about 0.019 for delta wings, a slightly greater amount than exhibited by the data at low α, but the difference is probably within the experimental error. At values of α_c of about 20°, the value of $(\bar{x}/c_r)_\delta$ approaches the centroid of the fin planform.

What is interesting about figure 8(d) is that $(\bar{x}/c_r)_\delta$ correlates on the basis of body angle of attack rather than the equivalent angle of attack as postulated previously. This could be explained by the fact that the wing-body interference on $(\bar{x}/c_r)_\delta$ is not a strong function of δ. Thus the variable gap geometry with changing δ does not appear to have a significant

23

effect on $(\bar{x}/c_r)_\delta$. Also any boundary-layer effects on $(\bar{x}/c_r)_\delta$
do not depend on δ probably because the short body length in
front of the canard control minimizes boundary-layer effects.

Using figures 6(c), 7(b), and 8(d), fairly good predictions
could be made of hinge moment for fin C_6 at $\phi = 0$ and $M_\infty = 1.3$
for the ranges of α and δ of the correlations.

Consider now the correlations of $(\bar{x}/c_r)_\delta$ at $M_\infty = 0.8$ for
fin C_6. A correlation for $M_\infty = 0.8$ is given in figure 9 for
$(\bar{x}/c_r)_\delta$ similar to that given in figure 8(d) for $M_\infty = 1.3$.
Figure 9 exhibits a number of significant points. First, the
data do not correlate nearly so well with α at $M_\infty = 0.8$ as at
$M_\infty = 1.3$. Also there is a much wider center-of-pressure travel.
It is clear that transonic nonlinearities are acting at $M_\infty = 0.8$
which are not present at $M_\infty = 1.3$.

One point that must be made is that over part of its range
the control is operating on the flat part of the normal-force
correlation curve, figure 6(a). The equivalent angle of attack
range for this flat spot is about 17° to 26°. In figure 10,
the fin normal-force coefficient and hinge-moment coefficient
increments due to 5° of control deflection at $M_\infty = 0.8$ are
plotted versus the equivalent angle of attack at $\delta = 0°$. The
fin thus acts between $\delta = 0°$ and $\delta = 5°$ on the flat part of the
curve in figure 6(a) for an equivalent angle of attack range
from 17° to 21°. Figure 10 shows fin normal-force increments
of nearly zero for this range. However, a significantly large
hinge-moment coefficient is exhibited over this range. Thus
control deflection produces substantially no normal force increase
but large pitching moment changes occur over this range. This
causes the center of pressure of the normal force due to control
deflection to move far rearward as exhibited in figure 9. If
the control produces zero normal force, the center of pressure
would move back to infinity. Whatever transonic wing flow-field
nonlinearity produces the flat spot in CNF versus α_{eq} thus
accounts for the behavior of $(\bar{x}/c_r)_\delta$ exhibited in figure 9.

24

Some correlation curves for fin normal-force coefficient actually show a maximum followed by a minimum in the "stall" region. This would further complicate the behavior of $(\bar{x}/c_r)_\delta$. Also, the reversal of control effectiveness would make such fins undesirable for transonic control.

The foregoing nonlinear behavior has certain implications for a hinge-moment prediction method. The curve of $(x/c_r)_\delta$ must be terminated at some finite value of this parameter as shown in figure 9, and a band exists over which hinge moment would not be predicted. However, from the predicted values on each side of the band, the values in the band would be determined by interpolation.

2.5 Some Transonic Correlations Based on Equivalent Angle of Attack Under Conditions of Roll with No Control Deflection, Case II

The success of the equivalent angle-of-attack concept to correlate both fin normal force and center-of-pressure position as a function of α_c and δ has been explored at zero roll angle, and now we explore its application at other roll angles. First we consider the joint effects of α_c and ϕ for zero control deflection. For this purpose the K_W and K_ϕ terms in equation (6) are relevant.

To obtain a range of ϕ values from $-90°$ to $+90°$, the Army generalized model had only to be rolled by $45°$ and data taken on all fins as follows.
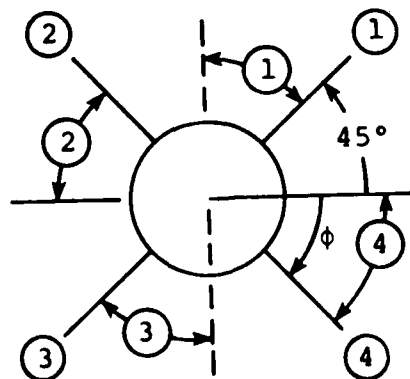
Fins 1, 2, 3, and 4 thus map out the complete equivalent region of fin 4 through the range $90° \geq \phi_4 \geq -90°$. The correlation curves which follow will contain data from all four fins since they cover the range $90° \geq \phi \geq -90°$.

Consider the correlations for $M_\infty = 0.8$ and 1.3 for roll angles of $\phi_4 = 0°$, 30°, 45°, 60°, and 80° with fin 4 in the fourth quadrant and for $\phi_4 = -30°$, -45°, -60°, and -80° with fin 4 in the first quadrant. These results are shown in figure 11. With respect to figure 11(a), the fin normal-force coefficient in the fourth quadrant correlates well for $M_\infty = 0.8$. In the first quadrant, ϕ negative, figure 11(b) exhibits some lack of correlation for the $\phi = -60°$ and $\phi = -80°$ data. However, this effect seems to be principally the result of tares existing at $\alpha_c = 0°$.

Figures 11(c) and 11(d) present the fin normal-force correlation for $M_\infty = 1.3$. Figure 11(c) for the fourth quadrant shows quite good correlation for $0 \leq \phi \leq 80°$ except near the upper end of the α_{eq} range for $\phi = 0°$ and 30°. The disagreement is not serious. The data for the first quadrant, $-80° \leq \phi \leq 0$ also shows good correlations except for the $\phi = 0°$ and $-30°$ cases at high equivalent angles of attack, $\alpha_{eq} > 18°$. It appears that by putting different fairings through the data for the two quadrants, the correlation error can be reduced to a tolerable amount.

Let us now consider the fin center-of-pressure position relative to the hinge line, $(\bar{x}_\alpha - x_{HL})/c_r$. This parameter is assumed to be a function only of equivalent angle of attack according to the equivalent angle concept. It is thus only a function of fin normal-force coefficient by the same token. We have correlated the parameter as a function of fin normal-force coefficient and roll angle in figure 12. The product of abscissa and ordinate yield the hinge-moment coefficient based on the root chord. Looking first at figure 12(a) for $M_\infty = 0.8$ and $0 \leq \phi \leq 80°$, it is seen that all the data correlate well. The travel of the center of pressure across the hinge line at both

26

low α_c and high α_c is an interesting transonic nonlinearity. Figure 12(b) for $-80° \leq \phi \leq 0$ shows the same trend as figure 12(a) for the $0 \leq \phi \leq 80°$ data. However, the $\phi = -80°$ data shows a departure from the correlation with rearward movement of the center-of-pressure position for $\alpha_c > 14°$. The half angle of the nose is approximately $19°$ so that vortices from the surface of the nose do not appear to be the problem at least initially. However, boundary-layer effects are a likely cause for $\alpha_c = 14°$ to $19°$ with separation vortices as the cause at the higher angles of attack. In this case the hinge-moment coefficient is not a maximum. This occurs at about CNF = 0.22 with $(\bar{x}_\alpha - x_{HL})/c_r$ of about -0.035.

Turning now to the data for $M_\infty = 1.3$ in figures 12(c) and 12(d), we see a good correlation for $0 \leq \phi \leq 80°$ generally within a band of ± 0.01. The data for $-80° \leq \phi \leq 0°$ in figure 12(d) exhibit good correlation. For $\phi = -80°$, the fin exhibits centers of pressure closer to the hinge line than the correlation curve in constrast to the $\phi = -80°$ data at $M_\infty = 0.8$ which shows movement away from the hinge line. However, the hinge moments are reduced thereby and the maximum hinge moment is unaffected.

Correlations of CNF and $(\bar{x}_\alpha - x_{HL})/c_r$ for $-90° \geq \phi \geq 90°$ and α_c up to $20°$ are thus adequate for estimating hinge moments for $\delta = 0$ at $M_\infty = 0.8$ and 1.3 for most of the roll range. For $\phi = -80°$, slight departures of $(\bar{x}_\alpha - x_{HL})/c_r$ from the correlation curves cause inaccuracy in hinge-moment prediction. However, these inaccuracies do not occur in a region of maximum hinge moment.

2.6 Correlations Based on the Equivalent Angle-of-Attack Concept Under Conditions of Combined Roll and Control Deflection, Case III

In this section we analyze control deflection data of the C_6 fin mounted in the canard position on the Army generalized missile. First, we will see how well the combined effects of roll and control deflection on fin normal force are correlated by use of the equivalent angle of attack concept. Then, we will examine

27

the effects of roll angle on the fin center-of-pressure position
due to the fin deflection. For these purposes we have data for
the following test conditions for both M_∞ = 0.8 and 1.3

ϕ	$\delta_{1,3}$	$\delta_{2,4}$
0	0	15°
0	15°	0
45°	0	15°
45°	15°	0

Since data for all four fins were obtained, we have results for
the following fin positions; -90°, -45°, 0°, 45°, and 90°.

The fin normal-force coefficient has been correlated as a
function of equivalent angle of attack in figure 13 for M_∞ = 0.8
and 1.3. Examining figure 13(a) for M_∞ = 0.8, we see the data
for ϕ = -45°, 0°, and 45° for an angle of attack range from
0 to over 20° correlate well. According to the equivalent angle
of attack concept, the normal forces acting on the vertical fins
for ϕ = 0 with 15° of control deflection should not change with
angle of attack. The data for these two fins, ϕ = -90° and
ϕ = +90°, are shown as data bands at an α_{eq} of 14°. The width
of the bands is within the scatter of the general correlation.
The data band for ϕ = -90° is biased upward by 0.05 due to tares
not accounted for in the data reduction.

Consider now the data for M_∞ = 1.3 in figure 13(b), which
has been plotted to an expanded scale. This figure shows the com-
bination of roll angles and fins which went into the data cor-
relation. The data generally correlated well. The only special
phenomenon worth noting is that the ϕ = -45° data exhibit normal-
force stall for the last data point, which corresponds to α_c
above 20°.

Several observations concerning these correlation curves
are relevant. Even though they are for δ = 15°, it is presumed
that they also are valid for $\delta \leq$ 15°. The fact that the α_{eq}
correlation works for negative ϕ's can be attributed to lack of
body viscous or vortex effects for $\alpha_c \leq$ 20° for any C_6 fin in

28

the canard section. It should not be expected for the C_6 fin in a tail position that the negative ϕ data could be so correlated since they will contain significant body vortex effects at large angle of attack. Also, all results so far apply to an $R = 3.53$ wing, and may be modified for lower aspect ratios and large taper ratios. This question will be addressed in connection with the data of the triservice data base.

Let us now examine the effect of roll angle on the center-of-pressure position of the fin load developed by fin deflection as exhibited in figure 14 for $M_\infty = 0.8$ and 1.3. With respect to figure 14(a) for $M_\infty = 0.8$, we note that the equivalent angle of attack for the fin at $\phi = \pm 90°$ is invariant with changes in angle of attack. The bands of fin center-of-pressure position from 0 to 22.5° of angle of attack are shown at $\alpha_{eq} = 14°$. Both deflected fins have this value of α_{eq} at $\alpha_c = 0$, and should all have the same center-of-pressure position at this point. The scatter is a measure of the precision at $\alpha = 0°$. It is noted that at the upper and lower ranges of α_{eq} the data correlates fairly well. However, in the 17° to 20° range of α_{eq}, the fin operates over the flat spot of the normal-force correlation, as seen in figure 6(a). In this range, control deflection produces very small additional normal forces but large hinge moments are generated as a result of downloads in front on the hinge line and uploads behind it. The result is that the center-of-pressure position migrates a long distance behind the hinge line. The flow phenomenon which produces this effect is sensitive to roll angle so that the absolute accuracy of correlation in the middle range of α_{eq} is not good, nor are the data repeatable with the same precision as at the two end ranges. Since the lever arm for hinge moment is long in the midrange, the percent error due to the increased scatter here is not so serious as it looks. It is clear that the equivalent angle of attack concept does a good job of correlating the effects of roll angle except in the midrange of equivalent angle of attack.

29

We now turn our attention to $M_\infty = 1.3$ in figure 14(b) which is plotted to a much expanded scale compared to figure 14(a). For the low range of α_{eq}, good correlation is obtained. For the high range there is a systematic departure from correlation which depends on ϕ. These results are due to a cause not present in the $M_\infty = 0.8$ data, a cause not understood. These departures from correlation are larger than the limits which we feel are required for good hinge-moment prediction for controls which have small hinge moments. This effect places limits on the angle of attack to which the equivalent angle-of-attack concept is valid as presently used. Further discussion of this behavior will be made in connection with the triservice missile.

2.7 Summary of Fin C_6 Correlation Curves

The discussion in the three preceding sections will now be summarized to bring the results into perspective. The following summary is presented for that purpose:

CASE I.- Effect of Control Deflections,

$$\phi = 0 \qquad \delta_p = 0°, 5°, 10°, 15° \qquad 0 < \alpha_c \le 20°$$

CNF versus α_{eq}
_____

      Figure 6(a), $M_\infty = 0.8$:

      Figure 6(b), $M_\infty = 1.3$:   Good Correlation

$(\bar{x}/c_r)_\alpha$ versus α_{eq}
_____

      Figure 7(a), $M_\infty = 0.8$:   No correlation

      Figure 7(b), $M_\infty = 1.3$:   involved

$(\bar{x}/c_r)_\delta$ versus α_c
_____

      Figure 9, $M_\infty = 0.8$:   Good correlation, $\bar{x}_s \to \infty$

      Figure 8(d), $M_\infty = 1.3$:   Good correlation

CASE II.= Effect of ϕ; no control deflections

$$-80° \le \phi \le 80°; \ \delta_p = 0, \ 0 \le \alpha_c \le 20°$$

CNF versus α_{eq}
_____

      Windward fins, $0 \leq \phi \leq 80°$

            Figure 11(a), $M_\infty = 0.8$:   Good correlation

            Figure 11(c), $M_\infty = 1.3$:   Good correlation

      Leeward fins, $-80° \leq \phi \leq 0°$

            Figure 11(b), $M_\infty = 0.8$:   Fair correlation

            Figure 11(d), $M_\infty = 1.3$:   Fair correlation

$(\bar{x}/c_r)_\alpha$ versus CNF
_____

      Windward fins, $0 \leq \phi \leq 80°$

            Figure 12(a), $M_\infty = 0.8$:   Good correlation

            Figure 12(c), $M_\infty = 1.3$:   Good correlation

      Leeward fins, $-80° \leq \phi \leq 0°$

            Figure 12(b), $M_\infty = 0.8$:   Good correlation

                                         except for $\phi = -80°$

                                         above $\alpha_c = 10°$

            Figure 12(d), $M_\infty = 1.3$:   Good correlation

                                         except fair

                                         for $\phi = -80°$

CASE III.= Combined effects of roll and fin deflection

          $-90° \leq \phi \leq 90°$, $\delta_p = 15°$, $0 \leq \alpha_c \leq 20°$

CNF versus α_{eq}
_____

            Figure 13(a), $M_\infty = 0.8$:   Good correlation

            Figure 13(b), $M_\infty = 1.3$:   Good correlation

$(\bar{x}/c_r)_\delta$ versus α_{eq}
_____

            Figure 14(a), $M_\infty = 0.8$:   Fair correlation;

                                         $x_\delta \to \infty$

            Figure 14(b), $M_\infty = 1.3$:   Good correlation up

                                         to $\alpha_{eq} = 24°$,

                                         departure from

                                         correlation thereafter

For Case I no departures from correlation occur. For Case II the values of $\bar{x}_\alpha$ do not correlate for $\phi_2 = -80°$ above $\alpha_c \approx 10°$ at $M_\infty = 0.8$. This could be the result of an inviscid or viscous effect. For Case III and $M_\infty = 1.3$, $\bar{x}_\delta$ does not correlate for $\alpha_{eq} > 24°$ for roll angles other than $\pm 90°$. This behavior puts a limit in angle of attack of the fin deflection results which depends on ϕ. For $M_\infty = 0.8$, $\bar{x}_\delta$ approaches infinity when the control between $\delta = 0$ and $\delta \neq 0$ acts over the fin stall region, but fair correlation is obtained.

3. CONTROL NONLINEARITIES AND CROSS COUPLING AT HIGHER ANGLES OF ATTACK

3.1 High Angle-of-Attack Transonic Control Nonlinearities

So far we have been concerned with a transonic hinge-moment prediction method for angles of attack to 20° and control deflections of ±20°. In this section some high angle-of-attack transonic control nonlinearities will be considered.

The nonlinearities to be investigated are control effectiveness at high angles of attack as influenced by roll angle and the effect of angle of attack on yaw control effectivness. These results are based on data for the C_6 fin in the canard position on the Army generalized missile. We will use the synthesized "wing-alone" curves for C_6 figure 6(a) and 6(c).

To obtain the control interference factor, k_w, we need to know the fin normal-force coefficient at deflection δ, CNF_δ, and the corresponding quantity for $\delta = 0$, $(CNF)_o$. Corresponding to these normal-force coefficients, we have equivalent angles of attack $\alpha_{eq,\delta}$ and $\alpha_{eq,o}$ from the wing-alone curve. Then from equation (2) we have

$$k_w = \frac{\alpha_{eq,\delta} - \alpha_{eq,o}}{\delta} \tag{8}$$

We have determined k_w for the C_6 fin for pitch control with $\delta = 5°$, 10°, and 15° for Mach numbers of 0.8 and 1.3. The results for the C_6 fin at $M_\infty = 0.8$ are shown in figure 15(a) and at $M_\infty = 1.3$ in figure 15(b). If the $\delta = 0$ and $\delta \neq 0$ data were not at the same angle of attack, the $\delta \neq 0$ data were interpolated to the correct angle before differencing.

The results in figure 15(a) for $M_\infty = 0.8$ show considerable scatter, but the data exhibit a clearcut drop in fin effectiveness between $\alpha_c = 20°$ and $\alpha_c = 50°$. With regard to the scatter in the data, this is due principally to the fact that the "wing-alone" curve, figure 6(a), has a flat spot in the approximate range $17° < \alpha_{eq} < 26°$. Consider now a fin at an equivalent angle of attack

33

equal to 17° and then add 5° of control deflection. The fin now operates on the flat spot and adds very little normal force at a large increase in α_{eq}, resulting in a large k_w. It is thus not possible to obtain α_{eq} accurately from CNF if $\partial(CNF)/\partial\alpha_{eq}$ is small or zero. If the derivative is anywhere negative, the α_{eq} for a given CNF can be triple valued. Accordingly trying to obtain k_w from a CNF correlation with a flat spot is not a well posed problem. It is noted that the scatter decreased as δ increases.

In this particular case, we do not have an experimental wing-alone curve but have used a synthesized wing-alone curve based on data for $\alpha_c \le 20°$. However, the falling off of k_w for $\alpha_c > 20°$ is a valid result. By using the slender-body value of k_w up to $\alpha_c = 20°$, a good correlation has been obtained. If we were to use a k_w based on a mean curve faired through the data for $20° \le \alpha_c \le 50°$, a good correlation would be obtained for the entire range.

The scatter of the k_w data for $M_\infty = 1.3$, figure 15(b) is not so great as for $M_\infty = 0.8$. The slender-body value of k_w should provide a fair correlation curve for CNF for $\delta = 5°$ and $10°$ nearly to $\alpha_c = 50°$. For $\delta = 15°$, the slender-body value of k_w would provide correlation to about $25°$, but thereafter the data, which exhibit the least scatter for any δ, show a definite drop off to about 0.7 at $\alpha_c = 50°$. This value at $M_\infty = 1.3$ is to be compared with a value of about 0.2 for $M_\infty = 0.8$ for all δ's. Thus, the loss of control effectivess at high angle of attack shown at $M_\infty = 0.8$ is much reduced at $M_\infty = 1.3$.

The effect of roll angle on control interference factor k_w has been determined for $\phi = 45°$ for the upper and lower fins. In this case, fins 2 and 4 were deflected $15°$ with fins 1 and 3 undelected. The calculated values of k_w are shown in figure 16 for $M_\infty = 1.3$. It is noted that the value of k_w for the windward fin, fin 4, is approximated in the mean by the slender-body value for angles of attack from 0 to $50°$. However, the leeward fin shows fair agreement with slender-body theory up to about $\alpha_c = 20°$,

but falls off in effectiveness thereafter to nearly zero at $\alpha_c = 50°$.

It is noted that these results in figures 15 and 16 are included in reference 2, but the values of k_w shown there are quite different. This results from the facts that the wing-alone curve is now different as well as the equivalent angle-of-attack definition.

It is of interest to see how yaw control is affected by angle of attack. As a preliminary introduction to this subject, we have plotted the normal-force coefficients developed by fins 1 and 3 with 15° of yaw control in figure 17. The test conditions correspond to $\phi = 0°$ and $M_\infty = 0.8$. The data were taken on a low-angle sting from $\alpha_c = 0°$ to $\alpha_c = 24.5°$ and on a high-angle sting from $\alpha_c = 20°$ to $\alpha_c = 50°$. It is noted that the fin normal-force coefficient does not change significantly between $\alpha_c = 0°$ and $\alpha_c = 20°$. This result would be predicted by the equivalent angle of attack concept since α_{eq} does not depend on α_c for $\phi = \pm 90°$. The loss in CNF above $\alpha_c = 20°$ shows that k_w is decreased below the slender-body value. What should be noted is the fact that fins 1 and 3 do not have the same CNF at $\alpha_c = 0$ where they should be equal. The data from the low-angle sting for fin 1 contains a significant tare, a fact which should be noted for subsequent discussion.

In figure 18(a), the values of the control interference factor derived from the data of figure 17 are shown. In the range $0 \leq \alpha_c \leq 20°$, the values of k_w for the windward fin are in good agreement with the slender-body values but the values for the leeward fin are nearly twice as large. This fact is associated with the tares in the data for the leeward fin as well as the fact it is operating on the flat spot of the wing-alone curve. The correct conclusion is that both fins follow slender-body theory well up to $\alpha_c = 20°$, but show a systematic decline in effectiveness as the angle of attack increases. Similar data for $M_\infty = 1.3$ are shown in figure 18(b). From $\alpha_c = 0°$ to $\alpha_c = 30°$, the slender-body

35

value of k_w is a fair approximation to the data, but k_w decreases as α_c increased above $\alpha_c = 30°$.

The loss of yaw control effectiveness above about $\alpha_c = 20°$ in figure 18 is also accompanied by nonlinear center-of-pressure travel. The centers of pressure of fins 1 and 3 are shown in figure 19 for the same conditions as figure 18. Neither fin shows large changes in $(\bar{x} - x_{HL})/c_r$ up to about 20° at either Mach number, but there are generally large forward shifts in center-of-pressure position above $\alpha_c = 20°$.

3.2 Control Cross-Coupling Effects to High Angles of Attack

Sufficient data are available to show the coupling between the pitch and yaw control functions for the C_6 fins mounted in the canard position on the Army generalized missile. Pitch control is defined by the following set of control deflections

$$\delta_2 = \delta_4 \neq 0; \quad \delta_1 = \delta_3 = 0 \tag{9}$$

and yaw control by

$$\delta_1 = \delta_3 \neq 0; \quad \delta_2 = \delta_4 = 0 \tag{10}$$

3.2.1 Effect of pitch control on yaw control

We look at the effects of pitch control on yaw control for the leeward and windward fins for $M_\infty = 0.8$ and 1.3 up to $\alpha_c = 50°$. Results for the leeward fin at $M_\infty = 0.8$ are shown in figure 20, where the normal-force coefficient, center-of-pressure position due to control deflection, and hinge-moment coefficient are shown with and without 15° of pitch control for 15° of yaw control at $\phi = 0$. The changes in CNF and $(\bar{x}_\delta - x_{HL})/c_r$ shown in figures 20(a) and 20(b) are not negligible, but their combined effects on hinge-moment coefficient, shown in figure 20(c) are not large.

36

Results for the windward fin are given in figure 21 corresponding to those for the leeward fin in figure 20. Again, the effects on CHM are small. The effects of pitch control on CNF and $\bar{x}_\delta$ for the yaw fins are much less at $M_\infty = 1.3$ than at $M_\infty = 0.8$.

Before examining the results for $M_\infty = 1.3$ in figures 22 and 23, let us consider the zone of influence of one fin on another for the supersonic speeds. To arrive at a neighboring fin in cruciform arrangement, a pressure impulse from the leading edge of the root chord of one fin must travel a lateral distance $\frac{\pi}{2}a$ around the body surface along the Mach line. The downstream distance traveled in this time is

$$x = \frac{\pi}{2}a\sqrt{M_\infty^2 - 1} \tag{11}$$

For dimensions of the C_6 fin on the A   generalized missile, we have:

$$
\begin{aligned}
a &= 2.5 \\
c_r &= 4.0 \\
x &= 3.26 \\
M_\infty &= 1.3
\end{aligned}
$$

Since the root chord is only 4.0 inches, only the last 0.76 inches of the root chord are subject to interference from the neighboring fins. Thus at $M_\infty = 1.3$ the fin-fin interference near $\alpha_c = 0$ should be greatly reduced. At angle of attack, the local Mach numbers betwen fins are not exactly 1.3 and the area of influence of one fin on another can change. Also, the effect of a fin may propagate forward through the boundary layer.

The results for the leeward fin at $M_\infty = 1.3$ are given in figure 22 for comparison with similar results for $M_\infty = 0.8$ in figure 20. The effects of pitch control on the yaw-control normal force and center of pressure are definitely less for $M_\infty = 1.3$

compared to those for $M_\infty = 0.8$. The effects of pitch control on the hinge-moment coefficient of the leeward fin are quite small.

To study the effects of Mach number on the cross-coupling effects on the windward fin, we compare figures 21 and 23. The magnitude of the effects on normal force and center-of-pressure position are about the same at both Mach numbers. What is of interest is that the effects are very small at both Mach numbers for $\alpha_c < 20°$. The effect on the hinge-moment coefficient is small.

In order to put the foregoing information into perspective the following listing summarizes the approximate changes in the vertical fin coefficients due to pitch control.

	$M_\infty = 0.8$	$M_\infty = 1.3$
Leeward fin:		
CNF:	20%	6%
$\bar{x}_\delta/c_r$:	0.06	0.005
CHM:	small	small
Windward fin:		
CNF:	5% – 6%	6%
$\bar{x}_\delta/c_r$:	0.007	0.02
CHM:	small	Low α: significant
		High α: small

The above changes are indicative of the size of the effects, but are not to be taken as quantitatively precise since they contain experimental error. The important results are that the leeward fin at $M_\infty = 0.8$ exhibits significant effects of fin-fin inter-ference on CNF and $\bar{x}_\delta$, but they are apparently compensating on hinge moments for the case in question. This is probably not a general result. The effects of pitch control on hinge-moment coefficient are small in all cases except for the windward fin at $M_\infty = 1.3$ at angle of attack up to 20° (figure 23(c)). At $M_\infty = 1.3$, the effects exhibited by the leeward fin are much less

than those exhibited at $M_\infty = 0.8$ probably as a result of the rule of forbidden signals.

3.2.2 Effects of yaw control on pitch control

We have seen that the application of pitch control had generally small effects on the hinge moments of the yaw panels even at high angles of attack at $M_\infty = 0.8$ and 1.3. We now examine the effects of yaw control on the aerodynamic characteristics of the pitch panels.

Figure 24 exhibits how 15° of yaw control changes the normal force, center of pressure, and hinge moments of the left horizontal fin with 15° of pitch control at $M_\infty = 0.8$. Positive yaw control, trailing edge to the right, puts negative pressure on the left side of the missile. At high angles of attack, the negative pressure change under fin 2 is greater than that above it so that yaw control caused a reduction in the normal force acting on the fin as shown in figure 24(a). A reduction in fin normal force causes a slight forward movement in center of pressure at high α in accordance with the results of figure 24(b). However, the effect on the hinge moments of fin 2 are small as shown in figure 24(c).

Figure 25 shows the same results for the right fin that figure 24 shows for the left fin. Generally the small changes in fin normal force and center-of-pressure position are opposite to those for the left fin, but the resulting changes in hinge-moment coefficient are small.

In figure 26 are shown the effects of yaw control on the hinge moments of the horizontal fins at $M_\infty = 1.3$ with 15° of pitch control. Neither the left nor right panels show any significant effect of the yaw control on their hinge moments.

Let us now summarize the effects of yaw control on the aerodynamic characteristics of the horizontal pitch fins.

39

	$M_\infty = 0.8$	$M_\infty = 1.3$

Left fin:

CNF:	10%	
$\bar{x}_\delta/c_r$:	0.003	
CHM:	small	small

Right fin:

CNF:	8%	
$\bar{x}_\delta/c_r$:	0.004	
CHM:	small	small

Clearly the hinge moments of the horizontal panels are not significantly influenced by yaw control.

4.   SOME RESULTS OF THE TRISERVICE DATA BASE

4.1   Introductory Remarks

Under an ONR contract, N00014-80-C-0700, jointly funded by the Army, Navy, and Air Force, a systematic data base is being compiled on the control effectivess and hinge moments of all-movable control surfaces through the range of Mach numbers up to high angles of attack.   The range of parameters is as follows:

$$M_\infty: \quad 0.6 - 4.5$$
$$\alpha: \quad 0 - 20°, \text{ transonic}$$
$$0 - 45°, \text{ supersonic}$$
$$\delta: \quad \pm\ 40°$$
$$AR: \quad 1 - 4$$
$$\lambda: \quad 0 - 1$$
$$\phi: \quad 0 - 180°$$

The aspect ratio and taper ratio ranges of the fins in the data base are given in the following matrix.

Aspect ratio \ Taper ratio	0	0.5	1.0
1		X	
2	X	X	X
4		X	

When completed, this data base will be adequate to perform purely empirical predictions of fin normal force, hinge moment, and bending moment over the range of parameters.

Two points are noteworthly in the data base. First, all fins have the same 6.3 percent double-wedge airfoil section in the streamwise direction. This fact permits interpolation between fins since changes in airfoil section are known to have significant effects on fin aerodynamic properties at transonic speed. A second point is that the usual method of making individual pitch control, yaw control, and roll control tests has not been used. Instead, only one fin has been deflected during the control tests, and the reaction on all four fins have been measured. In this way, any combination of fin deflections can be predicted accounting for fin-fin interference by linear superposition. Since fin-fin interference is a quantity of lower order than the primary quantities generated by a control on itself, linear superposition should yield sufficiently accurate results.

4.2 Sign Conventions and Symmetry Relationships

Certain conventions with respect to roll angle, fin deflection and fin normal-force coefficient are used in the triservice data base, and these conventions will be adhered to in the following sections. They differ from those previously used in the Army generalized missile tests.

The first convention refers to the fin numbering system. The fins are numbered in a clockwise fashion starting with fin 1 at the top vertical position in the zero roll position. Positive roll angle of the missile is in the clockwise direction.

It is our purpose to correlate the data for an $Æ$ = 2, λ = 0 control fin using the equivalent angle-of-attack concept for the range of α_c of 0 - 20° and δ of $\pm$ 20°. The same correlations will be used as for the C_6 fin of the Army generlized missile. If the correlations are successful, we hope to be able to reduce the calculations of hinge-moment coefficient to a hand

41

calculation based on experimental correlation curves. Also, the amount of data necessary to obtain the correlation curves is far less than that needed to obtain a complete data base over the test range of variables. After describing the sign conventions used in the triservice data base, we will consider the fin-fin interference factors.

The fin numbering system and positive fin normal-force directtions for $\phi = 0$ are pictured as follows:
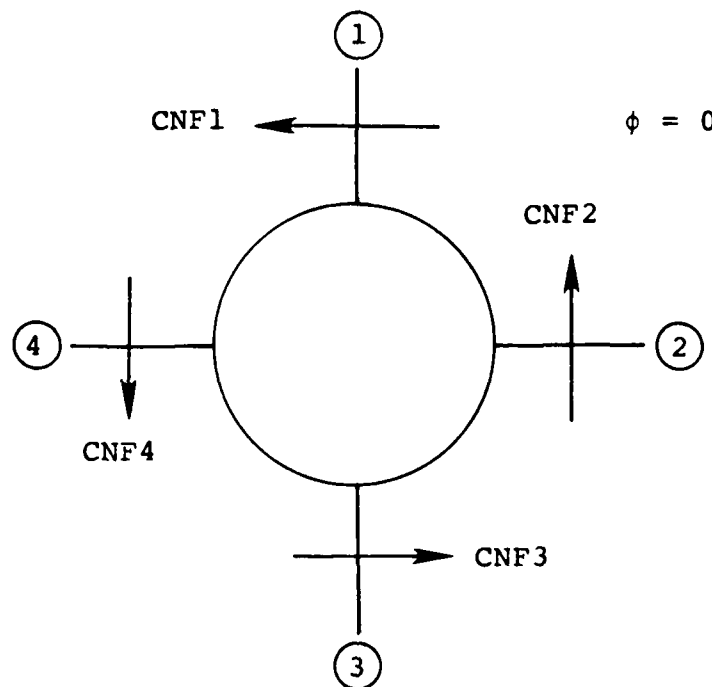
Positive control deflection is one which causes a counterclockwise rolling moment. The direction of the trailing-edge movement for positive deflection looking forward is as follows:
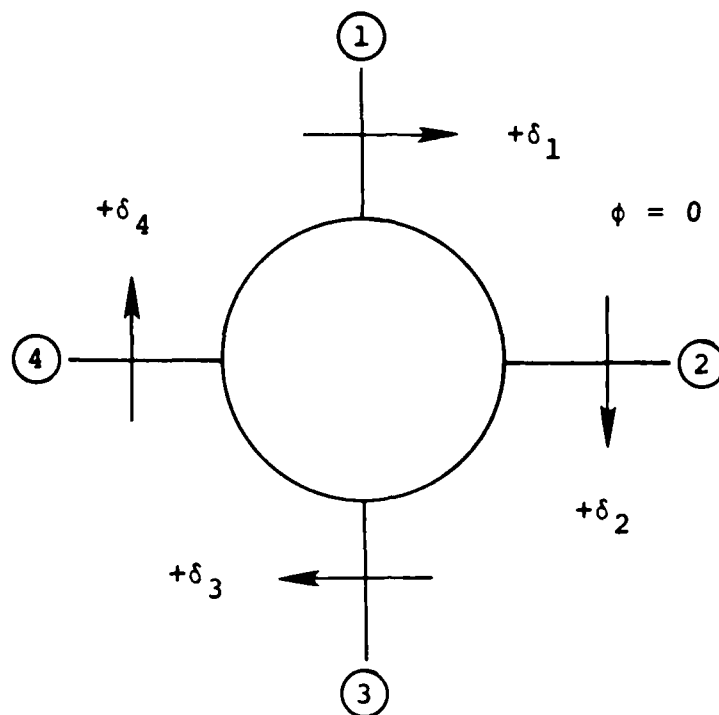
In general, we have the following signs of the increment in fin normal force, CNF, due to a positive deflection of fin 4

CNF1, CNF2, CNF3: negative

CNF4: positive

This follows then the fact that the swirl induced by fin 4 produces fin reactions which tend to reduce the swirl or rolling moment due to fin 4. While this relationship is a fairly general one, it is not without exceptions. Near fin stall an induced angle of attack by fin 4 might result in a normal-force increment of the opposite sign from that expected.

At $\phi = 90$ the direction of the normal forces induced by a positive deflection of fin 4 are as follows:

43

$\phi = 90°$
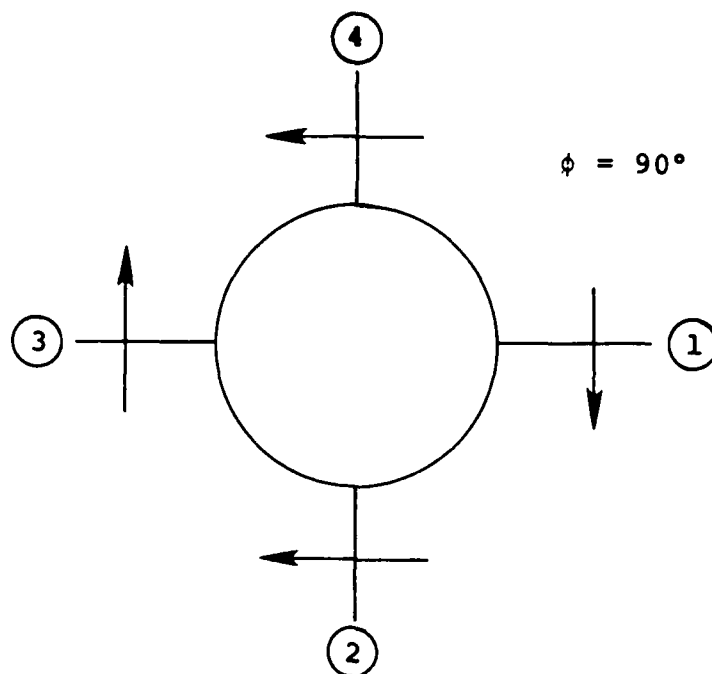
If the deflection of fin 4 were reversed, it would be expected from symmetry that the direction of the normal forces on fins 1, 2, and 3 would reverse and that the magnitudes would remain unchanged. The following symmetry conditions follow from those considerations

$$CNF1(\delta) = -CNF3(-\delta) \qquad \phi = \pm 90°$$
$$CNF2(+\delta) = -CNF4(-\delta) \qquad \delta = \delta_2 \text{ or } \delta_4$$

Those relationships hold also for -90°. They are useful for checking the repeatability of the data.

4.3 Extraction of Λ_{ij} from the Data

Consider that fin j is deflected by δ_j and that it induces a change in equivalent angle of attack of fin i of $(\Delta\alpha_{eq})_i$ by fin-fin interference. The factor Λ_{ij} is defined by the relationship

$$\Lambda_{ij} = \frac{(\Delta\alpha_{eq})_i}{\delta_j} \qquad (13)$$

Thus, Λ_{ij} is a basic fin-fin interference factor for induced angle of attack. To determine Λ_{ij} we measure $(CNF)_i$ for

44

$\delta_i = 0$, $\delta_j = 0$ and $\delta_i = 0$, $\delta_j \neq 0$ and use an equivalent angle of attack $(CNF)_i$ correlation to get $(\Delta\alpha_{eq})_i$ between the two conditions. We can then substitute into equation (13) to obtain Λ_{ij}. This procedure is adequate for obtaining Λ_{jj} since the changes in $(\Delta\alpha_{eq})_j$ due to δ_j are large. However, it is inaccurate for Λ_{ij} since the changes in normal-force coefficient in fin i are small, and it is difficult by hand to obtain the corresponding changes in $(\Delta\alpha_{eq})_i$ accurately from an equivalent angle of attack correlation of CNFi versus $(\alpha_{eq})_i$. A better procedure is based on the use of the measured change in CNFi and the slope of the correlation curve, $\partial(CNF)_i/\partial(\alpha_{eq})_i$. The value of Λ_{ij} is then given by

$$\Lambda_{ij} = \frac{(\Delta\alpha_{eq})_i}{\delta_j} = \frac{(\Delta CNF)_i}{\delta_j} \Big/ \frac{\partial(CNF)_i}{\partial(\alpha_{eq})_i} \qquad (14)$$

In this procedure the basic normal-force measurements are used to obtain $\Delta(CNF)_i$. An equivalent angle-of-attack curve was constructed from the $\phi = 0$ data using slender-body values of K_W and k_w (or Λ_{44}), and the slopes obtained. Basically we are linearizing the $(CNF)_i$ versus $(\alpha_{eq})_i$ relationship around a point since the $\Delta(CNF)_i$ changes are small.

4.4 Behavior at Λ_{ij} at $M_\infty = 1.2$

The values of Λ_{ij} have been determined for the $R = 2$, $\lambda = 0$ fin, fin51, of the triservice data base at $M_\infty = 0.8$ and 1.2 using the above methods. The values of Λ_{14}, Λ_{24}, Λ_{34}, and Λ_{44} have been determined for $\alpha_c = 0°$, $10°$, and $20°$ for $\phi_2 = 90°$, $40°$, $0°$, $-40°$, and $-90°$ for $M_\infty = 1.2$. We first examine the results for $\alpha_c = 0°$ and $M_\infty = 1.2$ in figure 27.

Examining first figure 27(a) for Λ_{14}, we note that Λ_{14} does not depend on ϕ within the accuracy of the data, but it depends on the sign of δ. For δ positive, that is trailing edge up, there is positive pressure on the upper side of fin 4 and negative pressure on the lower. The zone of influence of fin 4 thus depends on the sign of δ_4. For positive pressure in the region between fin 4 and fin 1, the value of Λ_{14} is greater than when the

45

pressure is negative. The slender-body theory gives a value of Λ_{14} independent of δ, and is thus only a rough approximation of Λ_{14}. It should be noted at this point that ϕ_2 is the roll orientation parameter for the complete missile. Positive ϕ_2 places fin 4 on the leeward side of the missile and negative ϕ_2 places fin 4 on the windward side of the missile.

The value of Λ_{24} in figure 27(b) is extremely small and is negligible. If fins 1 and 3 were not present, fin 2 would be out of the zone of influence of fin 4 for $M_\infty = 1.2$. However, some very small influence is transmitted through fins 1 and 3. The values of Λ_{34} are related to those of Λ_{14} by the reciprocal relationship of equation (12). The lines shown on figure 27(a) and 27(c) express this reciprocal relationship which is valid within the accuracy of the data. The values of Λ_{44} shown in figure 27(d) should all be the same for a given δ_4 independent of ϕ. They should also follow the reciprocal relationship of equation (12) for $\phi = 90°$ and $-90°$. The scatter is due to accuracy of the data. It is clear that the slender-body values of Λ_{44} or k_w are good average values for this quantity.

We now examine the values of Λ_{14}, Λ_{24}, Λ_{34}, and Λ_{44} at $\alpha_c = 10°$ and $M_\infty = 1.2$ as shown in figure 28. The values of Λ_{ij} now depend on roll angle. The peak values of Λ_{14} and Λ_{34} have now gone up to about 0.16 from 0.1 at $\alpha_c = 0°$; that is, the fin-fin interference between neighboring fins has increased 60%. The values of Λ_{24} are still negligible. The values of Λ_{34} show the same general reciprocal relationship to those of Λ_{14}. The peak values of Λ_{44} are slightly higher at $\alpha_c = 10°$ than at $\alpha_c = 0°$.

Values of Λ_{14}, Λ_{34}, and Λ_{44} for $\alpha_c = 20°$ and $M_\infty = 1.2$ are shown in figure 29. The peak values of Λ_{14}, and Λ_{34} are still higher for $\alpha_c = 20°$ than $\alpha_c = 10°$ indicating higher fin-fin interferences. The results for Λ_{24} are not shown since they are still negligible. The values of Λ_{44} for $\alpha_c = 20°$ are comparable to those for $\alpha_c = 10°$.

46

Values of Λ_{ij} have been calculated at $M_\infty = 0.8$ for $\alpha_c = 0°$ and $\alpha_c = 10°$ in the same manner as for $M_\infty = 1.2$ with only one small change. Since only fin 4 was deflected, Λ_{44} rather than k_w was used in determining the CNF versus α_{eq} correlation. The calculated results for $\alpha_c = 0°$ are shown in figure 30. The values of Λ_{14} shown in figure 30(a) depend on deflection angle δ_4 to a lesser extent than those for $M_\infty = 1.2$, figure 28(a), and are generally less than the value given by slender-body theory. The values of Λ_{24} in figure 30(b) are negligible. The values of Λ_{34} in figure 30(c) do not obey the reciprocal relationship

$$\Lambda_{14}(\delta) = -\Lambda_{34}(-\delta) \tag{15}$$

so well as the results for $M_\infty = 1.2$ for reasons which are not known. The slender-body value of Λ_{34} is a good approximation to the data. The values of Λ_{44} in figure 30(d) should not depend on ϕ for $\alpha_c = 0°$. The scatter of the data about the slender-body value is small enough that the value can be used for engineering purposes.

The Λ_{ij} results for $\alpha_c = 10°$ at $M_\infty = 0.8$ are shown in figure 31. One point worthy of note is that some values of Λ_{44} are quite low for a $- 20°$ deflection (trailing edge down). The correlation curve of CNF versus α_{eq} for various δ shows a pronounced flattening at high α_{eq} which can account for the low values of Λ_{44} for a fin operating in this region.

4.5 Repeatability of Data, Reynolds Number Effects

Data have been taken at $\phi = 0$ for all four fins so that a comparison of fins 2 and 4 yields an idea of the repeatability of the data. Also, data were taken by changing α_c sequentially for fixed ϕ (α_c sweeps) or by changing roll angle sequentially for fixed α_c (roll sweeps). Repeatability can be affected by zero shift of the force measuring gauges, least count of the instruments, geometric differences between left and right fins, tunnel streamangle effects, and many other sources.

47

The effect of Reynolds number and of left-right symmetry on fin normal-force coefficient, CNF, are shown in figure 32 for M_∞ = 0.8, 0.9, and 1.2. The effect of left-right symmetry only is shown for M_∞ = 0.9. At M_∞ = 0.8 and $\alpha_c \geq 15°$, there is a definite difference between the left and right fins. At M_∞ = 0.9 the difference is not significant. At M_∞ = 1.2 not only is there a difference between left and right fins, but there is a significant Reynolds number effect. The earlier stall of the α-sweep data causes a normal-force decrement of 0.1 to 0.15 at the highest angle of attack when compared with the ϕ-sweep data.

Comparisons are made in figure 33 for fin hinge-moment coefficient comparable to those for CNF in figure 32. At high angles of attack there are significant differences in CHM due to left versus right asymmetry and due to Reynolds number. Changes in CHM of the order 0.005 are due to left-right asymmetry and of 0.01 due to Reynolds number. At M_∞ = 0.9 the left-right symmetry effect is small.

Figure 34 shows the effects of left-right symmetry and Reynolds number on the center-of-pressure position due to angle of attack, $(\bar{x}/c_r)_\alpha$. At M_∞ = 0.8 and 0.9 no significant differences arise except near α_c = 0° where both numerator and denominator are approaching zero in the ratio CHM/CNF. At M_∞ = 1.2 errors in $(\bar{x}/c_r)_\alpha$ of about 0.01 occur at high angles of attack due to Reynolds number effects.

In the following correlations the ϕ-sweep data will be utilized because of their higher Reynolds numbers. In addition, the earlier stall of the α_c-sweep data makes correlations at values of angle of attack near 20° more difficult.

4.6 Correlation Curves and Prediction Method for No Fin Deflections; Windward Side (Case A)

The basic quantities needed in the hinge-moment prediction method are CNF, $(\bar{x}/c_r)_\alpha$, and $(\bar{x}/c_r)_\delta$. When vortex effects are important, we need also $(\Delta\alpha_{eq})_v$ and $(\bar{x}/c_r)_v$. The basic formulas are

48

$$CNF = (CNF)_\alpha + (CNF)_\delta + (CNF)_v \qquad (16)$$

$$\frac{\bar{x}}{c_r} = \frac{(CNF)_\alpha\left(\dfrac{\bar{x}}{c_r}\right)_\alpha + (CNF)_\delta\left(\dfrac{\bar{x}}{c_r}\right)_\delta + (CNF)_v\left(\dfrac{\bar{x}}{c_r}\right)_v}{CNF} \qquad (17)$$

$$CHM = CNF\left(\frac{x_{HL}}{c_r} - \frac{\bar{x}}{c_r}\right) \qquad (18)$$

The quantities $(CNF)_\alpha$ and $(CNF)_\delta$ will be obtained from the CNF versus α_{eq} correlation curves. Separate correlation curves of $(\bar{x}/c_r)_\alpha$ and $(\bar{x}/c_r)_\delta$ will be made. $(CNF)_v$ is obtained from $(\Delta\alpha_{eq})_v$, which is obtained in turn from a vortex theory using reverse-flow theorems. The quantity $(\bar{x}/c_r)_v$ obtained using a simplified model of the vortex loading distribution is inaccuate and will be obtained by a supersonic missile code, NWCDM, as will subsequently be described.

The correlations are considered in the following order.

CASE	FINS	ϕ_2	δ_4
A	Windward	0(20°)-80°	0
B	Leeward	0(20°)+80°	0
C	Windward	0(20°)-80°	-20°(10°)20°
D	Leeward	0(20°)+80°	-20°(10°)20°

For cases A and B fin deflection is not considered. The differences between the windward and leeward fin results are primarily due to strong body vortex effects.

Let us now consider the CNF versus α_{eq} correlation for Case A. The form of equation (6) used to obtain α_{eq} for $\delta_1 = \delta_2 = \delta_3 = 0$ is

49

$$\alpha_{eq} = K_W \, \alpha_c \, \cos \phi - \Lambda_{44} \, \delta_4$$

$$+ \frac{4}{AR} \quad \frac{K_\phi \, \alpha_c \, |\alpha_c|}{57.3} \quad \sin \phi \, \cos \phi + (\Delta\alpha_{eq})_V \qquad (19)$$

$$-90° \le \phi \le 90°$$

In this equation all angles are in degrees. It will be applied to fin 4 for the most part, and the value of ϕ to use in that value of ϕ_2 for which fin 2 occupies the position of fin 4. The value of radius-semispan ratio, a/s_m, for the triservice missile with fin 51 is 0.5. For this value of a/s_m, slender-body theory gives the following quantities for use in equation (19): $K_W = 1.45$, $\Lambda_{44} = 0.905$, $K_\phi = 0.471$.[*] The only remaining quantity needed in equation (19) is $(\Delta\alpha_{eq})_V$. This quantity has been evaluated for the present case using MISSILE2, reference 10. For illustrative purposes, the values of $(\Delta\alpha_{eq})_V$ are plotted versus body angle of attack, α_c, in figure 35 with ϕ_2 as parameter. The figure shows results for $M_\infty = 0.8$ and 1.2 and for leeward and windward roll positions. It is noted that the effect of the vortices is much greater on the leeward side than the windward side, and that the effect of Mach number is small. These curves have been used in constructing the following correlation curves.

For Case A, correlation curves of CNF2 versus α_{eq} have been constructed for $\phi_2 = 0$, 20°, 40°, 60°, and 80° for Mach numbers of 0.8 and 1.2 and are given in figure 36. It is noted that the effects of roll angle are well correlated by the equivalent angle-of-attack concept for $M_\infty = 0.8$ over the entire roll angle range and for $M_\infty = 1.2$ for all roll angles but $\phi_2 = 80°$. This latter effect is subsequently explained.

Correlation curves of $(\bar{x}/c_r)_\alpha$ to go along with the CNF versus α_{eq} correlation curves of figure 36 are given in figure 37. At $M_\infty = 0.8$ the values of $(\bar{x}/c_r)_\alpha$ correlate within about ± 0.005 except for $\phi_2 = 80°$ when the maximum error is about 0.012. These

---

[*] See "Missile Aerodynamics" by Jack N. Nielsen

tolerances are close to ± 0.01 limits we consider desirable for accurate hinge-moment prediction. (In some subsequent cases we will have to settle for ± 0.02.) The value for $\phi = 80°$ are probably not affected by stream angle.

For $M_\infty = 1.2$ the correlation of $(\bar{x}/c_r)_\alpha$ is still within acceptable limits for $\phi_2 = 0$ to $60°$. Again the results for $\phi_2 = 80°$ are suspect. Values given for $\alpha_{eq} = -2°$ illustrate the usual problem of obtaining accurate center-of-pressure positions as the fin normal force goes to zero.

Turning now to special considerations of the $\phi_2 = 80°$ data, we note that the following quantities yield repeat data of the CNF measurements if left-right symmetry is assumed.

$$CNF2, \ \phi_2 = 80°$$
$$CNF4, \ \phi_2 = -80°$$
$$CNF3, \ \phi_2 = 10°$$
$$CNF3, \ \phi_2 = -10°$$

These quantities are plotted with appropriate changes in sign to facilitate comparison in figure 38 for $M_\infty = 0.8$ and 1.2. When the fin is in the fourth quadrant, CNF2 (80°) and CNF3(-10°) represent repeat data; when the fin is in the third gradrant, CNF4(-80°) and CNF3(10°) should be equal. It is noted that the fourth quadrant quantities are in good agreement and the third quadrant quantities are in good agreement, but they are not in good agreement with each other. In an attempt to explain the anomolous $\phi_2 = 80°$ results in figure 36, the equivalent angle of attack was corrected for sidewash. The $\phi_2 = 0$ values of CNF3 were converted to sidewash angle through use of $\partial CNF/\partial \alpha_{eq}$ obtained from figure 36. Sidewash angles greater than one degree were calculated as a function of angle of attack. Correcting α_{eq} for these sidewash angles resulted in the CNF versus α_{eq} curves shown in figure 39. One set of data for quadrant four and one set for quadrant three were corrected. The arrows on some of the data points on figure 39(a) indicate the direction and magnitude of

51

the corrections to α_{eq} due to sidewash. What is important is that the data for the third and fourth quadrants is brought into agreement by the sidewash corrections. However, the results lie about 50 percent above the correlation curve for ϕ_2 = 20°, 40°, and 60°. Thus a real departure from correlation exists for ϕ_2 = 80°.

An explanation for this behavior is suggested by figure 39(b) for M_∞ = 1.2. Here again the third and fourth quadrant corrected results form a fair correlation curve which lies about that for ϕ_2 = 20°, 40°, 60°. It is suspected that the discrepancy is not a viscous effect because of the thin boundary layer near the windward meridian. An inviscid supersonic missile code, NWCDM, reference 11, was used to predict the fin loading, and the results are shown on figure 39(b). It is seen that most of the difference between the two correlation curves is due to invisicid causes. At the higher angles of attack some of the differences may be due to nonlinear inviscid effects not accounted for in code NWCDM. For this case calculated normal forces due to leading edge suction by the Polhamus method (ref. 12) were negligible.

It is presumed that the differences between the two correlation curves in figure 39(a) for M_∞ = 0.8 are also due to inviscid causes. It is not possible to verify this point at M_∞ = 0.8 because of the lack of a code similar to NWCDM for M_∞ < 1.0.

It is not clear whether inviscid effects explain the results for ϕ_2 = 80° in figure 37(b). While code NWCDM yields a constant center-of-pressure position of $(\bar{x}/c_r)_\alpha$ equal to 0.663, in good agreement with the data, any fin thickness effects have not been accounted for in the theoretical results.

For Case A we can thus say that the correlation curves will give good predictions of the quantities needed to predict hinge moments except for ϕ_2 = 80° at high angle of attack. Code NWCDM will improve the ϕ_2 = 80° predictions for M_∞ = 1.2.

4.7 Correlation Curves and Prediction Method for No Fin Deflection; Leeward Side (Case B)

Correlation of the data for the leeward fin is fundamentally a more difficult problem than for the windward side because of the complicating effect of the body vortices and separated flow. It might be thought that the hinge-moment coefficients on the leeward side are less than those on the windward side since the fin forces are generally less but this is not necessarily so. For the present fin T51 mounted on the triservice missile with the hinge line at $(x/c_r)_{HL} = 0.611$, the maximum hinge moments of fin 4 including fin deflection are shown versus ϕ_2 in figure 40 for $M_\infty = 0.8$ and 1.2. These maximum hinge moments are the maximum measured values obtained from a tabulation of CHM4 against the test angle of attack. The figures exhibit the result that at $M_\infty = 0.8$ the maximum values of CHM can occur at $\phi_2 = 60°$ or $80°$ with fin 4 near a body vortex. At $M_\infty = 1.2$ the maximum values of CHM fall near $\phi_2 = 20°$ and $40°$ for negative δ_4 and don't depend much on ϕ_2 for positive δ_4. These results demonstrate the importance of hinge-moment predictions for Case B and Case D.

Significant difference in the values of α_{eq} for the windward and leeward side stem from the fact that the K_ϕ term is negative for the leeward side and positive for the windward side and has a maximum magnitude of about $4°$. Another difference of even greater importance is that while the maximum magnitude of $(\Delta\alpha_{eq})_v$ shown in figure 35 for the windward side, $0 \le \phi_2 \le 90°$, ranges up to $3°$ to $4°$, its maximum magnitude for $\phi_2 = -60°$ ranges up to about $15°$ on the leeward side. The correlation of CNF versus α_{eq} for the leeward side is thus a test of the vortex model used to obtain $(\Delta\alpha_{eq})_v$.

A short discussion of how $(\Delta\alpha_{eq})_v$ is determined is now given. A fin at any roll position is subject to a vortex-induced flow normal to its chord plane which can be calculated with the vortex model. This model consists of a symmetrical external vortex pair the strength and position of which are based on experimental data

53

plus an image vortex pair in the body. The induced flow normal
to the fin chord plane is then calculated by the Biot-Savart law
and assumed not to vary along the local fin chord. The average
angle of attack of the fin due to the body vortices is obtained
by averaging the induced angles normal to the fin along the fin
span with certain weighting factors. According to linear theory
the appropriate weighting factor is the span loading of the fin
of the cruciform wing-body combination in reverse flow. In
practice we use the span loading based on slender-body theory,
but nondimensionalize the results in a way so that only the
shape of the span loading is relevant. A modification of this
procedure yielded the lateral center of pressure of the vortex
loading $(\bar{y}_v - a)/(s_m - a)$. It does not yield the axial position
of the center of pressure due to vortex loading which is needed
in calculating hinge moment.

Turning now to the correlation curves for CNF versus α_{eq},
we present the correlations for M_∞ = 0.8 and 1.2 in figure 41.
For both Mach numbers, it is noted that the values of CNF corre-
late quite well except for ϕ_2 = 80° at the lower equivalent angle
of attack (highest α_c). It is noted that the ϕ_2 = 60° data cor-
relate well, being generally less than 1° of α_{eq} from the faired
mean curve. Since $(\Delta\alpha_{eq})_v$ for ϕ_2 = 60° is as large as 15°, this
means that the vortex theory predicts $(\Delta\alpha_{eq})_v$ within about
±6 percent. For ϕ_2 = 80° a larger error in predicting $(\Delta\alpha_{eq})_v$
would be needed to explain deviations.

The question arises whether sidewash existing at ϕ_2 = -90°
may explain the data points for ϕ_2 = -80° which do not correlate.
This matter was investiagted at M_∞ = 1.2 using the same sidewash
correction procedure as for figure 39. The results are presented
in figure 42 where the corrected data are shown in figure 42(a)
and the uncorrected data in figure 42(b). The corrected data in
figure 42(a) do not correlate any better than the uncorrected
data in figure 42(b). Thus, the sidewash correction technique
that worked in Case A is unsuccessful in Case B. The suspected

reason is that the superposition procedure works for the un-
separated flow of Case A (windward side) but not for the separated
flow of Case B (leeward side). Since vortex effects are present
in all the data for this case, we cannot use Code NWCDM to see if
the equivalent angle-of-attack concept properly explains the
inviscid effects near the leeward meridian.

Before the center-of-pressure correlation, we will present
an analysis of the center-of-pressure results along special lines.
Large effects of the body vortices on the center-of-pressure
positions are to be anticipated. In figure 43 the measured values
of the center-of-pressure position of fin 4 are plotted versus
α_{eq}. At both Mach numbers a strong tendency is exhibited for
$(\bar{x}/c_r)_\alpha$ to move rearward as the fin position becomes more leeward.
Also for $\phi_2 = 60°$ and $80°$ the values of α_{eq} tend to reduce after
a certain angle of attack is reached. The $\alpha_c = 10°$ line on the
curves demonstrate that for $\phi_2 \geq -40°$ this rearward movement starts
for $\alpha_c < 10°$. We will now see if the present model for the effect
of body vortices explains the rearward movement.

The primary assumption (reference 1) in determining the effect
of body vortices on $(\bar{x}/c_r)_\alpha$ is that the center of pressure of the
fin without vortex effect and the center of pressure of the vortex
loading both lie on a straight lifting line, and that this line
is a constant percent-chord line. The center-of-pressure data
yield the location of the constant percent-chord line. The vortex
theory previously described yields the lateral center of pressure
due to the vortex loading, $\bar{y}_v$. This value in turn determines the
point on the lifting line of the vortex center of pressure, $(\bar{x}/c_r)_v$
and hence a value of $(\bar{x}/c_r)_v$. For a sweptback lifting line, as in
the present case, if $\bar{y}$ due to the vortex is greater than $\bar{y}$ as
measured, the download due to the vortex tends to push $(\bar{x}/c_r)$ for
the fin forward. The lateral center-of-pressure position for the
vortex loading as calculated is sometimes inboard and sometimes
outboard of the lateral center-of-pressure position as measured.
It will be shown that the center of pressure of the vortex loading
does not usually lie on the lifting line in the present case.

The problem will now be examined from another point of view to gain further insight. If CHM is plotted versus CNF, lines of constant slope through the origin will be lines of constant $(\bar{x}/c_r)$ for a given hinge-line location. Such a plot is presented in figure 44 for $M_\infty = 0.8$ and $\phi_2 = 60°$. Similar behavior is evidenced for $\phi_2 = 80°$ at $M_\infty = 0.8$ and for $\phi_2 = 60°$ and $80°$ at $M_\infty = 1.2$. Note that the center of pressure has moved back a significant distance for $\alpha_c < 8°$, a region of no free vortices from the body. As the angle of attack increases, the center of pressures move back to ∞, and a large pitching moment exists at CNF = 0. This couple is the result of a potential normal force at one point and an equal and opposite vortex force acting at another point so that a pure couple is developed. There also remains the possibility of some additional forces and moments due to unknown causes. In order to see if the phenomenon exhibited by figure 44 can be explained by a potential flow plus concentrated body vortices, a special study was made as follows.

At $M_\infty = 1.2$ it is possible to compute the fin loading as a function of α_c and roll angle using program NWCDM, reference 11. This program can compute loads and center-of-pressure locations due to potential flow and to the body vortices separately. Calculations were made for fin 2 located on the leeward side at $\phi_2 = -20°$, $-40°$, $-60°$, and $-80°$ for $M_\infty = 1.2$ with all fins unde-flected for an angle-of-attack range up to $20°$. The calculated centers of pressure due to the vortex loading are tabulated in Table 1. No fin thickness was included in the calculations.

Table I illustrates some points which are noteworthly. It considers first body vortices only and secondly, the combined effect of body vortices and fin leading-edge vortices which develop normal force in accordance with the hypothesis of Polhamus, reference 12. With the effect of body vortices only, $(\bar{x}/c_r)_v$ is far in front of the hinge line ($x_{HL} = 0.611\, c_r$) for fin positions near the vortex, $\phi_2 = -60°$ and $-80°$. Proximity of

56

the vortex to the fin also causes the lateral center of pressure to move inboard.

In accordance with the Polhamus analogy, leading-edge suction can be converted to vortex lift. Code NWCDM can include this effect and determine the center-of-pressure position due to the leading-edge vortices. Part B of the table compares the center-of-pressure locations for two cases: $\phi_2 = -20°$ and $\phi_2 = -60°$. The leading-edge vortex effect (Polhamus effect) is greater at $\phi_2 = -20°$ than at $\phi_2 = -60°$ since the fin upwash angles are greater. However, while the Polhamus effect causes a significant effect on normal force at $\phi_2 = -20°$, it has negligible effect on hinge-moment coefficient as will be shown. When the effect on $(\bar{x}/c_r)$ of the body vortices is a maximum near $\phi_2 = -60°$ (and hence on CHM2), the effect of the leading-edge vortices is small. This follows because of the small upwash angles for $\phi_2 = -60°$. Thus the effects of loading associated with leading-edge vortices on hinge moments is negligible for both cases for the present fin.

The fin planform is shown in figure 45 together with the center of pressure due to body vortex loading for $\phi_2 = -60°$ and $-80°$. Note the lifting line, a line of constant percent chord through the fin center-of-pressure position as measured. Also the hinge line at 0.611 c_r is shown. For low angles of attack the centers of pressure are well in front of the hinge line, by as much as 0.2 c_r. As the angle of attack increases the centers of pressure move backward across the hinge line. The magnitude of the vortex loading increases as angle of attack increases and the lever arm becomes smaller so that a maxiumum hinge moment due to body vortex loading can be expected at some intermediate angle of attack. In fact, this effect dominates the total hinge moment for fins under strong body vortex influence. It is clear that the assumption that the center of pressure of the body vortex loading lies on the lifting line is not a valid one at $\phi_2 \neq 0$. Values of $(\bar{x}/c_r)_v$ can be easily calculated with NWCDM for $M_\infty = 1.05$ and greater.

57

For M_∞ < 1.0 we have no similar code for doing the calculations for cruciform wing-body combinations.

Code NWCDM has been used to calculate CNF4 and CHM4 for ϕ_2 = 60° at M_∞ = 1.2 and the results are shown in figure 46. The principal nonlinearities are predicted by the code. The break in slope of the normal-force curve at α_c = 8° is due to the onset of body vortex separation. The peaking of the hinge-moment curve at α_c = 10° is predicted by the code. Note that the leading-edge normal-force effects on CNF and CHM are negligible. At the higher angles of attack, the predictions are not as good. A shift of 2 to 3 percent in the center-of-pressure position of the potential normal force would explain the difference. This shift may be due to neglecting fin thickness. The quantities calculated by code NWCDM are summarized in Table II. The total normal force and hinge moment consist of a part due to potential flow and a part due to body vortices. It is clear that in the region of maximum hinge moment and minimum fin normal force the body vortices dominate.

A hand calculation for the same case, ϕ_2 = -60°, as shown in figure 46, has been attempted, and the results are shown in figure 47. It is noted that at the higher angles of attack the normal-force coefficient is predicted better than by code NWCDM, but the hinge-moment coefficient is not predicted so well at high angles of attack. The hand calculations are summarized in Table III. The normal-force calculation follows the usual pro-cedure using the Case B correlation curve for CNF versus α_{eq}, figure 41(b), M_∞ = 1.2. Since we have no correlated $\bar{x}/c_r$ data for Case B, it was assumed that $(\bar{x}/c_r)_\alpha$ correlation for Case A is valid for Case B. This procedure assumes that the effect of roll angle on $(\bar{x}/c_r)_\alpha$ is negligible and the Case A results are free of body vortex effects. The values of $(\bar{x}/c_r)_v$ were taken from the results of code NWCDM as input to the method. The calcu-lated results are only slightly inferior to those of code NWCDM.

Code NWCDM was also used to predict CNF and CHM at $\phi_2 = -20°$, and the results are shown in figure 48. With respect to the CNF predications in figure 48(a), a substantial contribution of the Polhamus normal force to the total is seen at the higher angles of attack. With respect to CHM, good prediction is shown in figure 48(b) up to $\alpha_c = 20°$. Note that leading-edge normal force has very little contribution to CHM. This follows from the fact that this component of normal force has a small lever arm about the hinge line. For other planforms this may not be the case. The difference in fin center-of-pressure location with or without leading-edge normal force is less than $0.01 \, c_r$ as shown in figure 48(c).

The code NWCDM calculations on which figure 48 is based are summarized in Table IV. The parts of CNF and CHM included a potential part, a body-vortex part and a leading-edge vortex part. The contributions of all three parts are significant for CNF, but the contribution of the leading-edge vortices to CHM is negligible.

A hand calculation was attempted to obtain CNF and CHM for $\phi_2 = -20°$, and the results are tabulated in Table V and shown in figure 49. The normal CNF versus α_{eq} correlation was used to predict CNF with good success. It is noted that the measured CNF values in the correlation curve include leading-edge vortex normal force. In predicting CHM, values of $(\bar{x}/c_r)_\alpha$ for $\phi_2 = 0$ were used on the assumption these would be free of body vortex interference. The prediction is accurate only to about $\alpha_c = 10°$. Above $\alpha_c = 10°$ it is suspected that the lever arms for $(CNF)_p$ are too small by comparison with those given by code NWCDM in Table IV.

In summary, code NWCDM does a good job of predicting CHM near the vortex ($\phi_2 = -60°$), but for high α_c is only fair. The hand method is only slightly inferior to NWCDM. For $\phi_2 = -20°$ code NWCDM does a good job of predicting CHM, but the hand method is accurate only to $\alpha_c = 10°$.

59

4.8 Correlation Curves and Prediction Method for Fin Deflection; Windward Side (Case C)

For Case C we are interested in the hinge-moment contributions due to δ_4 which are additive to those for $\delta_4 = 0$. The two quantities of interest are $(CNF)_\delta$ and $(\bar{x}/c_r)_\delta$. These quantities have been extracted from the data assuming that the $\delta = 0$ and $\delta \neq 0$ results are additive. We have correlated CNF4 versus α_{eq} for $\delta_4 = \pm 10°$, and $\pm 20°$ for $\phi_2 = -20°$, $-40°$, $-60°$, and $-80°$. A separate correlation curve for each ϕ_2 has been made. Since $\phi_2 = 0$ constitutes an important case, a special CNF versus α_{eq} curve has been constructed for this case. Correlation curves of $(\bar{x}/c_r)_\delta$ versus α_c rather than α_{eq} have been constructed since correlation is obtained in this fashion. We discuss first the $M_\infty = 0.8$ results in their entirety.

Consider now the CNF versus α_{eq} correlation curves for $M_\infty = 0.8$ shown in figure 50 for $\delta_4 = -10°$, $-20°$, $10°$, and $20°$. For $\delta_4 = -10°$ and $-20°$ the fins are highly loaded as shown in figure 50(c) and 50(d). A definite stall occurs in both cases starting at about $\alpha_{eq} = 24°$. Positive deflection angles, $\delta_4 = 10°$ and $20°$, tend to unload the fins and no stall is indicated. For these deflection angles at $\phi_2 = -80°$ with fin 4 near the windward meridian, the correlation of CNF4 for high α_c falls above the curve. This phenomenon is also shown for $\delta_4 = 10°$ at $M_\infty = 1.2$ in figure 54(a). For Case A it is exhibited for $M_\infty = 1.2$ (but not for $M_\infty = 0.8$) where it was found to be an inviscid effect predicted by code NWCDM.

For $\phi = 0°$ a correlation curve was made for $\delta_4 = 0$, $\pm 10°$, and $\pm 20°$ as shown in figure 51. Very good correlation was obtained including the stall region starting near $\alpha_{eq} = 30°$.

Considering now center-of-pressure location due to control deflection, $(\bar{x}/c_r)_\delta$, the values of this parameter turn out to be a function of α_c up to the stall. This is shown in figure 52 for $\delta_4 = \pm 10°$, and $\pm 20°$ and $\phi_2 = 0$ (20°) $-80°$ for fin 4. For

60

$\delta_4 = +10°$, the values of $(\bar{x}/c_r)_\delta$ are well correlated up almost to $\alpha_c = 20°$ lying generally within the ± 0.01 limit. For $\delta_4 = +20°$, the angle of attack limit for correlation is between 15° and 20°, and is not associated with the stall. For $\delta_4 = -10°$ and $-20°$ we noticed fin stall near $\alpha_{eq} = 24°$ in figure 50. In figures 52(c) and 52(d) we have used open symbols for lower values of α_{eq} and filled symbols for larger vales of α_{eq}. From these symbols, an approximate α_c limit for correlation is established for each ϕ_2 and $\delta_4 = -10°$ and $\delta_4 = -20°$, and the limits correspond approximately to the values of α_{eq} for stall. The limits were established as the average between the highest angle of attack for correlation and the lowest angle of attack for no corre-lation. The limits, given in figure 53, show that for negative values of δ_4, a significant region in the α_c, ϕ space is subject to fin stall at $M_\infty = 0.8$. From figures 50(c) and 50(d), it can be seen that not much control effectiveness exists above these limits, and control deflection limitation (as a function of ϕ) would not seriously limit the maneuverability of the missile. No attempt has been made to correlate $(\bar{x}/c_r)_\delta$ in the stall region. Whatever phenomenon is the cause, it must account for both large forward and backward shifts in axial center-of-pressure location.

To summarize briefly Case C for $M_\infty = 0.8$, it can be said that with exception of the $\phi_2 = -80°$ data CNF is correlated well over the entire range of interest ($\alpha_c = \leq 20°$, $0 \leq \phi \leq 90°$). The axial center-of-pressure correlation is limited to some angle of attack between 15° and 20° for positive value of δ_4 by some phenomenon other than stall. For negative deflection angles, the $(\bar{x}/c_r)_\delta$ correlations are not valid beyond stall which occurs for $\alpha_{eq} > 24°$ except for large roll angles. Additional control effectiveness is not obtained above the stall, and no attempt to correlate $(\bar{x}/c_r)_\delta$ for this region was made.

61

We now turn our attention to $M_\infty = 1.2$ for Case C. The correlation curves of CNF4 versus α_{eq} for $\phi_2 = -20°$, $-40°$, $-60°$, and $-80°$ are shown in figure 54 for $\delta_4 = \pm10°$ and $\pm 20°$. For $\delta_4 = \pm20°$, good correlations are obtained. However, the usual anomolous behavior of the $\phi_2 = -80°$ data at high α_c for $\delta_4 = \pm10°$ is exhibited. A gradual stall of the fin occurs for $M_\infty = 1.2$ at high equivalent angles of attack, and it would be difficult to specify the value of α_{eq} for the onset of stall.

A calculation has been made using code NWDCM for the $\phi_2 = -80°$ case in figure 54(a) to gain insight into the lack of correlation. The calculated results are summarized in Table VI. We examine these results from the viewpoint of $(CNF)_\delta$ only. A comparison is made of the predictions of code NWCDM and the measured data for $(CNF)_\delta$ in figure 55. Code NWCDM slightly underpredicts the measurement. The question arises whether the lack of correlation for $\phi_2 = -80°$ in figure 54(a) for $\delta_4 = 10°$ is simply a reflection of the lack of agreement in figure 36(b) for $\delta_4 = 0°$. If so, the difference $(CNF)_\delta$ calculated from these two correlation curves should approximate the data. This hand calculation was carried out and the results are shown as squares in figure 55. The results fall below the data slightly at low angles of attack, but by about 25 percent at the highest angle of attack. Only part of the lack of correlation at $\delta_4 = 10°$ is a reflection of the lack of correlation at $\delta_4 = 0°$.

Code NWCDM is a code based on panel and line singularity methods derived from the wave equation with isolated point vortices used to model body vorticity. It can thus be considered an inviscid code. The good agreement between the measured values of $(CNF)_\delta$ and those predicted by the code indicates that an inviscid aerodynamic process is involved. Since the code neglects gap effects, it is thought that gap effects on $(CNF)_\delta$ are small.

To complete the means for predicting CNF4 for the windward side, we present a special correlation for $\phi_2 = 0$ in figure 56. Figure 56(a) demonstrates a good correlation for normal-force

62

coefficient for $\delta_4 = \pm 10°$ and $\pm 20°$. The correlation of $(\bar{x}/c_r)_\delta$ for $\phi_2 = 0$ given in figure 56(b) is within ± 0.01 except for two points which probably contain experimental error. Accordingly, the equivalent angle-of-attack concept provides correlation curves which are adequate for this important case.

We now turn to the question of the correlation of $(\bar{x}/c_r)_\delta$ for $\phi_2 \neq 0$. This quantity is needed to obtain hinge-moment coefficient due to fin deflection. The experimental values of $(\bar{x}/c_r)_\delta$ are plotted versus α_c in figure 57 for $\delta_4 = \pm 10°$ and $\pm 20°$. For $\delta_4 = +10°$ and $+20°$, good correlation of the data are shown up to about $\alpha_c = 20°$ for $\phi_2 = -20°$, $-40°$, $-60°$, and $-80°$. The $\phi_2 = 0°$ data pulls away from the correlation curve by 0.01 at an angle of attack near $10°$. In this behavior, the $\phi_2 = 0$ data behaves like other data for the leeward fins at $M_\infty = 1.2$ as will be discussed in connection with Case D. The discussion of the behavior is postponed to Case D.

Consider now the deflection angles $\delta_4 = -10°$ and $-20°$ for which the fin becomes more highly loaded. Figure 57(c) and 57(d) show departures of the data from correlation which depend on ϕ_2. For $\delta_4 = -10°$, the data for all ϕ_2 values except $+80°$ depart from correlation between $\alpha_c = 10°$ and $\alpha_c = 15°$. This behavior is similar to that for $M_\infty = 0.8$ in figure 52(c) and 52(d), although the rate of departure at $M_\infty = 0.8$ is much more rapid. At $\delta_4 = -20°$, the departure from correlation occurs at lower angle of attack, between $\alpha_c = 5°$ and $8°$ except for the $\phi_2 = -80°$ data. We thus have a limitation on the applicability of the data correlation depending on δ_4 and ϕ_2 similar to that found for $M_\infty = 0.8$.

The limits in α_c for the validity of the correlation are shown in figure 58 which is to be compared with figure 53 for $M_\infty = 0.8$. Several significant points need to be made concerning the differences between the results for the two Mach numbers. At $M_\infty = 0.8$, the limitations were associated with fin stall.

63

At $M_\infty = 1.2$ there is generally no clear-cut stall of the fin in figure 54 for $\delta_4 = -10°$. (For $\delta_4 = -20°$, there appears to be a clear-cut stall for $\phi_2 = -60°$.) There is thus an increase in fin normal force available for control above the limits for $M_\infty = 1.2$ in contrast to those for $M_\infty = 0.8$.

An alternate method of correlating $(\bar{x}/c_r)_\delta$ was attempted. In this attempt $(\bar{x}/c_r)_\delta$ was plotted versus α_c with δ_4 as parameter for a fixed value of ϕ_2. This method fails for $M_\infty = 0.8$ and 1.2 for $\phi_2 = -20°$, $-40°$, and $-60°$ but is successful for both Mach numbers at $\phi_2 = -80°$. The results shown in figure 59 correlate generally within the desired limits of ± 0.01. The point can be made that if $(\bar{x}/c_r)_\delta$ correlates as a function of α_c for various values of δ_4, then the equivalent angle of attack is not the correct correlating parameter. The values of $(\bar{x}/c_r)_\delta$ in figure 57 for $\delta_4 = 10°$ and $20°$ generally correlate but those for $\delta_4 = -10°$ and $-20°$ do not. For negative values of δ_4 positive pressure exists under the fin. A phenomenon which is compatible with the known facts and which could explain the lack of correlation is interference of the positive pressure field on the body boundary layer approaching the fin from below. This explanation is also compatible with the fact that the boundary layer at $\phi_2 = -80°$ is very thin so that the effect is miminal. It is of interest that this alternate method of correlation also goes through for Case D (described later) when the fin is on the leeward side of the body.

We have used the supersonic missile code NWCDM to predict values of $(\bar{x}/c_r)_\delta$ for Case C to see if it yields accurate values. For this purpose, the case of fin 4 ten degrees off the windward meridian was chosen. Calculations were carried out at $M_\infty = 1.2$ for $\delta_4 = 0$ and $\delta_4 = 10°$ and the results are tabulated in Table VI. The corresponding measured quantities are tabulated in Table VII. Comparison between the values of $(\bar{x}/c_r)_\delta$ in Table VI and VII show good agreement in the low angle range. However, the theoretical values of $(\bar{x}/c_r)_\delta$ remain almost constant with changes in

64

angle of attack while the measured results show a progressive forward movement. The code thus fails to predict the values of $(\bar{x}/c_r)_\delta$ within the accuracy limits (± 0.02) which we would like to achieve for values outside the low range. Whether this is due to accuracy limitations of the code or to some unknown aerodynamic phenomenon is not known.

To summarize the results for Case C for $M_\infty = 1.2$, we find that good prediction of CNF is obtained except for $\phi_2 = -80°$. Here the values of $(\bar{x}/c_r)_\delta$ depart from correlation for negative values of δ_4 and a limit is set on α_c dependent on ϕ_2 for which the correlation curves are valid. The code NWCDM does not predict $(\bar{x}/c_r)_\delta$ accurately for conditions where body vortex effects and leading-edge vortex effects are negligible. We are thus presently limited in prediction to the angle-of-attack limits for negative δ_4 given in figure 58.

4.9 Correlation Curves and Prediction Method for Fin Deflection; Leeward Side (Case D)

Case D represents the most complicated of all four cases because it involves the combined effects of fin deflection and body vortices. In the previous work on hinge moment (reference 1) it was assumed that for a fixed roll position of the fin, the vortex effects on the fin are independent of fin deflection angle. This assumption implies that the effect of the vortices on the fin are unchanged even though the vortices may move under the influence of fin deflection. This point will come in for consideration in the following pages.

For Case D we will present first the data for $M_\infty = 1.2$ followed by that for $M_\infty = 0.8$. Consider first the CNF versus α_{eq} correlation for $M_\infty = 1.2$ in figure 60 as given for $\delta_4 = \pm 10°$ and $\pm 20°$. It is noted that very good correlation is generally obtained for $\phi_2 = 20°$ and $40°$ but for $\phi_2 = 60°$ and $80°$ the correlations show more scatter about the correlation curve. This is probably

associated with strong fin-vortex interaction. As an example, to show this effect, consider the variation of α_{eq} with α_c for a particular case.

$$\phi_2 = 60°$$
$$M_\infty = 1.2$$
$$\delta_4 = 10°, \quad \delta_1 = \delta_2 = \delta_3 = 0°$$

In applying equation (19) to calculate α_{eq}, a value of $\phi_2 = -60°$ is used since fin 4 has the same equivalent angle of attack as fin 2 at $\phi_2 = -60°$.

α_c	$K_W \alpha_c \cos \phi_4$	$\dfrac{4}{\mathcal{R}} \dfrac{K_\phi}{57.3} \sin \phi_4 \cos \phi_4 \, \alpha_c \lvert \alpha_c \rvert$	$-\lambda_{44}\delta_4$	$(\Delta\alpha_{eq})_v$	α_{eq} [eq (19)]
-2.01	-1.46	+0.03	-9.05	0	-10.5
.04	.03	0	-9.05	0	- 9.0
1.90	1.30	-0.03	-9.05	0	- 7.7
5.07	3.67	-0.18	-9.05	0	- 5.6
10.09	7.31	-0.72	-9.05	-3.4	- 5.9
15.25	11.06	-1.65	-9.05	-7.5	- 7.1
20.15	14.61	-2.89	-9.05	-11.8	- 9.1
21.73	15.75	-3.36	-9.05	-13.7	-10.4

As α_c increases, α_{eq} increases, but as the vortex induced $(\Delta\alpha_{eq})_v$ comes in, α_{eq} starts to decrease. Thus the correlation points move up the correlation curve for a while and thereafter move back down. An error of 2° in any of the components in α_{eq} could account for almost all of the scatter in the correlation. Since $(\Delta\alpha_{eq})_v$ at $\alpha_c = 21.7°$ is = -13.7°, a 2° error here represents a 15 percent error in the vortex model.

Turning now to the center of pressue due to control deflection $(\bar{x}/c_r)_\delta$ for fin 4, an initial correlation of this parameter versus α_c or α_{eq} for a fixed value of δ_4 but different ϕ_2 did not yield correlation as in the previous cases. It was found that better correlations can be obtained by correlating the data for a fixed ϕ_2 but variable δ_4. Thus separate correlation curves

66

are given in figure 61 for ϕ_2 = 20°, 40°, 60°, and 80°.
At α_c = 0 the variation in $(\bar{x}/c_r)_\delta$ with δ_4 is about ± 0.005
where it is ideally zero. It is noted that data generally corre-
late within ± 0.02 except for ϕ_2 = 40° as α_c = 20° is approached.
It is noted that the correlations for ϕ_2 = 60° and 80° are generally
better than those for ϕ_2 = 20° and 40°. Thus any vortex effect
on $(\bar{x}/c_r)_\delta$ is not a strong function of δ_4. It is also to be
inferred that any gap effects on $(\bar{x}/c_r)_\delta$ do not vary much with
δ_4. One is tempted to conclude that the gap effects are probably
small. The shape of the correlation curves certainly change
character with roll angle proving that roll angle is a more
significant parameter than δ_4.

It is important to know the reason for the trends shown in
figure 61 if we are to apply the results to other body lengths
or radius/semispan ratios. If the trends exhibited by the cor-
relation curves of figure 61 can be predicted by the supersonic
missile program NWCDM, then a possible basis for extrapolating
the correlation curves is obtained. Accordingly, calculations
were made for ϕ_2 = 20° and ϕ_2 = 60° to obtain $(\bar{x}/c_r)_\delta$ using the
panel code. The ϕ_2 = 20° case involves moderate body vortex
effects and the ϕ_2 = 60° case involves large body vortex effects.
The comparison of predicted and measured results are given in
figure 62 for ϕ_2 = 20°. Considering first figure 62(a) for
CNF4, we note two different predictions. The predicted CNF4 with-
out normal-force increment associated with the Polhamus leading-
edge suction analogy (square symbols) does not compare well with
the data (shown as solid lines). However, including the normal
force due to leading edge vortices causes good agreement between
data and prediction (circles).

Similar comparisons are made between predicted and measured
hinge-moment coefficients in figure 62(b). Leading edge suction
has only a minor effect on CHM. The predictions are good for
δ_4 = 0 but are otherwise generally only fair. This result must

67

be associated with errors in $(\bar{x}/c_r)_\delta$ load distribution since CNF4 was well predicted. The $(\bar{x}/c_r)_\delta$ results are shown in figure 62(c). Code NWCDM predicts an almost uniform value of $(\bar{x}/c_r)_\delta$ whereas the data show rearward movement with increase in α_c. Thus in this instance the missile code does not explain the rearward movement with α_c of $(\bar{x}/c_r)_\delta$. The reason for the trend in not known although several hypotheses can be advanced. Until the reason is isolated, using the curves for different body lengths or (a/s_m) ratios should be done only with caution.

A similar comparison is made between the predicted and measured fin characteristics for $\phi_2 = 60°$ in figure 63. The peaks in hinge-moment coefficient are overpredicted because the code does not yield precise values of $(\bar{x}/c_r)_\delta$ as shown in figure 63(c).

Let us now consider the CNF4 versus α_{eq} curves for $M_\infty = 0.8$ given in figure 64. The correlations exhibit the same behavior as those for $M_\infty = 1.2$ in figure 60. The center-of-pressure correlations for $M_\infty = 0.8$ are given in figure 65. These results are to be compared with those for $M_\infty = 1.2$ in figure 61. The trends of the curves with α_c are generally different although there is striking similarity between the curves for $\phi_2 = 80°$. If an error in $(\bar{x}/c_r)_\delta$ of ± 0.02 is accepted, then all the data correlate except that for $\phi_2 = 60°$ and $80°$ for $\delta_4 = 20°$. The values of α_{eq} are shown for the points in figure 65 which do not correlate. The limits in α_c for correlation can be added to figure 53 as a limitation in the current prediction method.

To summarize the present situation with respect to Case D, for $M_\infty = 1.2$ the correlation curves of figures 60 and 61 can be used to predict CHM4 with accuracies represented by about ± 0.02 error in $(\bar{x}/c_r)_\delta$. The reason for the trends of $(\bar{x}/c_r)_\delta$ with α_c are not understood so that application of the curves to missiles with different fin locations or different ratios (a/s_m) can only be done with caution. With respect to $M_\infty = 0.8$, the correlation

curves of figures 64 and 65 can be used to predict CHM4 with the same accuracy as for $M_\infty = 1.2$. However, at $\phi_2 = 20°$ and $\delta_4 = -10°$ and $-20°$, angle of attack limits on the accuracy of predictions exist which are similar to those of figure 53 for Case C.

5. CONCLUDING REMARKS

In these concluding remarks, we will try to bring the present investigation with its large mass of data into perspective with regard to what has been accomplished, and what is desirable for future work. Basically three areas of study that have been examined, control cross coupling and fin-fin interference in the transonic range, correlation of hinge-moment quantities for a cruciform canard all-movable control where body vortex interference in minimal, and correlation of hinge-moment quantities for cruciform delta fins of $R = 2$ where significant body vortex effects occur. The set of data for the canard fins was obtained on the Army generalized missile several years ago. The data base for the $R = 2$ delta fin is from an ongoing triservice program sponsored by the Army, Navy, and Air Force.

With respect to control cross coupling, the effect of yaw control on the pitch control fins was investigated for the canard case as it influences fin normal force and hinge moment. Negligible effects were found for the present body-diamter/fin-span ratio of 0.4 although for very small values of this ratio significant coupling is to be anticipated. Conversely the effect of pitch control on the yaw control was investigated with the same general conclusion.

The study of fin-fin control interference is based on measurements made for all four cruciform fins as a function of angle of attack and roll angle for various deflections of only one fin. The basic quantity of interest is how much the normal force on the undeflected fin is changed as a result of normal force on another fin due to control deflection. Interference factors were

69

obtained as the ratio of the change in equivalent angle of attack of the undeflected fin to the control deflection δ of the deflected fin. For engineering purposes these ratios were approximated closely enough for Mach numbers of 0.8 and 1.2 and small angles of attack by slender-body theory. The interference of the deflected fin on the opposing fin was negligible, but its effect on the adjacent fins may not be at angles of attack between 10° and 20°.

A special study of the normal force, axial center of pressure, and hinge moment was made for the canard fins of $R = 3.53$ and taper ratio 0.06 mounted in the forward position on the Army generalized missile where body vortex effects are small. The equivalent angle-of-attack concept was used to correlate the fin normal-force coefficients for various angles of attack, roll angles, and control deflections. Generally good correlation was obtained for fin normal-force coefficient. For a fin rolled 10° from the windward meridian the normal-force correlation was not good. Application of a supersonic missile program (NWCDM) to predict fin normal-force coefficient for the same conditions for another fin yielded estimates in fair agreement with data, showing that the effect is probably an inviscid one. The values of fin center of pressure for $\delta = 0$ correlated well as functions of α_c for various roll angles with the exception of some data for the fin rolled 10° from the windward meridian. The center of pressure due to control deflection correlated at $M_\infty = 0.8$ well up to fin stall, after which little or no more control effectiveness was obtained. Similar behavior was obtained at $M_\infty = 1.3$, but the stall was much more gradual for this case. A special study to correlate this parameter above the stall was not made.

The remaining part of the work was directed at studying the hinge-moment characteristics of an $R = 2$ delta cruciform fin for which an extensive systematic data base has been obtained to high angles of attack from subsonic to hypersonic Mach numbers in a

70

triservice program aimed at obtaining a comprehensive data base on all-movable cruciform controls. The program when completed will contain data for five fin planforms varying in aspect ratio from 2 to 4 and taper ratio 0 to 1, but with uniform double-wedge airfoil sections. The motivation for this study was to try to establish a rational modeling procedure to estimate hinge moment so that the data base results can be generalized to bodies of varying length, to different body-diameter/fin-span ratios, and to fins influenced by vortices from forward surfaces. It is impossible to obtain a complete data base covering those additional conditions.

For this last study the operating regime was decomposed into four cases to cover the different aerodynamic phenomena existing for the different cases as follows:

Case A: Windward fins, no control deflection
Case B: Leeward fins, no control deflection
Case C: Windward fins, control deflection
Case D: Leeward fins, control deflection

The study was based on using correlations suggested by the equivalent angle-of-attack concept augmented with theoretical aerodynamic calculations made at $M_\infty = 1.2$ by the supersonic missile code, NWCDM.

For Case A it was found generally that correlation curves based on the equivalent angle-of-attack concept provided adequate means for determining the hinge-moment coefficient. Some anomolous correlation was obtained for normal-force data for fins rolled 10° from the windward meridian, but code NWCDM was successful in predicting the discrepancies except at the high angles of attack where its accuracy is marginal for $M_\infty = 1.2$

For Case B the normal-force data generally correlated well. It was found for fins near the horizontal roll position that significant normal-force increments are associated with the fin leading-edge vortices but these effects were small on hinge-moment

coefficients. The correlation curves account for the effect of leading-edge suction on normal-force coefficient. It was found that the fin center-of-pressure results did not correlate on equivalent angle of attack, but correlated better on body angle of attack. However, at large angles of attack where significant vortex effects influenced the fin, the values of center of pressure did not correlate. The simplified vortex model used in the preliminary hinge-moment prediction method of reference 1 was not sufficiently accurate to predict the center of pressure of the body vortex loading on the fin. Code NWCDM showed positions of the center of pressure well forward of the hinge line for intermediate angle of attack where the vortices are weak. As the angle of attack is increasing, the predicted vortex center of pressures moves aft and the vortex download increases. This, combined with an upload on the fin behind the hinge line due to the nonvortical component of the normal force, produces a couple when the two components of normal force are equal and opposite. At this condition the hinge moment is a pure couple and is close to a maximum at moderate angles of attack. This couple cannot be reduced by repositioning the hinge line. The code NWCDM was fairly successful in predicting the peak hinge moments although some inaccuracy existed at high angles of attack because the code does not predict the center of pressure of the nonvortical loading accurately. The presently proposed hand estimation method for this case consists of correlation curves of all quantities except the center-of-pressure locations of the vortex normal force. It is recommended that code NWCDM be used to obtain design charts for this quantity for use with the correlation curves. Unfortunately a subsonic program similar to NWCDM does not exist so that this procedure is currently not possible for the subsonic part of the transonic range.

For Case C the correlation curves generally predict fin normal force adequately. Also, good values of the center-of-pressure position due to fin deflection were obtained up to angles

72

of attack depending on roll angle and the sign of the fin deflection angle. For fin deflections which tend to unload the fin normal force, good correlation was obtained to $\alpha_c = 20°$, but for fin deflection angles of the opposite sign the above mentioned limits exist for the current method except for fins near the windward meridian. Code NWCDM was not successful in removing this limitation. The facts are consistent with the hypothesis that the positive pressure field under the fins interacts with the body boundary layer in a fashion that changes the fin center-of-pressure location. Means for overcoming this limitation were not found.

With respect to Case D it was feared that interaction between control deflection and body vortices would complicate the correlation procedure. This was found not to be the case for normal-force coefficient nor for center-of-pressure position due to control deflection for fin deflections which tend to unload up the fin. However, for control deflections of the opposite sign, it was not possible to correlate the fin center-of-pressure position due to control deflection at high angles of attack for $\phi_2 = 20°$. Accordingly, limits in angles of attack similar to those for Case C were found on the applicability of the method for trailing edge down control deflections except near the leeward meridian.

As a result of the present study, certain suggestions for future analytical work and experimental work arise. First with respect to the triservice data base, the other four fins of the triservice data base should be analyzed in a similar manner to the present fin T51 to see if the results obtained for that fin are general. Then a hand method for calculating hinge moment at transonic speeds can be assembled based on the correlation curves and certain data supplied by code NWCDM. It is desirable to develop a subsonic code analogous to NWCDM to obtain the center-of-pressure position of the vortex loading at subsonic speeds.

The triservice data base is for controls utilizing uniform double-wedge sections in the streamwise direction. It is known that airfoil sections can have important effects on the normal-force and center-of-pressure characteristics of transonic wings for M_∞ near 1.0. If this problem can be resolved, then the data base can be extended to fins of different airfoil sections. Some exploratory data to aid this study are desirable.

The method is presently limited in angle of attack for trailing edge down control deflection. Further study of this limitation is possible with a view to its amelioration. It may be possible to correlate the deviation from the center-of-pressure position given by the equivalent angle-of-attack concept. This advance is worthwhile not only to remove the angle-of-attack limitations of the current method, but also to be able to extrapolate the method in configuration space.

The triservice data base as presently envisioned will contain definitive data for $M_\infty = 0.8$ and $M_\infty = 1.2$ For $M_\infty = 0.9$ only zero control deflection data is being taken. It would be desirable to fill out the data base at $M_\infty = 0.9$ so that three transonic Mach numbers are available.

Generally we have found from former studies that fins of low taper ratio, $\lambda = 0$ to 0.25, yield the least hinge moments without much loss in control effectiveness. It appears desirable to concentrate on such low-taper-ratio wings in future investigations. Aspect ratios less than 2 are of lesser interest since the root chord tends to be very long for fins of adequate planform area.

ACKNOWLEDGEMENTS

REFERENCES

1. Nielsen, Jack N. and Goodwin, Frederick K.: Preliminary Method for Estimating Hinge Moments of All-Movable Controls. NEAR TR 268, March 1982.

2. Smith, C. A. and Nielsen, J. N.: Nonlinear Aerodynamics of All-Movable Controls. Paper presented at AGARD Fluid Dynamics Panel Symposium, Pozzuoli, Italy, 14-17 May 1979. Paper 25, AGARD Conference Proceedings No. 262, Aerodynamic Characteristics of Controls.

3. No author listed: High Alpha Aerodynamics - Fin Alone (Data report in AEDC-TR-75-124, Vols. I and II), Propulsion Wind Tunnel Facility, ARO, Inc., July 1974.

4. Baker, W. B., Jr.: Static Aerodynamic Characteristics of a Series of Generalized Slender Bodies With and Without Fins at Mach Numbers of 0.6 to 3.0 and Angles of Attack From 0 to 180 Degs. AEDC-TR-75-124, Vols. I and II, May, 1976.

5. Stallings, Robert L., Jr. and Lamb, Milton: Wing-Alone Aerodynamic Characteristics for High Angles of Attack at Supersonic Speeds. NASA TP 1889, July, 1981.

6. Briggs, M. M., Reed, R. E., and Nielsen, J. N.: Wing-Alone Aerodynamic Characterisitcs to High Angles of Attack at Subsonic and Transonic Speeds. NEAR TR 269, September, 1982.

7. Hemsch, M. J. and Nielsen, J. N.: Equivalent Angle-of-Attack Method for Estimating Nonlinear Aerodynamics of Missile Fins. Jour. of Spacecraft and Rockets, Vol. 20, No. 4, July-August, 1983, pp. 356-362.

8. Schwind, R. G.: High Angle Canard Test in the Ames 11-Foot Transonic Wind Tunnel. NASA CR 2993, 1978.

9. Hemsch, M. J. ,and Nielsen, J. N.: Test Report for Canard Missile Tests in Ames 6- by 6-Foot Supersonic Wind Tunnel. NEAR TR 72, 1974.

10. Smith, C. A. and Nielsen, J. N.: Prediction of Aerodynamic Characteristics of Cruciform Missiles to High Angles of Attack Utilizing a Distributed Vortex Wake. NEAR TR 208, January, 1980 (MISSILE2).

11. Dillenius, M. F. E.: Program NWCDM for Prediction of Detailed Aerodynamic Loading Acting on Supersonic Wing-Body-Tail Missiles with Axisymmetric Bodies and Steady Rotational Rates(U). NEAR TR 300, August, 1983, (Confidential).

12. Polhamus, Edward C.: A Concept of Vortex Lift Based on Sharp-Edge Delta Wings Based on a Leading-Edge Suction Analogy, NACA TN D-3767, December 1966.

TABLE I.- CALCULATED CENTER-OF-PRESSURE LOCATIONS DUE TO VORTEX LOADING ON FIN 51 ON TRISERVICE MISSILE

CASE B $M_\infty = 1.2$

A. BODY VORTICES ONLY

α_c \\ $-\phi$	$(\bar{x}/c_r)_v$				$[(\bar{y}-a)/(s_m-a)]_v$			
	20°	40°	60°	80°	20°	40°	60°	80°
8	0.652	0.573	0.412	0.440	0.338	0.320	0.212	0.229
10	0.670	0.593	0.432	0.473	0.334	0.326	0.250	0.251
12	0.684	0.610	0.560	0.524	0.331	0.331	0.308	0.289
15	0.691	0.635	0.635	0.607	0.326	0.336	0.344	0.362
20	0.704	0.664	0.664	0.675	0.325	0.336	0.351	0.410

B. BODY VORTICES PLUS LEADING-EDGE VORTICES

α_c \\ $-\phi$	BODY VORTICES PLUS LEADING-EDGE VORTICES				BODY VORTICES ONLY			
	$(\bar{x}/c_r)_v$		$[(\bar{y}-a)/(s_m-a)]_v$		$(\bar{x}/c_r)_v$		$[(\bar{y}-a)/(s_m-a)]_v$	
	20°	60°	20°	60°	20°	60°	20°	60°
8	0.639	0.418	0.371	0.264	0.652	0.412	0.338	0.212
10	0.653	0.423	0.375	0.240	0.670	0.432	0.334	0.250
12	0.660	0.556	0.380	0.317	0.684	0.560	0.331	0.308
15	0.658	0.632	0.394	0.365	0.691	0.635	0.326	0.344
20	0.655	0.657	0.424	0.380	0.704	0.664	0.325	0.351

TABLE II.- MACHINE CALCULATION OF NORMAL-FORCE AND HINGE-MOMENT
COEFFICIENTS OF FIN 51 USING CODE NWCDM

CASE B

$\phi_2 = -60°$, $\delta_4 = 0$

α_c	$(CNF)_p$	$\left(\dfrac{\bar{x}}{c_r}\right)_p$	$\left(\dfrac{\bar{x}-x_{HL}}{c_r}\right)_p$	$(CHM)_p$	$(CNF)_v$	$\left(\dfrac{\bar{x}}{c_r}\right)_v$	$\left(\dfrac{\bar{x}-x_{HL}}{c_r}\right)_v$	$(CHM)_v$	$(CHM)_t$
2.08	0.064	0.652	0.041	+0.0026	0	--	--	0	0.0026
5.07	0.153	0.650	0.035	0.0060	0	--	--	0	0.0060
8.00	0.235	0.648	0.037	0.0087	-0.142	0.418	-0.193	0.0274	0.0362
10.11	0.291	0.646	0.035	0.0102	-0.179	0.423	-0.188	0.0337	0.0440
12.0	0.339	0.645	0.034	0.0115	-0.318	0.556	-0.055	0.0175	0.0290
15.17	0.414	0.644	0.033	0.0137	-0.501	0.632	0.021	-0.0104	0.0033
20.06	0.522	0.647	0.036	0.0188	-0.635	0.657	0.046	-0.0290	-0.104
21.68	0.555	0.644	0.033	0.0183	-0.654	0.656	0.045	-0.0293	-0.107

$(CHM)_p = (CHM)_t - (CHM)_v$
No leading-edge normal force
CNF is positive upward
CHM is positive trailing-edge up

TABLE III.- HAND CALCULATION OF NORMAL-FORCE AND HINGE-MOMENT COEFFICIENTS OF FIN 51 USING CORRELATION CURVES

CASE B

$$M_\infty = 1.2, \quad \phi_2 = -60°$$

A. NORMAL-FORCE COEFFICIENT

α_c	α_{eq} [eq. (6)]	$(\Delta\alpha_{eq})_v$ [fig. 35(d)]	$(\alpha_{eq})_p$	$(CNF)_p$ [fig. 41(b)]	$(CNF)_v$ [fig. 41(b)]	$(CNF)_t$
2°	1.47		1.47	0.061		0.061
4	2.85		2.85	0.118		0.118
6	3.85		3.85	0.159		0.159
8	2.70	- 3.12	5.84	0.242	-0.130	0.112
10	2.10	- 4.56	6.66	0.276	-0.189	0.087
12	1.6	- 6.09	7.69	0.314	-0.252	0.072
14	1.1	- 7.70	8.70	0.361	-0.320	0.041
16	0.55	- 9.44	9.99	0.415	-0.391	0.024
18	-0.2	-11.30	11.10	0.460	-0.469	-0.009
20	-1.2	-13.07	11.87	0.493	-0.542	-0.049
22	-2.3	-14.95	12.65	0.525	-0.620	-0.095

Fig. 41(b): $\dfrac{\partial CNF4}{\partial \alpha_{eq}} = 0.0415$ up to $\alpha_{eq} = 12°$

TABLE III.- CONCLUDED

B. HINGE MOMENT COEFFICIENT

α_c	$(CNF)_p$ TABLE IIIA	$\left(\dfrac{\bar{x}}{c_r}\right)_p$ * Fig. 37(b)	$\left(\dfrac{\bar{x}-x_{HL}}{c_r}\right)_p$	$(CHM)_p$	$(CNF)_v$ TABLE IIIA	$\left(\dfrac{\bar{x}}{c_r}\right)_v$ TABLE I	$\left(\dfrac{\bar{x}-x_{HL}}{c_r}\right)_v$	$(CHM)_v$	$(CHM)_t$
2	0.061	0.632	0.021	+0.0013	0			0	+0.0013
4	0.118	0.633	0.022	+0.0026	0			0	+0.0026
6	0.159	0.633	0.022	+0.0035	0			0	+0.0035
8	0.242	0.632	0.021	+0.0051	-0.130	0.418	-0.193	0.0250	+0.0301
10	0.276	0.632	0.021	+0.0058	-0.189	0.423	-0.188	0.0355	0.0413
12	0.314	0.632	0.021	+0.0066	-0.252	0.556	-0.055	0.0139	0.0205
14	0.362	C.631	0.020	+0.0072	-0.320	0.610	-0.001	0.0003	0.0075
16	0.415	0.631	0.020	+0.0083	-0.391	0.634	0.023	-0.0090	-0.0007
18	0.460	0.630	0.019	+0.0087	-0.469	0.648	0.037	-0.0174	-0.0084
20	0.493	0.631	0.020	+0.0099	-0.542	0.657	0.046	-0.0250	-0.0151
22	0.525	0.632	0.021	+0.0110	-0.620	0.662	0.051	-0.0316	-0.0206

* Case A; $\left(\dfrac{x}{c_r}\right)_{HL} = 0.611$

TABLE IV.- MACHINE CALCULATIONS OF NORMAL-FORCE AND HINGE-MOMENT
COEFFICIENTS OF FIN 51 USING CODE NWCDM

CASE B

$\phi_2 = 20°$, $\delta_4 = 0$

α_c	POTENTIAL PART			BODY VORTEX PART			LEADING-EDGE PART			TOTAL		
	CNF	CHM	$\left(\dfrac{\bar{x}-x_{HL}}{c_r}\right)$	CNF	CHM	$\left(\dfrac{\bar{x}-x_{HL}}{c_r}\right)$	CNF	CHM	$\left(\dfrac{\bar{x}-x_{HL}}{c_r}\right)$	CNF	CHM	$\left(\dfrac{\bar{x}-x_{HL}}{c_r}\right)$
2	0.1143	0.00476	0.0416	0	0	--	0.00326	-0.00003	-0.009	0.1176	0.00473	0.040
5	0.2713	0.01069	0.039	0	0	--	0.02035	-0.00016	-0.008	0.2917	0.01053	0.036
6	0.3183	0.01231	0.037	0	0	--	0.0293	-0.00024	-0.008	0.3475	0.01207	0.035
8	0.4039	0.01535	0.038	-0.0474	-0.00193	0.041	0.0440	-0.00003	-0.001	0.4005	0.01339	0.033
10	0.4797	0.01865	0.039	-0.0655	-0.00393	0.060	0.0670	-0.00002	0	0.4812	0.01469	0.031
12	0.5464	0.02248	0.041	-0.0831	-0.00610	0.073	0.0937	0.00003	0	0.5570	0.01642	0.030
15	0.6313	0.02918	0.046	-0.1157	-0.00932	0.081	0.1346	0.00034	0.003	0.6502	0.0202	0.031
20	0.7429	0.04308	0.058	-0.2009	-0.01868	0.093	0.1858	0.00164	0.009	0.7278	0.02604	0.036

CNF is positive upward
CHM is positive trailing edge up

TABLE V.- HAND CALCULATION OF NORMAL-FORCE AND HINGE-MOMENT
COEFFICIENTS OF FIN 51 USING CORRELATION CURVES

CASE B

$M_\infty = 1.2, \phi_2 = -20°$

A. NORMAL-FORCE COEFFICIENT

α_c	$(\alpha_{eq})_p$ (eq. 6)	$(CNF)_p$ fig. 41(b)	$(\Delta\alpha_{eq})_v$ fig. 35(d)	$(\Delta\alpha_{eq})_t$	$(CNF)_t$	$(CNF)_v$
2	2.70	0.12	0.0	2.70	0.12	0.0
4	5.27	0.27	0.0	5.37	0.23	0.0
6	7.98	0.33	0.0	7.98	0.33	0.0
8	10.56	0.44	-1.06	9.50	0.40	-0.04
10	12.09	0.54	-1.96	11.13	0.46	-0.08
12	15.58	0.65	-2.80	12.78	0.54	-0.11
14	18.04	0.755	-3.65	14.39	0.60	-0.155
16	20.44	0.855	-4.51	15.93	0.665	-0.190
18	22.81	0.94	-5.36	17.45	0.735	-0.205
20	25.13	1.005	-6.17	18.96	0.795	-0.210
22	27.40	1.075	-6.94	20.46	0.855	-0.220

84

TABLE V.- CONCLUDED

B. Hinge-Moment Coefficient

α_c	$(CNF)_p$ (A)	$(\bar{x}/c_r)$ fig. 43(b) $\phi=0°$	$\dfrac{\bar{x}-x_{HL}}{c_r}$ $x_{HL}/c_r=0.61$	$(CHM)_p$	$(CNF)_v$ (A)	$\left(\dfrac{\bar{x}}{c_r}\right)_v$ TABLE IIA	$\left(\dfrac{\bar{x}-x_{HL}}{c_r}\right)_v$	$(CHM)_v$	$(CHM)_t$
2	0.12	0.647	0.036	0.0043	0.0				0.0043
4	0.23	0.645	0.034	0.0078	0.0				0.0078
6	0.33	0.642	0.031	0.0102	0.0				0.0102
8	0.44	0.640	0.029	0.0128	-0.04	0.652	0.041	-.0016	0.0112
10	0.54	0.638	0.027	0.0146	-0.08	0.670	0.059	-.0047	0.0099
12	0.65	0.636	0.025	0.0162	-0.11	0.684	0.073	-.0080	0.0082
14	0.755	0.655	0.024	0.0181	-0.155	0.688	0.077	-.0119	0.0062
16	0.855	0.635	0.024	0.0205	-0.190	0.694	0.083	-.0158	0.0047
18	0.94	0.635	0.024	0.0226	-0.205	0.699	0.088	-.0180	0.0044
20	1.005	0.636	0.025	0.0251	-0.210	0.702	0.091	-.0191	0.0060
22	1.075	0.636	0.026	0.0280	-0.220	0.703	0.092	-.0202	0.0078

TABLE VI.- MACHINE CALCULATION OF NORMAL-FORCE AND HINGE-MOMENT CHARACTERISTICS OF FIN 51 USING CODE NWCDM

$\phi_2 = -80°$, WINDWARD FIN, $\delta_4 = 0°$, $10°$, CASE C

α_c (degs)	CNF $\delta_4=10°$	CNF $\delta_4=0°$	$(CNF)_\delta$	CHM $\delta_4=10°$	CHM $\delta_4=0°$	$(CHM)_\delta$	$\left(\dfrac{\bar{x}}{c_r}\right)_\delta$
2	.3428	−.0219	.3647	−.0175	.0009	−.0184	.661
5	.3264	−.0539	.3803	−.0172	.0024	−.0196	.663
6	.3203	−.0628	.3831	−.0171	.0029	−.0200	.663
8	.3068	−.0925	.3993	−.0166	.0040	−.0206	.663
10	.2921	−.1173	.4094	−.0162	.0051	−.0213	.663
12	.2759	−.1426	.4185	−.0157	.0062	−.0219	.663
15	.2489	−.1811	.4300	−.0147	.0078	−.0225	.663
20	.1978	−.2447	.4414	−.0124	.0107	−.0231	.663

Positive CNF_4 is to right in Quadrant III

Positive CHM_4 is trailing edge left in Quadrant III

Positive δ_4 is trailing edge left in Quadrant III

No leading-edge normal force

TABLE VII.- EXPERIMENTAL DATA FOR COMPARISON OF COMPUTER RESULTS IN TABLE VI

$\phi_2 = -80°$, WINDWARD FIN 4, $\delta_4 = 0°$, $10°$, CASE C

α degs	CNF4 $\delta=10°$	CNF4* $\delta=0°$	$(CNF)_\delta$	CHM $\delta=10°$	CHM $\delta=0°$	$(CHM)_\delta$	$\left(\dfrac{\bar{x}}{c}\right)_\delta$
-1.96	.3795	-.0008	.3803	-.0201	.0003	-.0204	.665
.06	.3625	-.0194	.3819	-.0163	.0010	-.0173	.656
2.07	.3561	-.0436	.3977	-.0128	.0018	-.0146	.648
5.07	.3275	-.0816	.4088	-.0081	.0033	-.0114	.639
10.10	.2648	-.1773	.4421	.0006	.0099	-.0093	.632
15.14	.1852	-.2869	.4721	.0096	.0164	-.0068	.625
20.05	.1047	-.3879	.4926	.0186	.0208	-.0022	.615
21.61	.0766	-.4195	.4561	.0216	.0208	+.0008	.610

Positive CNF_4 is to right in Quadrant III

Positive CHM_4 is trailing-edge left in Quadrant III

Positive δ_4 is trailing-edge left in Quadrant III

* These quantities contain the effects of about 2° of sidewash as the value of CNF at $\alpha_c=-1.96°$ shows.

Tail Fin Config	S_r, in.²	AR	b/2, in.	λ	Λ	A, in.	C_T, in.	B, in.	C_R', in.	HL/C_R	t_R', in.	t_t', in.	$\dfrac{t_R}{C_R}$
16	7.916	2.0	2.821	1.0	90°	0.800	2.813	1.140	2.813	0.45	0.140	0.140	0.050
13	7.916	2.0	2.821	0.5	56°19'	1.158	1.873	1.140	3.749	.55	0.187	0.187	0.050
12	7.942	2.0	2.821	0.	26°34'	1.172	0	1.140	5.625	0.62	0.187	0.187	0.033
21	3.5119	2.0	1.874	1.0	90°	0.696	1.874	0.696	1.874	0.45	0.125	0.125	0.067
23	3.6066	2.0	1.875	0.5	55°38'	0.713	1.282	0.694	2.565	0.55	0.125	0.125	0.049
22	3.5156	2.0	1.875	0	26°34'	0.728	0	0.694	3.750	0.62	0.125	0.125	0.033
11	7.028	1.0	1.875	1.0	90°	0.800	3.749	0.800	3.749	0.45	0.140	0.140	0.037
15	7.024	1.0	1.875	0.5	36°54'	1.165	2.497	1.140	4.996	0.55	0.187	0.187	0.037
14	7.028	1.0	1.875	0	14°3	1.195	0	1.140	7.499	0.62	0.187	0.187	0.025
32	14.036	0.5	1.875	1.0	90°	1.587	7.499	1.587	7.499	0.45	0.250	0.250	0.033
31	14.030	0.5	1.875	0.5	20°36'	1.626	4.990	1.587	9.980	0.55	0.250	0.125	0.025
36	14.056	0.5	1.875	0	7°8'	1.602	0	1.587	14.998	0.62	0.250	0.250	0.017
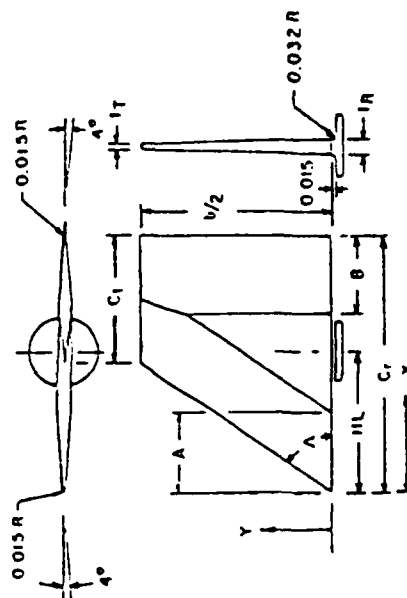
Figure 1.- Summary of characteristics of wings of Baker data base.

t_{max} $\theta_W = 15°$

$\theta_W = 15°$ normal to all edges

c_t

$\frac{b}{2}$

c_r
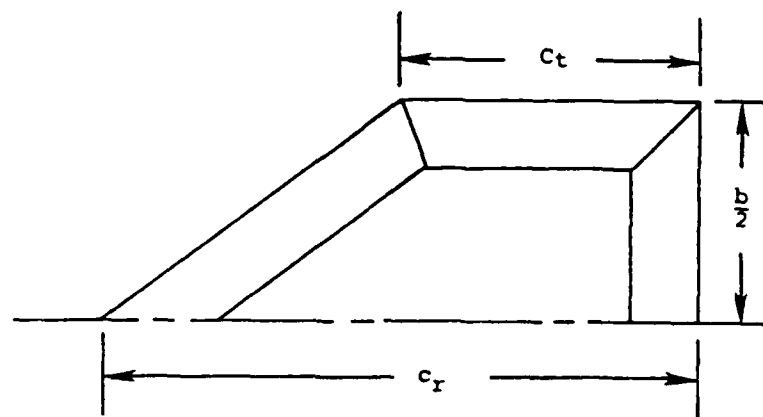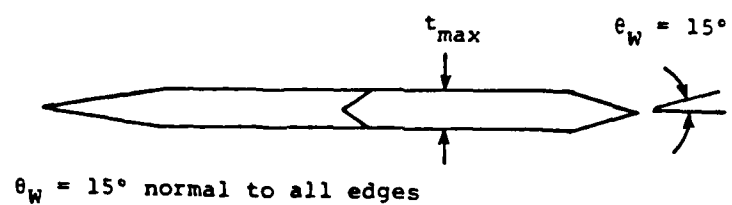
Wing	R	b in.	c_t in.	c_r in.	λ	t_{max} in.	$\dfrac{t_{max}}{c_r}$
P_1	0.5	4.243	0	16.971	0	0.500	0.029
P_2	0.5	4.243	5.657	11.314	0.50	0.500	0.044
P_3	0.5	4.243	8.486	8.486	1.00	0.500	0.059
P_4	1.0	6.000	0	12.000	0	0.500	0.042
P_5	1.0	6.000	4.000	8.000	0.50	0.500	0.062
P_6	1.0	6.000	6.000	6.000	1.00	0.500	0.083
P_7	2.0	8.486	0	8.486	0	0.500	0.059
P_8	2.0	8.485	2.828	5.657	0.50	0.500	0.088
P_9	2.0	8.485	4.243	4.243	1.00	0.500	0.118
P_{10}	4.0	12.000	2.000	4.000	0.50	0.500	0.125

Figure 2.- Summary of characteristics of wings of
Stallings-Lamb-Briggs data base.

89
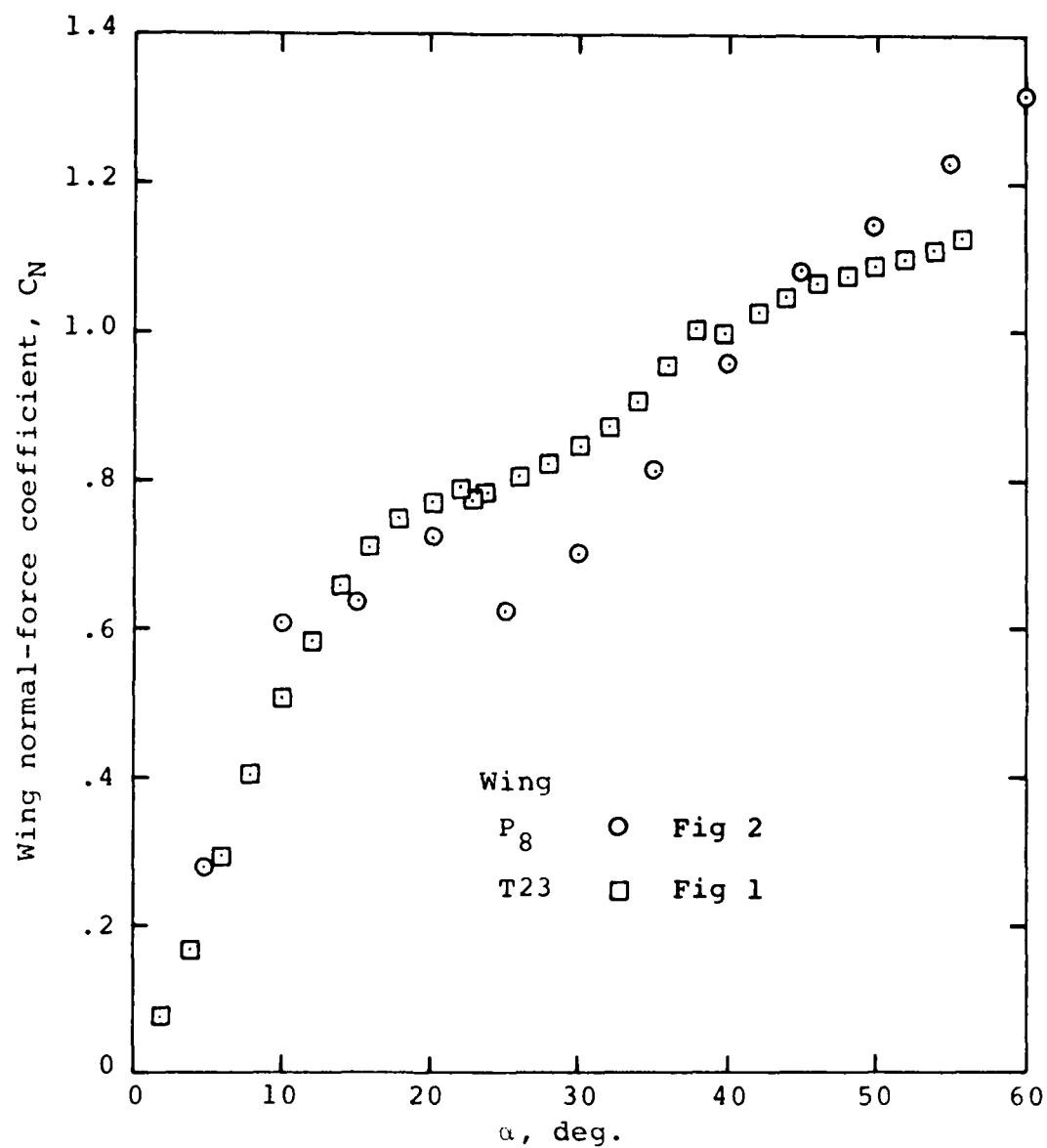
(a) AR = 2, λ = 0.5, M_α = 0.8

Figure 3.- Comparison of wing-alone normal-force
curves at transonic speeds.
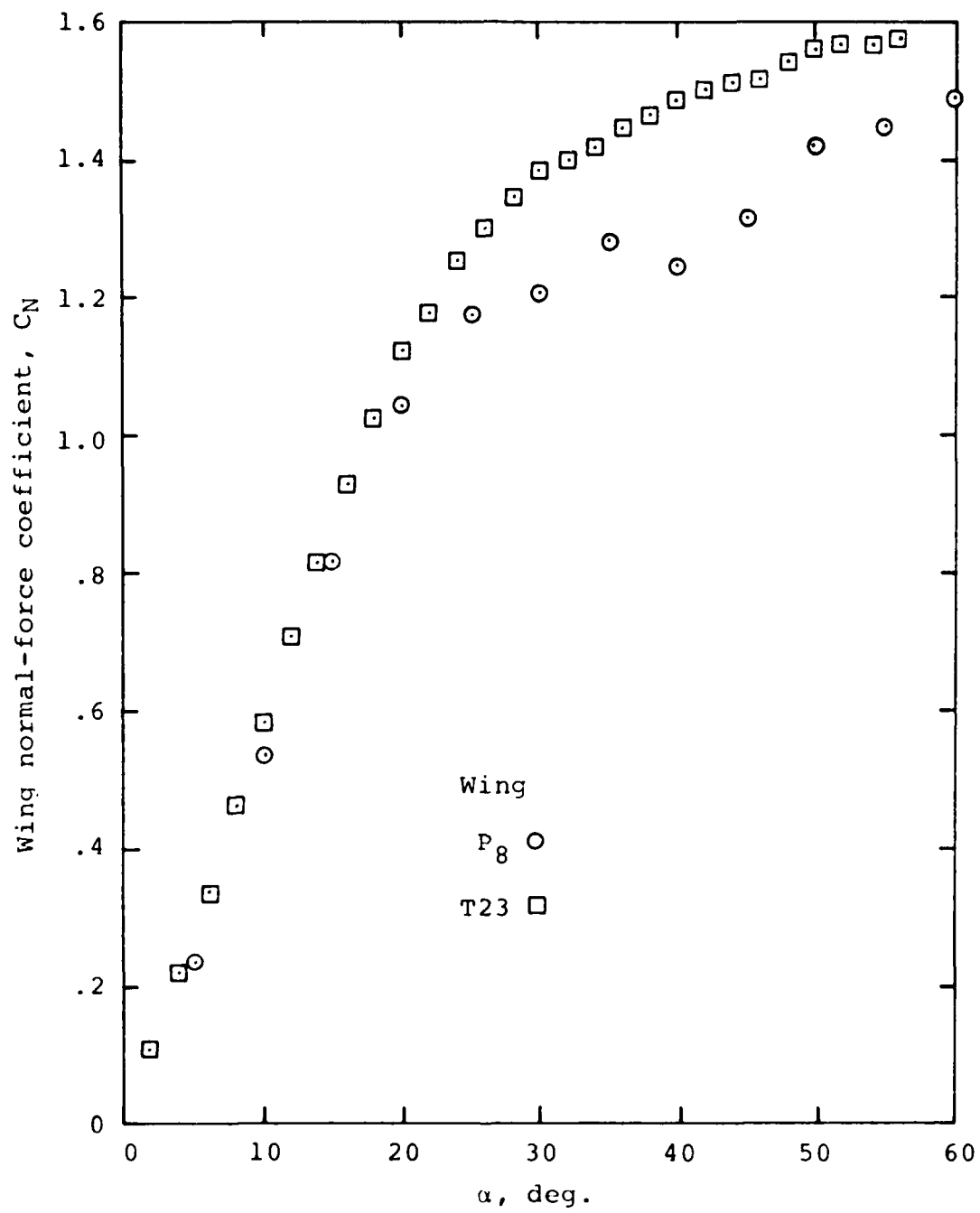
(b) $\text{Æ} = 2$, $\lambda = 0.5$, $M_\infty = 1.2$

Figure 3.- Concluded.
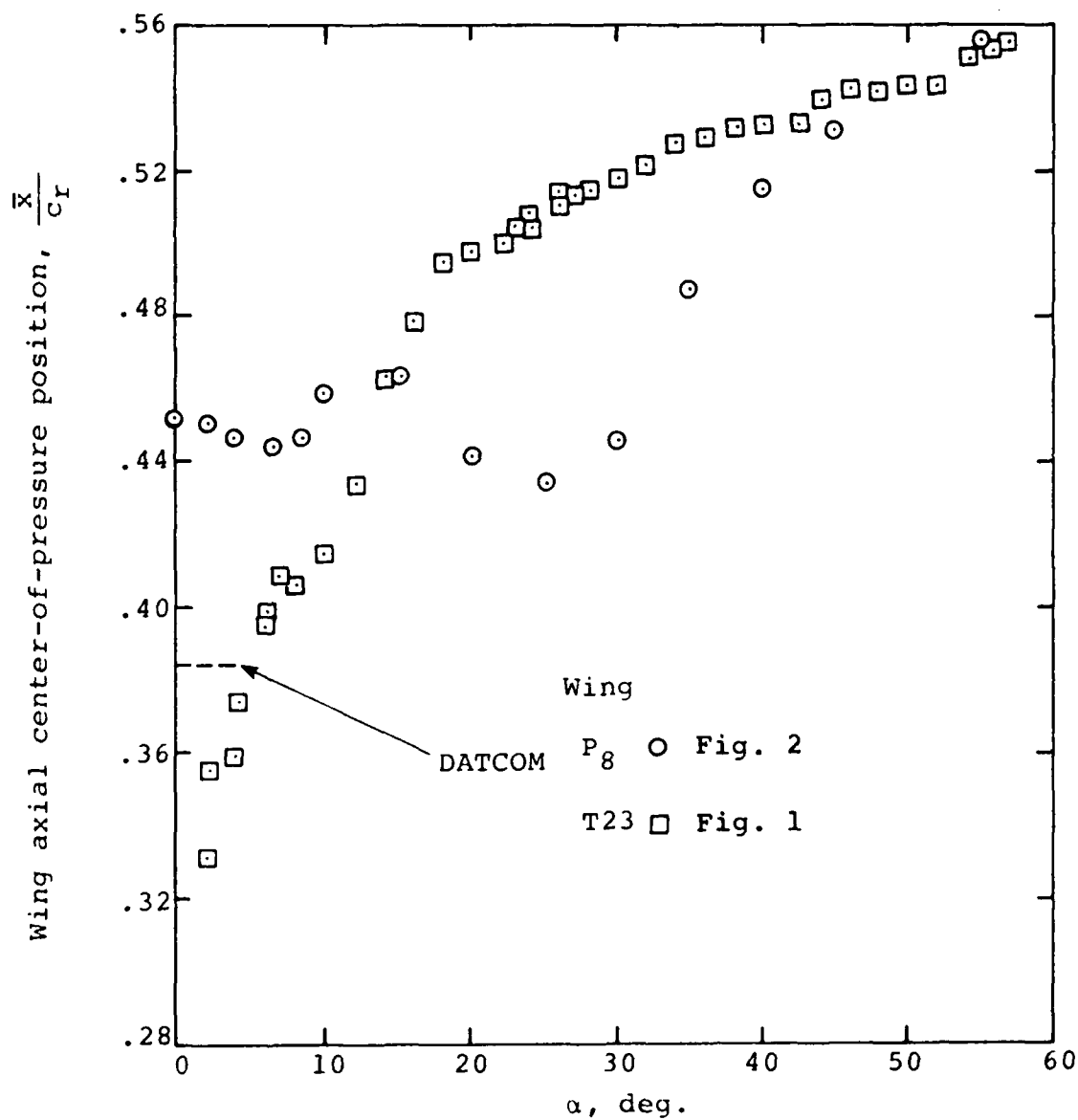
(a) $AR = 2$, $\lambda = 0.5$, $M_\infty = 0.8$

Figure 4.- Comparison of wing-alone axial center-of-pressure positions at transonic speeds.

92
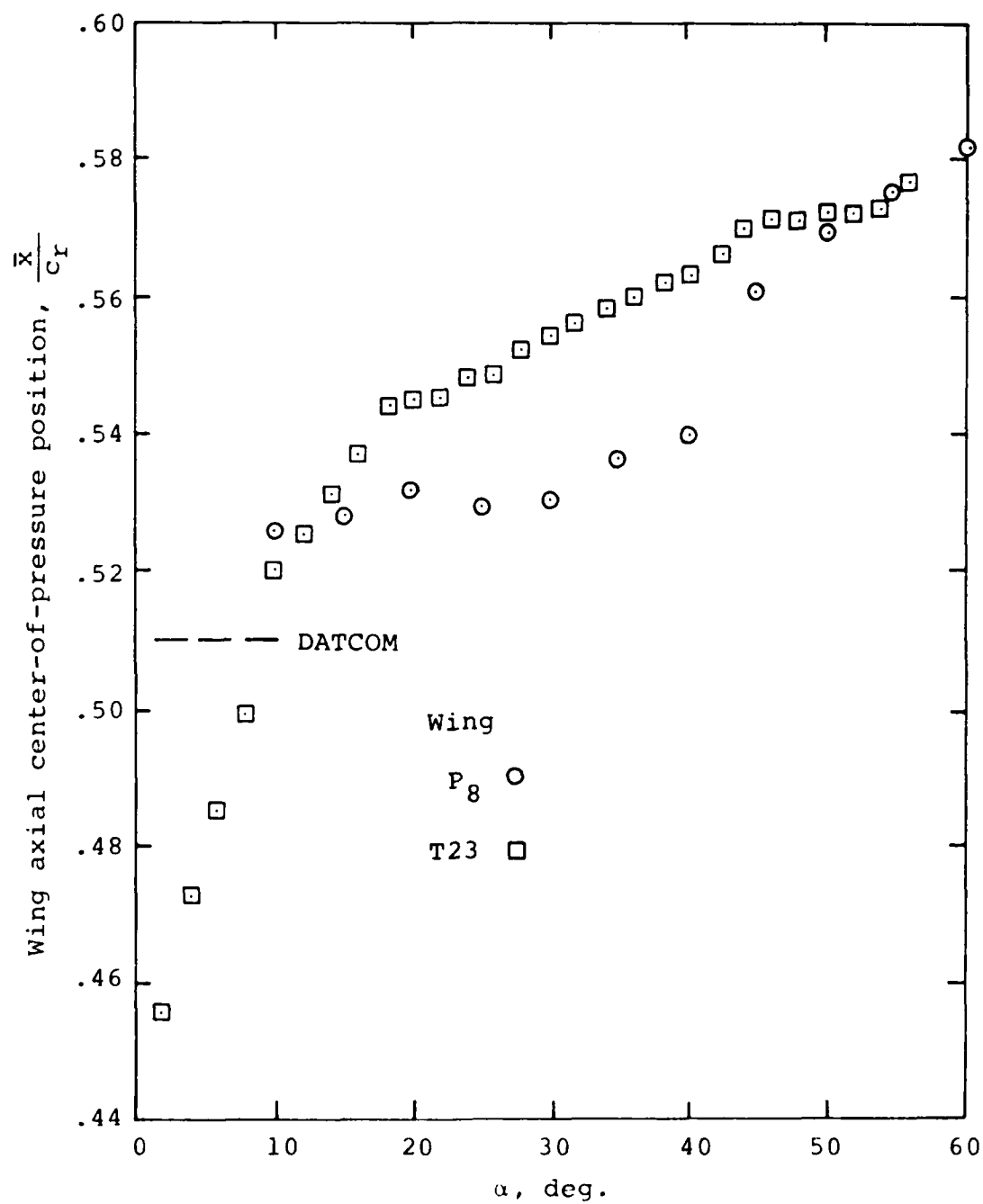
(b) AR = 2.0, λ = 0.5, M_α = 1.2

Figure 4.- Concluded.

MICROCOPY RESOLUTION TEST CHART

NATIONAL BUREAU OF STANDARDS-1963-A

42.5
(16.72)

32.3
(12.72)

109.2
(43.0)

127.0
(50.0)

3 CALIBER
OGIVE

15.9
(6.25)

15.2
(6.0)

12.7
(5.0)

1.4
(0.56) R

HINGE
LINE

MOMENT
CENTER

HINGE
LINE

132.1
(52.0)

O MISSILE
STATION
ZERO

38.1
(15.0)

66.0
(26.0)

116.0
(46.0)

132.1
(52.0)
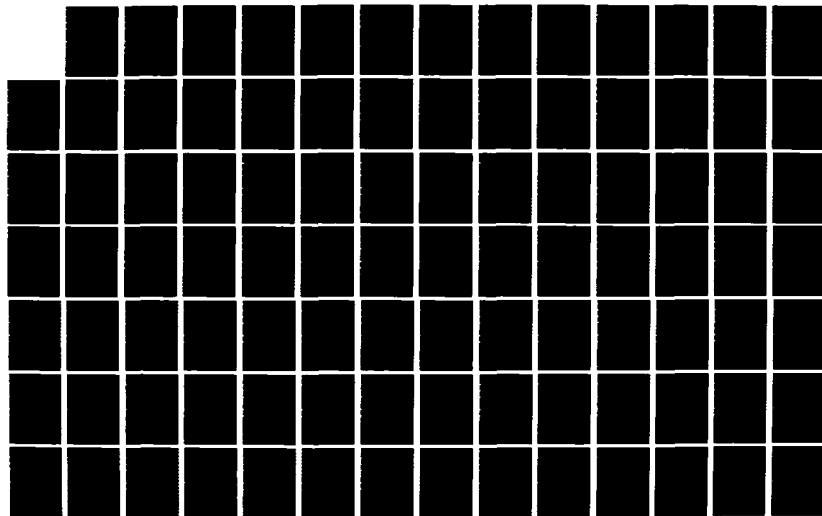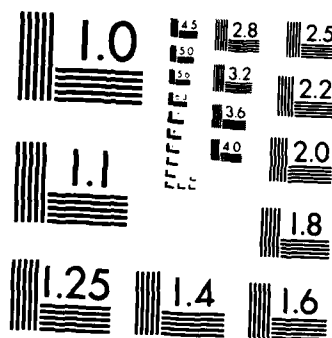
CENTIMETERS
(INCHES)
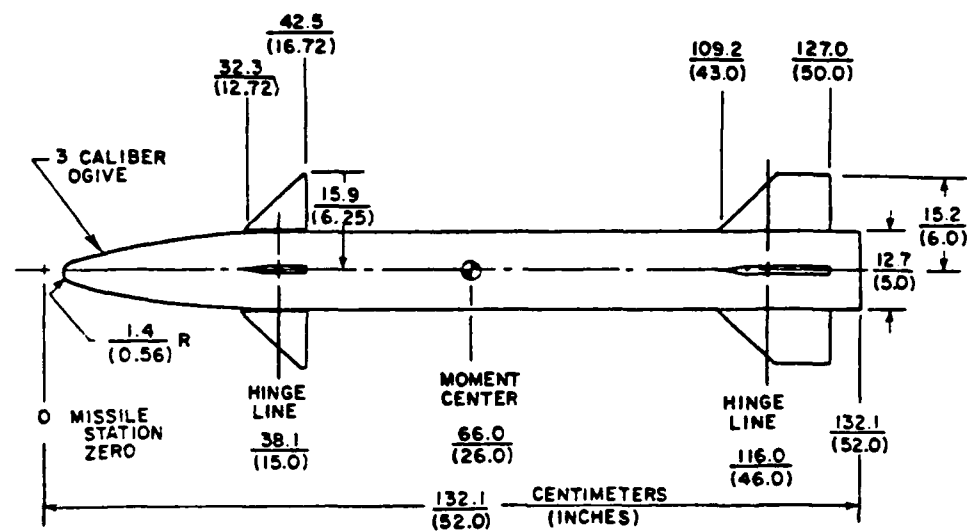
(a) Army generalized missile

Figure 5.- Missile configurations considered.
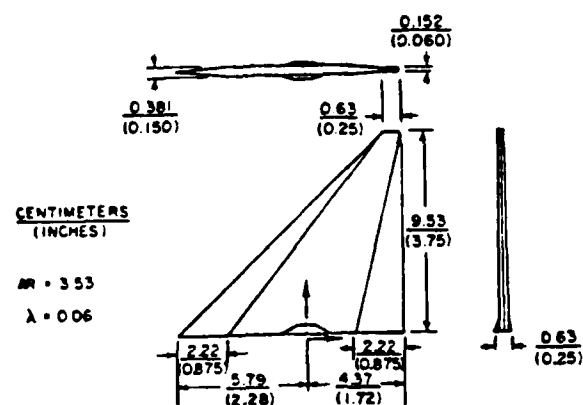
(b) Fin C_6 of Army generalized missile

Figure 5.- Continued.

All dimensions in centimeters (inches)
Hinge line at MS 74.300 (29.252)
Balance center at MS 47.178 (18.574)

$\underline{7.620}$
$\overline{(3.000)}$

Afterbody

Control

$\underline{87.630}$
$\overline{(34.500)}$

$\underline{77.069}$
$\overline{(30.342)}$

Wiring

$\underline{64.844}$
$\overline{(25.529)}$

Balance

$\underline{56.335}$
$\overline{(22.179)}$

$\underline{33.719}$
$\overline{(13.275)}$

Motor

$\underline{20.066}$
$\overline{(7.900)}$

shoulder

$\underline{16.510}$
$\overline{(6.500)}$

Nose

MSO

$\underline{-6.350}$
$\overline{(-2.500)}$
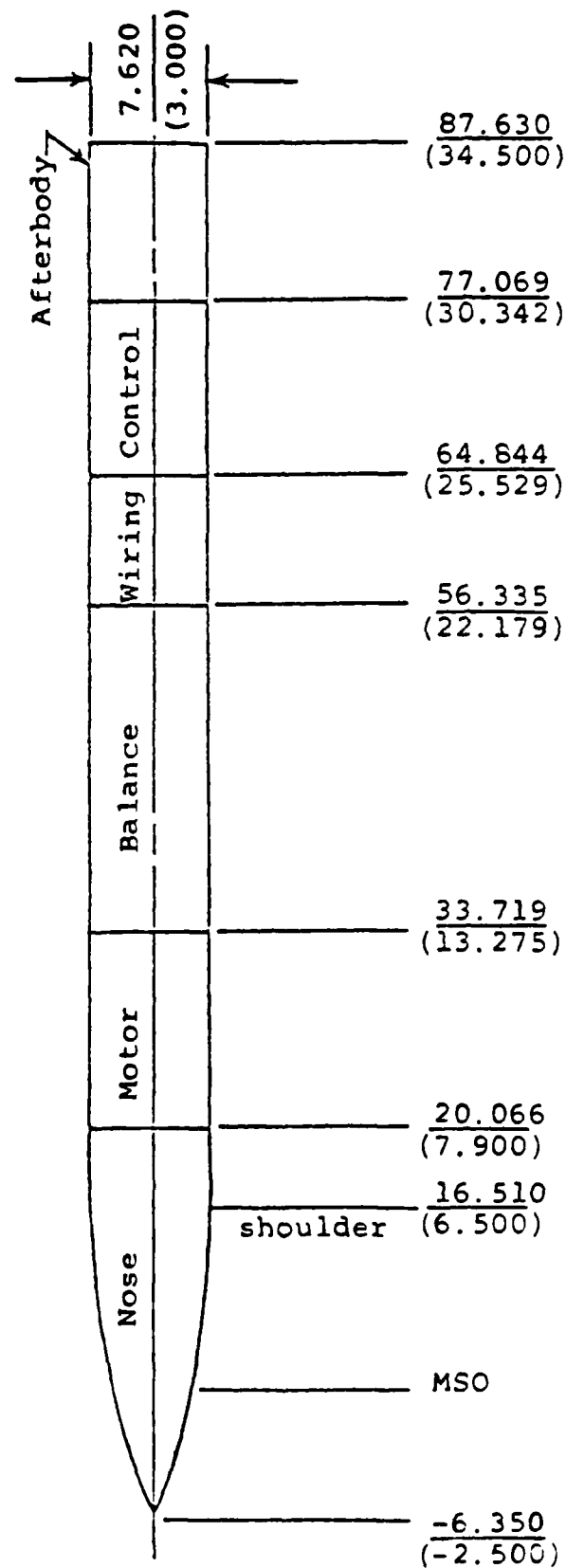
(c) Body layout - triservice missile

Figure 5.- Continued.

96
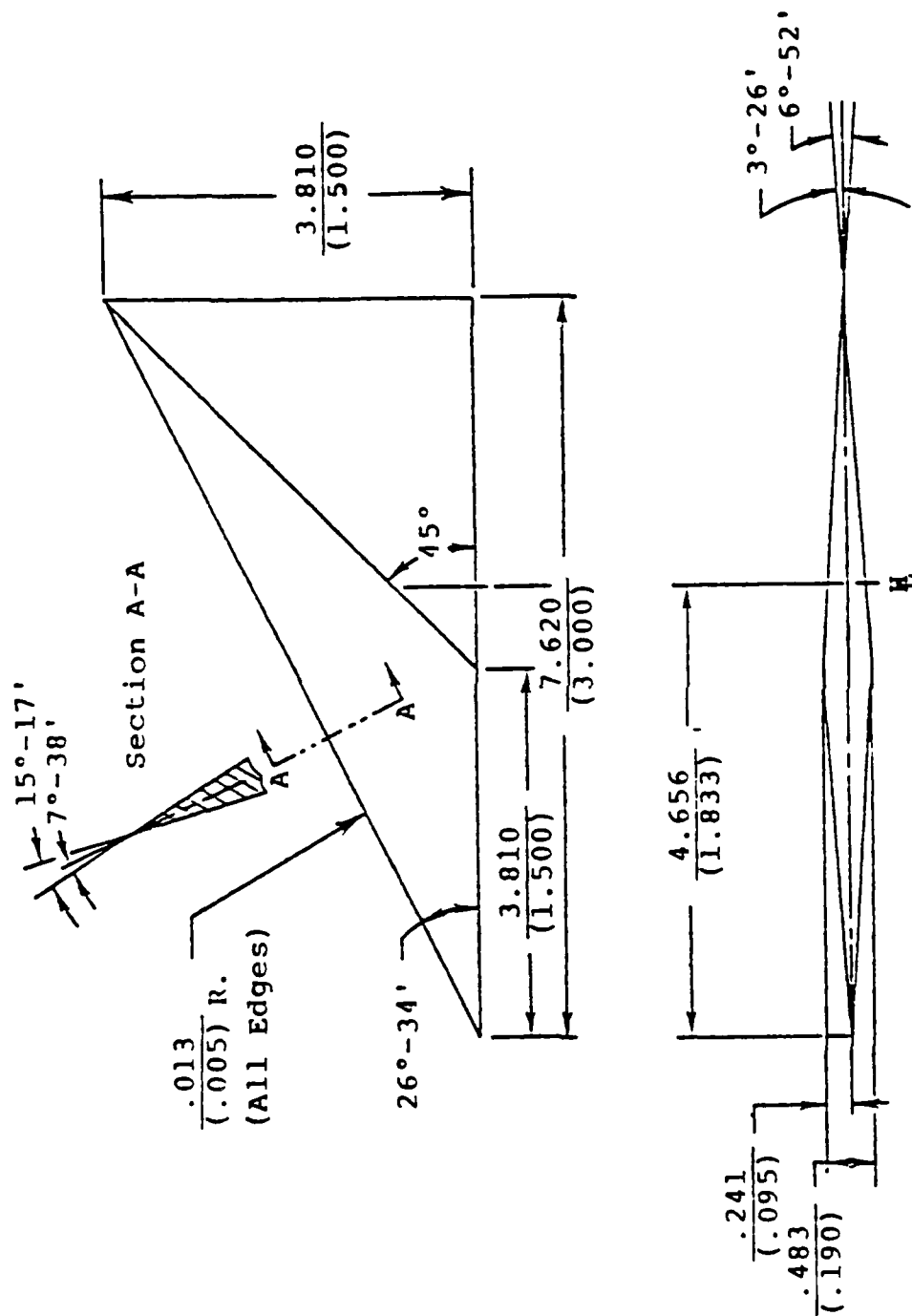
(d) Fin 51 of triservice missile

Figure 5.- Concluded.
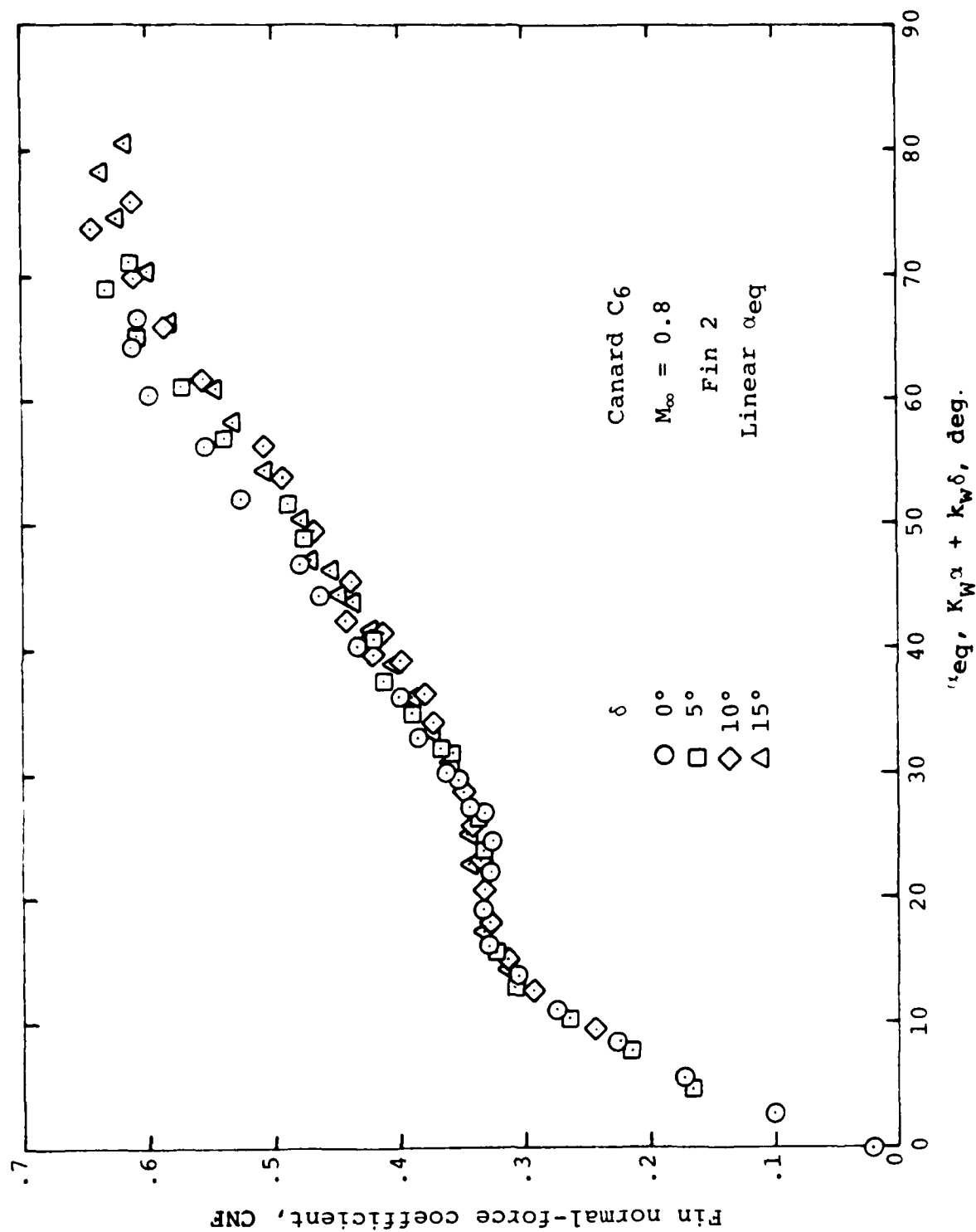
Figure 6.- Correlation of CNF data for canard fin C_6 on Army generalized missile.

(a) $M_\infty = 0.8$, linear α_{eq}

(b) $M_\infty = 0.8$, nonlinear α_{eq}

Figure 6.- Continued.

α_{eq}, $K_W\alpha + k_w\delta$, deg.

(c) $M_\infty = 1.3$, linear α_{eq}

Figure 6.- Continued.

100
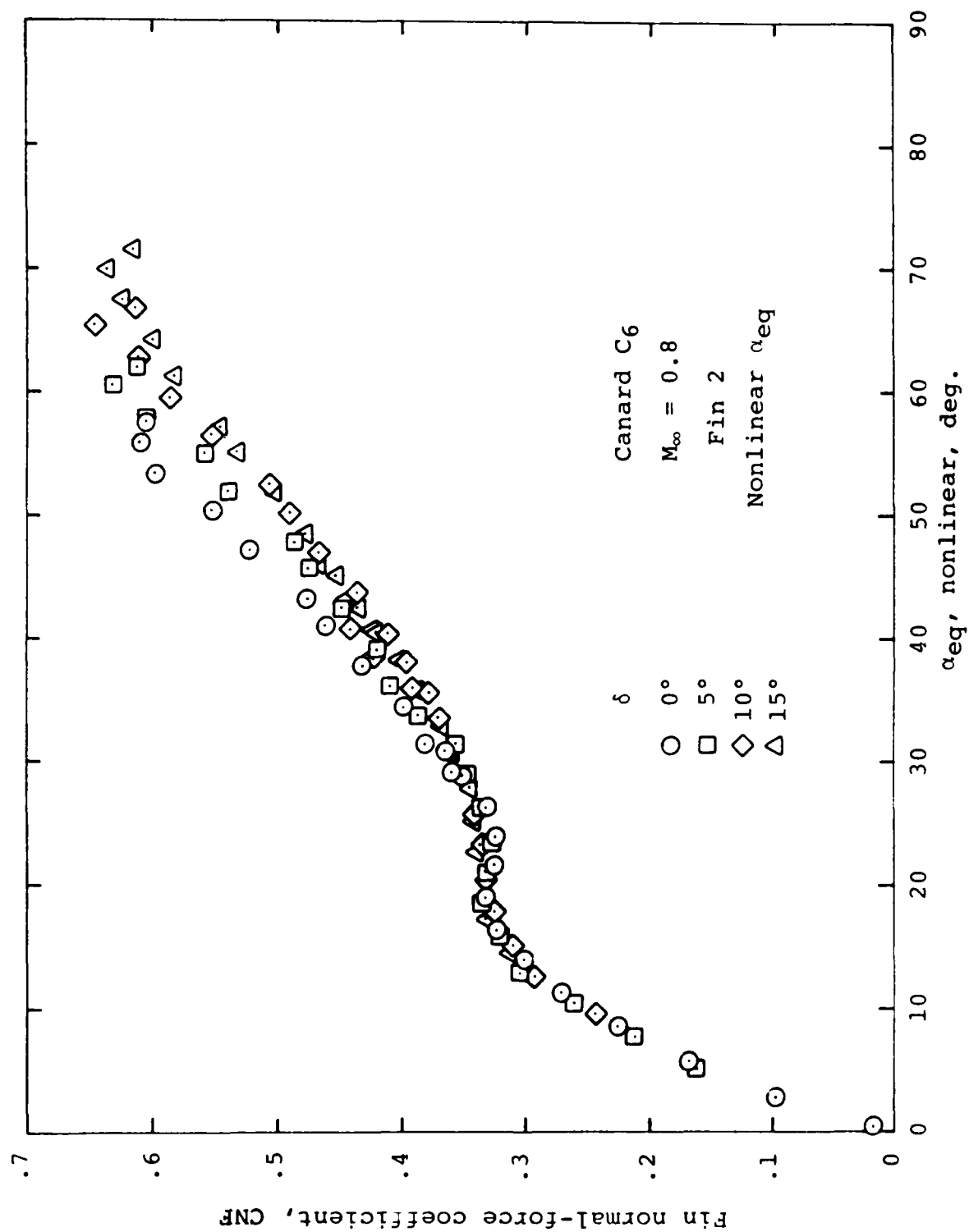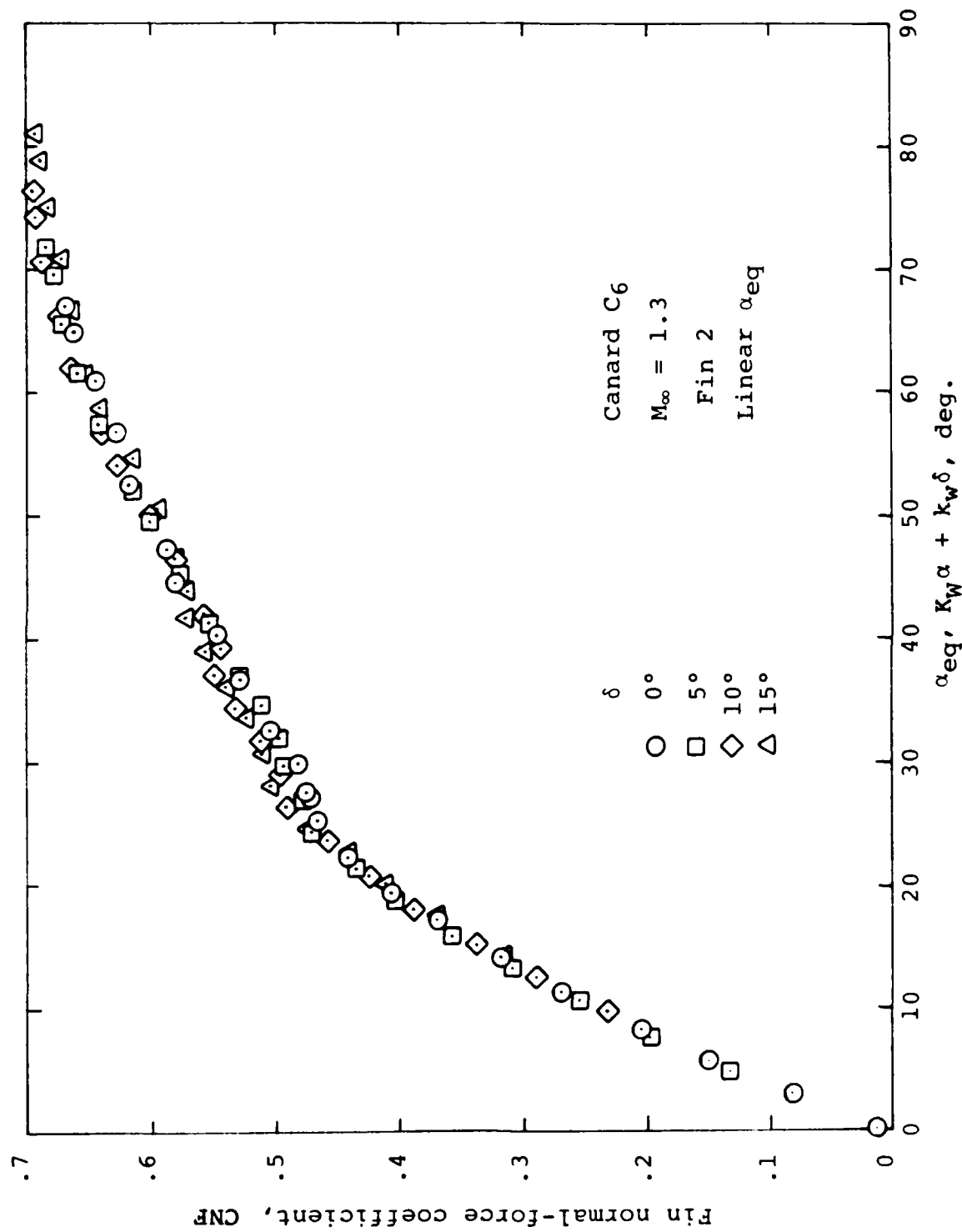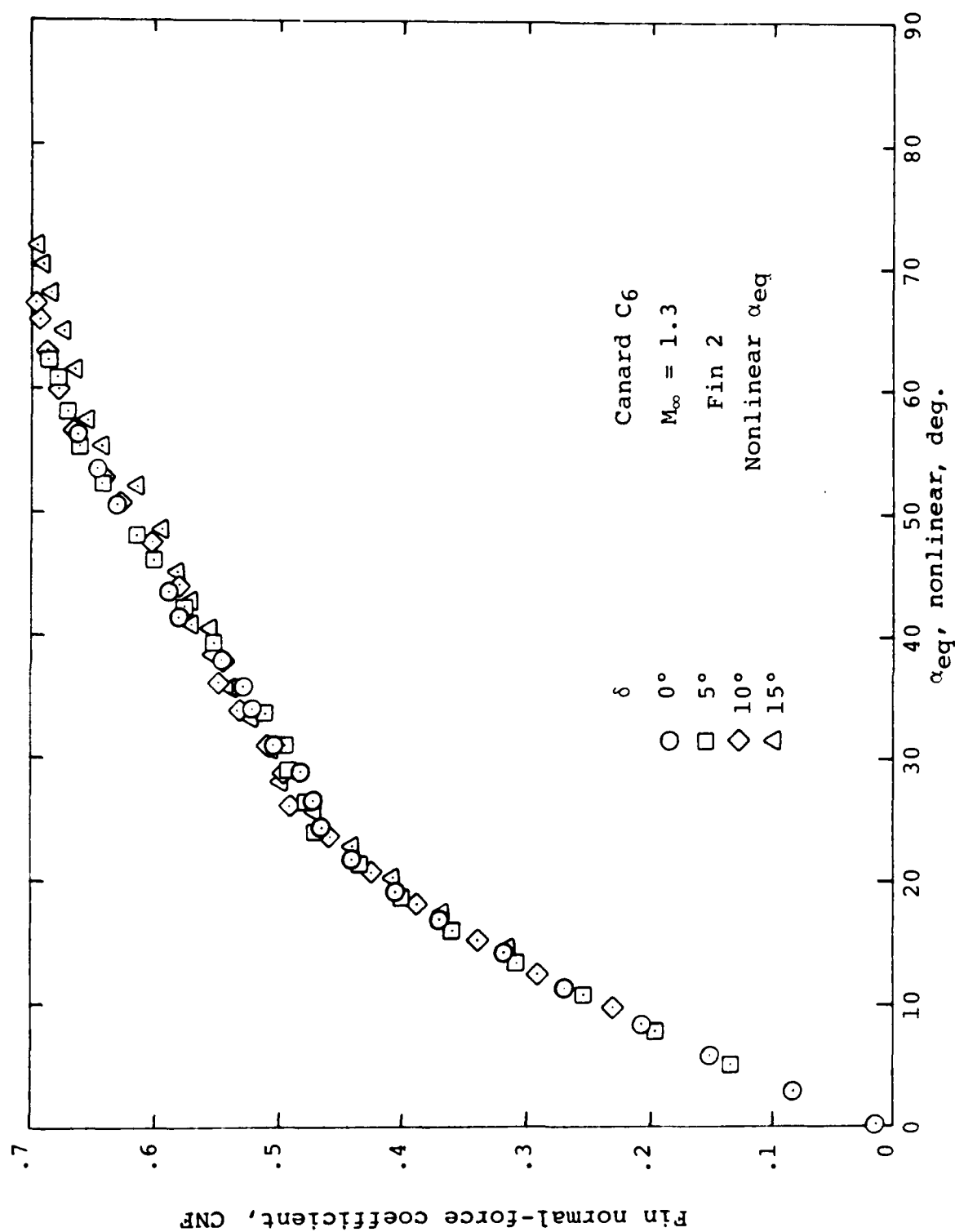
(d) $M_\infty = 1.3$, nonlinear α_{eq}

Figure 6.- Concluded.

101
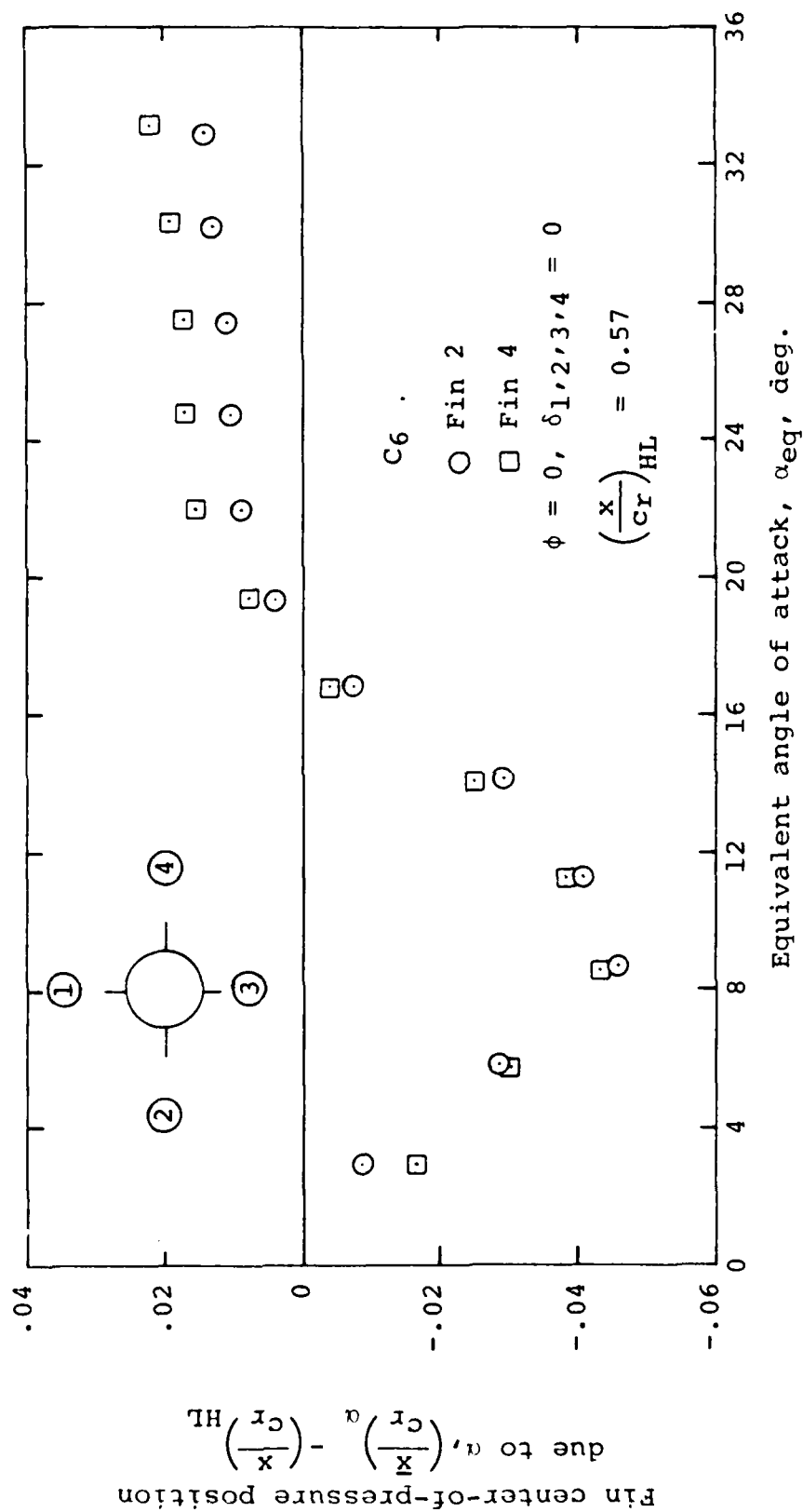
(a) $M_\infty = 0.8$

Figure 7.- Fin center-of-pressure position for C_6 fin mounted on Army generalized missile; $\phi = 0$.
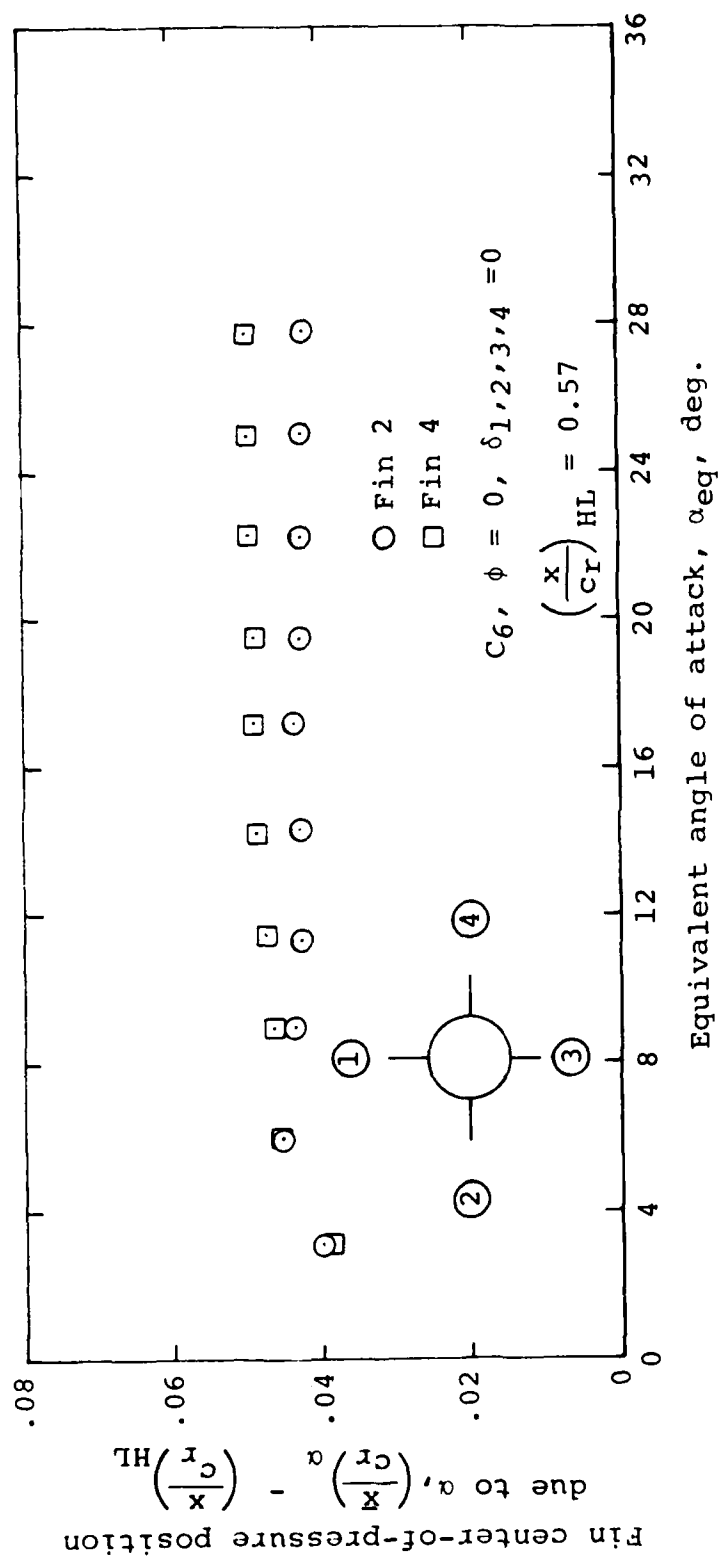
102

(b) $M_\infty = 1.3$

Figure 7.- Concluded.
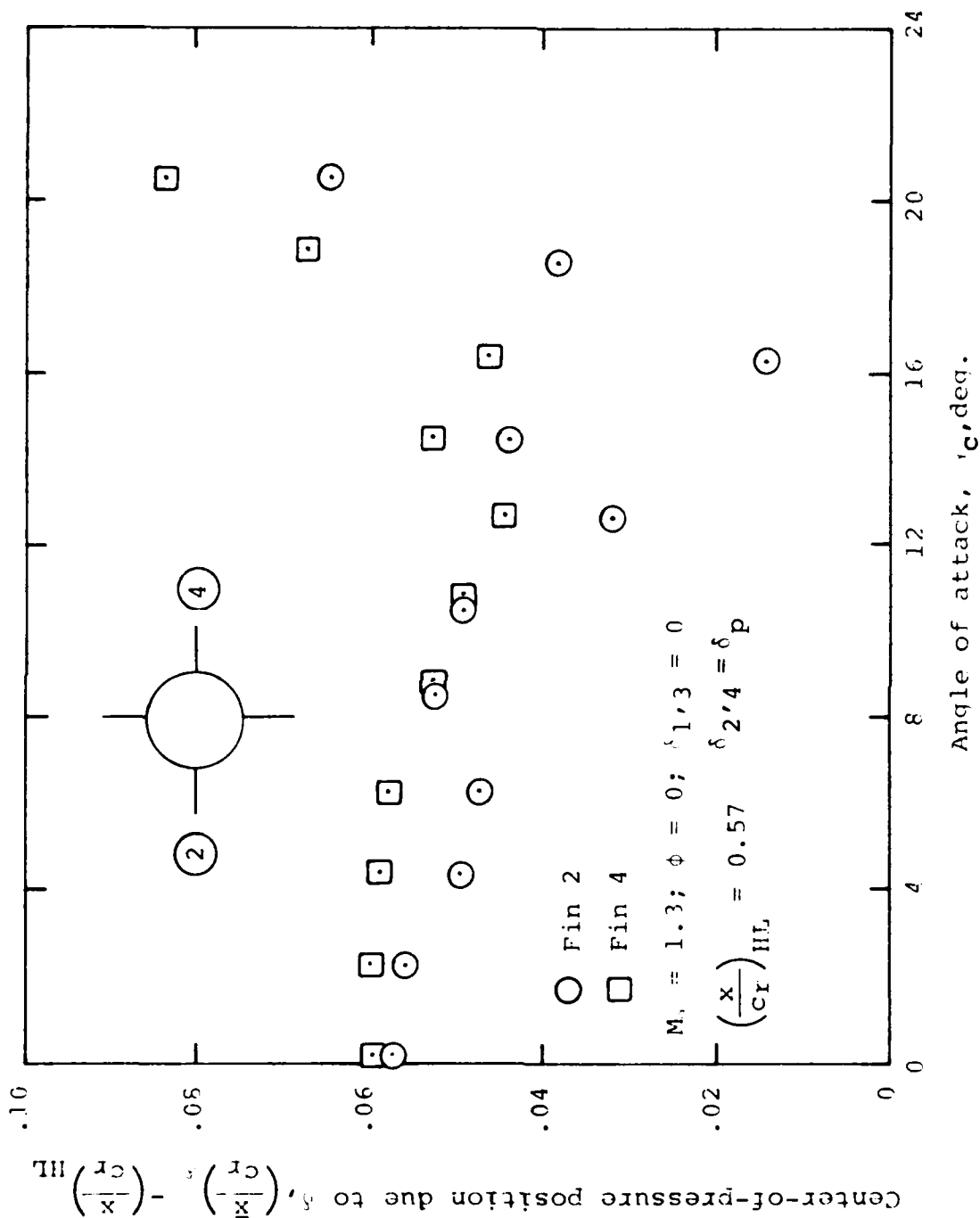
Figure 3.– Center-of-pressure position due to canard fin C_6 mounted on Army generalized missile; $\delta = 0°$.

(a) $\delta_p = 5°$

Center-of-pressure position due to δ, $\left(\frac{x}{c_r}\right)_\delta - \left(\frac{x}{c_r}\right)_{HL}$

Angle of attack, α_c, degrees

○ Fin 2
□ Fin 4

$M_\infty = 1.3$

$\phi = 0$

$\left(\frac{x}{c_r}\right)_{HL} = 0.57$

$\delta_{1,3} = 0$

$\delta_{2,4} = \delta_p$
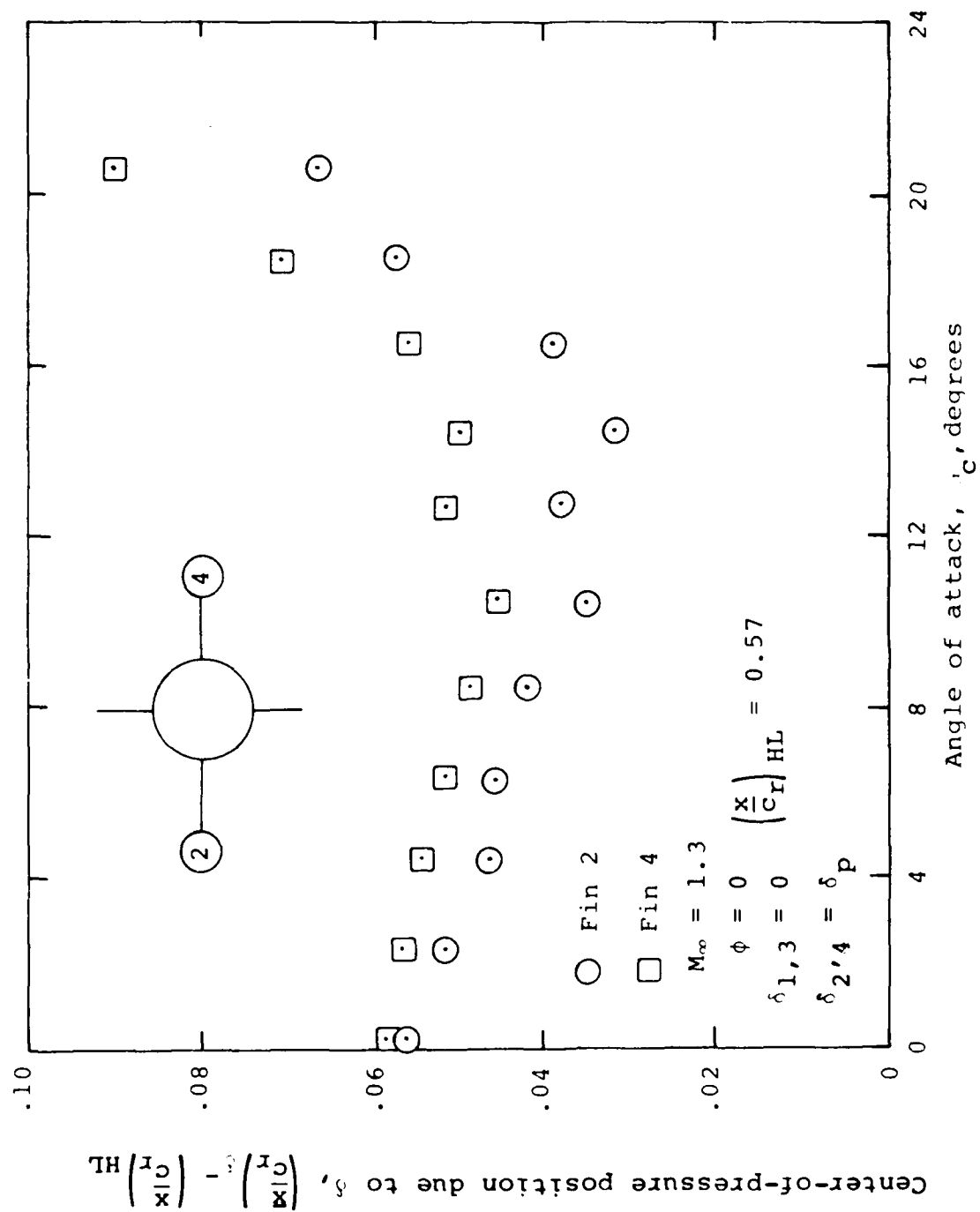
(b) $\delta_p = 10°$
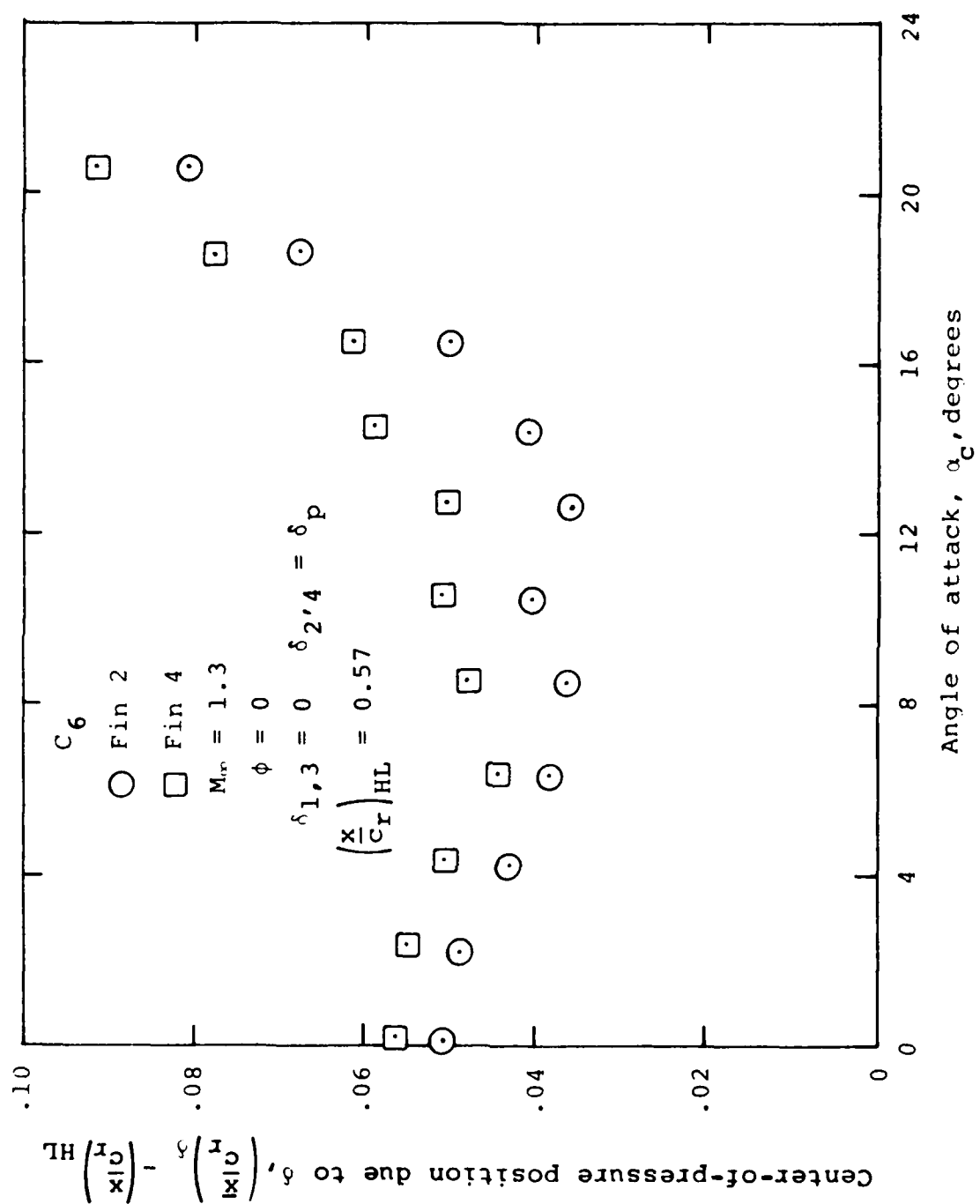
Figure 8.- Continued.

(c) $\delta_p = 15°$

Figure 8.- Continued.

106
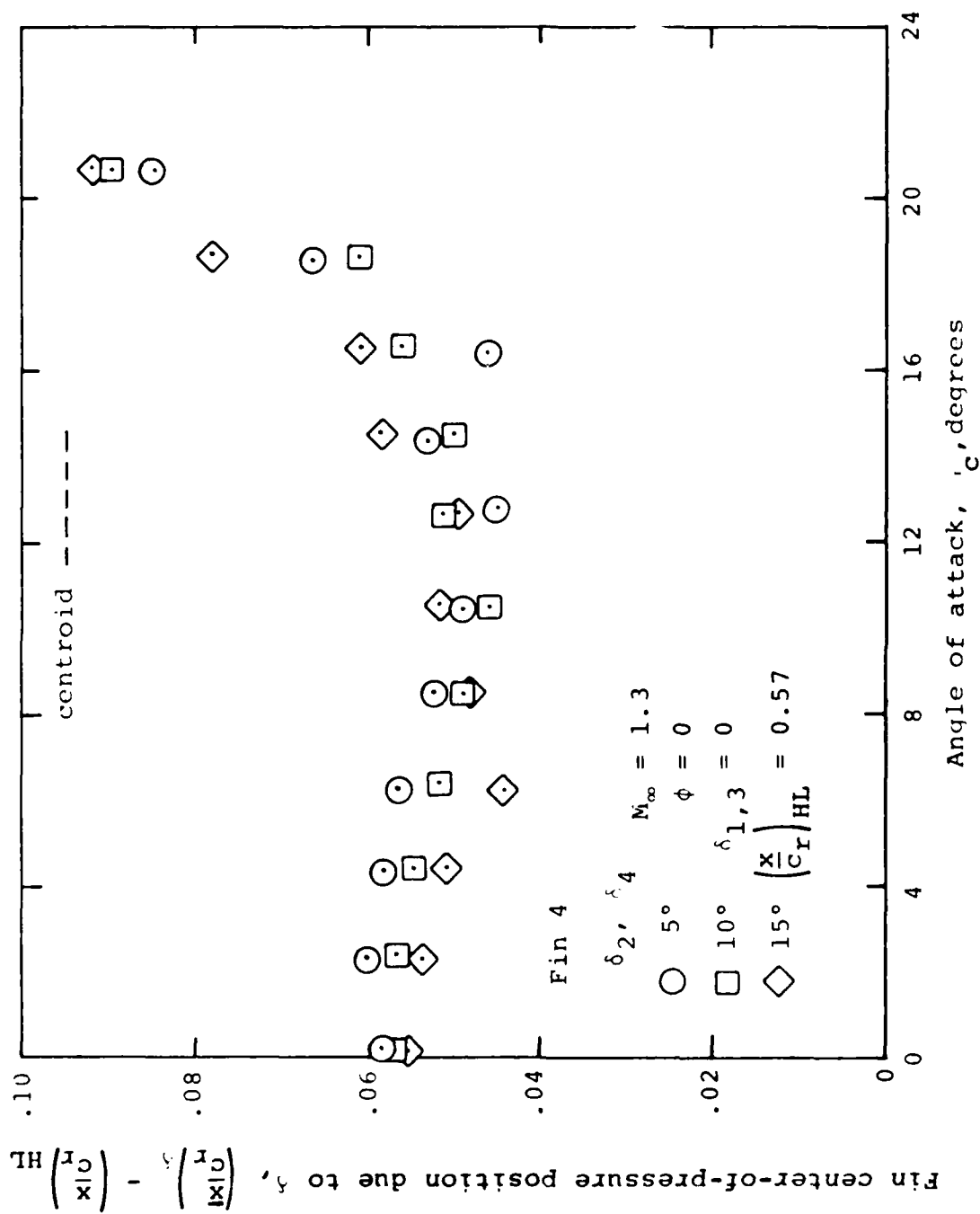
(d) $\delta_p = 5°$, $10°$, $15°$

Figure 8.- Concluded.
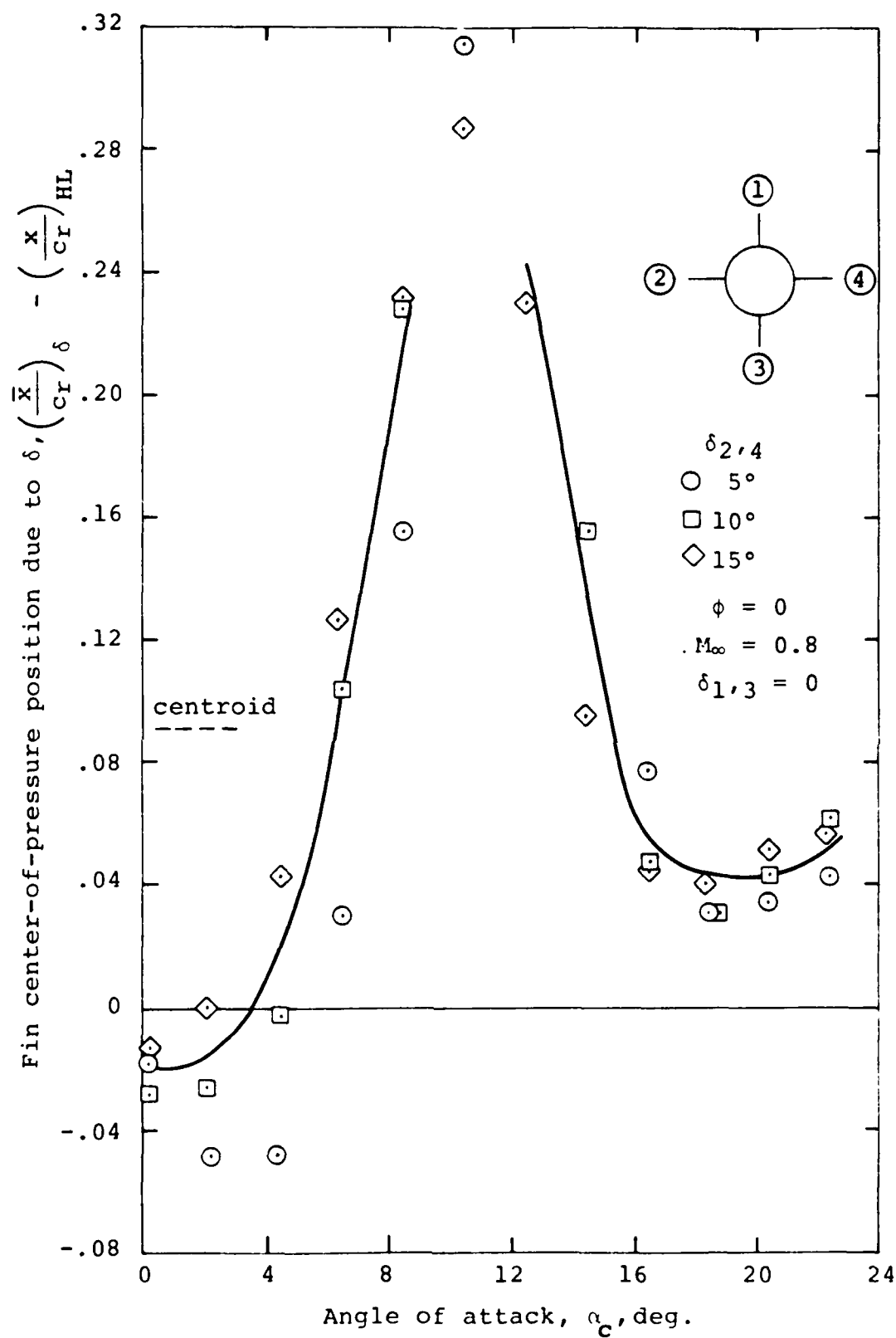
Figure 9.- Correlation of center-of-pressure position due to δ for canard fin C_6 mounted on Army generalized missile, $M_\infty = 0.8$.
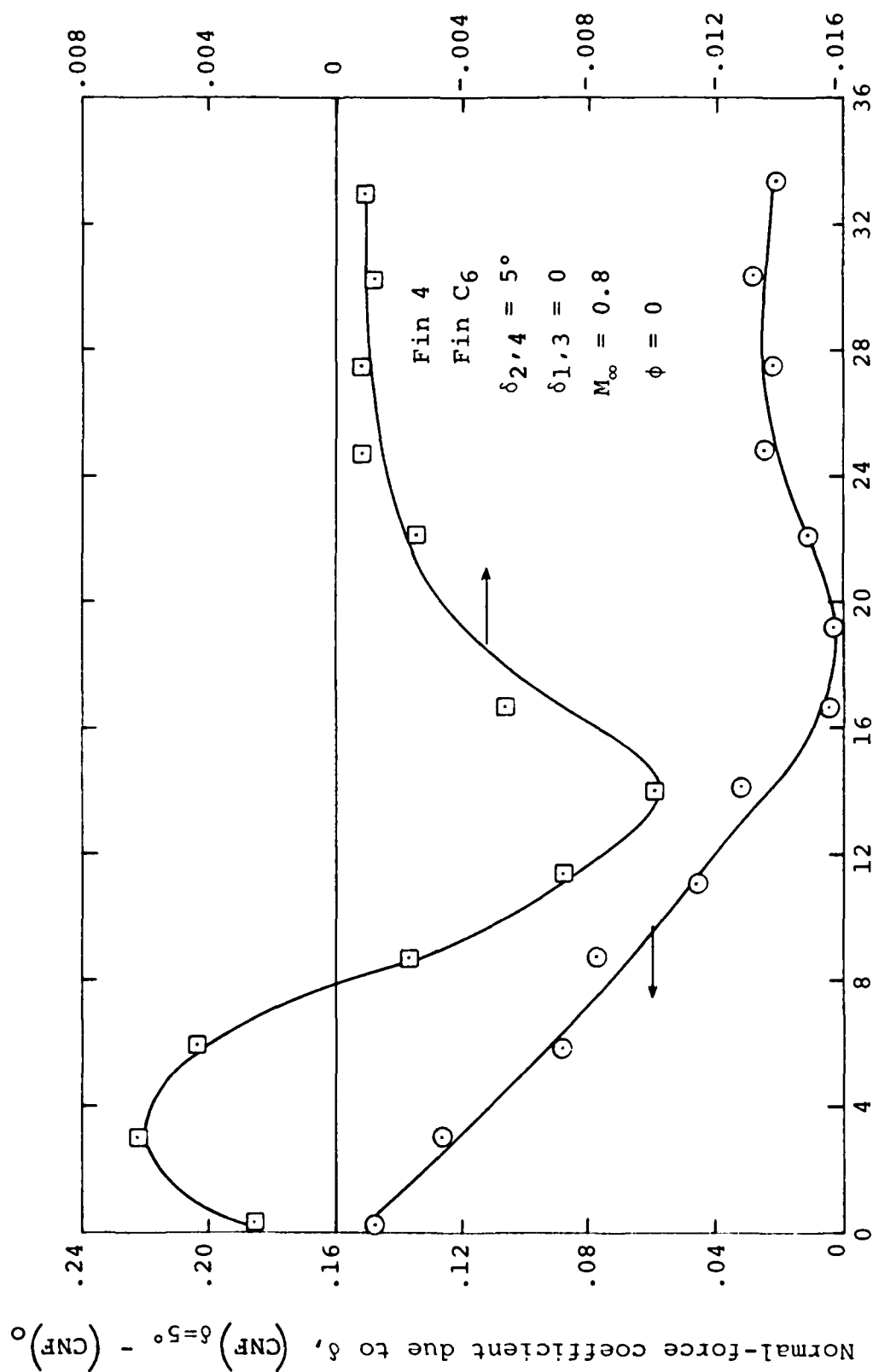
Figure 10.- Fin C_6 normal-force coefficient and hinge-moment coefficient increment for $5°$ of control deflection of canard C_6 fin mounted on Army generalized missile.
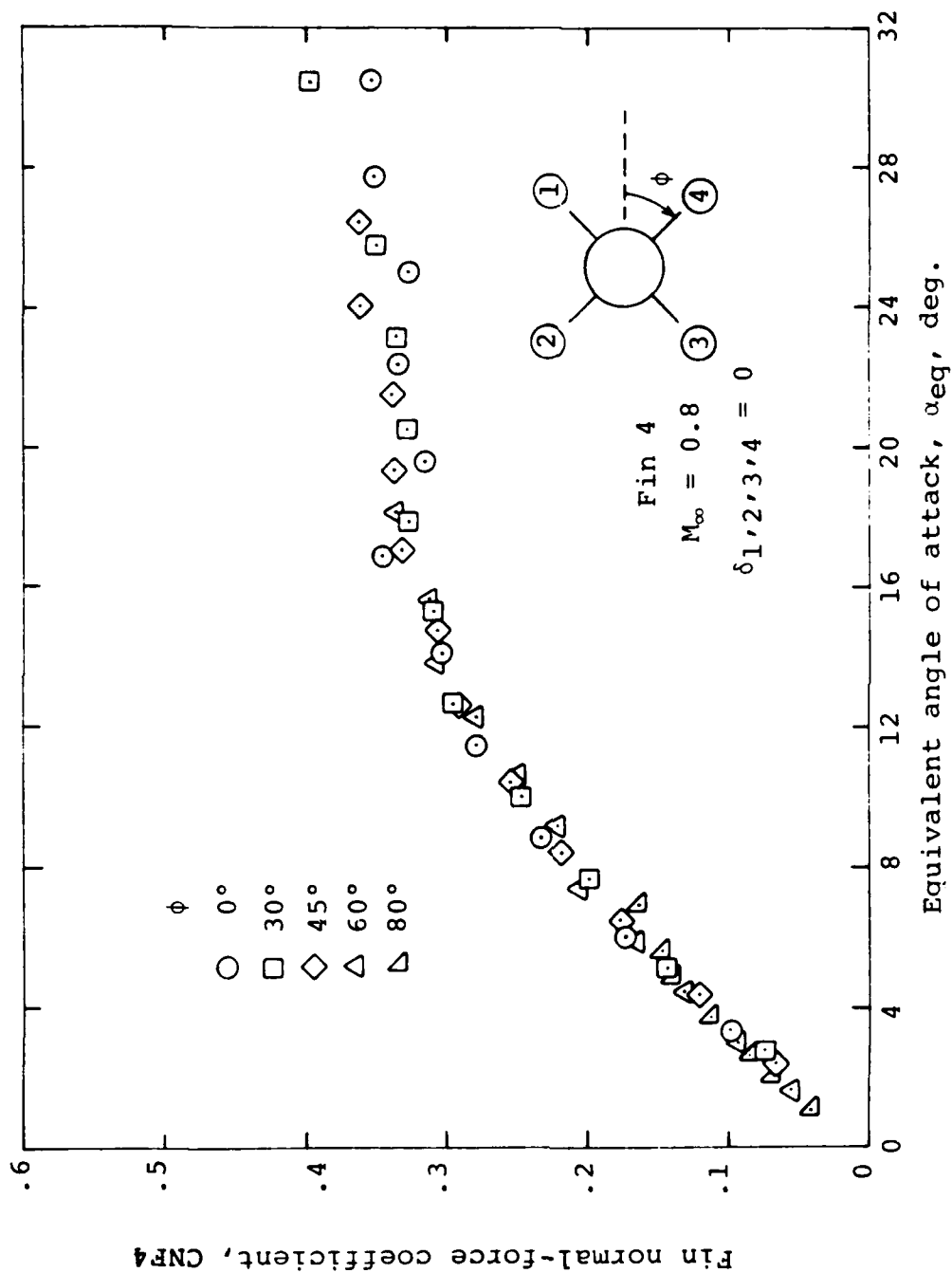
Figure 11.- Correlation of normal-force data for canard fin C_6 mounted on Army generalized missile as a function of roll angle.
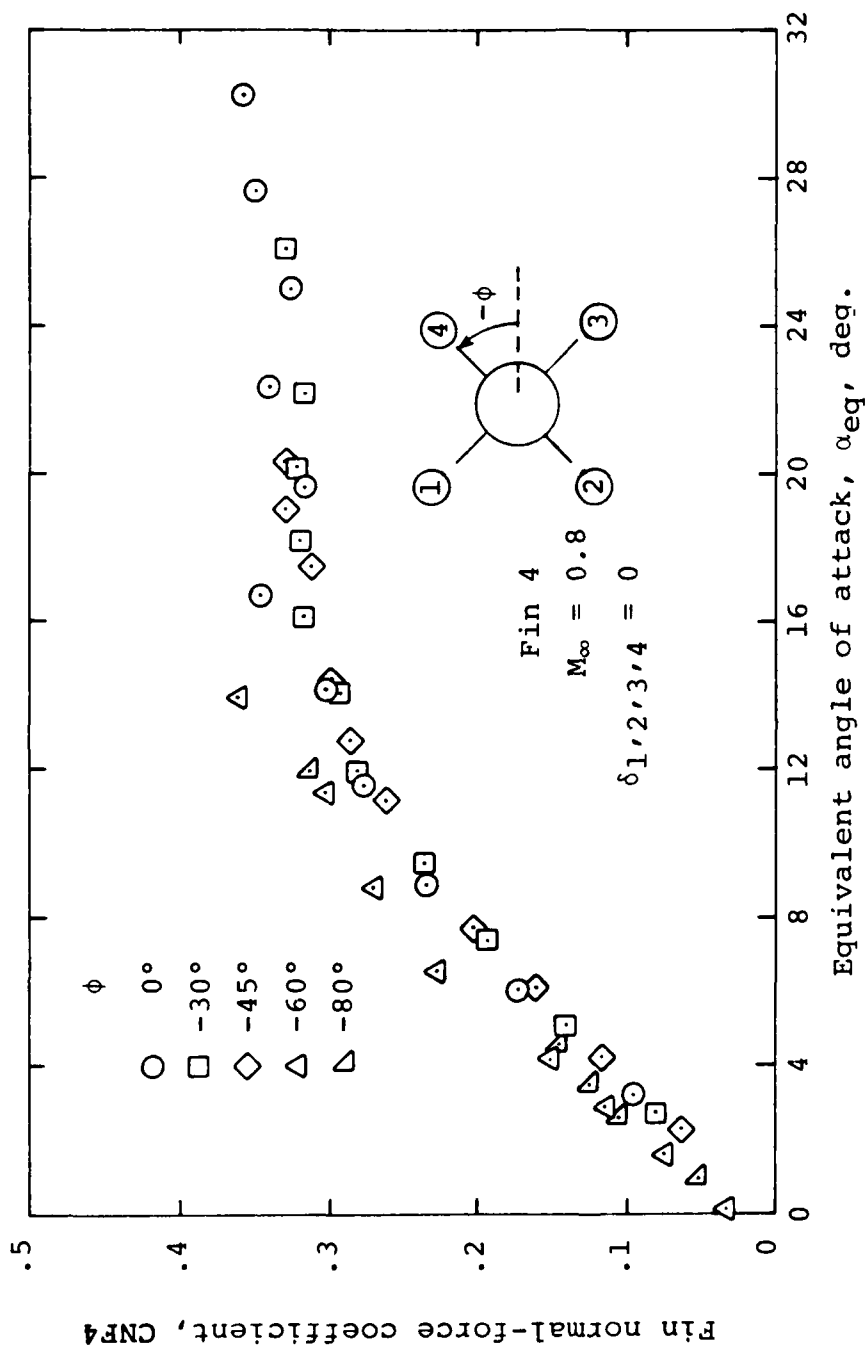
(a) $M_\infty = 0.8$; $0 \le \phi \le 80°$

(b) $M_\infty = 0.8$; $0 \geq \phi \geq -80°$

Figure 11.- Continued.

111
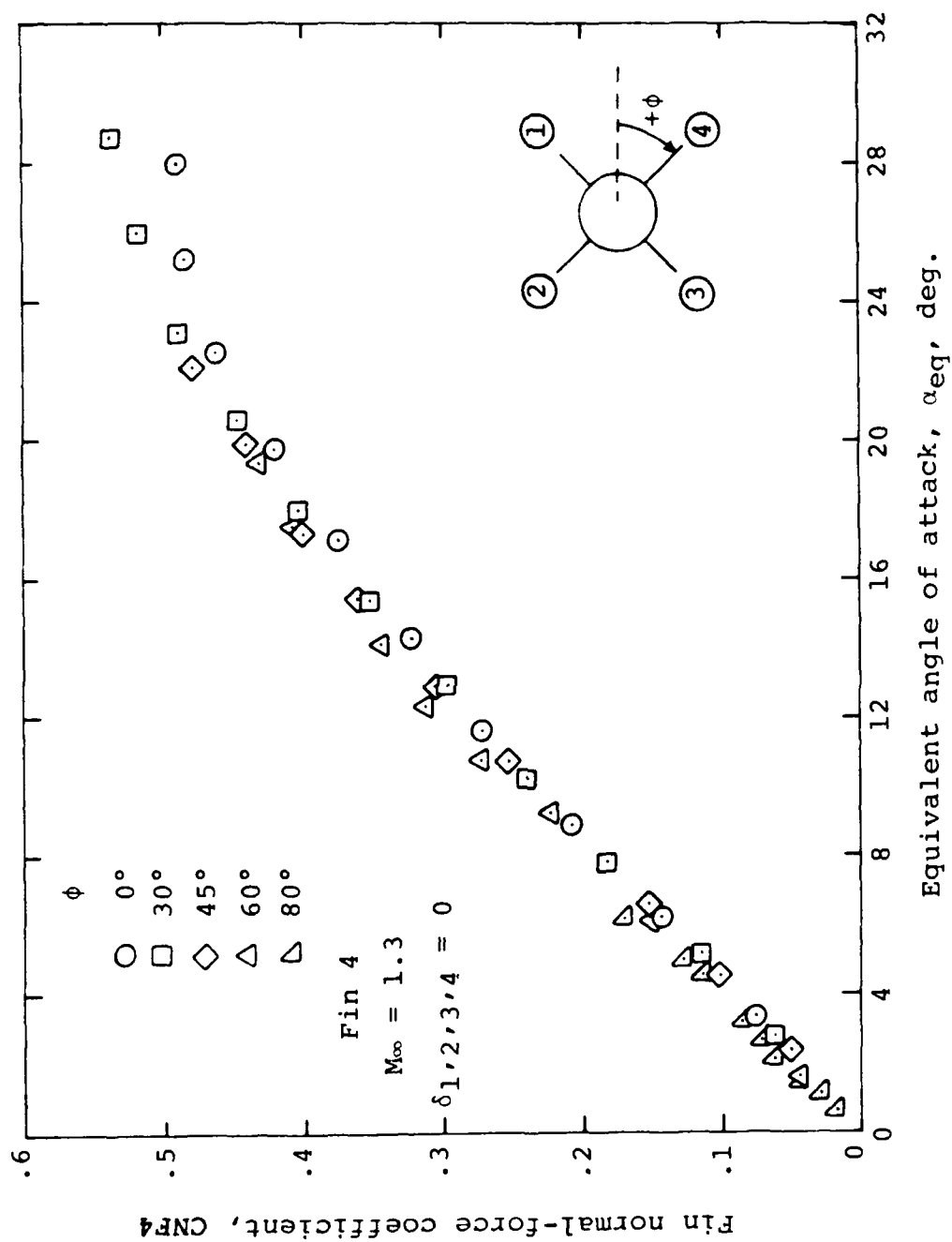
(c) $M_\infty = 1.3$; $0 \leq \phi \leq 80°$

Figure 11.- Continued.

112
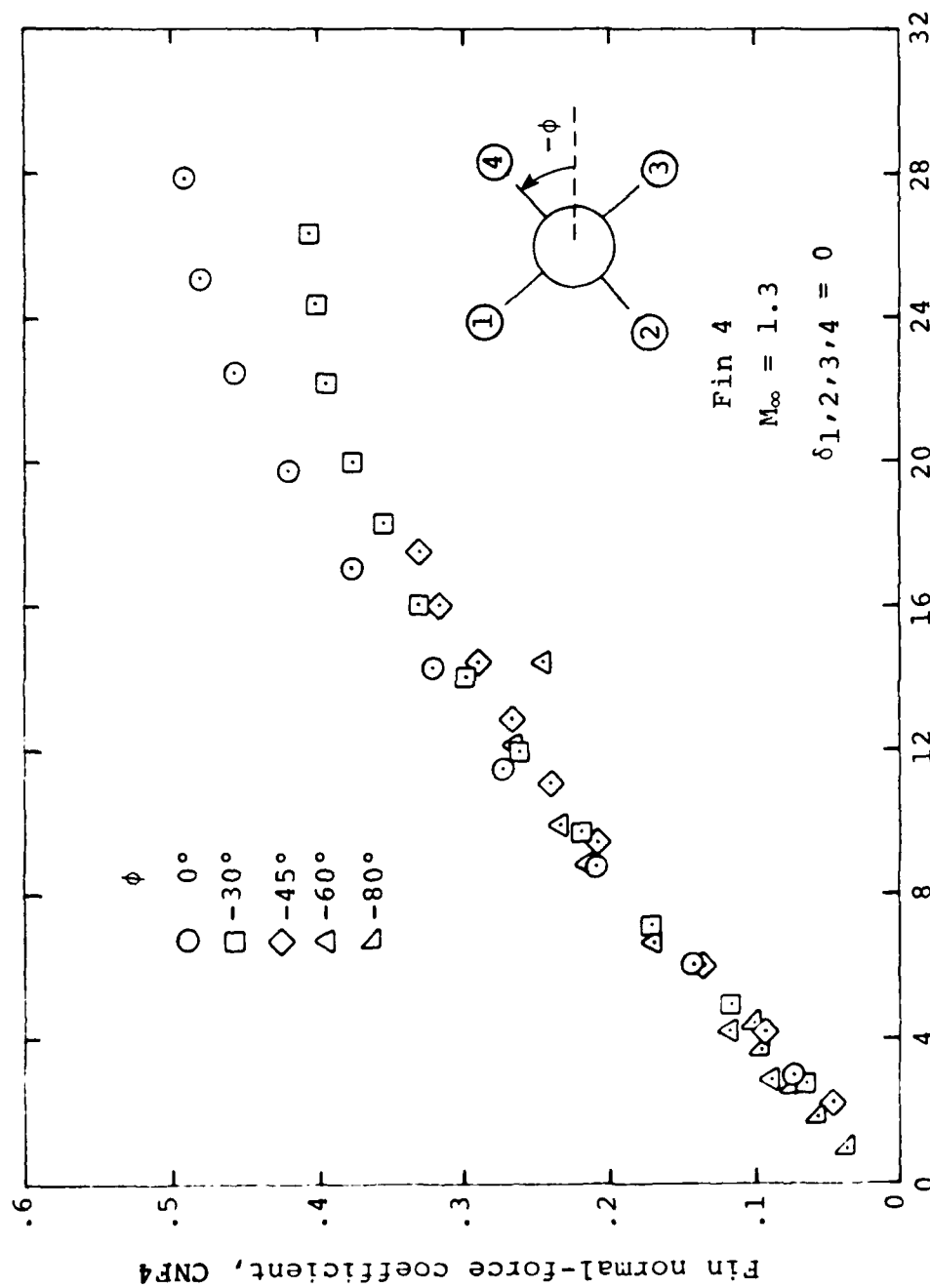
(d) $M_\infty = 1.3$; $0 \geq \phi \geq -80°$

Figure 11. Concluded.

113
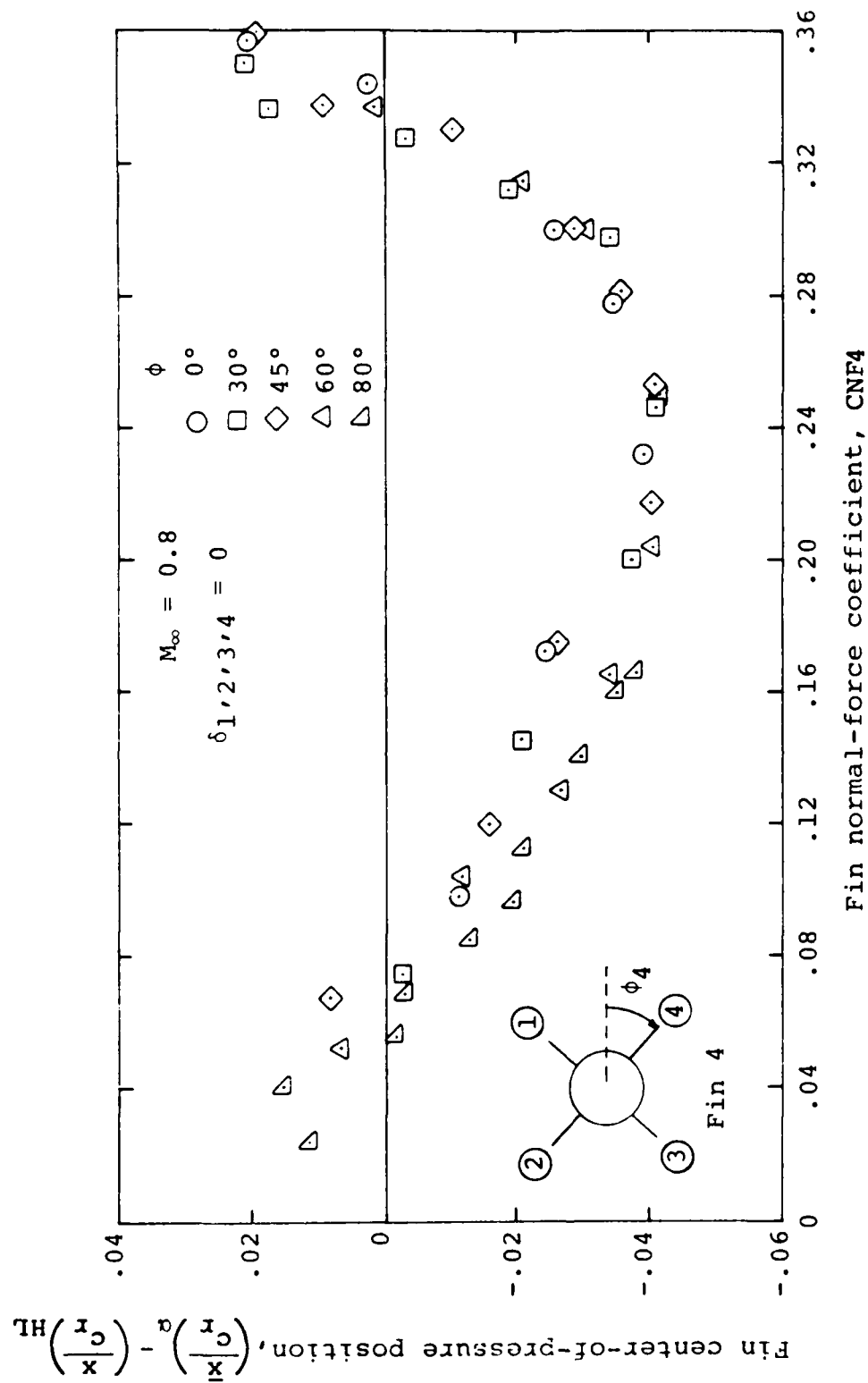
(a) $M_\infty = 0.8$; $0° \leq \phi \leq 80°$

Figure 12.- Fin center-of-pressure position due to α for C_6 canard fin mounted on Army generalized missile as a function of roll angle.

Fin normal-force coefficient, CNF4
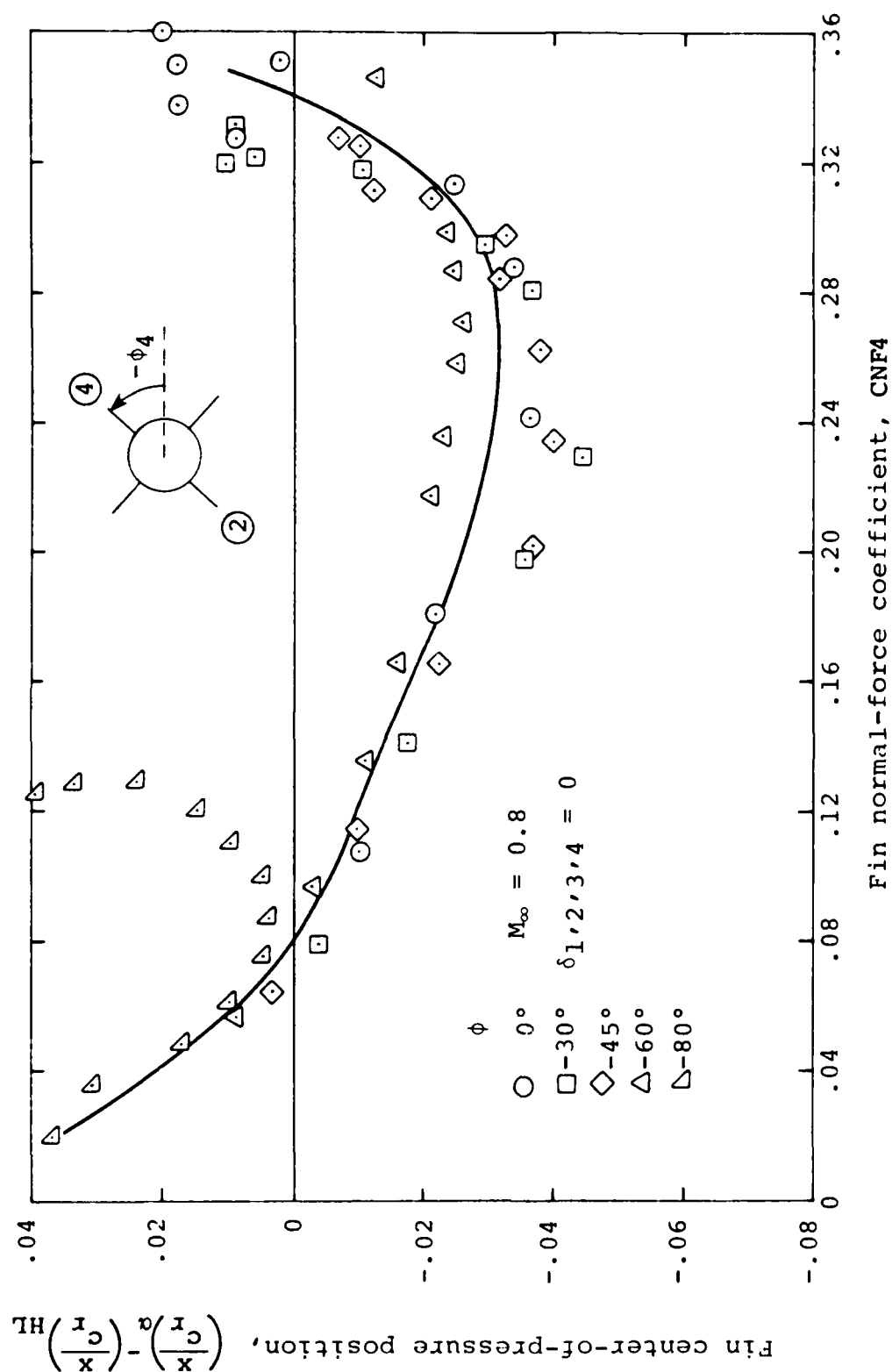
(b) $M_\infty = 0.8$; $-80° \leq \phi \leq 0°$

Figure 12.- Continued.

115
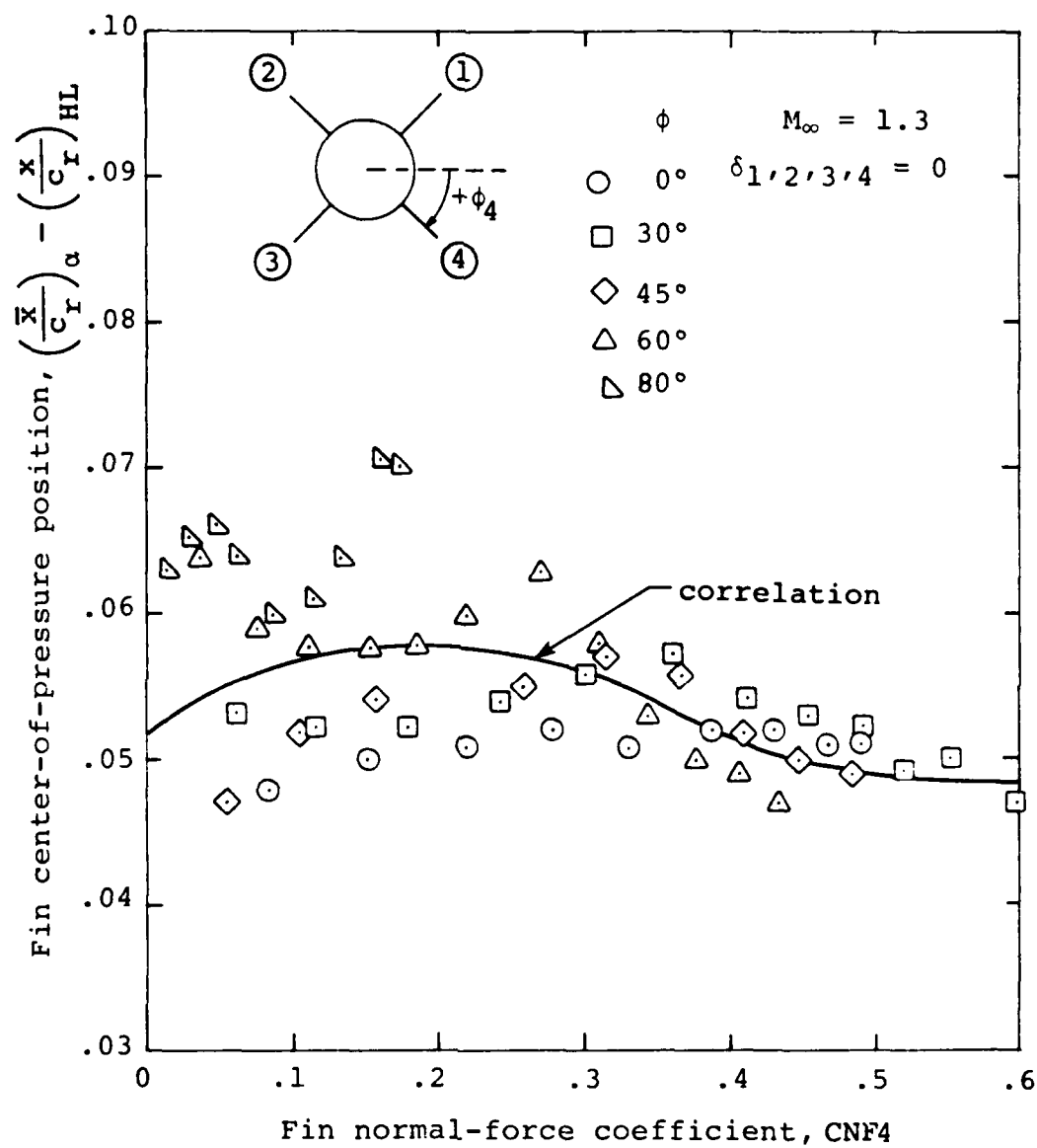
(c) $M_\infty = 1.3$; $0 \le \phi \le 80°$

Figure 12.- Continued.

116
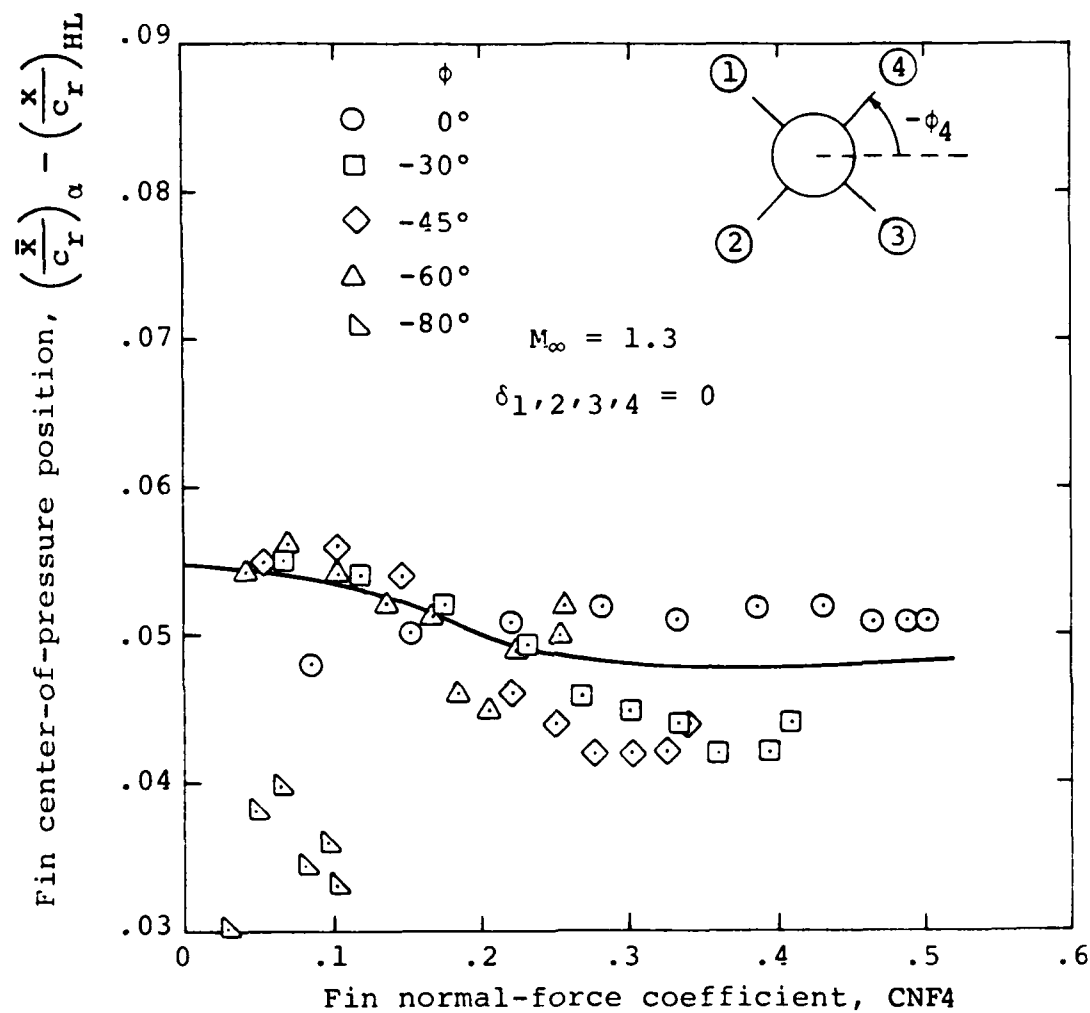
(d) $M_\infty = 1.3$; $-80° \leq \phi \leq 0°$

Figure 12.- Concluded.

117
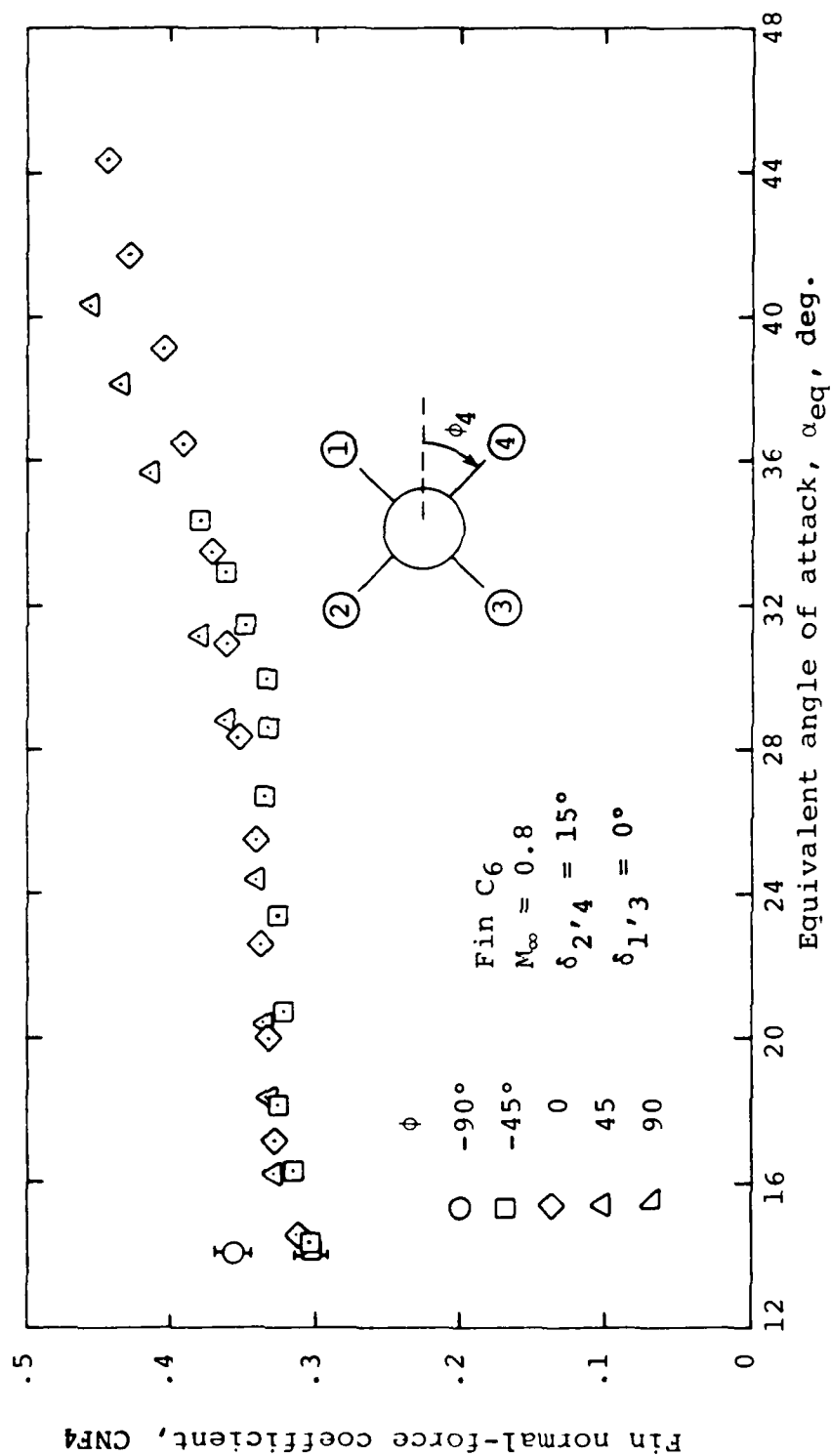
Figure 13.- Correlation of fin normal force with pitch-control deflection as a function of roll angle for fin C_6 mounted on Army generalized missile.

(a) $M_\infty = 0.8$

118
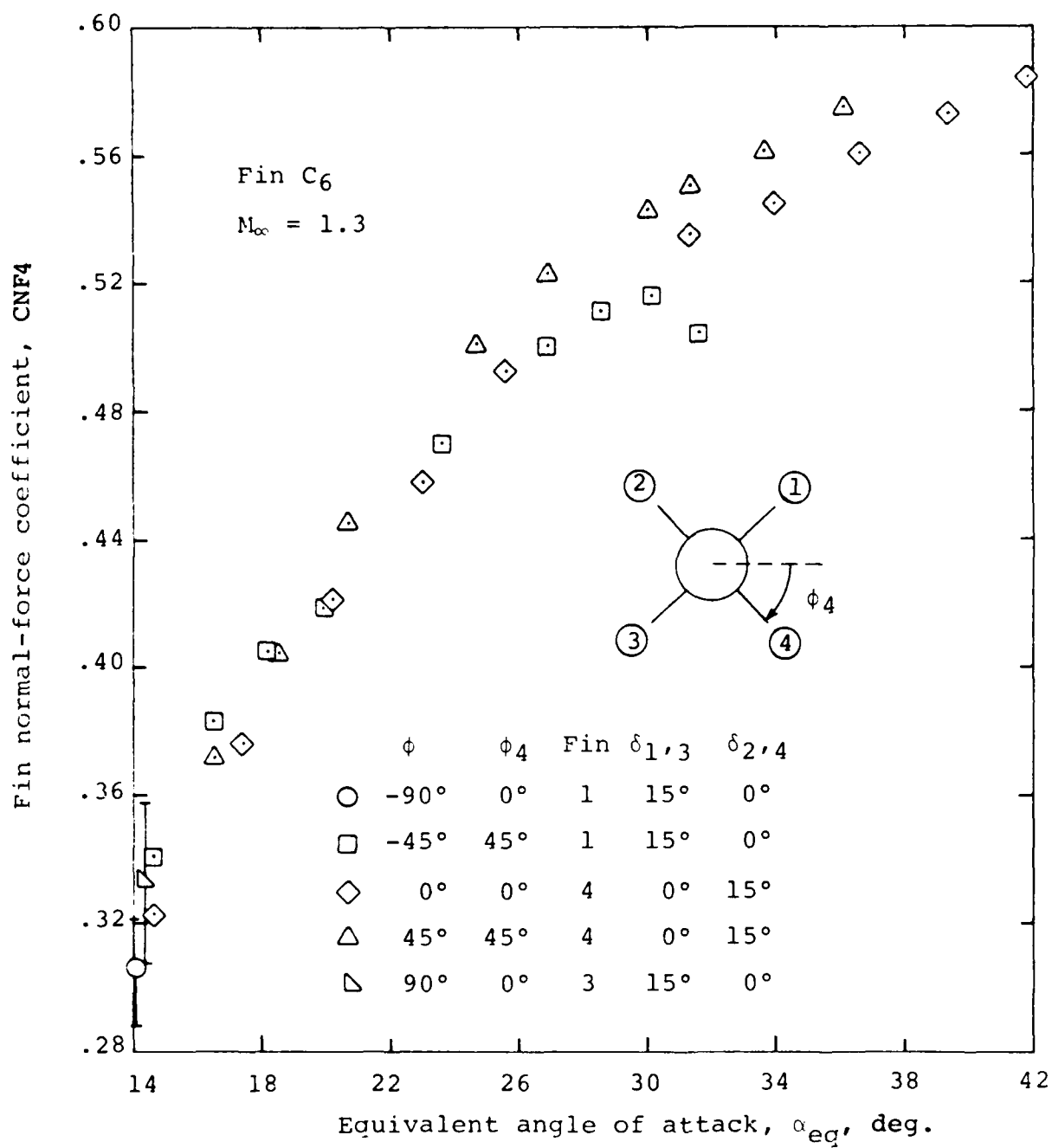
(b) $M_\infty = 1.3$

Figure 13.- Concluded.
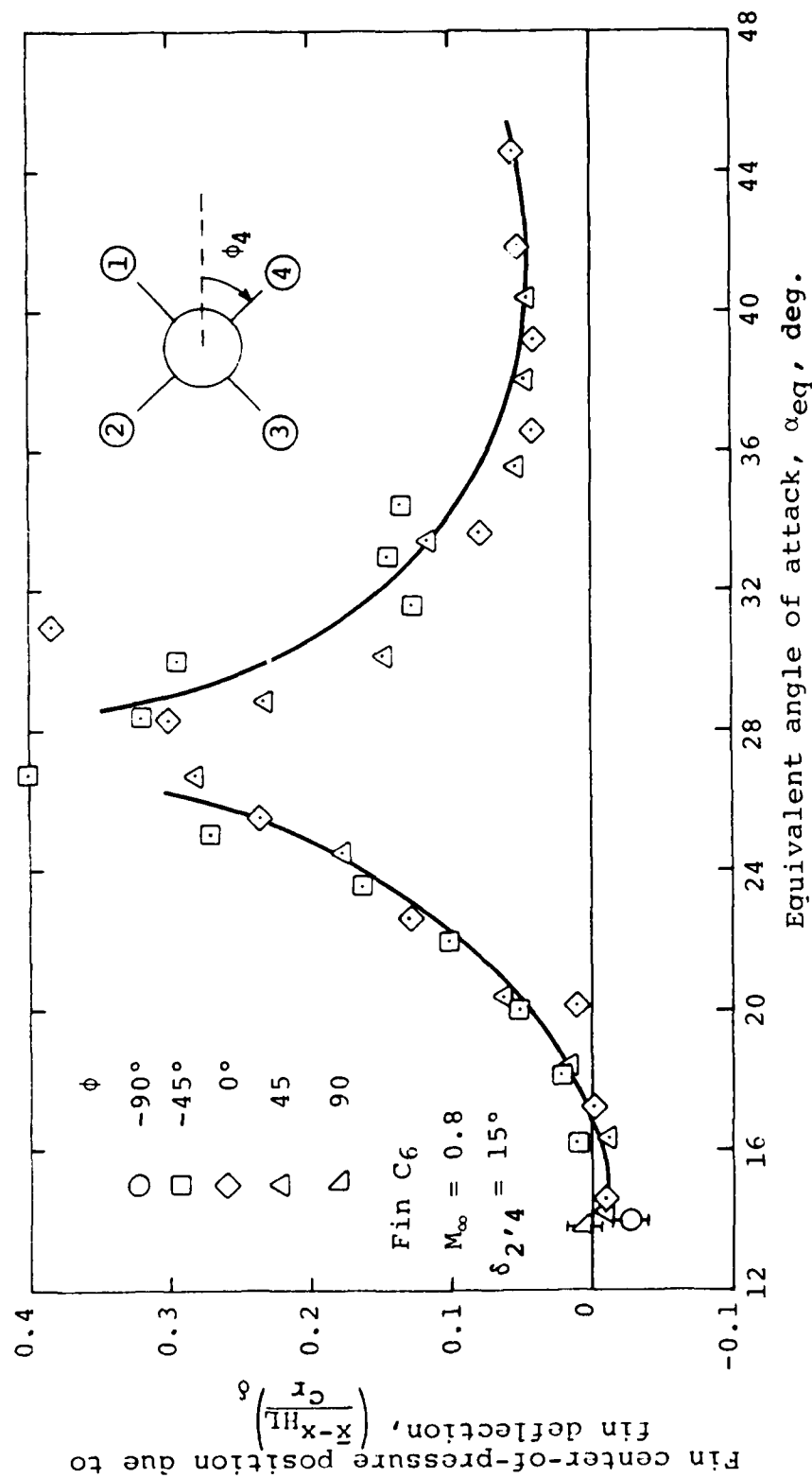
(a) $M_\infty = 0.8$

Figure 14.- Effect of roll angle on fin center-of-pressure position due to deflection for fin C_6 mounted on Army generalized missile.

120
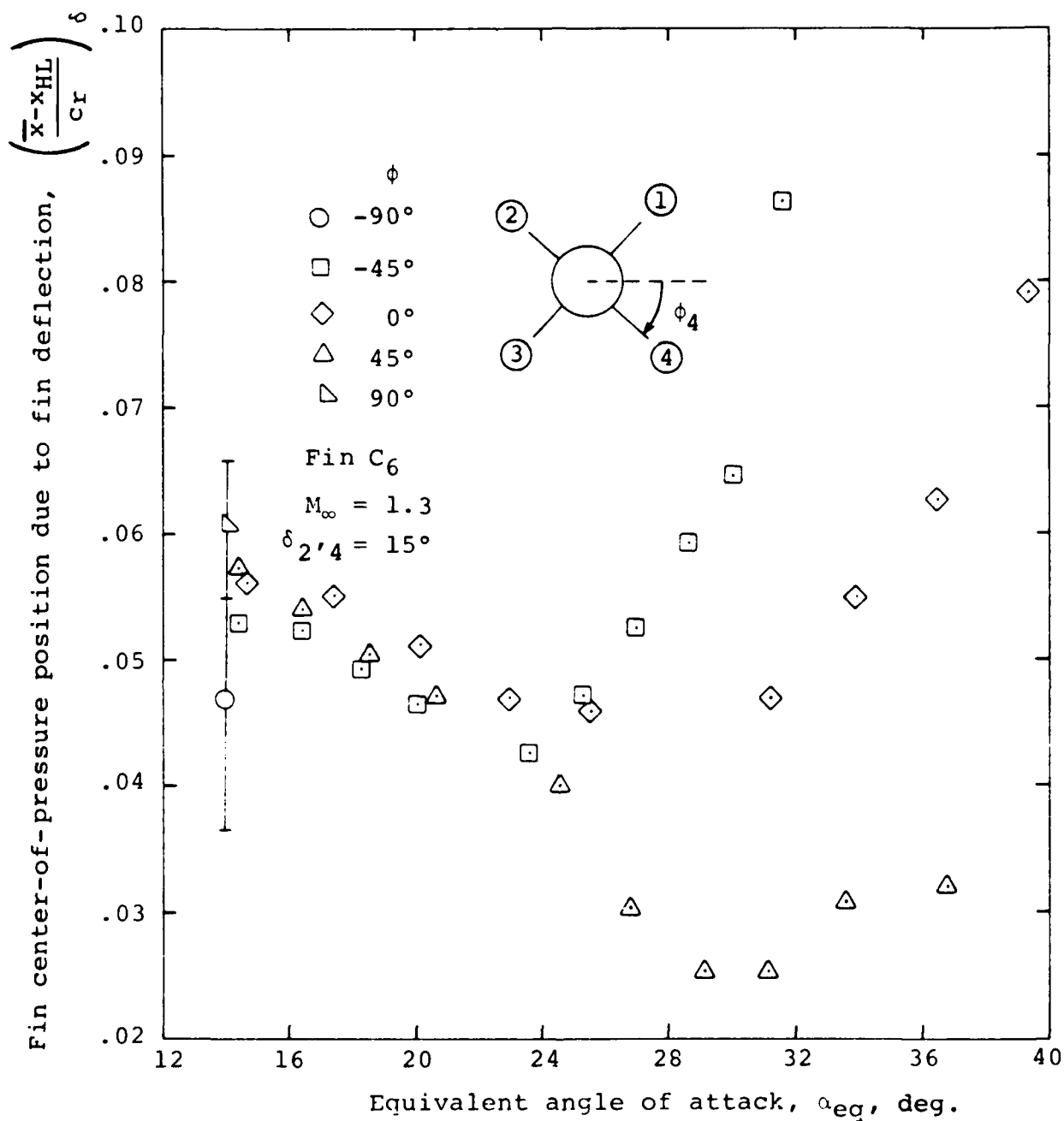
(b) $M_\infty = 1.3$

Figure 14.- Concluded.

121
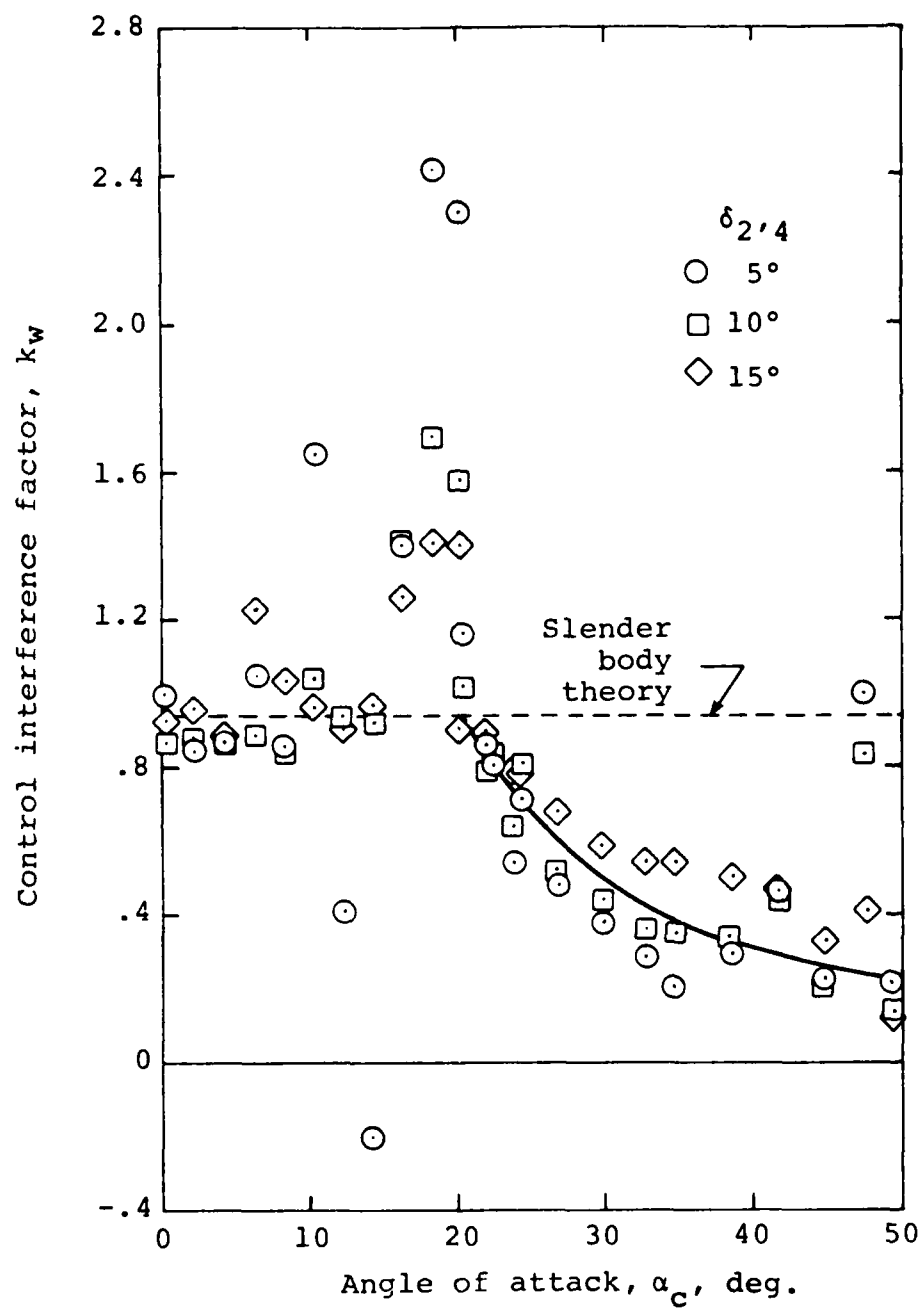
(a) $M_\infty = 0.8$

Figure 15.- Control interference factor for pitch control of C_6 canard fin on Army generalized missile, $\phi = 0°$ (Interpolated C_6 data).
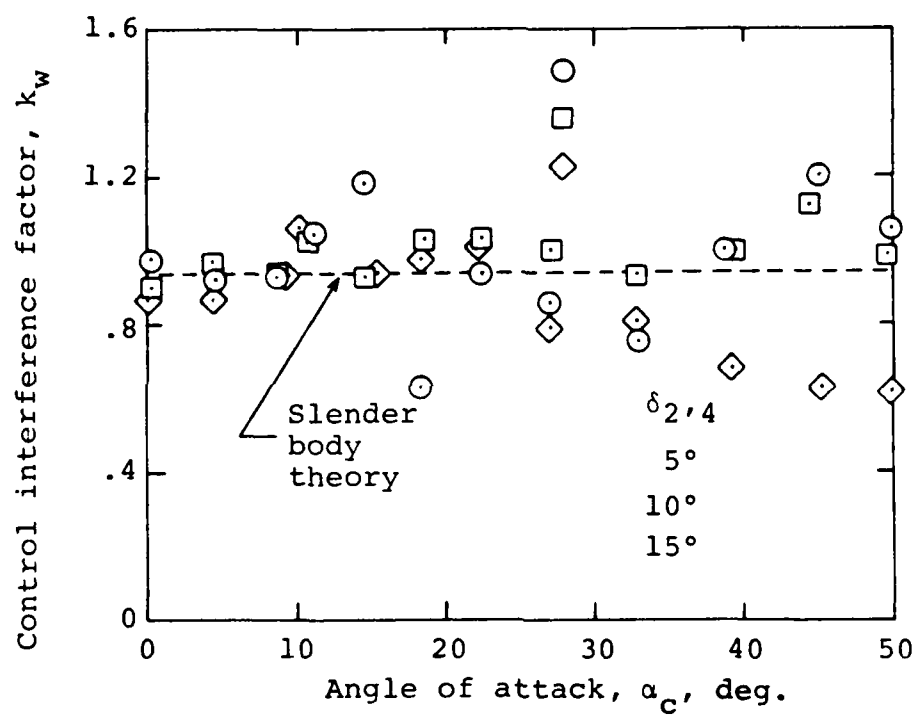
(b) $M_\infty \approx 1.3$

Figure 15.- Concluded.

123
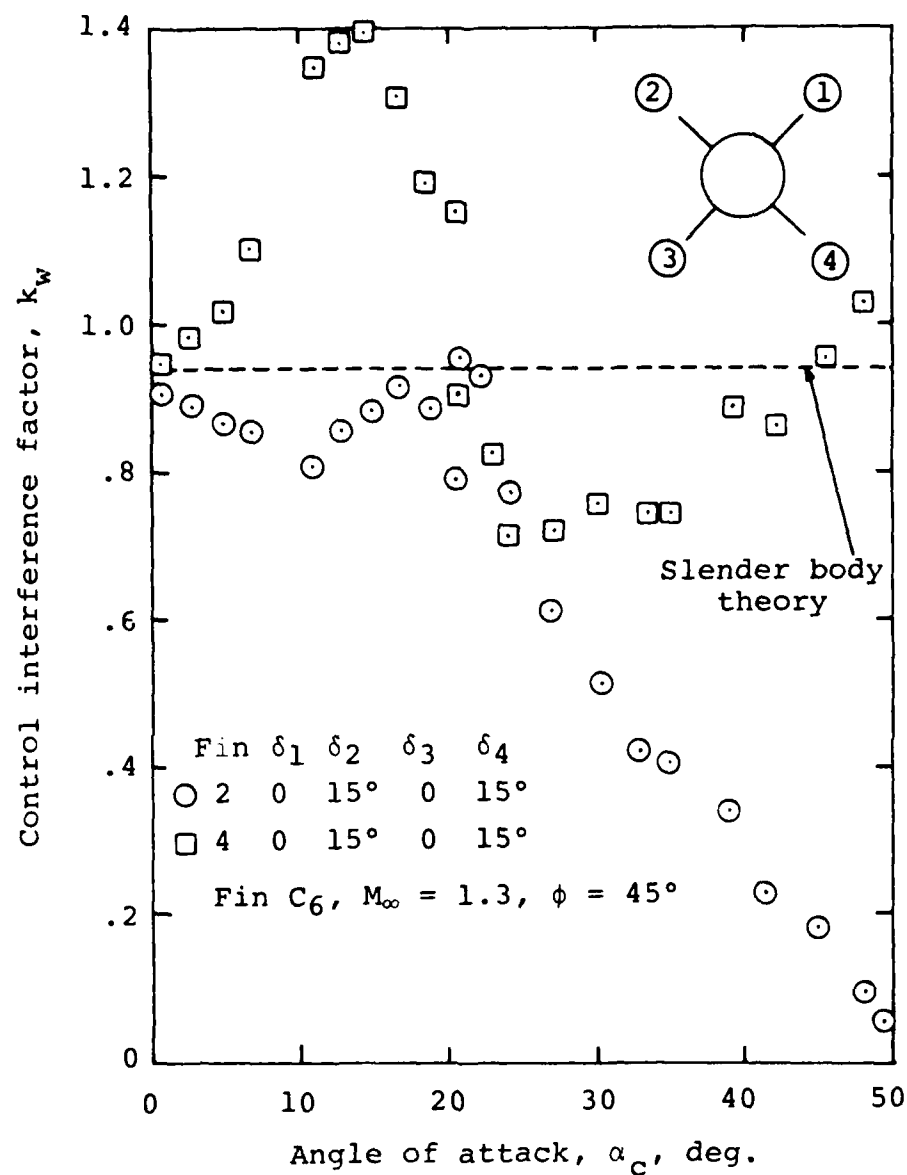
Figure 16.- Effect of roll angle on control interference
factor for pitch control of C_6 canard fin on Army
generalized missile at M_∞ = 1.3.

124
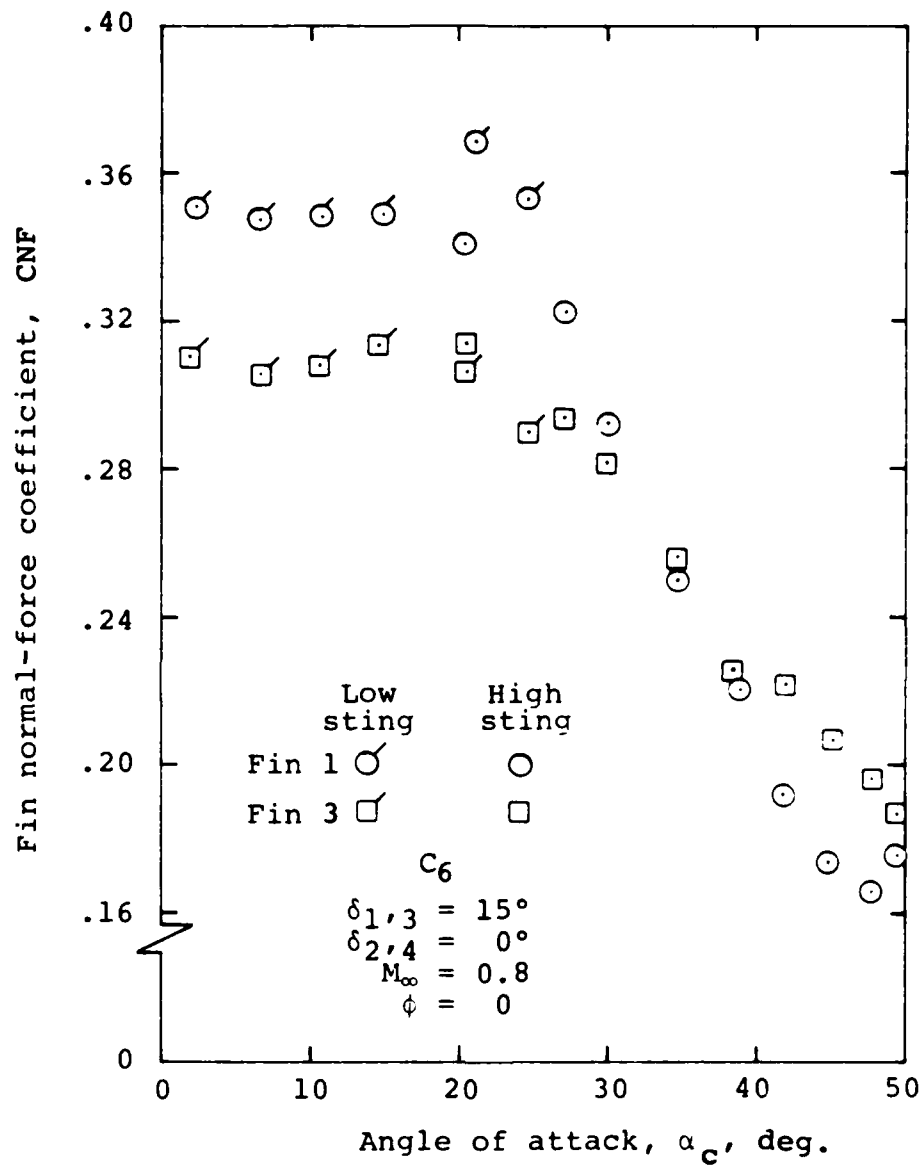
Figure 17.- Effect of angle of attack on the normal force of upper and lower fins deflected 15°; C_6 fins mounted on Army generalized missile.
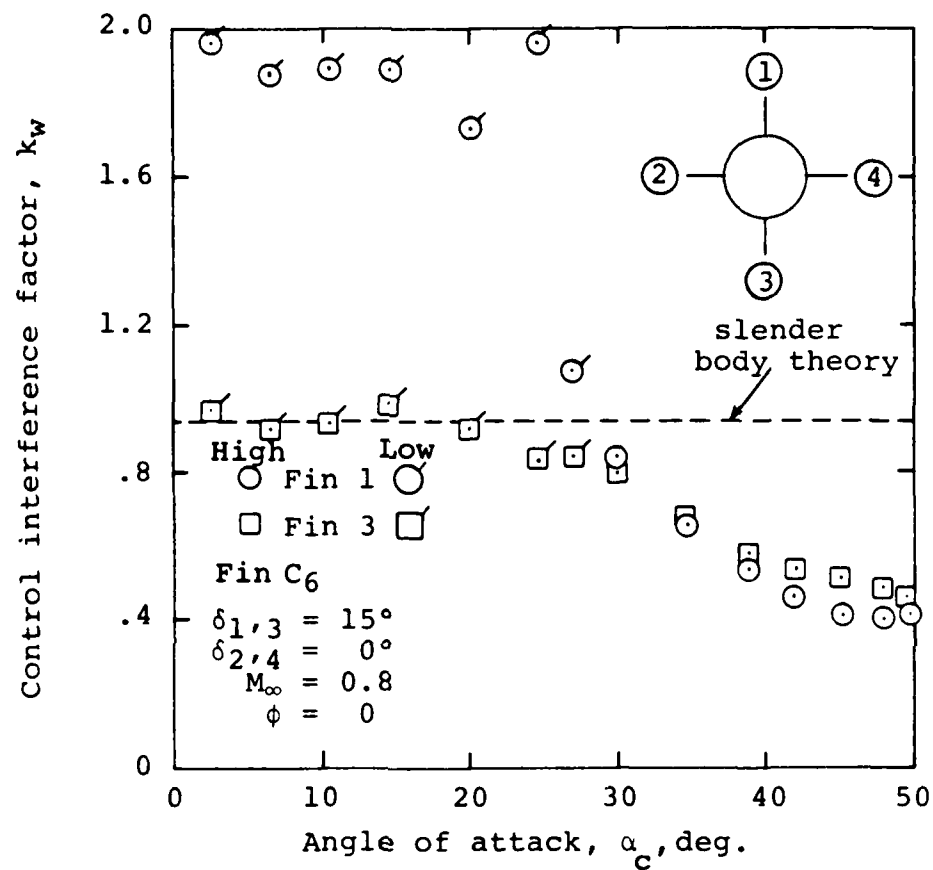
(a) $M_\infty = 0.8$

Figure 18.- Control interference factor of vertical fins with yaw control but no pitch control.

126
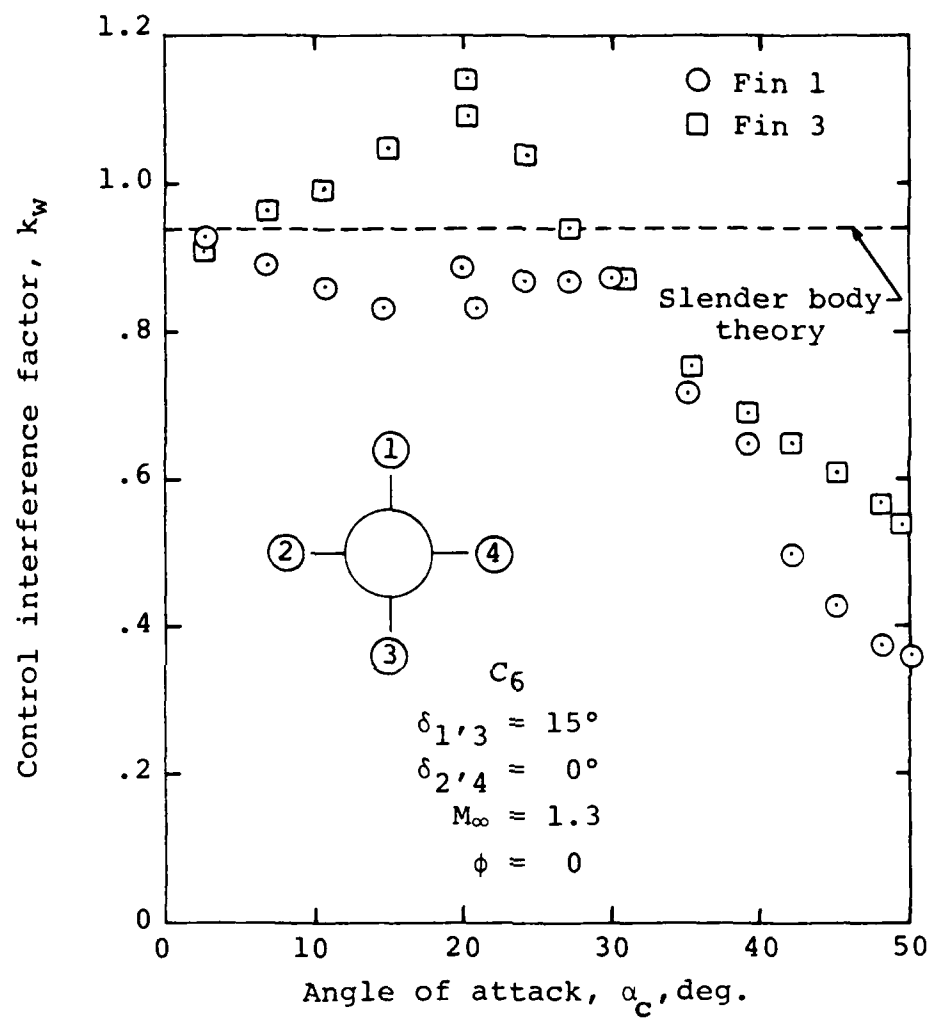
(b) $M_\infty = 1.3$

Figure 18.- Concluded.
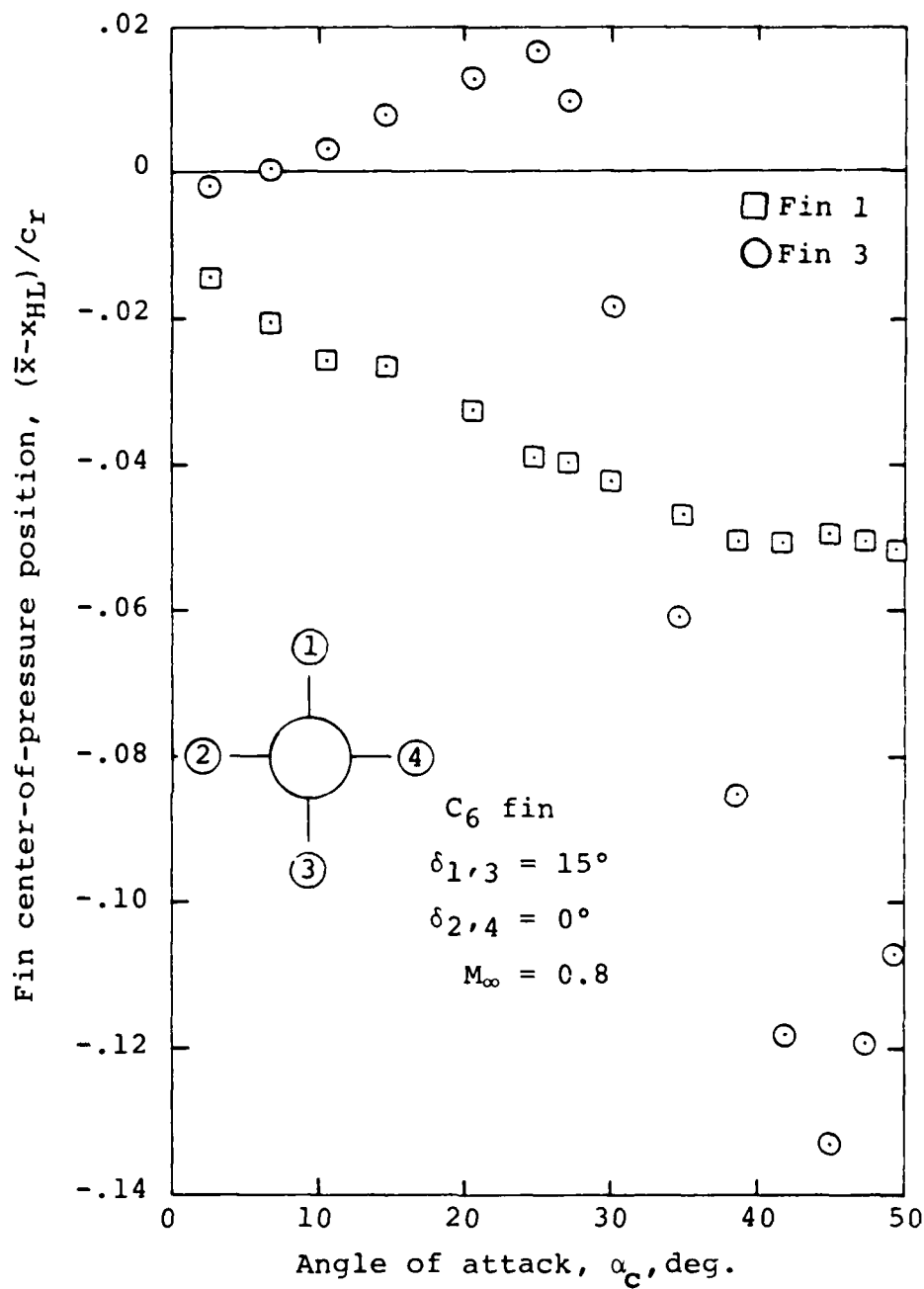
(a) $M_\infty = 0.8$

Figure 19.- Center of pressure of vertical fins with
yaw control but no pitch control.
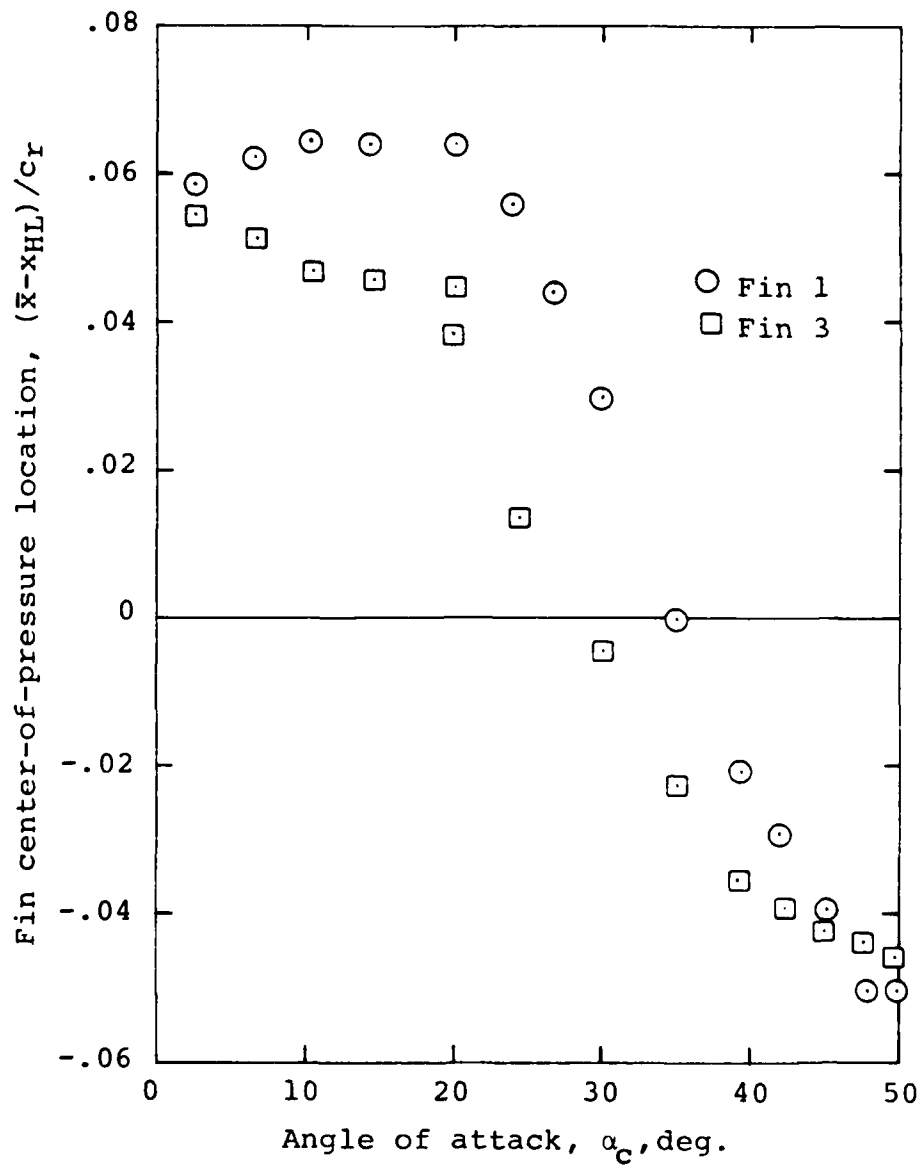
(b) $M_\infty = 1.3$

Figure 19.- Concluded.
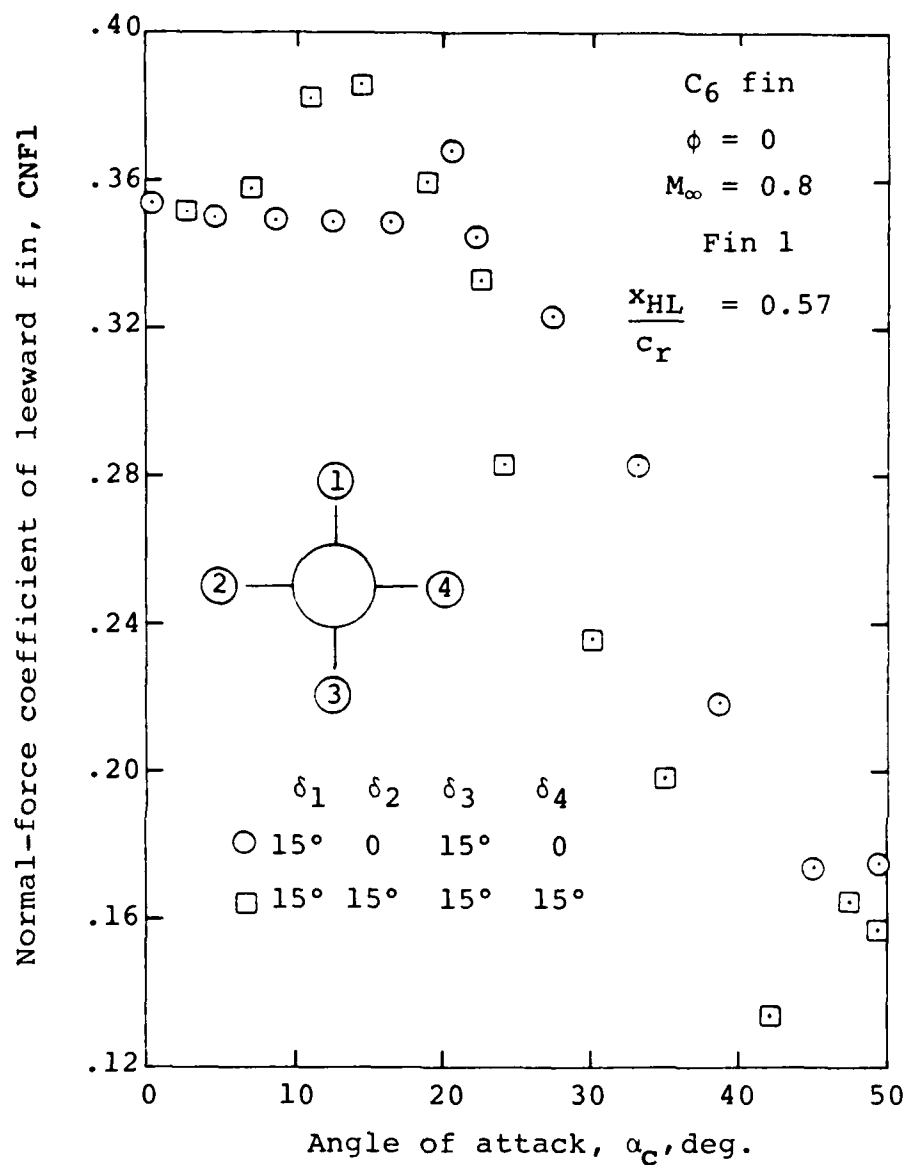
(a) Fin normal force, leeward fin

Figure 20.- Effect of pitch control on yaw control of leeward fin C_6 on Army generalized missile, $M_\infty = 0.8$.

130

.04

C_6

$\phi = 0$

$M_\infty = 0.8$

Fin 1

	δ_1	δ_2	δ_3	δ_4
◯	15°	0°	15°	0°
□	15°	15°	15°	15°

Fin center-of-pressure position, $(\bar{x}_\delta - x_{HL})/c_r$

0

-.04

-.08

-.12

-.16

-.20

0   10   20   30   40   50

Angle of attack, α_c, deg.
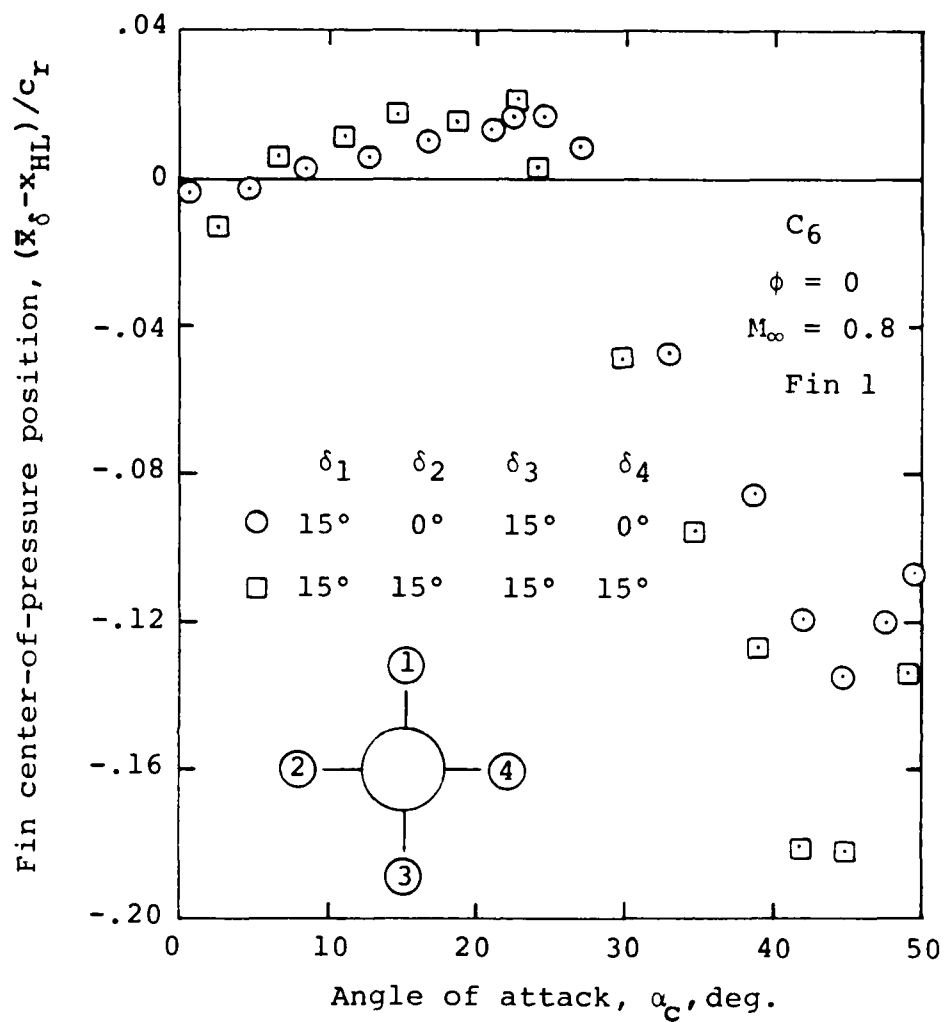
(b) Fin center-of-pressure position,
leeward fin

Figure 20.- Continued.
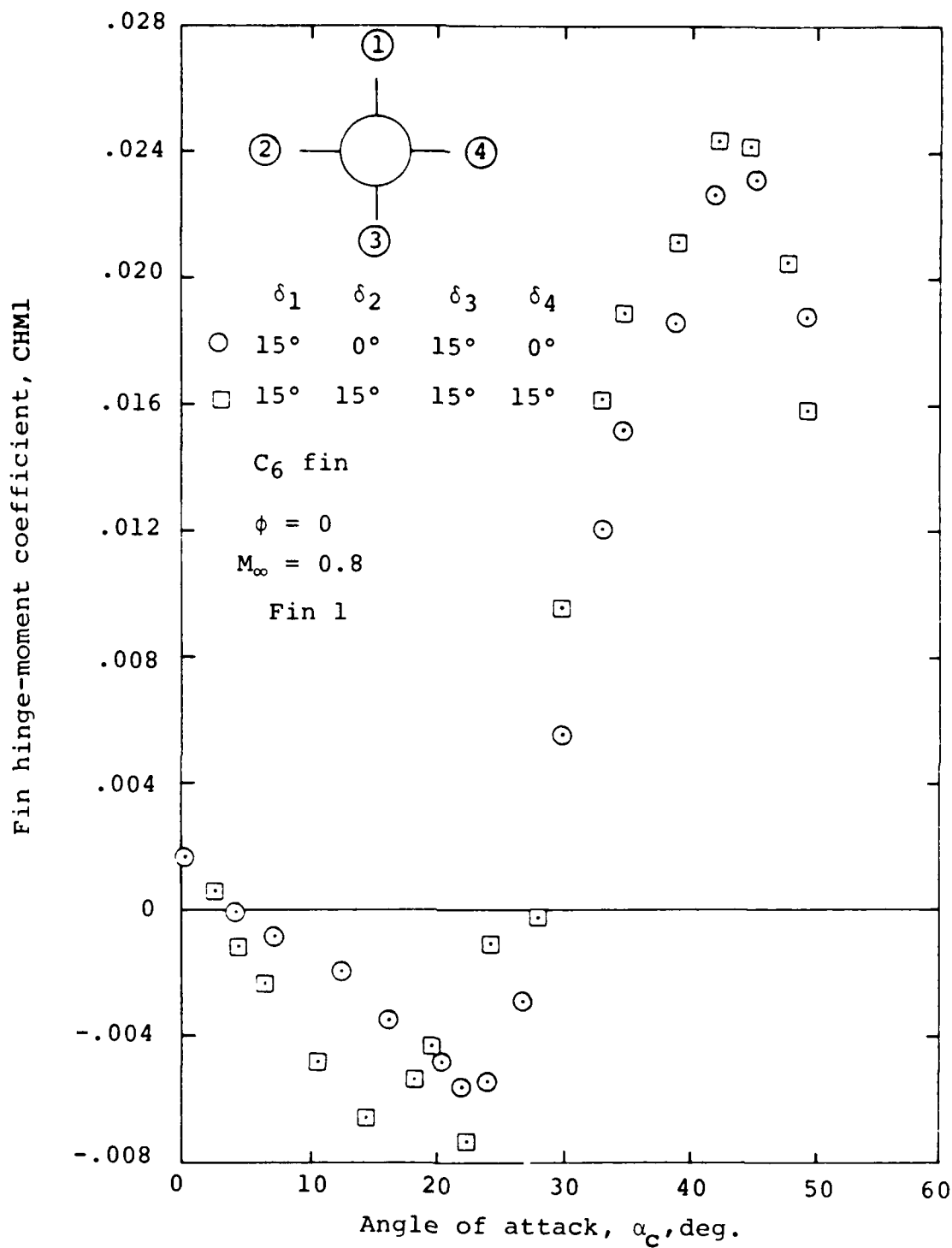
(c) Hinge moment, leeward fin

Figure 20.- Concluded.

132
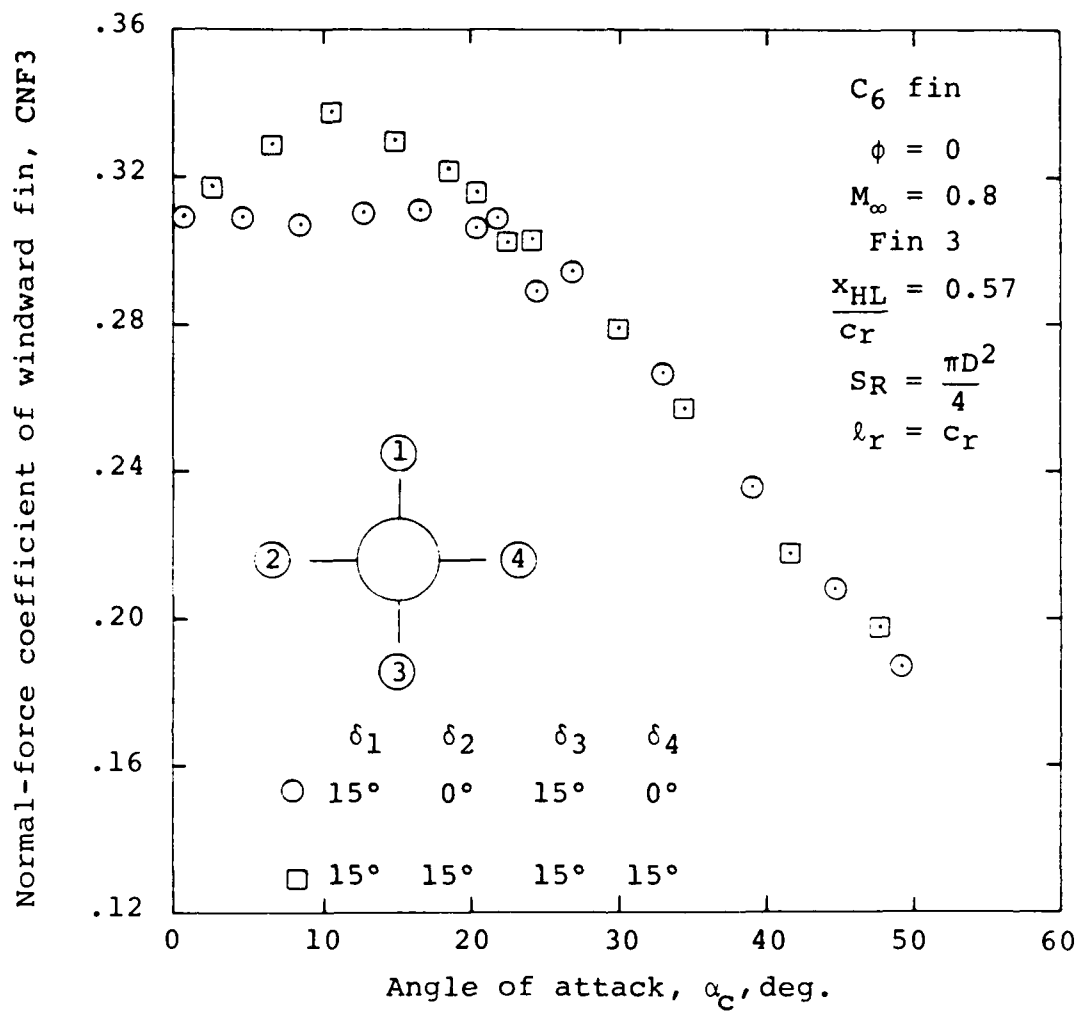
(a) Fin normal force, windward fin

Figure 21.- Effect of pitch control on yaw control of windward fin C_6 mounted on Army generalized missile, $M_\infty = 0.8$.

133

Fin center-of-pressure position, $(\bar{x}_\delta - \bar{x}_{HL})/c_r$

Angle of attack, α_c, deg.

	δ_1	δ_2	δ_3	δ_4
⊙	15°	0°	15°	0°
□	15°	15°	15°	15°

C_6 fin
$\phi = 0$
$M_\infty = 0.8$
Fin 3
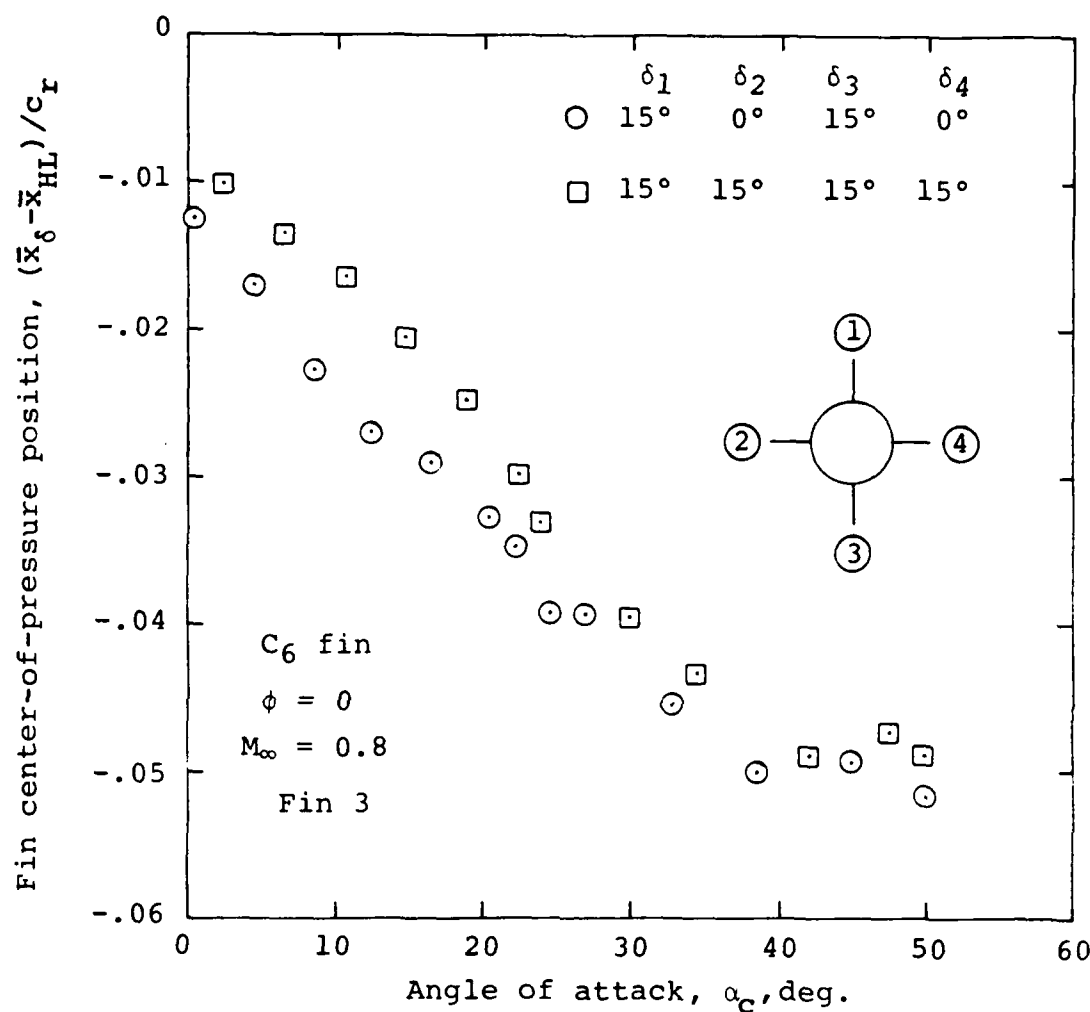
(b) Fin center-of-pressure position,
windward fin

Figure 21.- Continued.

134
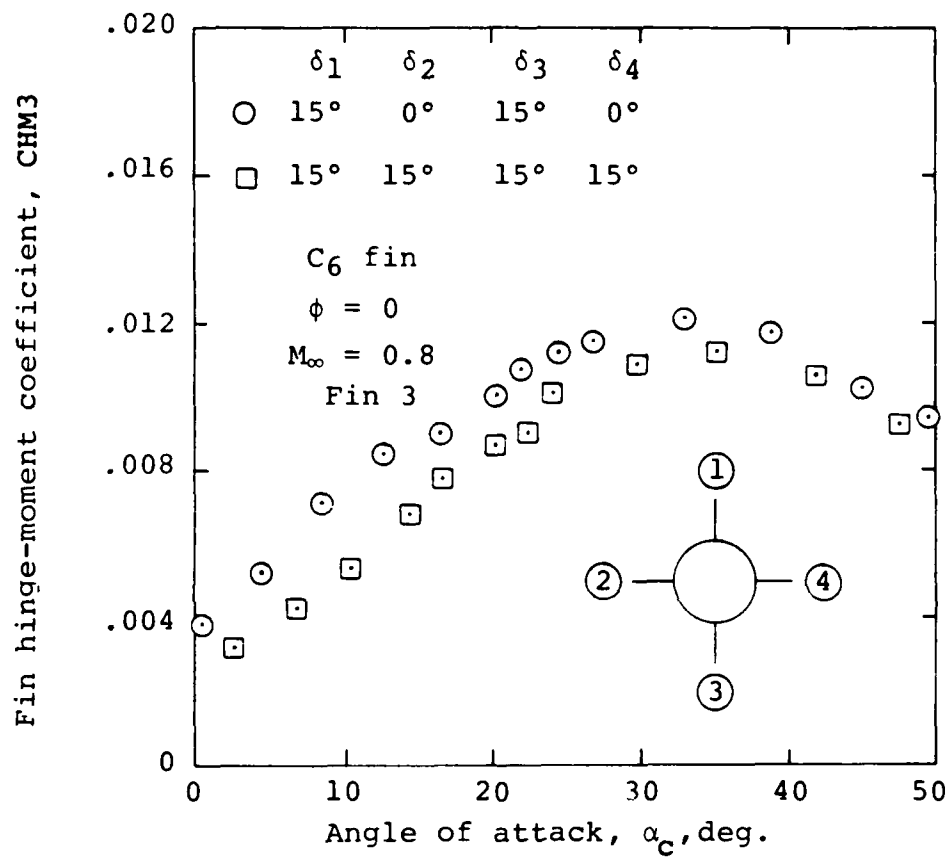
(c) Hinge moment, windward fin

Figure 21.- Concluded.

135
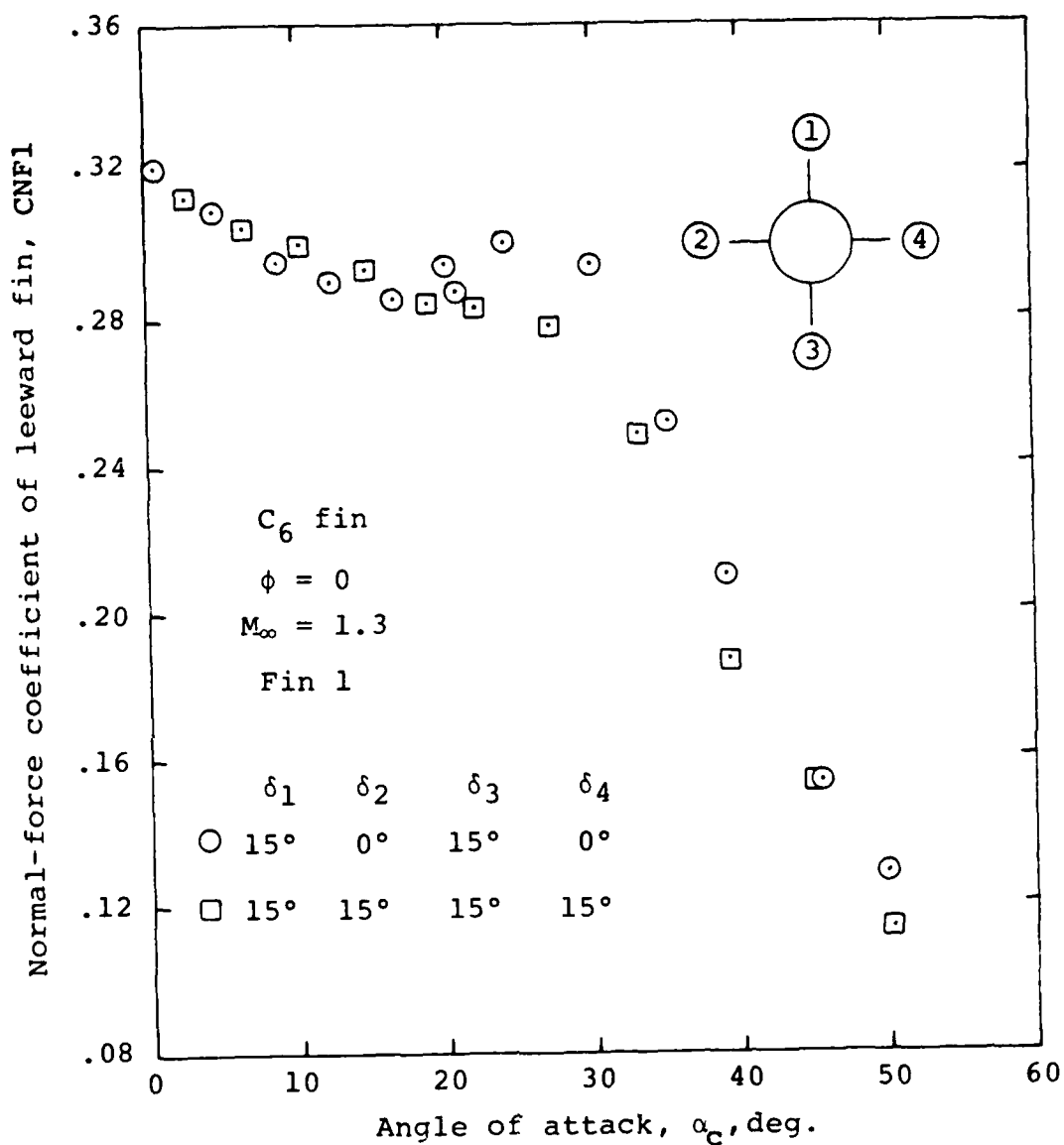
(a) Fin normal force, leeward fin

Figure 22.- Effect of pitch control on yaw control for leeward fin C_6 on Army generalized missile; $M_\infty = 1.3$.

136
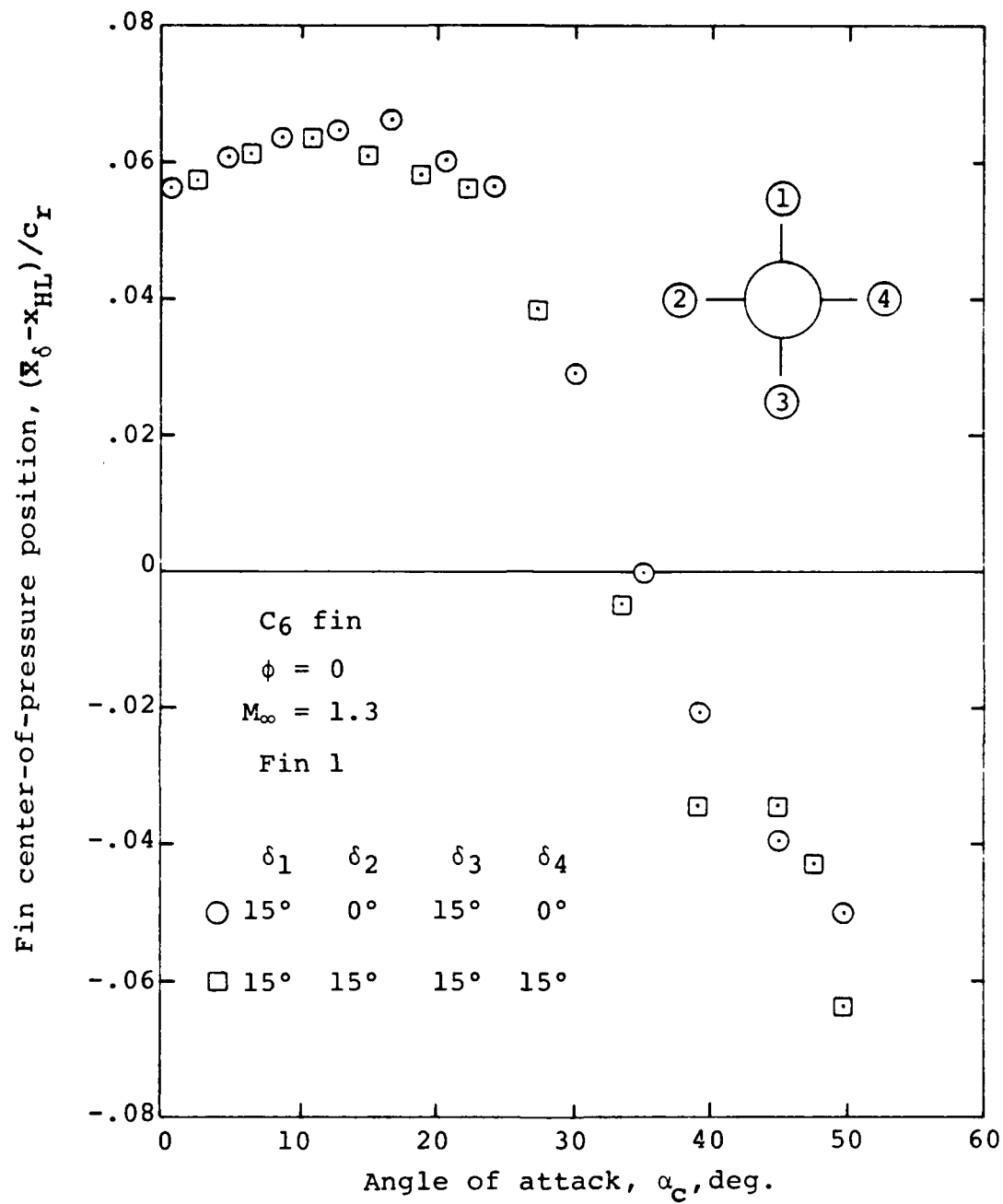
(b) Fin center-of-pressure position, leeward fin

Figure 22.- Continued.

137
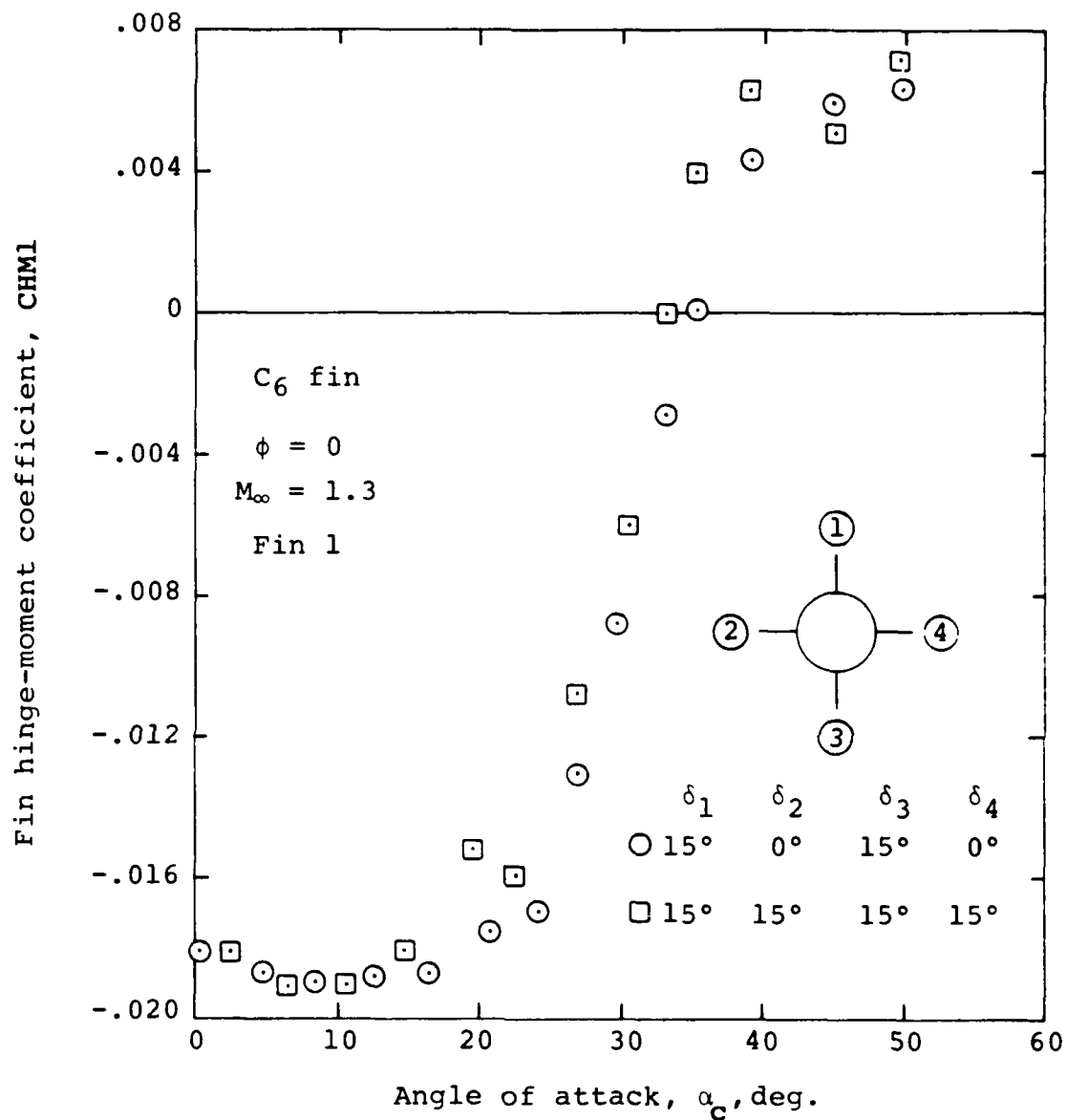
(c) Hinge moment; leeward fin

Figure 22.- Concluded.

Normal-force coefficient of windward fin, CNF3

.40

.36

.32

.28

.24

.20

.16

.12

0   10   20   30   40   50

Angle of attack, ι_c, deg.

C_6 Fin
$\phi = 0$
$M_\infty = 1.3$
Fin 3

	δ_1	δ_2	δ_3	δ_4
○	15°	0°	15°	0°
□	15°	15°	15°	15°

1
2   4
3
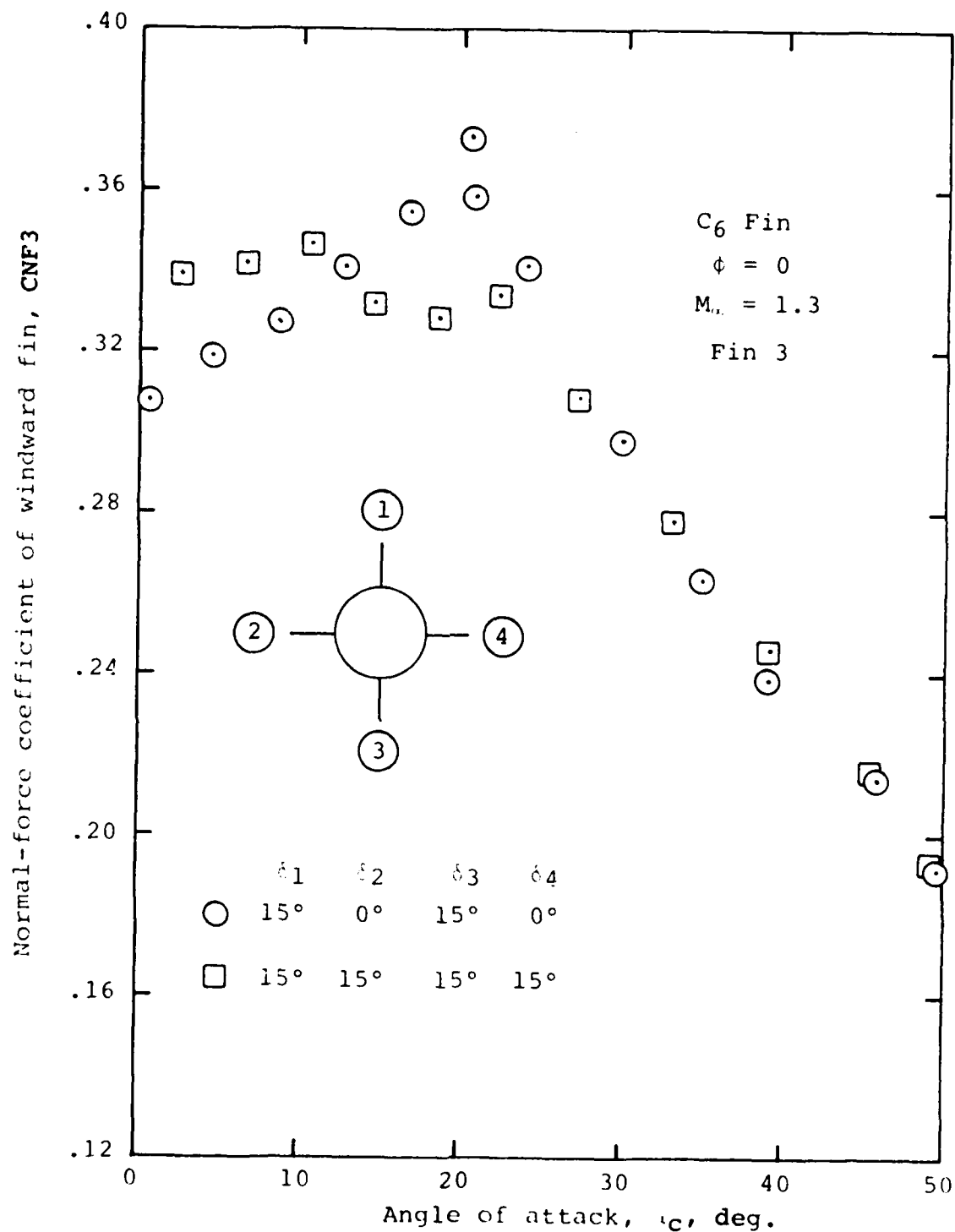
(a) Fin normal force, windward fin

Figure 23.- Effect of pitch control on yaw control of windward fin C_6 mounted on **Army** generalized missile, $M_\infty = 1.3$.

139
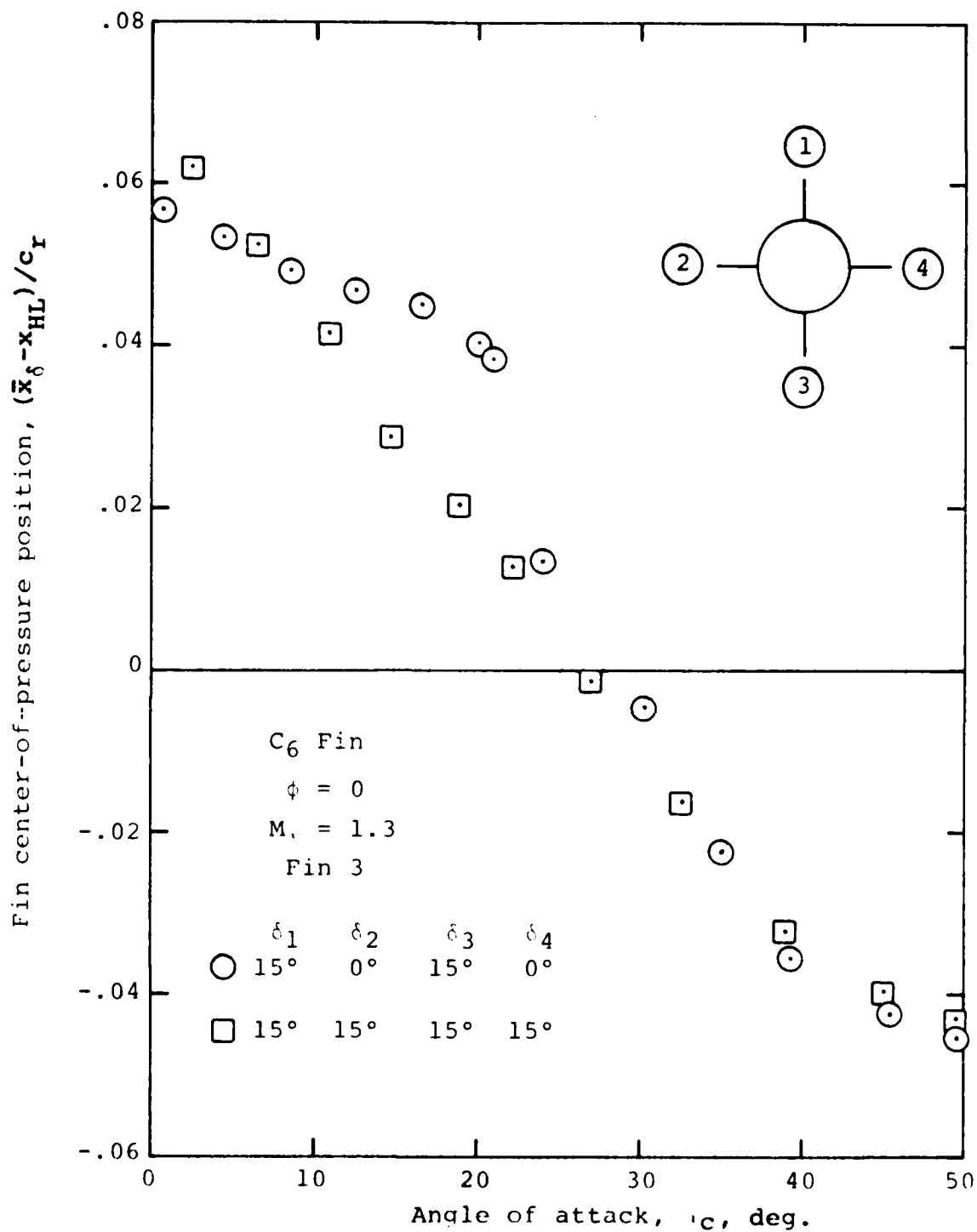
(b) Fin center-of-pressure
position, windward fin

Figure 23.- Continued.

140
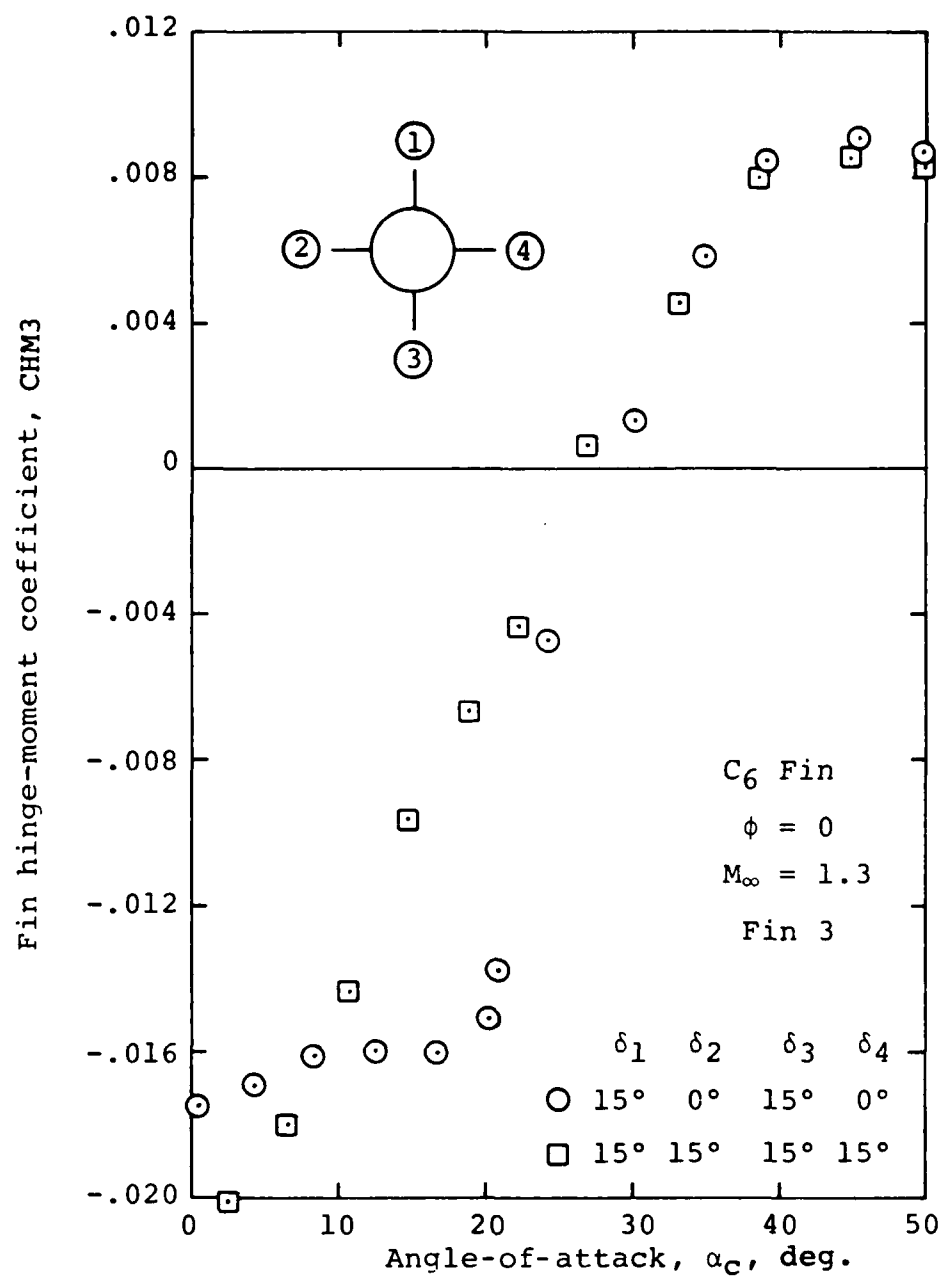
(c) Hinge moment, windward fin

Figure 23.- Concluded.

141
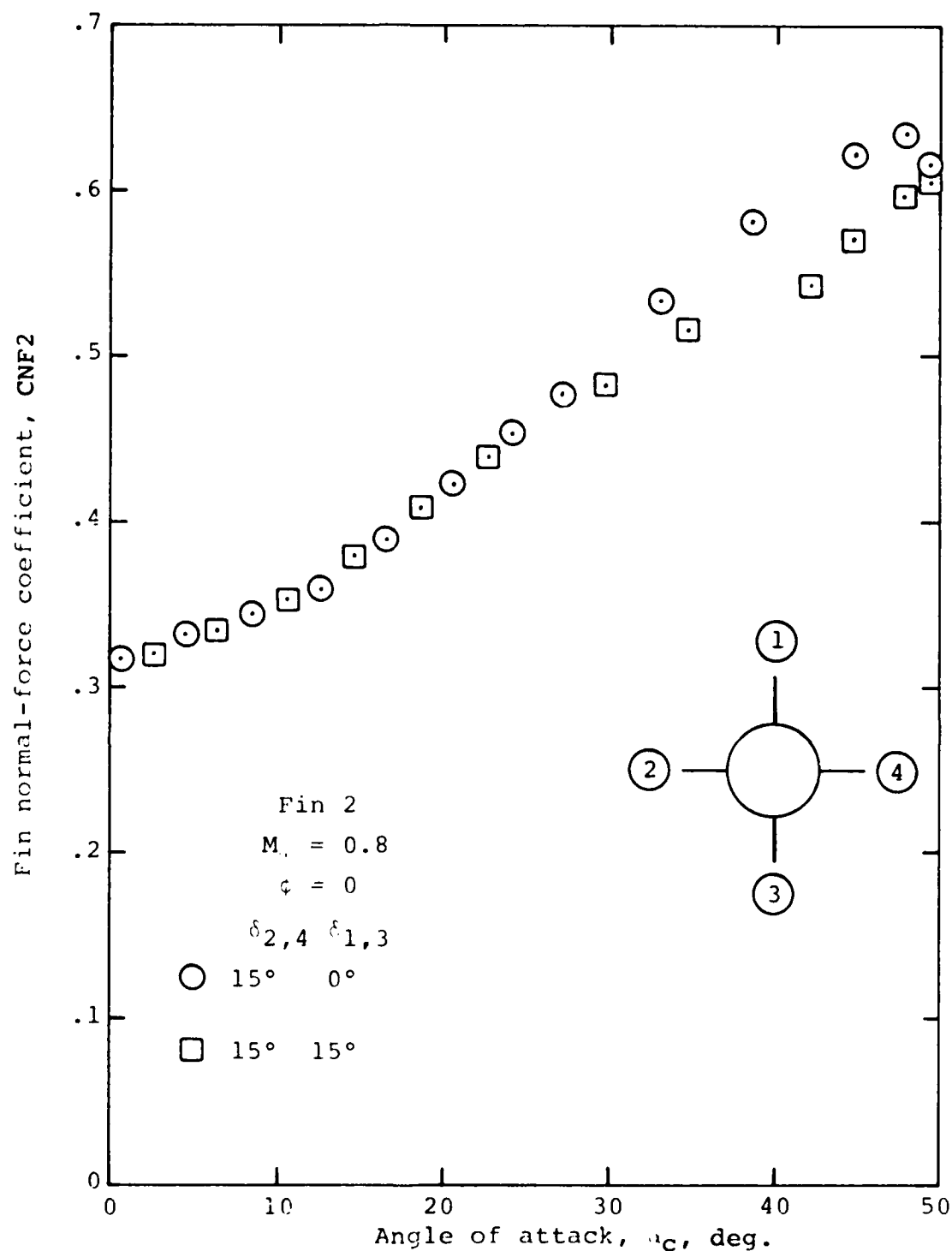
(a) Normal force

Figure 24.- Effect of yaw control on pitch-control characteristics
of horizontal left fin C_6 mounted on Army generalized
missile at $M_\infty = 0.8$; fin 2.

142
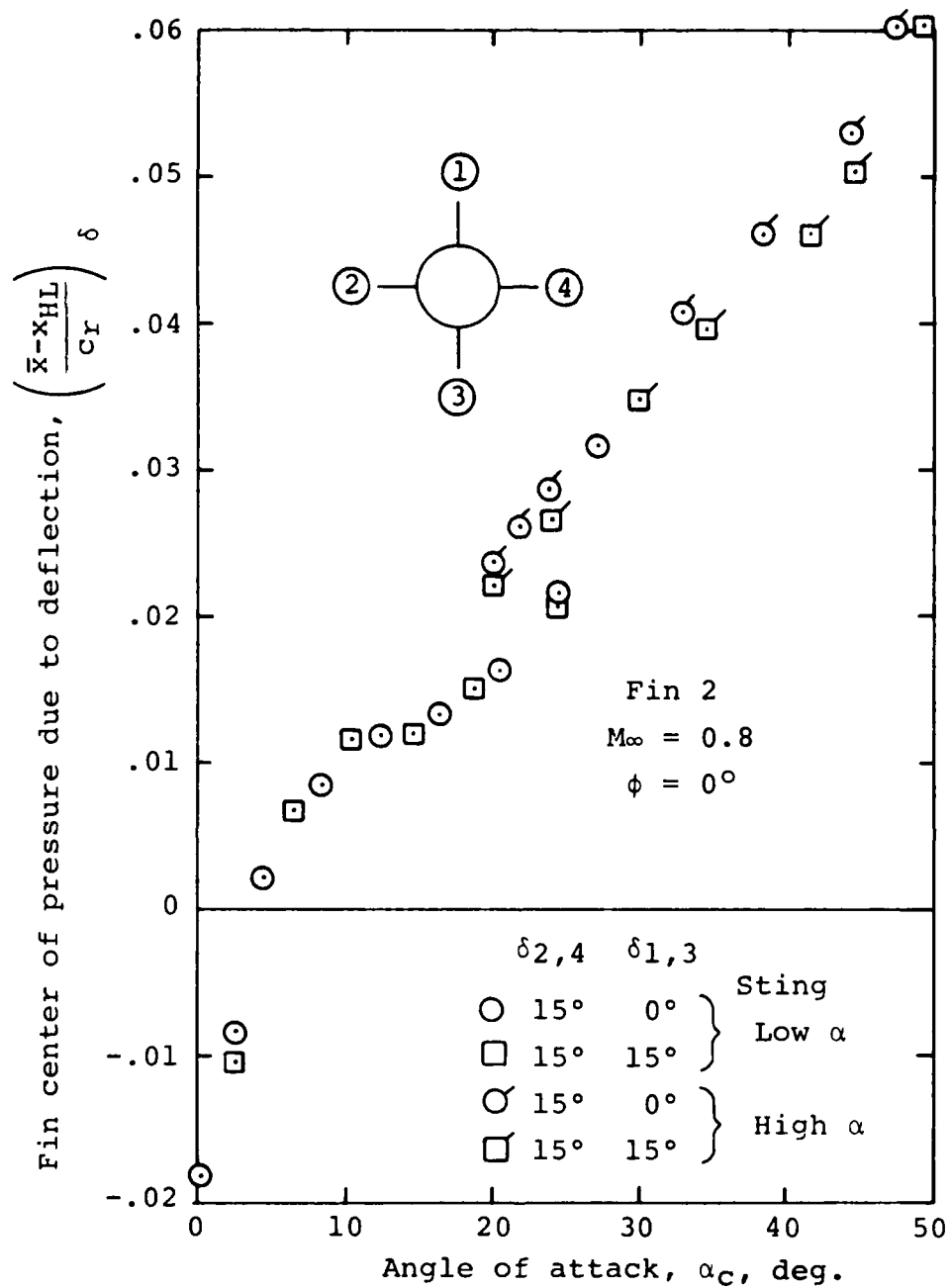
(b) Center of pressure due
to fin deflection

Figure 24.- Continued.

143
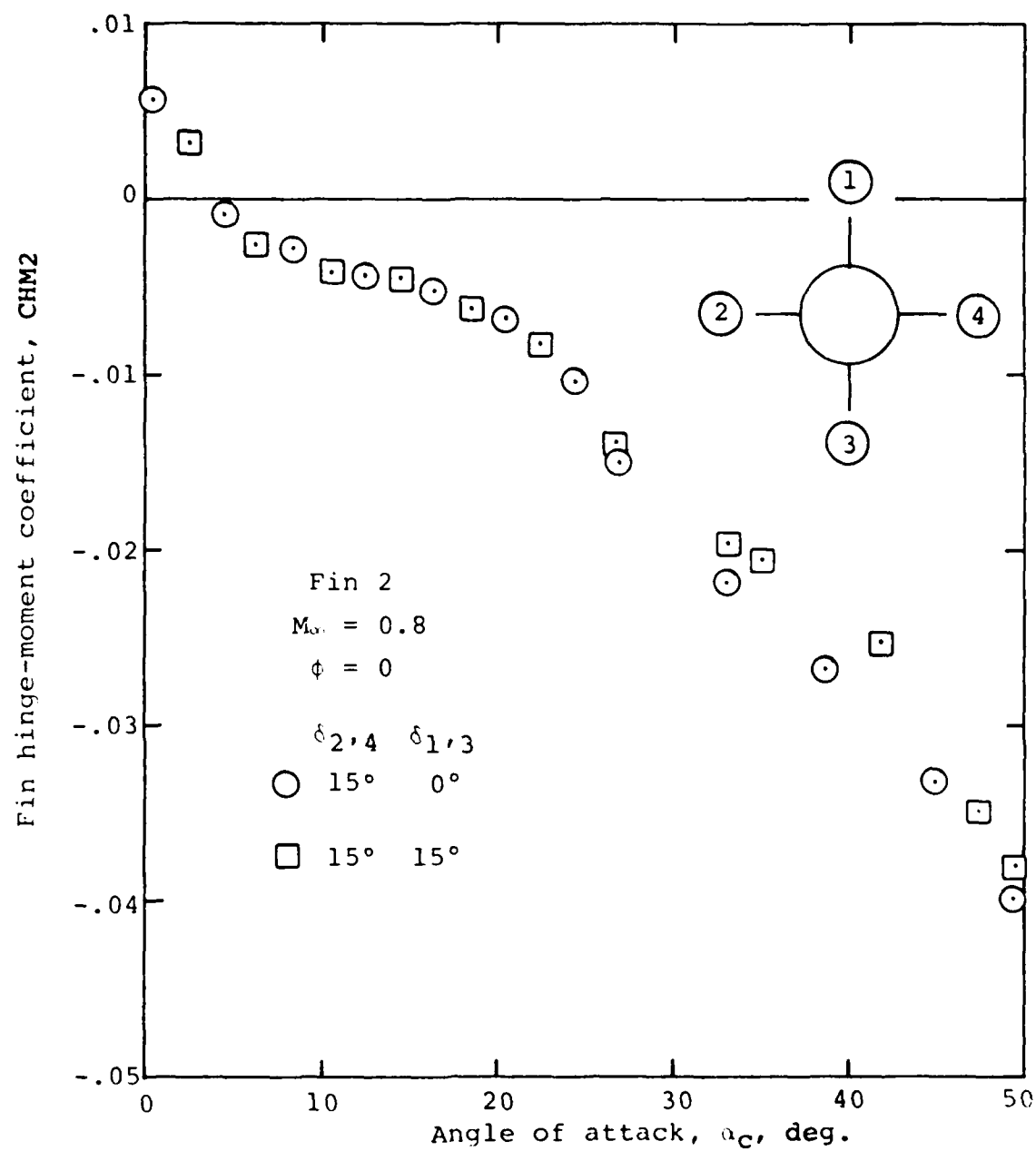
(c) Hinge moment

Figure 24.- Concluded.

144
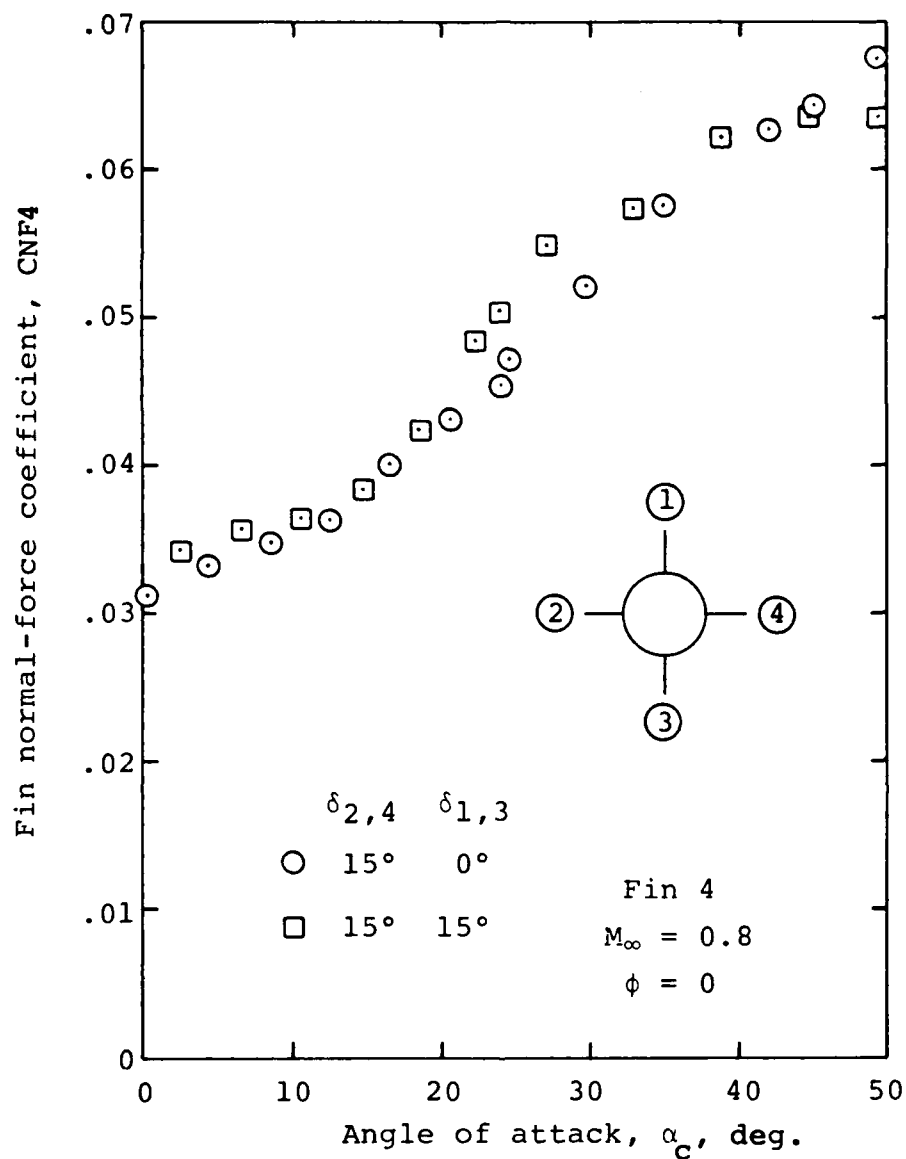
(a) Normal force

Figure 25.- Effect of yaw control on pitch control
characteristics of horizontal right fin C_6
mounted on Army generalized missile
at $M_\infty = 0.8$, fin 4.

145

Fin center-of-pressure position due to deflection, $\left(\dfrac{\bar{x}-x_{HL}}{c_r}\right)_\delta$

.06

.05

.04

.03

.02

.01

0

-.01

-.02

Fin 4

$M_\infty = 0.8$

$\phi = 0$

	$\delta_{2,4}$	$\delta_{1,3}$
◯	15°	0°
☐	15°	15°

0   10   20   30   40   50

Angle of attack, α_c, deg.
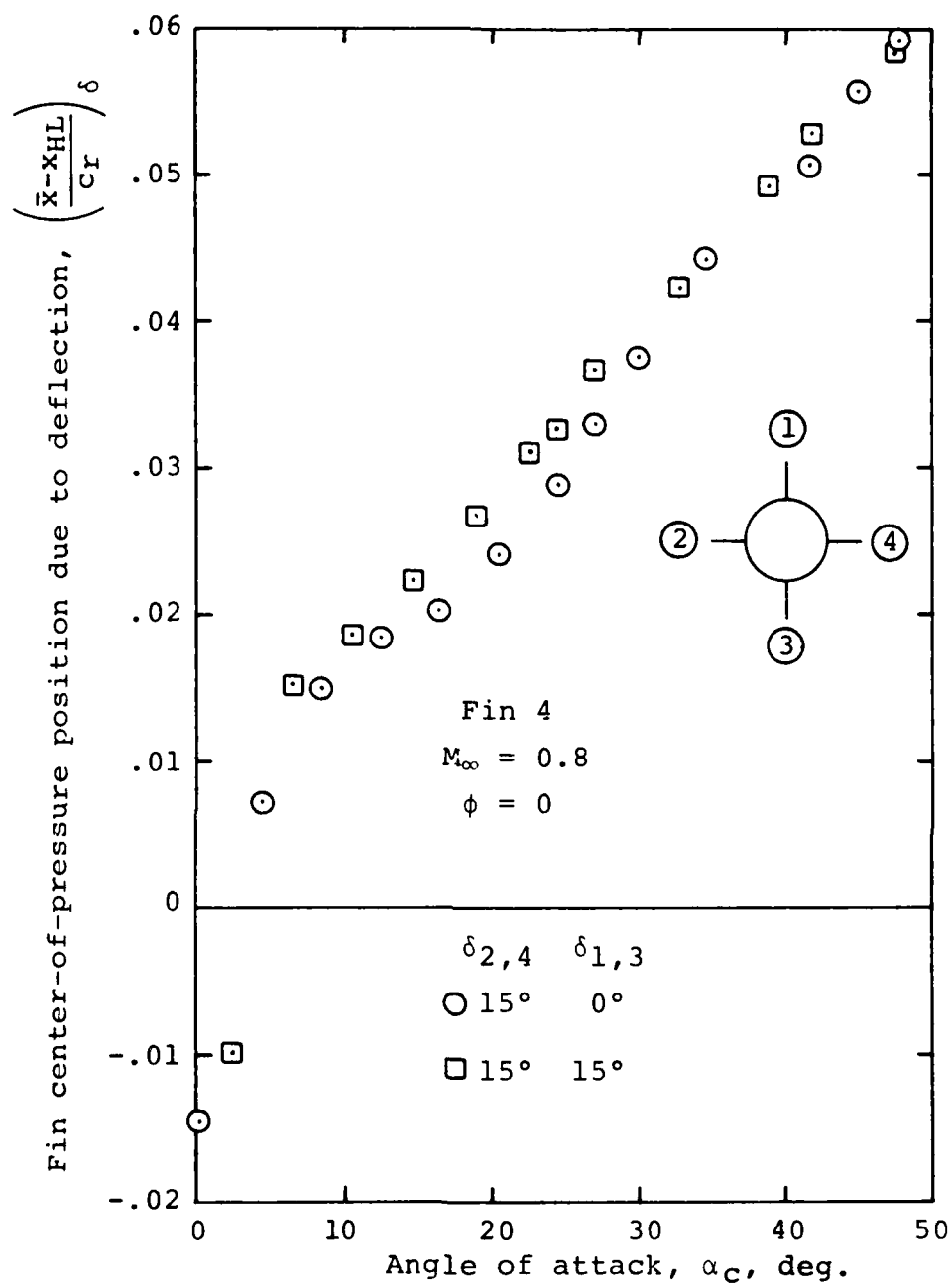
(b) Center of pressure due
to fin deflection

Figure 25.- Continued.
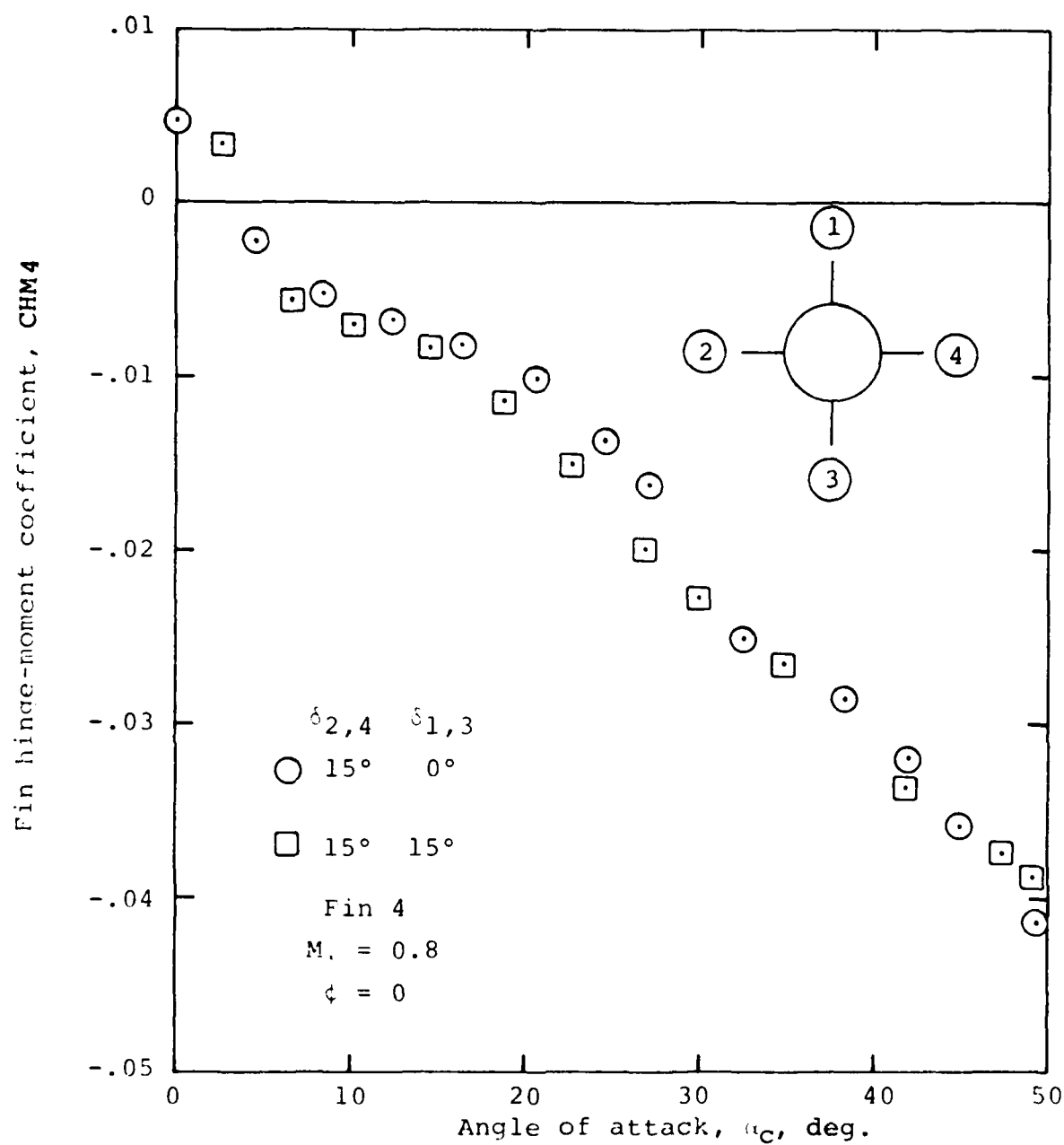
(c) Hinge moment

Figure 25.- Concluded.

.01

0

−.01

Fin hinge-moment coefficient, CHM2

−.02

−.03

−.04

−.05

① 1

② 2   ④ 4

③ 3

Fin 2

$M_\cdot = 1.3$

$\phi = 0$

$\delta_{2,4}$ $\delta_{1,3}$

○   15°   0°

□   15°   15°

0   10   20   30   40   50

Angle of attack, α_c, deg.
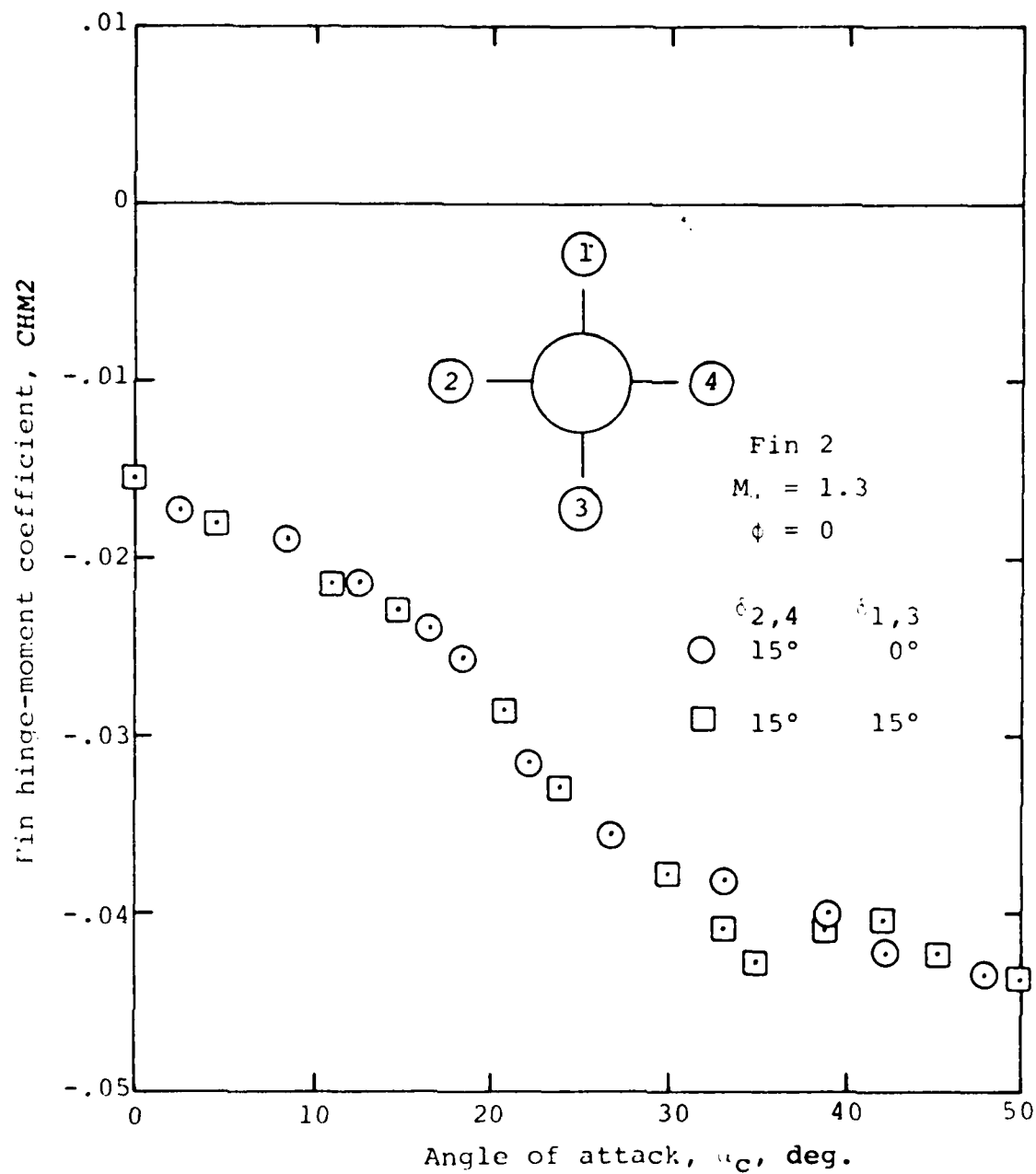
(a) Left fin

Figure 26.- Effect of yaw control on hinge moments of
horizontal fin C_6 mounted on **Army** generalized
missile at $M_\cdot = 1.3$.
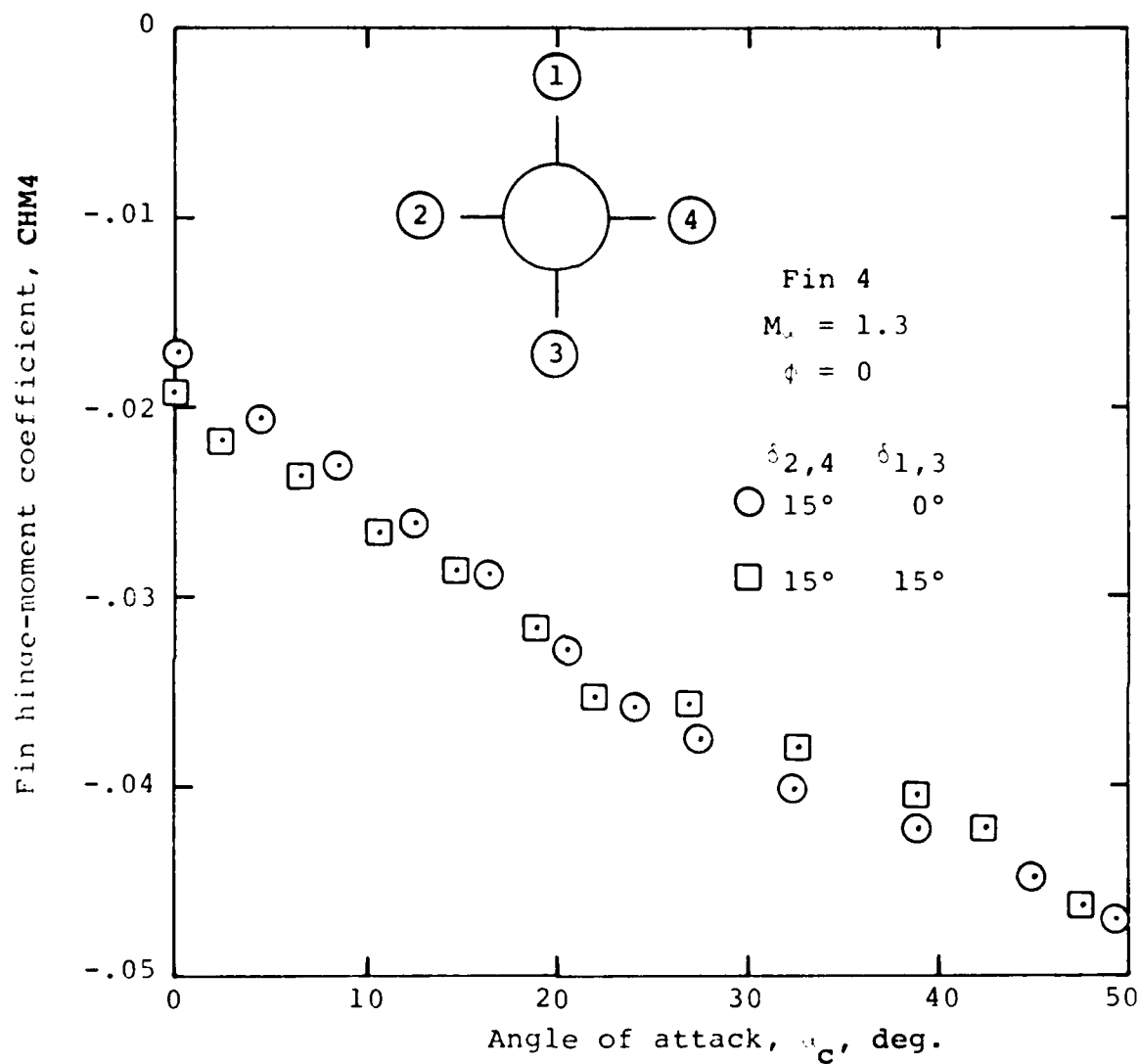
(b) Right fin

Figure 26.- Concluded.
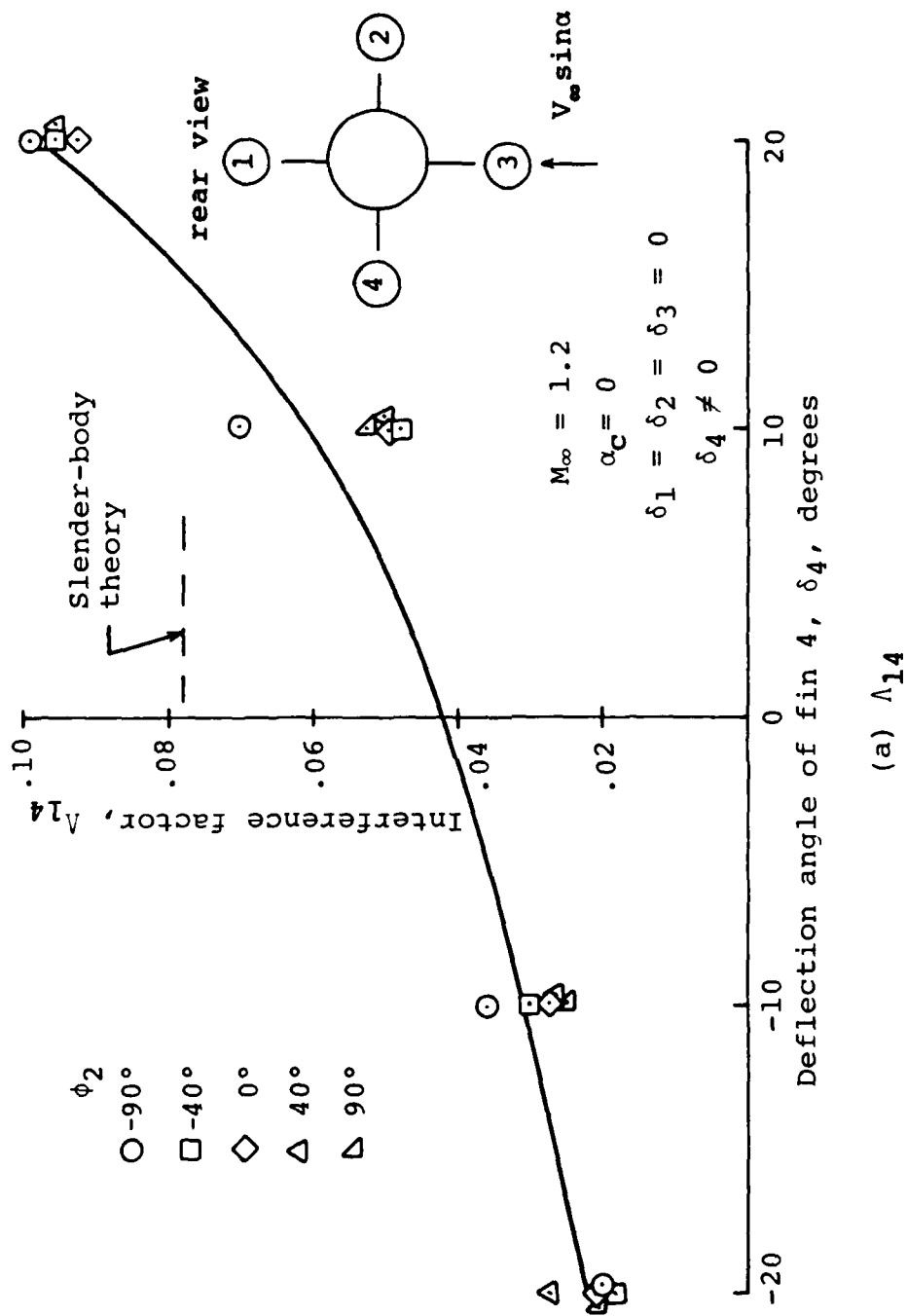
Figure 27.– Control interference factor Λ_{ij} for fin 51 mounted on triservice missile; $M_\infty = 1.2$, $\alpha_c = 0°$.

150
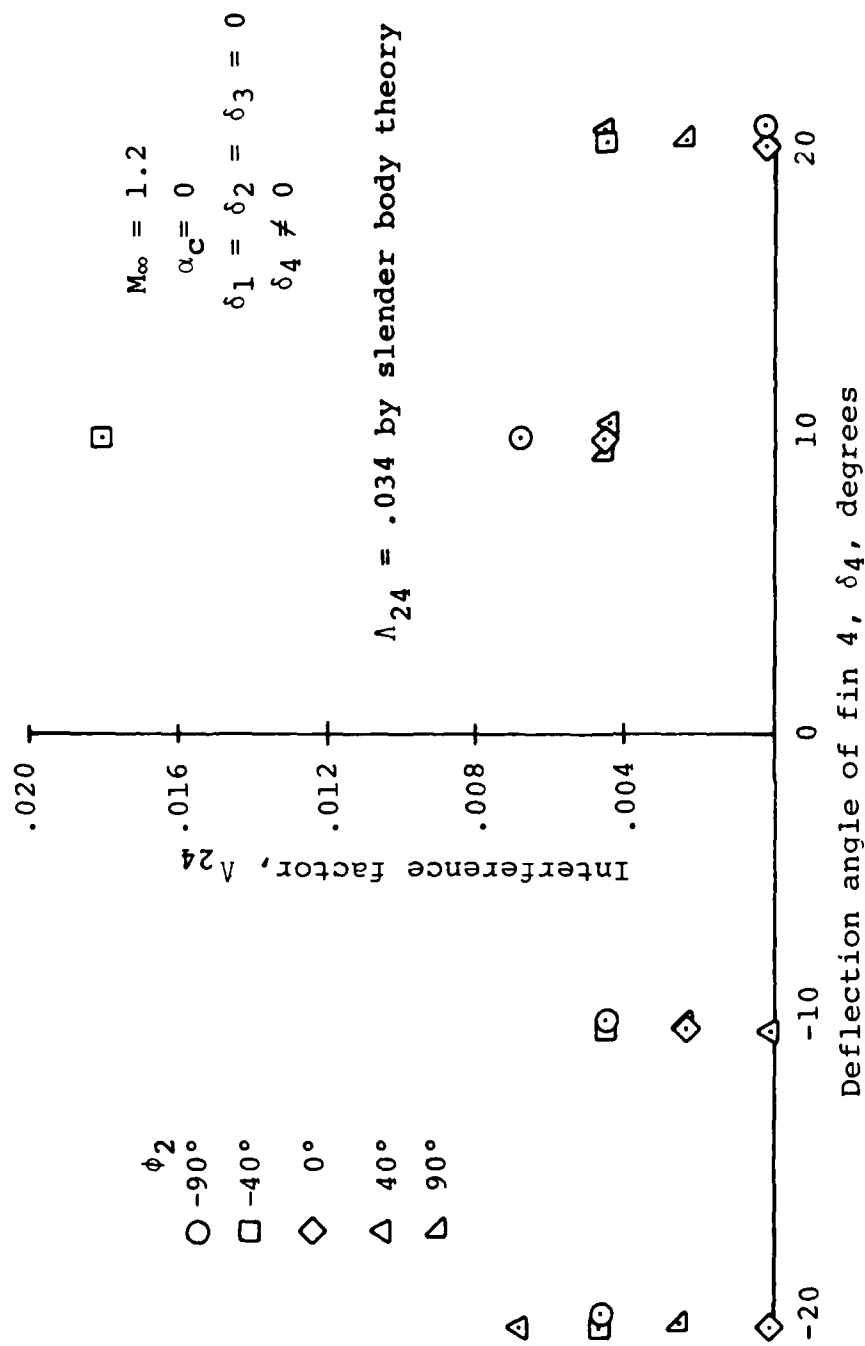
(b) Λ_{24}

Figure 27.- Continued.
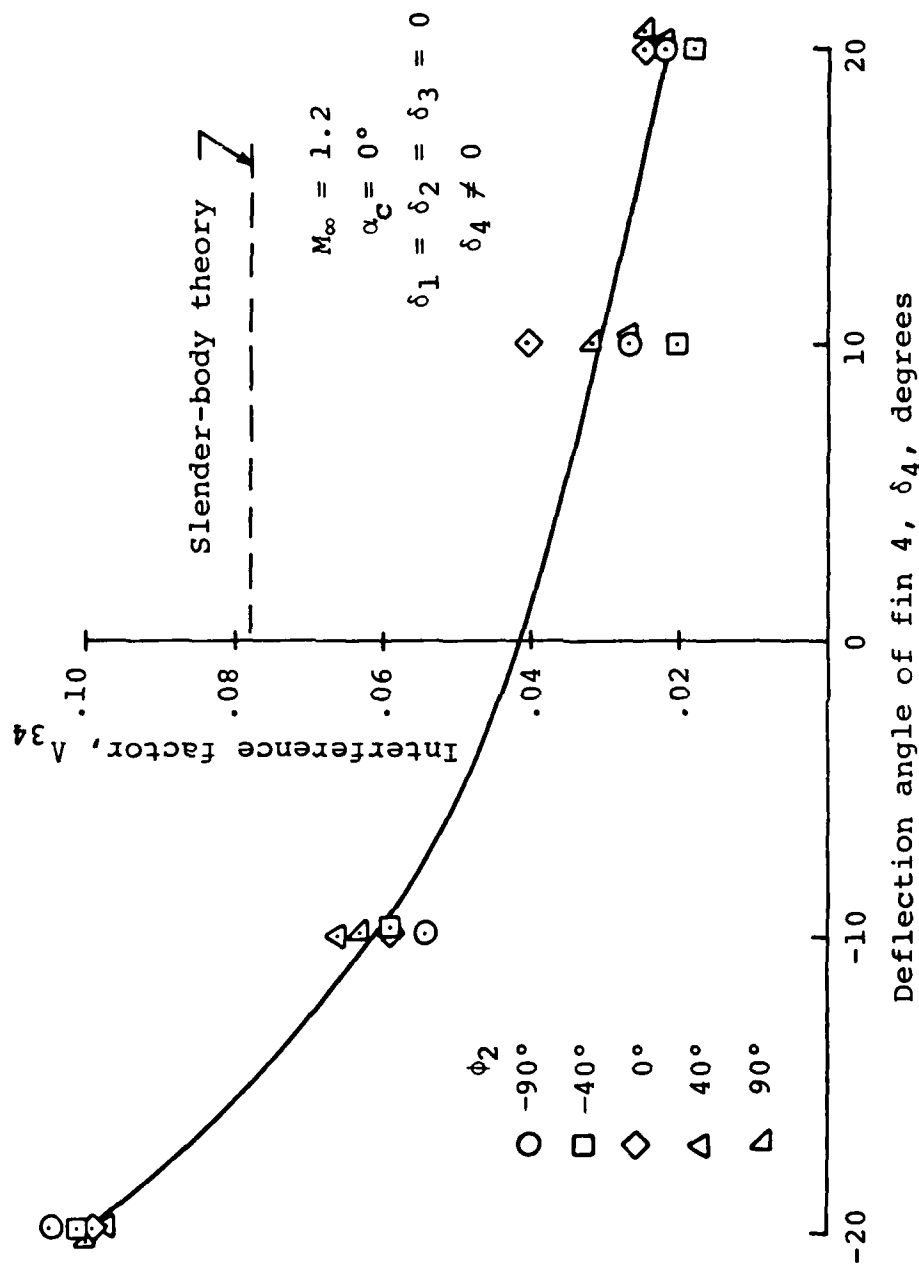
(c) Λ_{34}

Figure 27.- Continued.

152
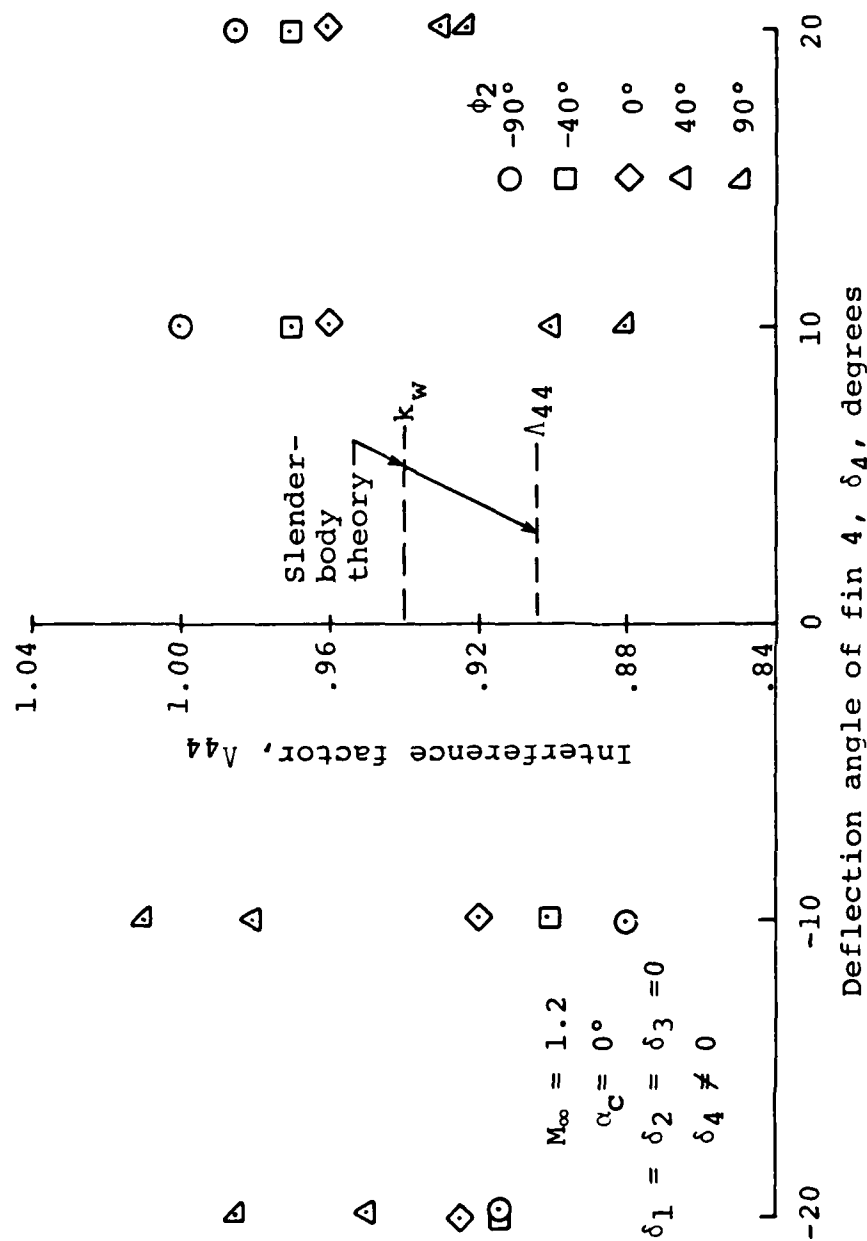
(d) Λ_{44}

Figure 27.- Concluded.

153
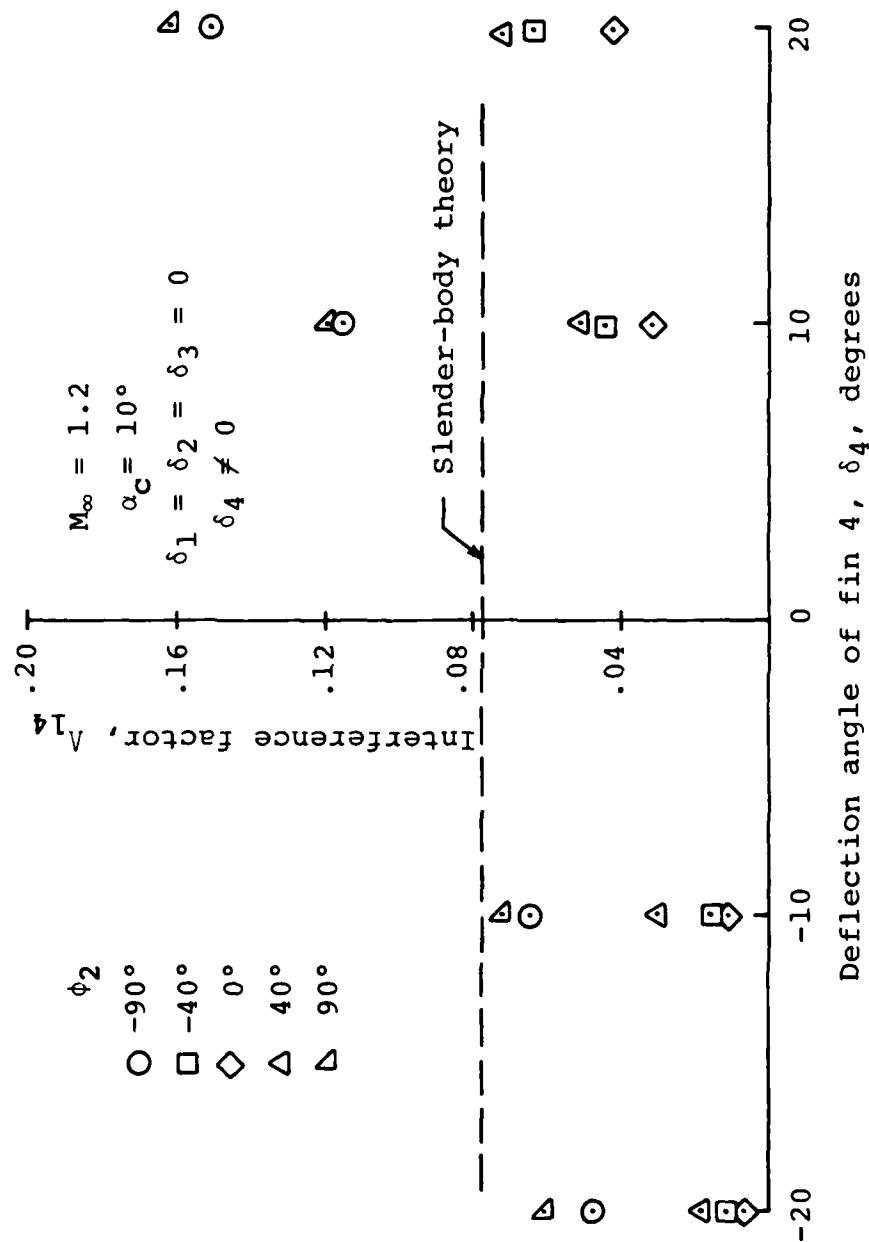
(a) Λ_{14}

Figure 28.- Control interference factor Λ_{ij} for fin 51 mounted on triservice missile; $M_\infty = 1.2$, $\alpha_c = 10°$.

154
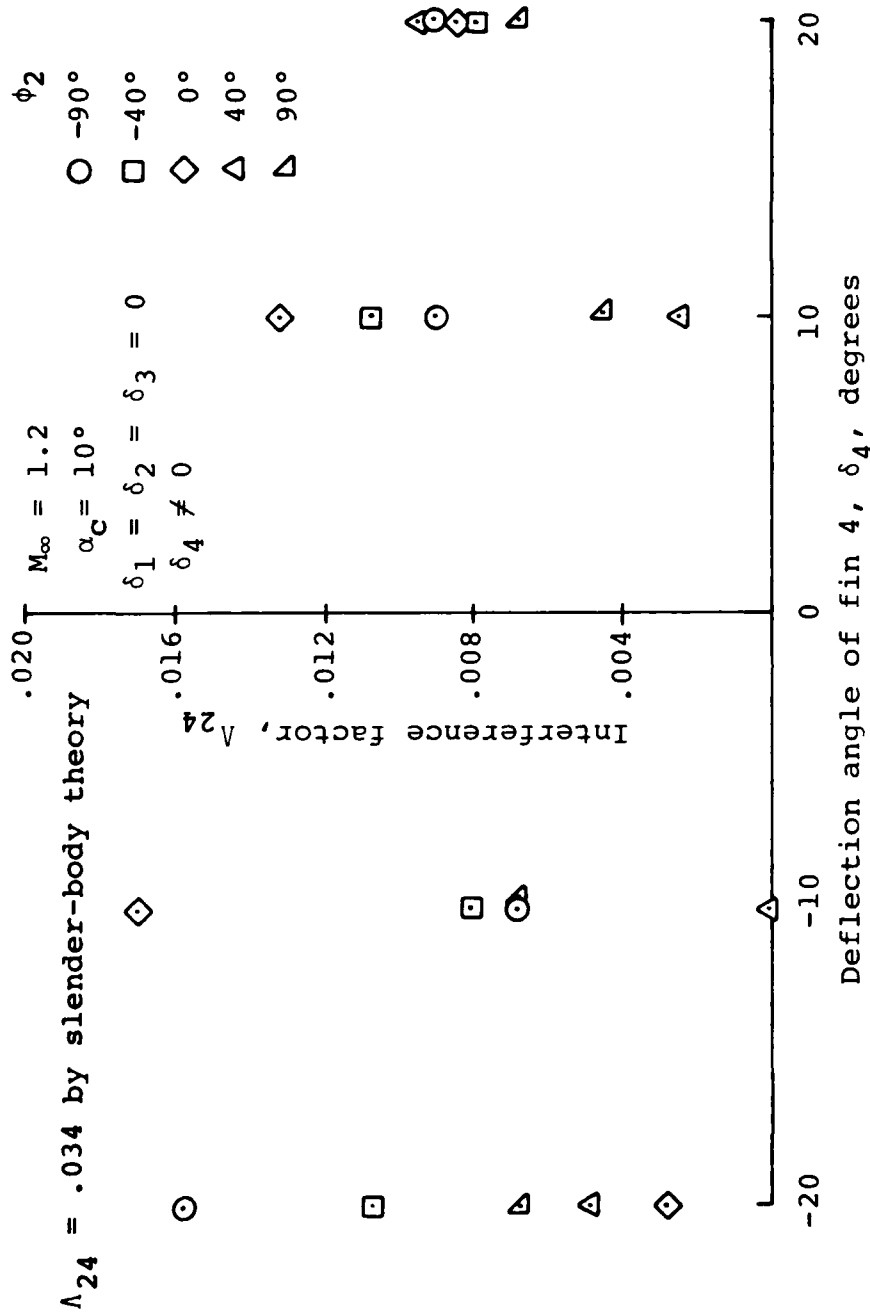
(b) Λ_{24}

Figure 28.- Continued.
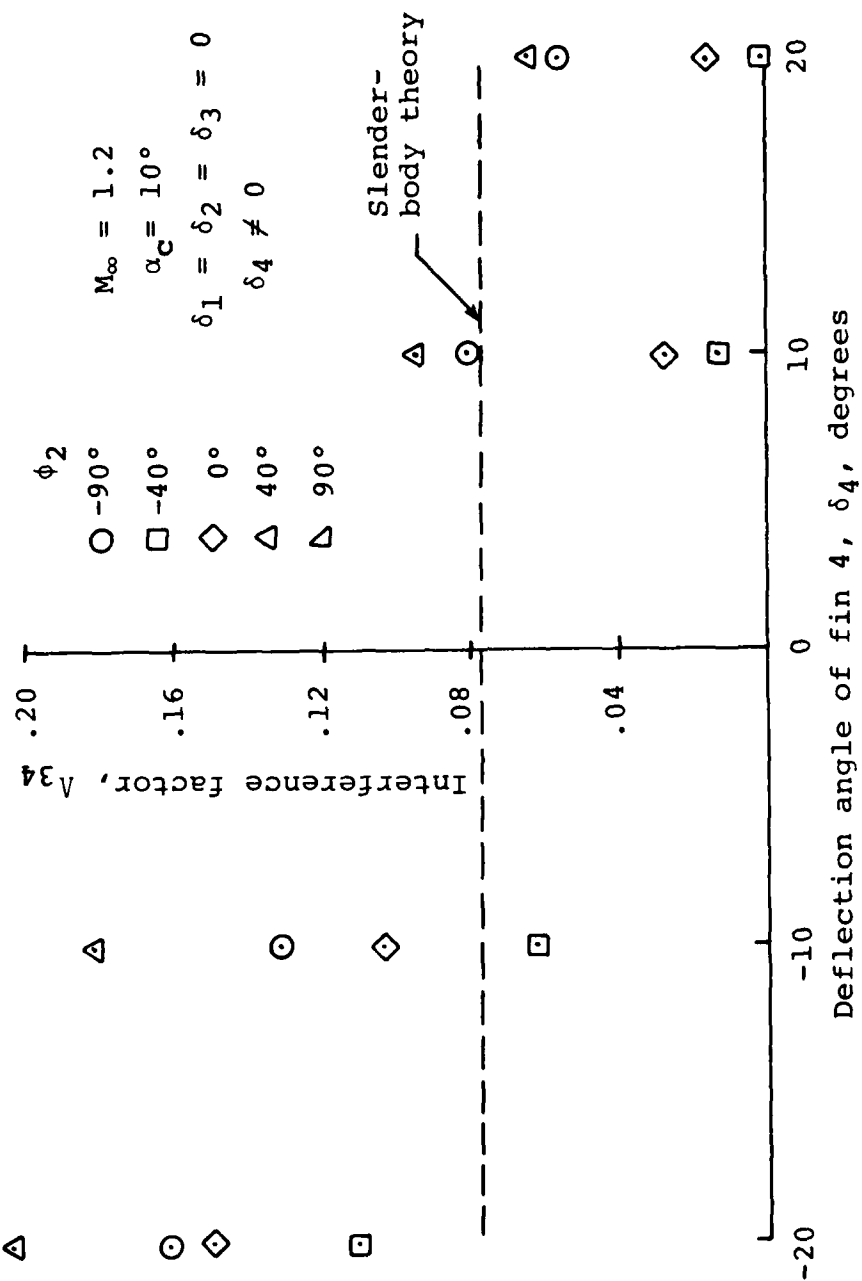
(c) Λ_{34}

Figure 28.- Continued.

156
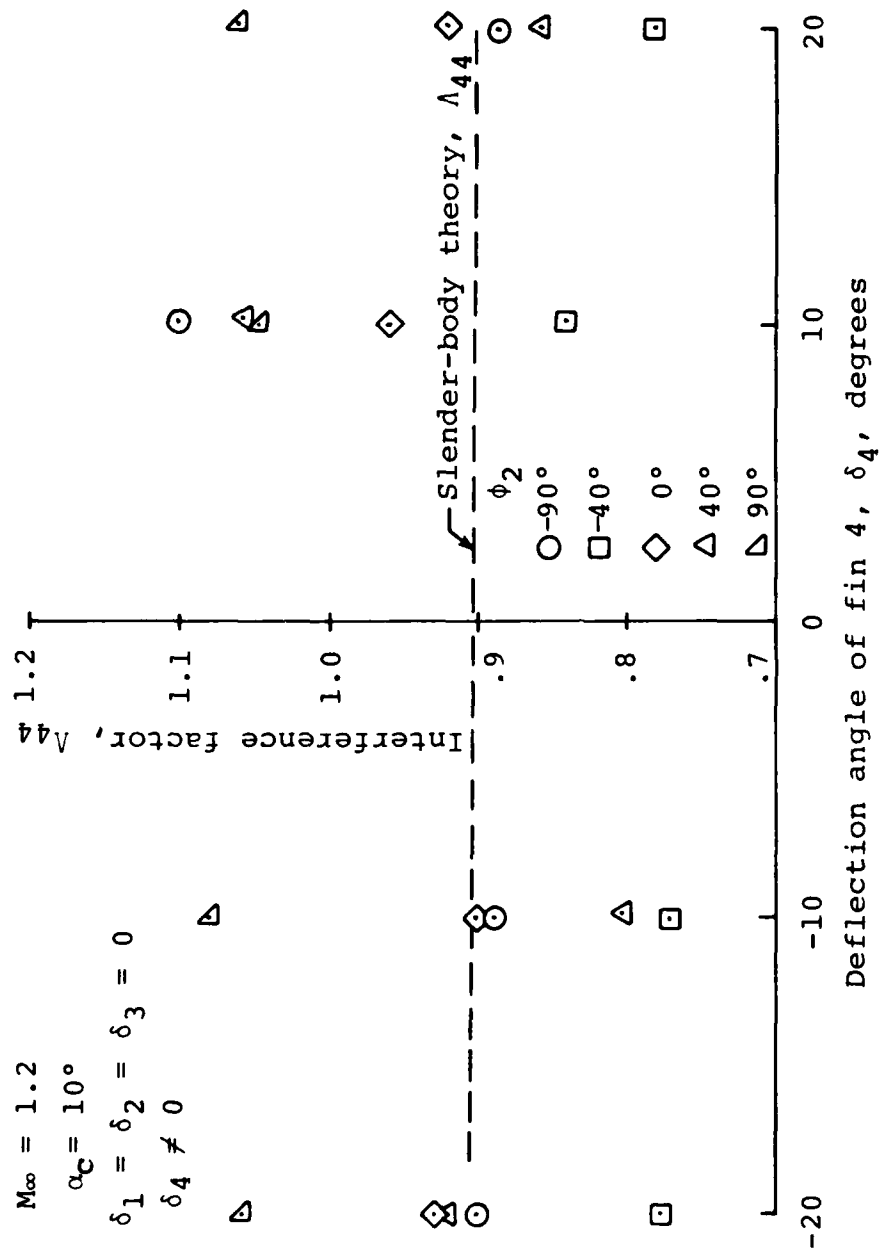
(d) Λ_{44}

Figure 28.- Concluded.

157
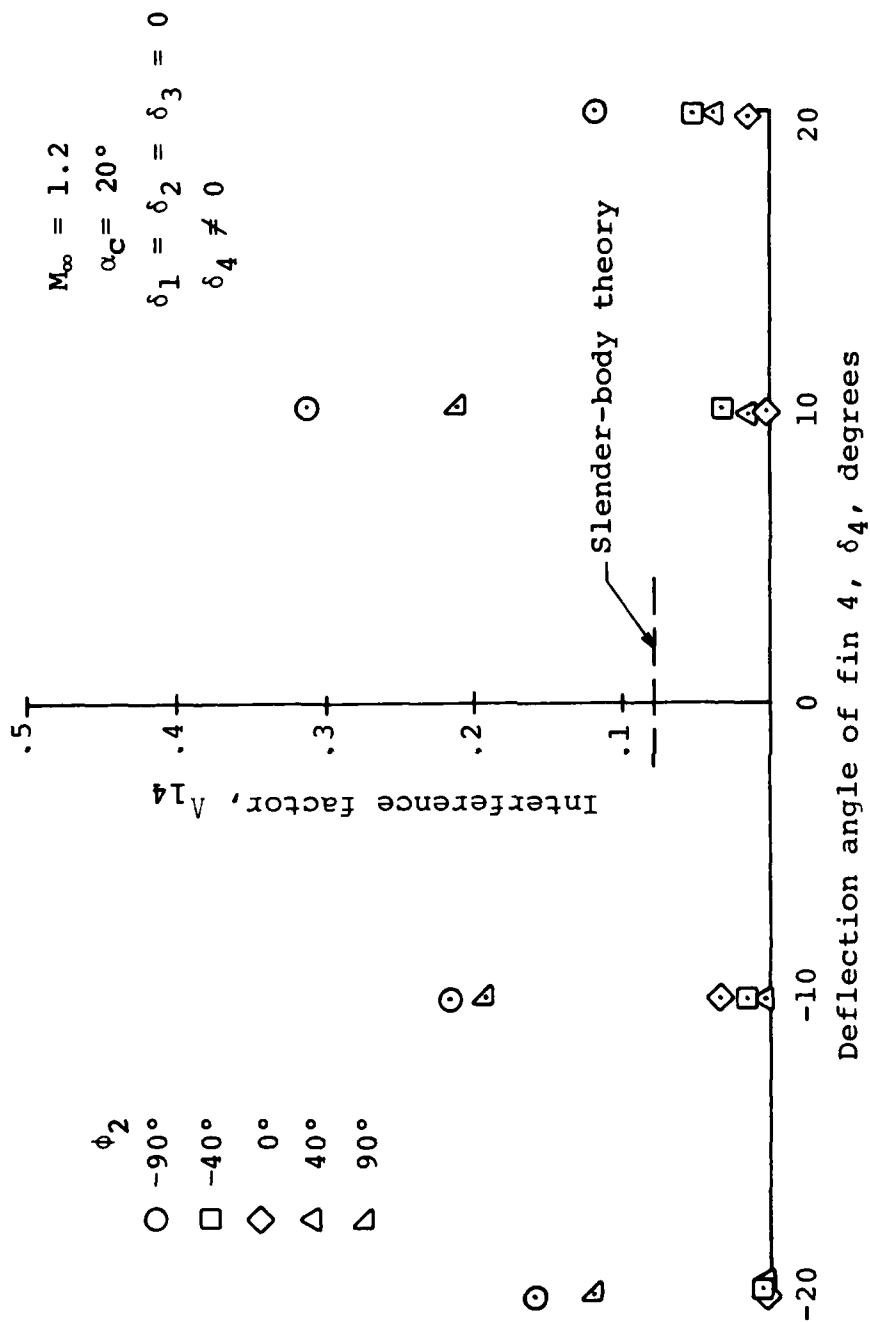
(a) Λ_{14}

Figure 29.- Control interference factor Λ_{ij} for fin 51 mounted on triservice missile; $M_\infty = 1.2$, $\alpha_c = 20°$.
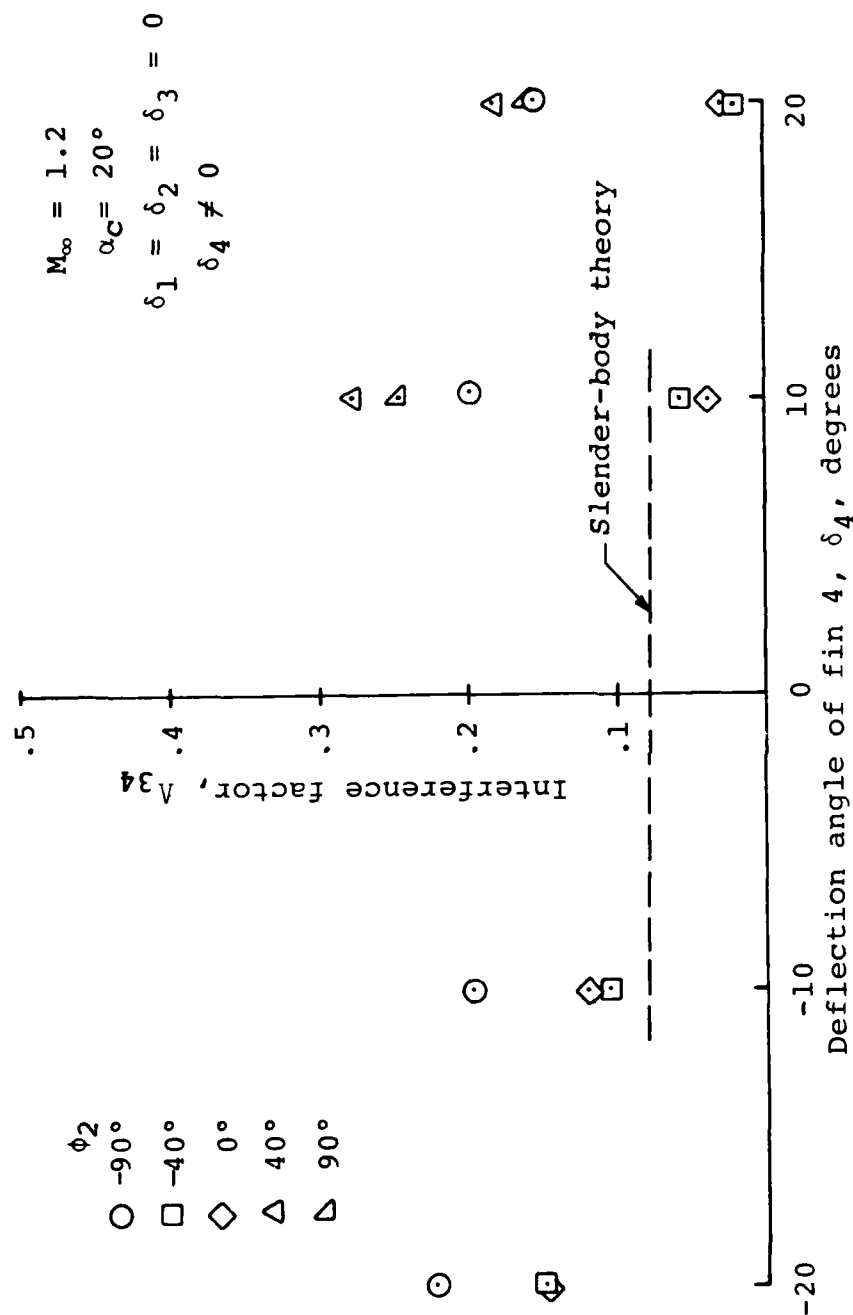
(b) Λ_{34}

Figure 29.- Continued.

159
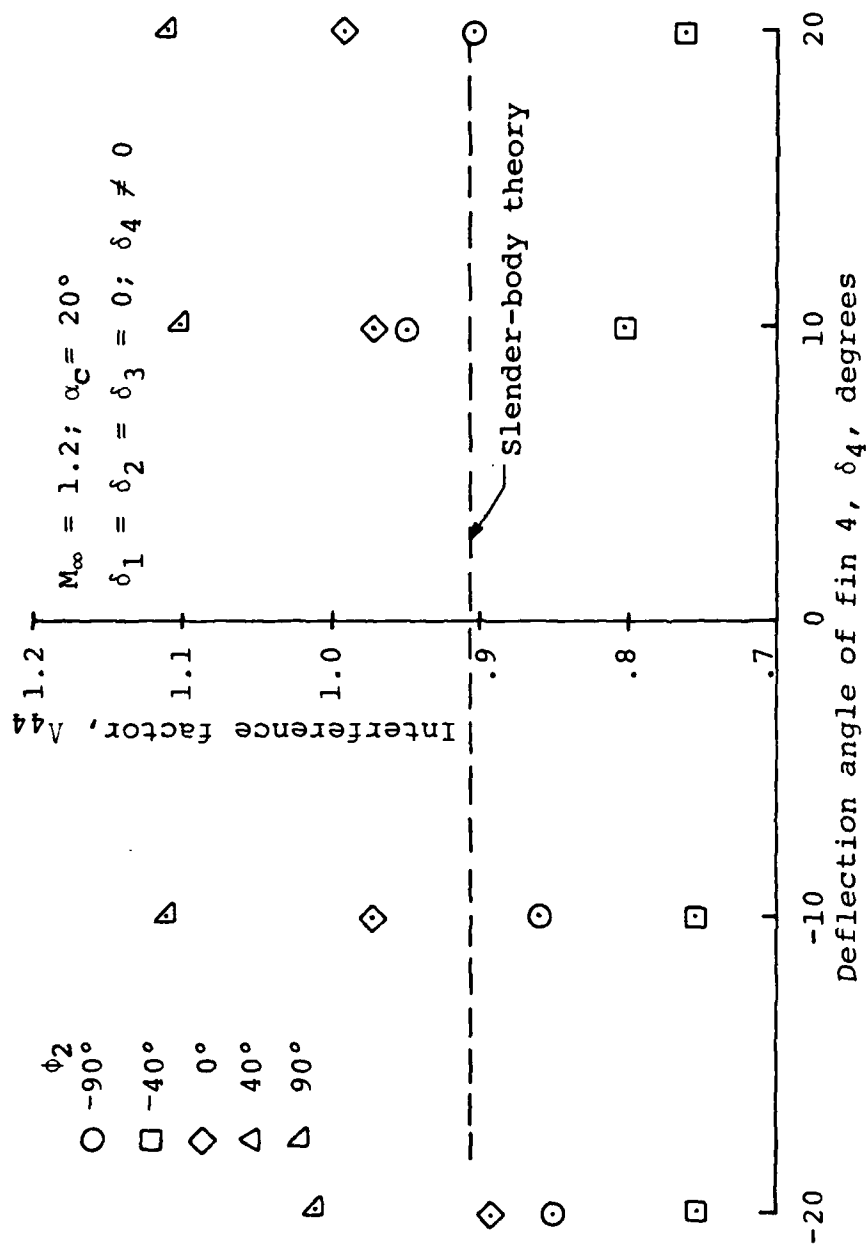
(c) Λ_{44}

Figure 29.- Concluded.
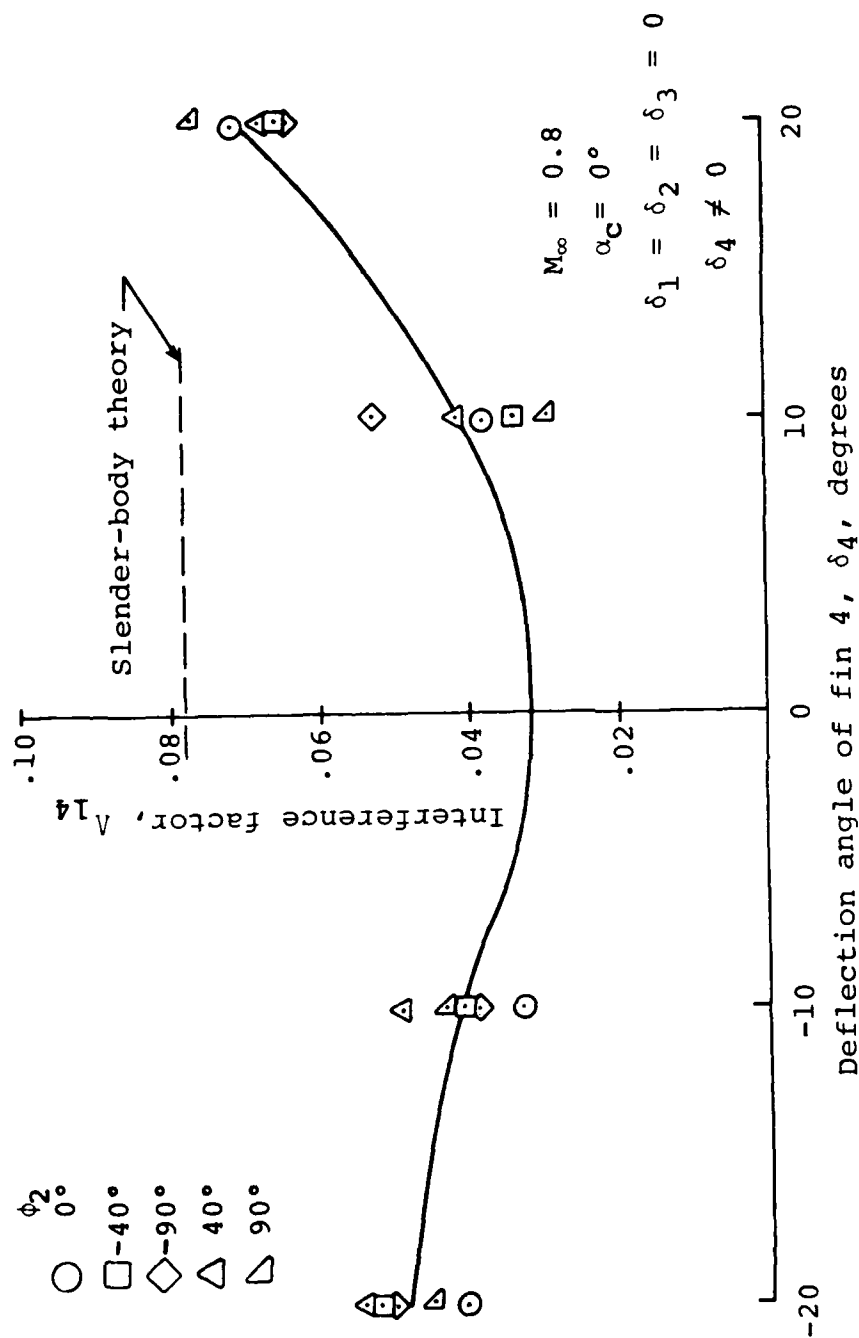
Figure 30.- Control interference factor Λ_{ij} for fin 51 mounted on triservice missile; $M_\infty = 0.8$, $\alpha_c = 0°$.

(a) Λ_{14}

161
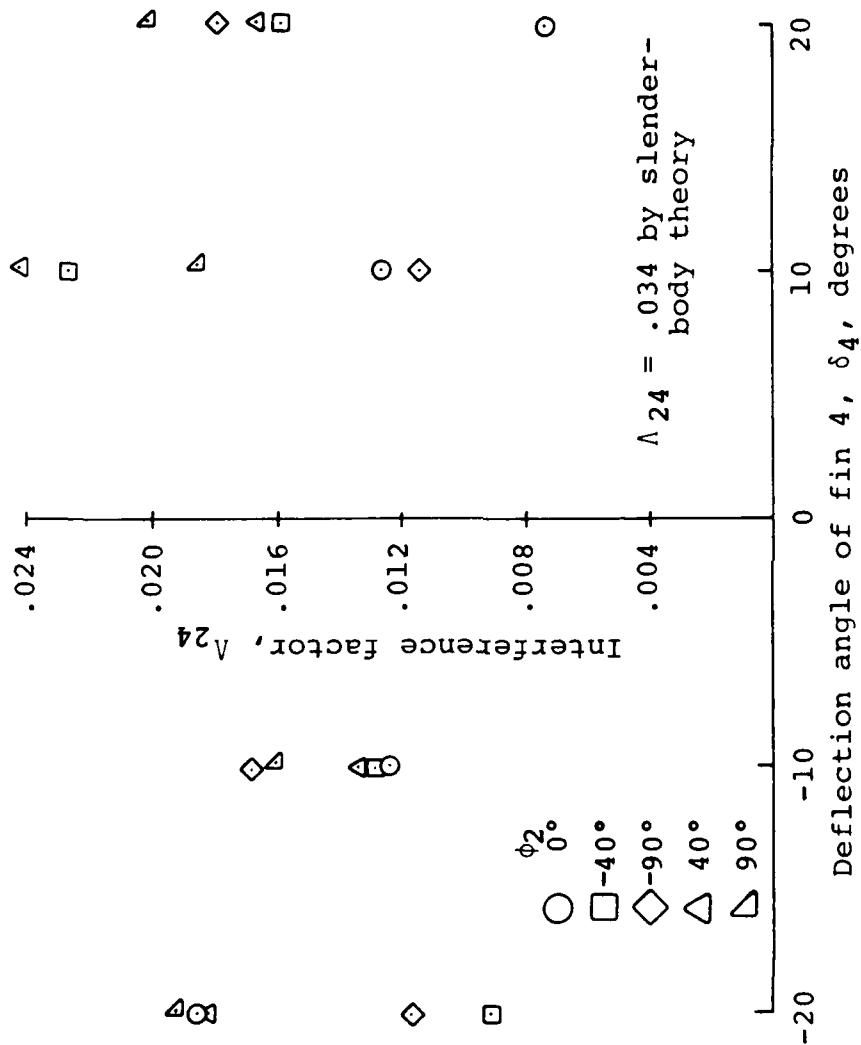
(b) Λ_{24}

Figure 30.- Continued.

162
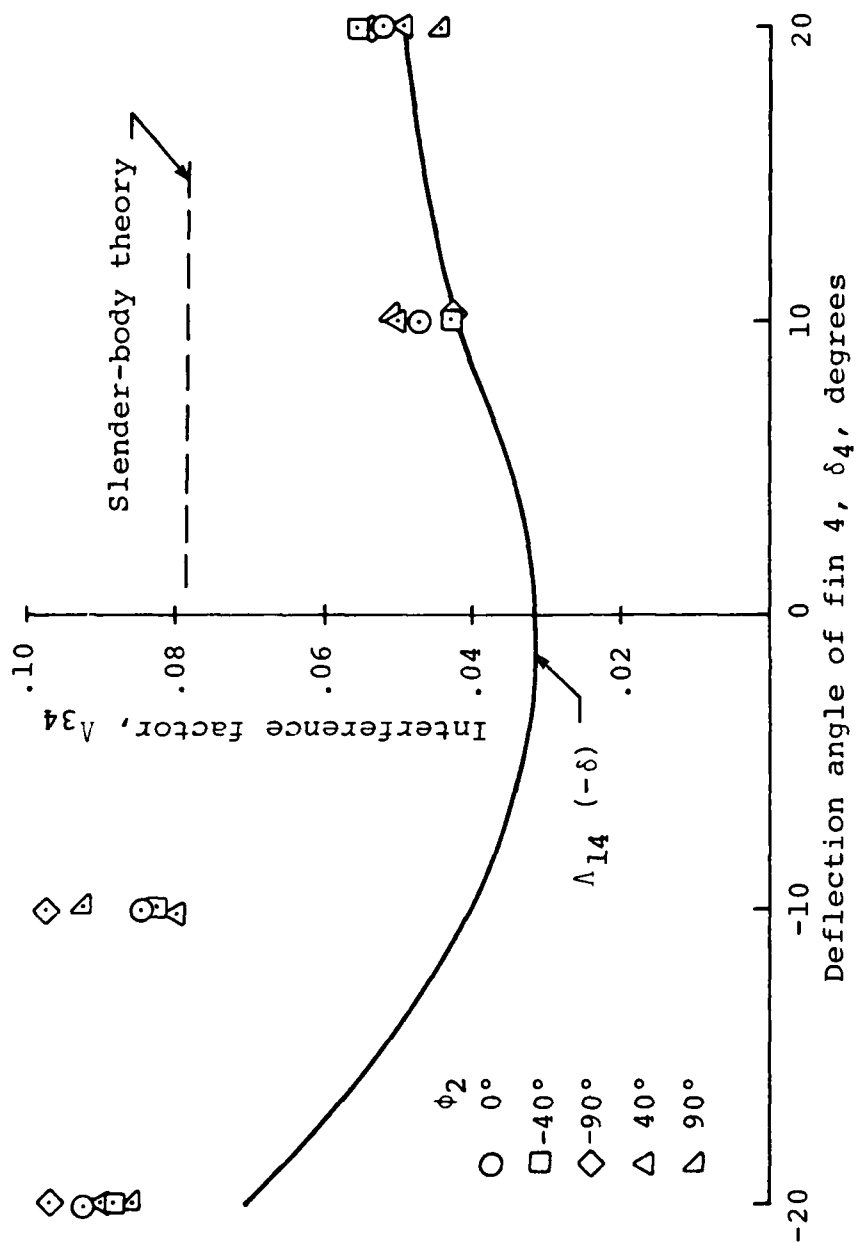
(c) Λ_{34}

Figure 30.- Continued.

163
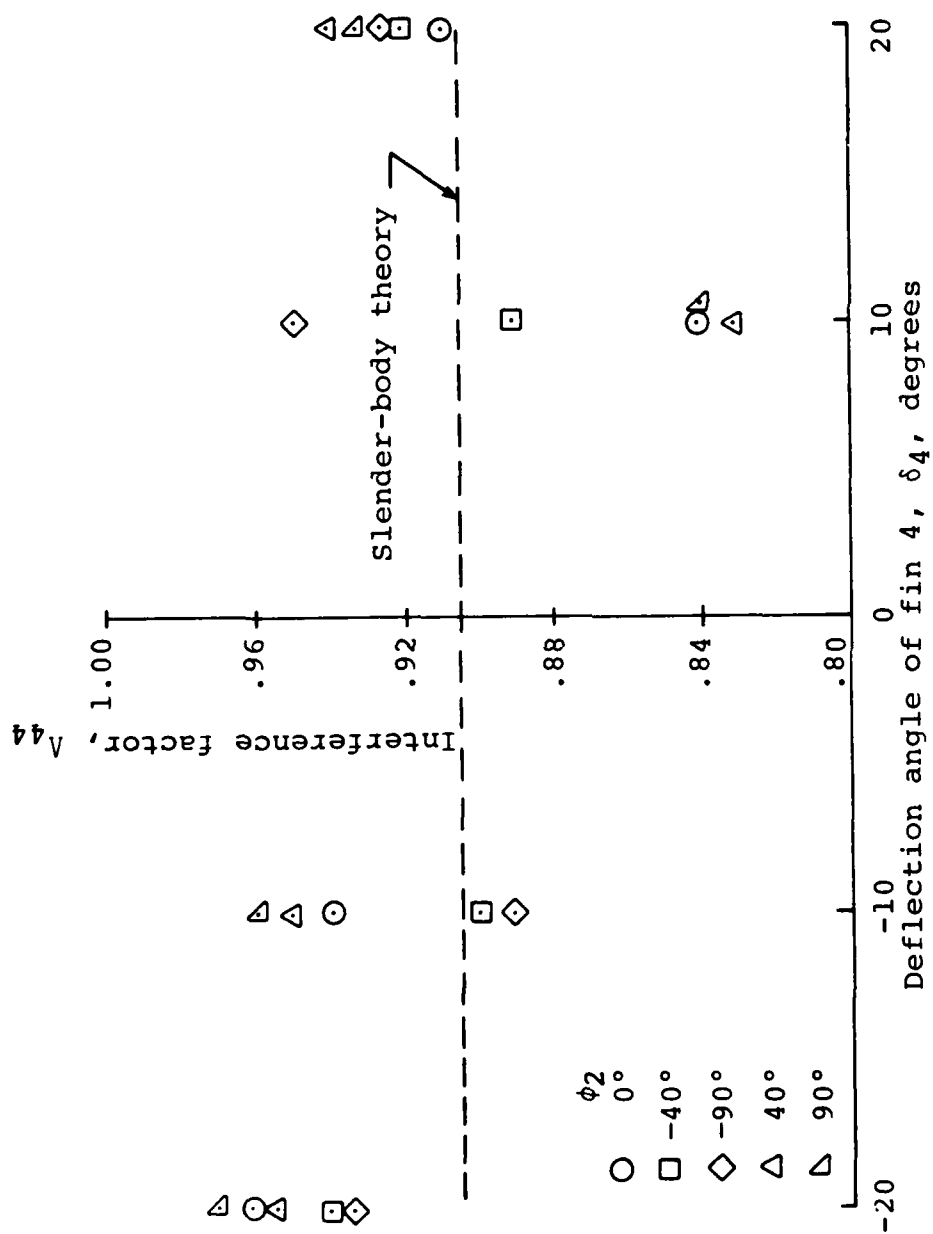
(d) Λ_{44}

Figure 30.- Concluded.
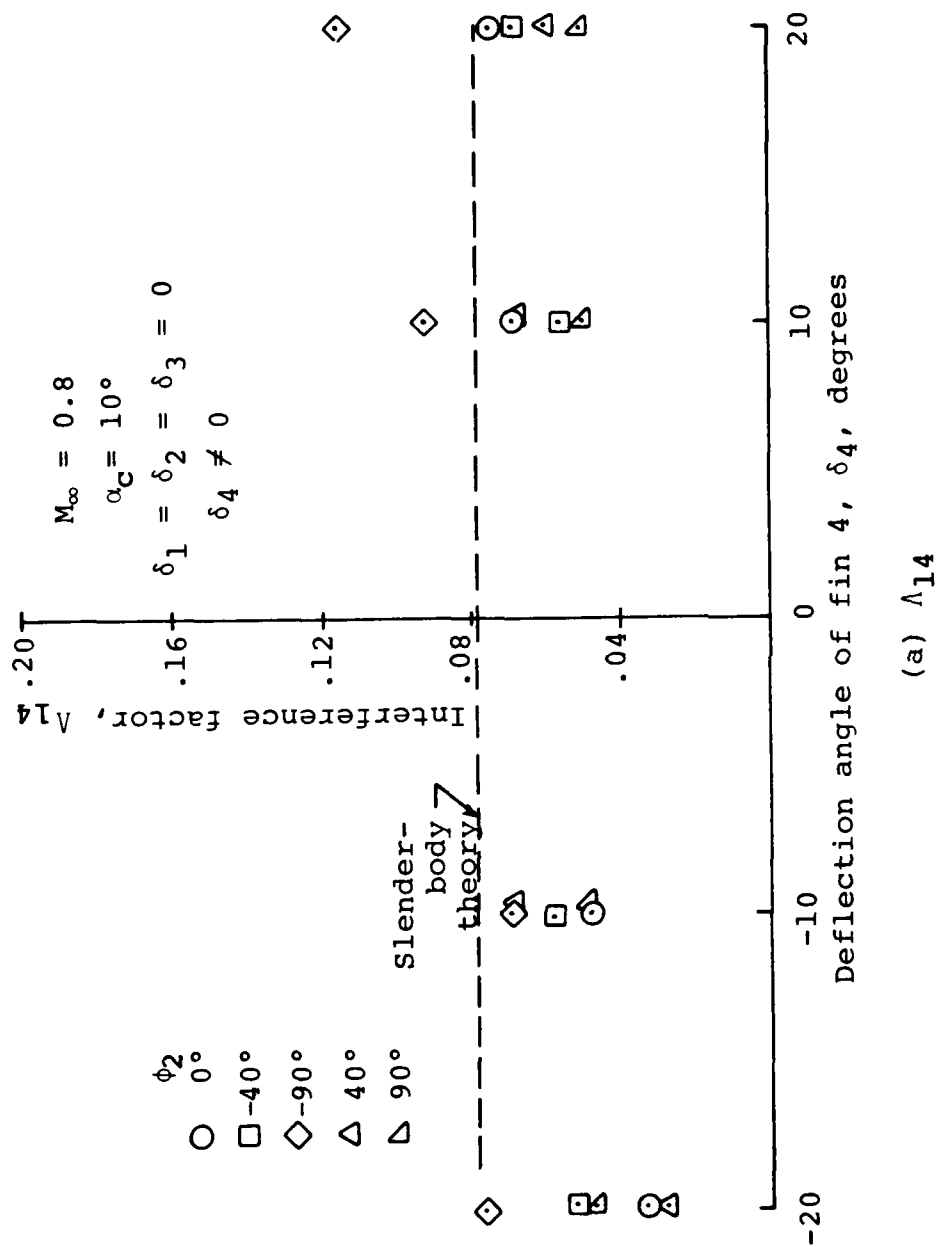
Figure 31.- Control interference factor Λ_{ij} for fin 51 mounted on triservice missile; $M_\infty = 0.8$, $\alpha_c = 10°$.

(a) Λ_{14}
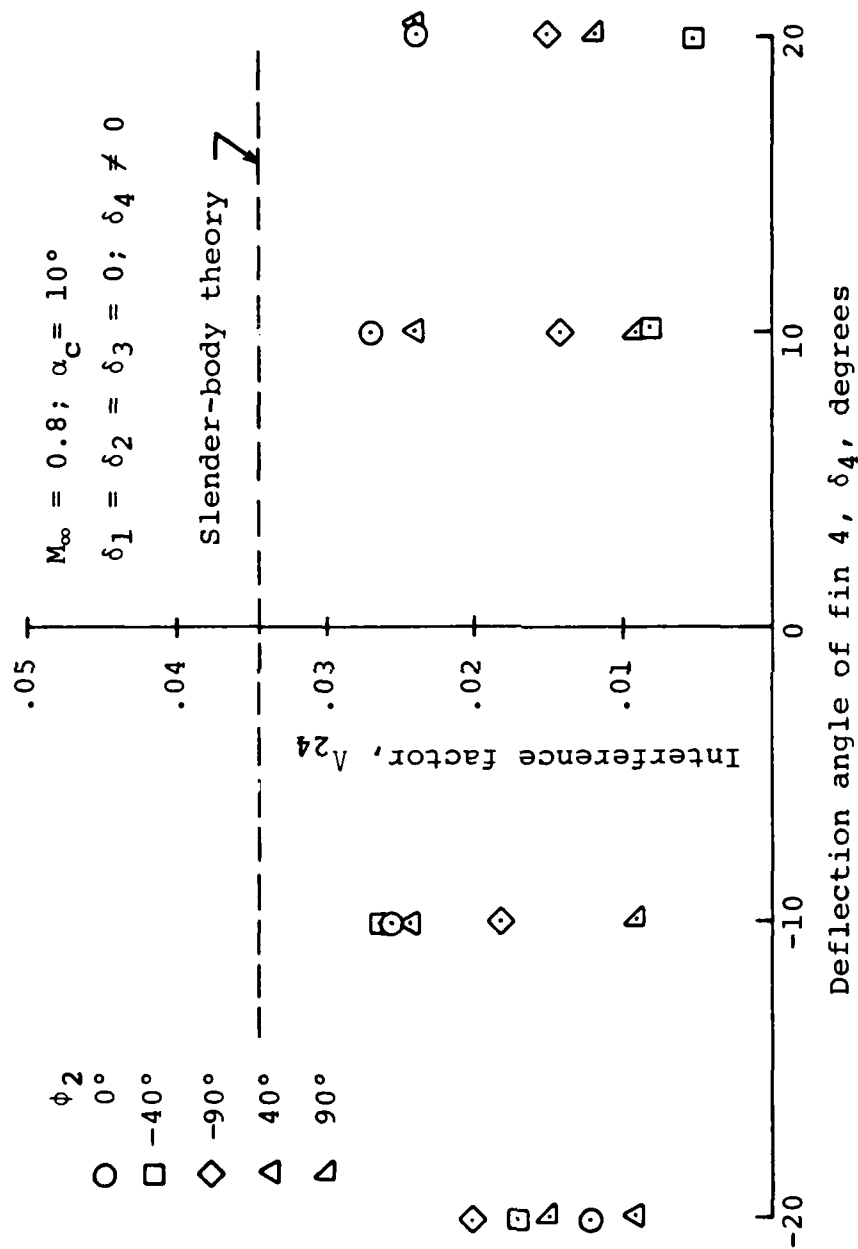
(b) Λ_{24}

Figure 31.- Continued.

166
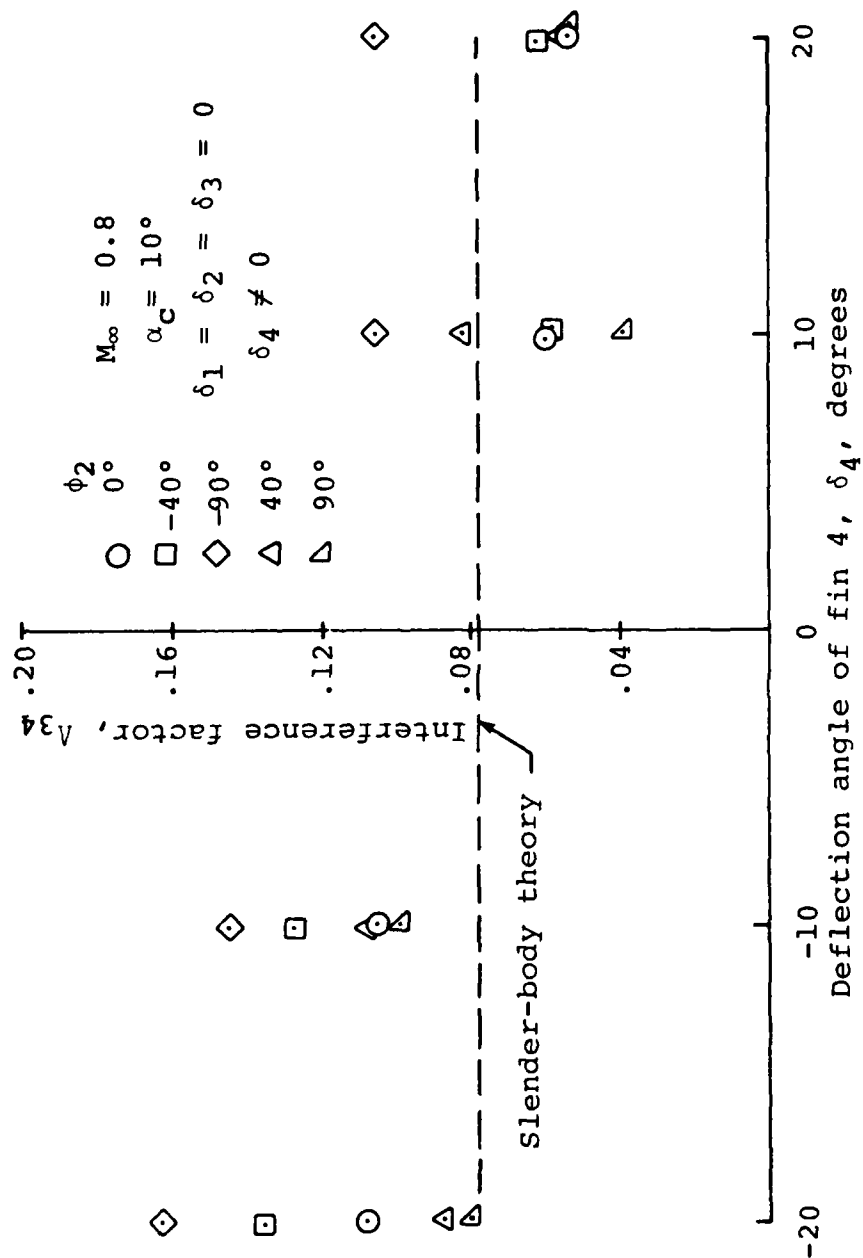
(c) Λ_{34}

Figure 31.- Continued.
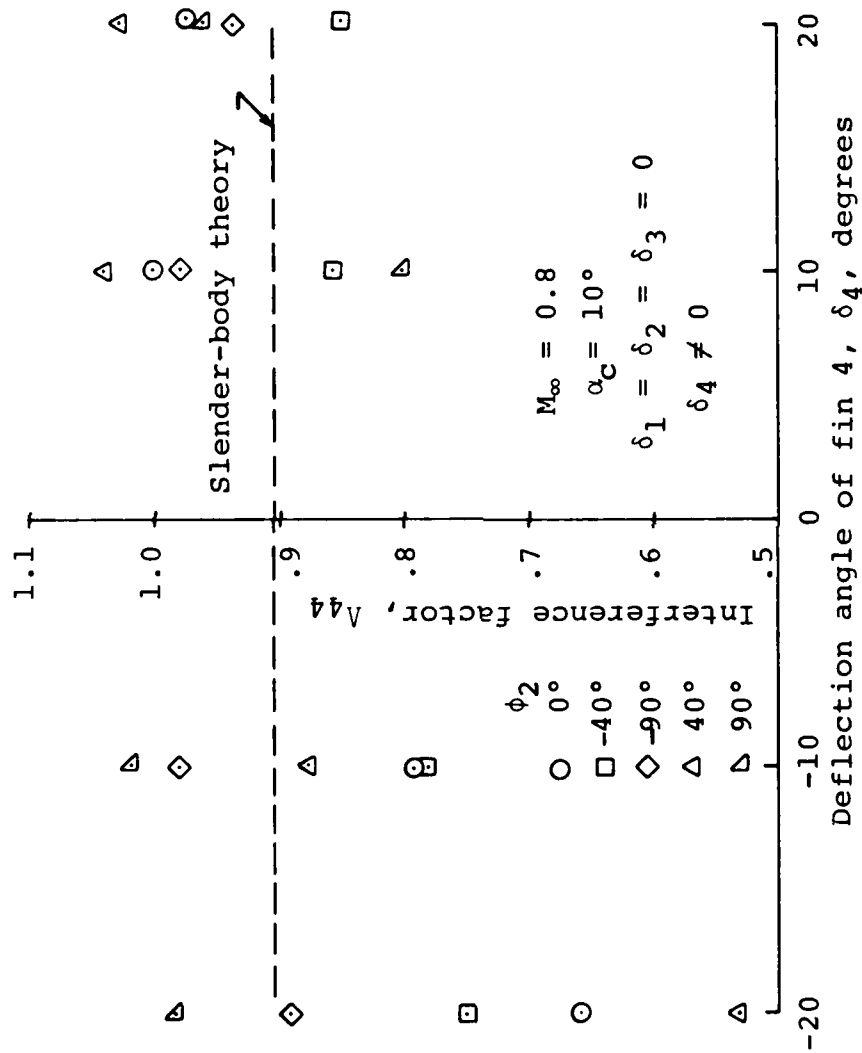
(d) $\Lambda_{44} = 0$

Figure 31.- Concluded.

168
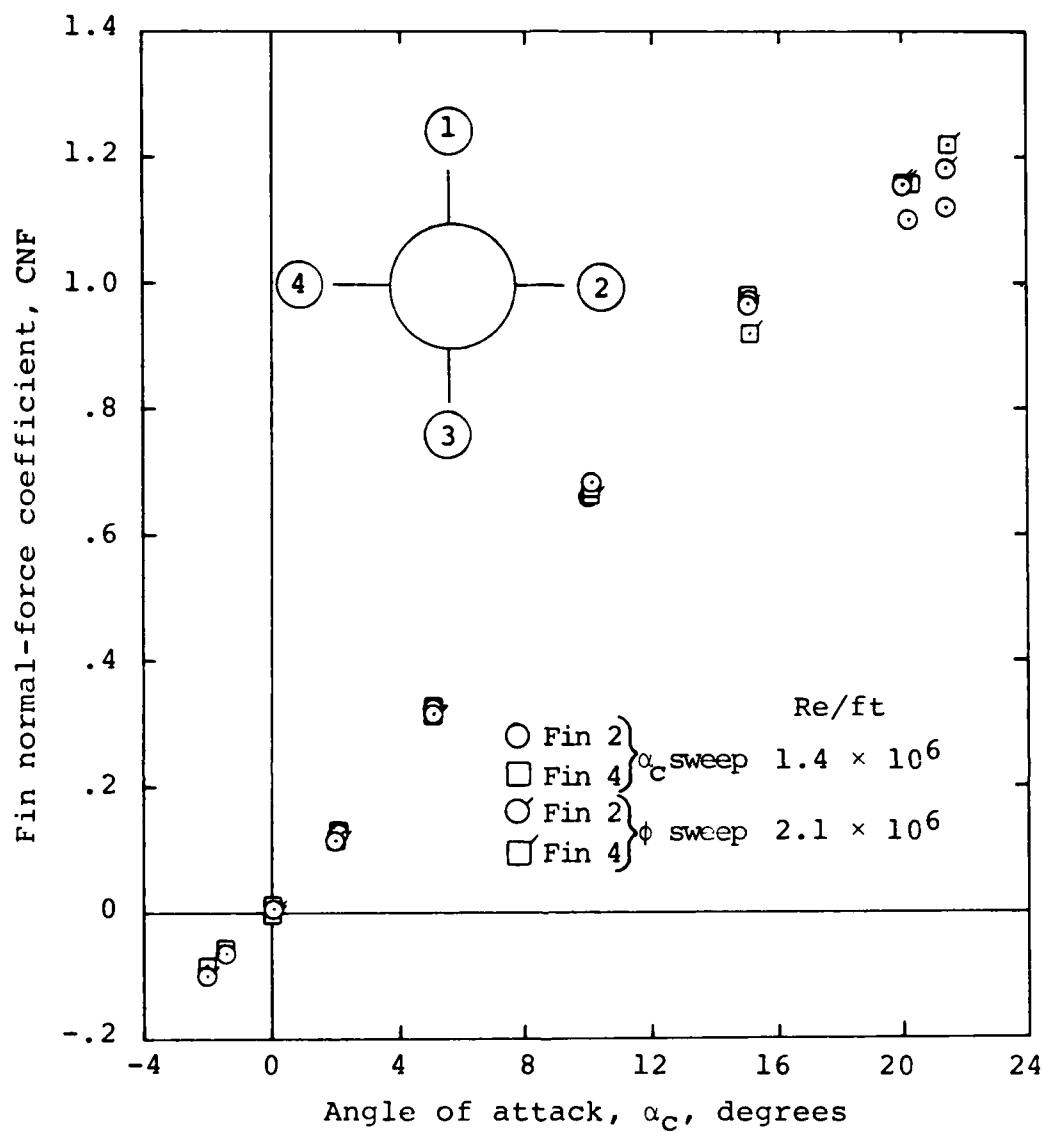
(a) $M_\infty = 0.8$

Figure 32.- Normal force acting on fin T51; $\phi = 0°$,
$\text{Æ} = 2.0$, $\lambda = 0.0$, $\delta = 0°$.

169
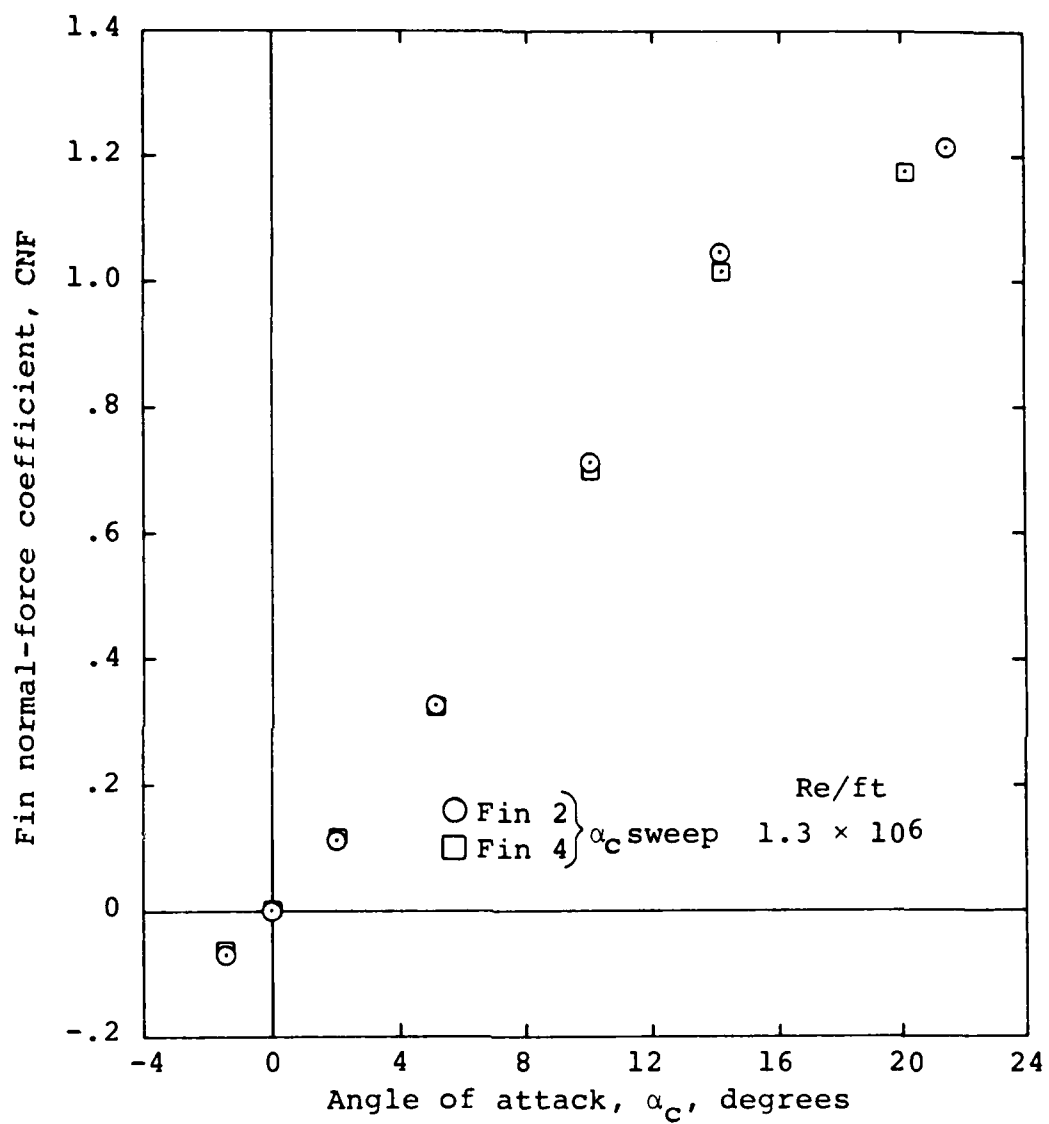
(b) $M_\infty = 0.9$

Figure 32.- Continued.

170
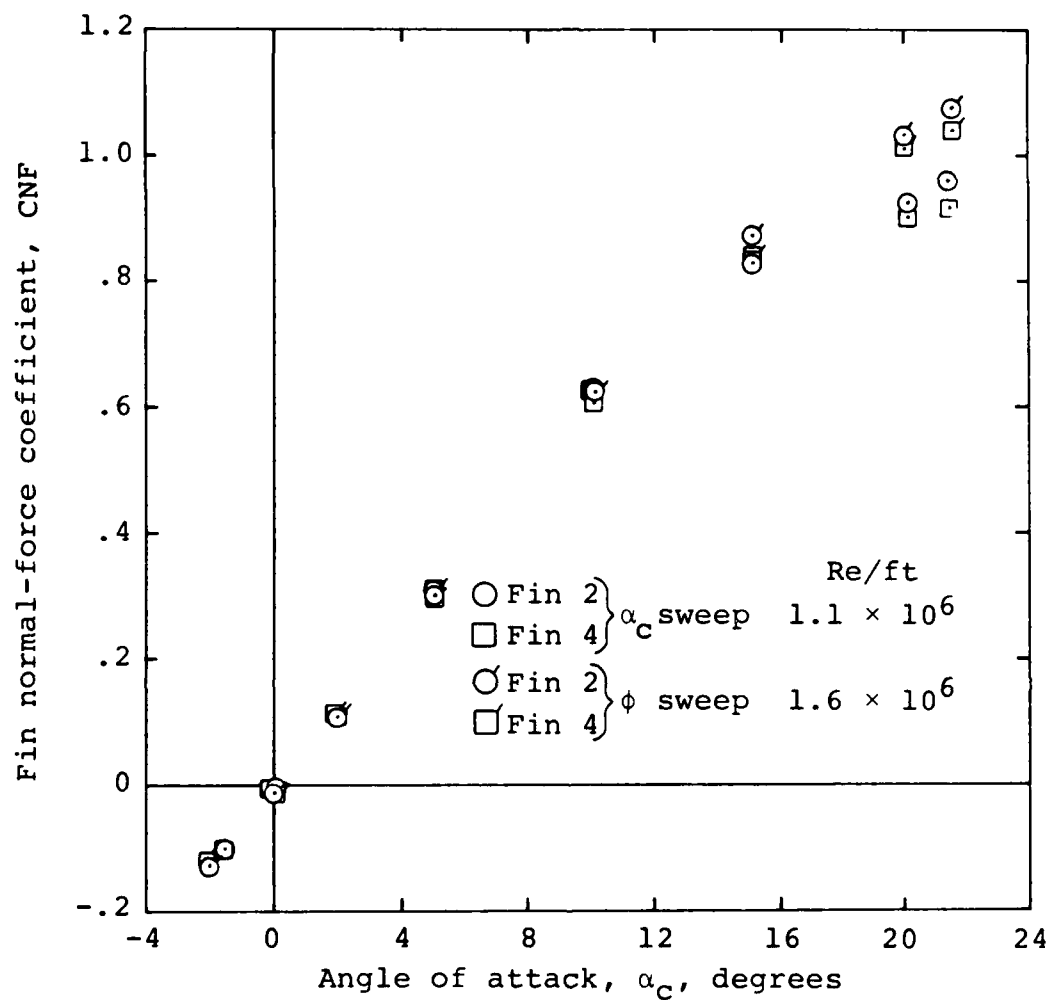
(c) $M_\infty = 1.2$

Figure 32.- Concluded.

171
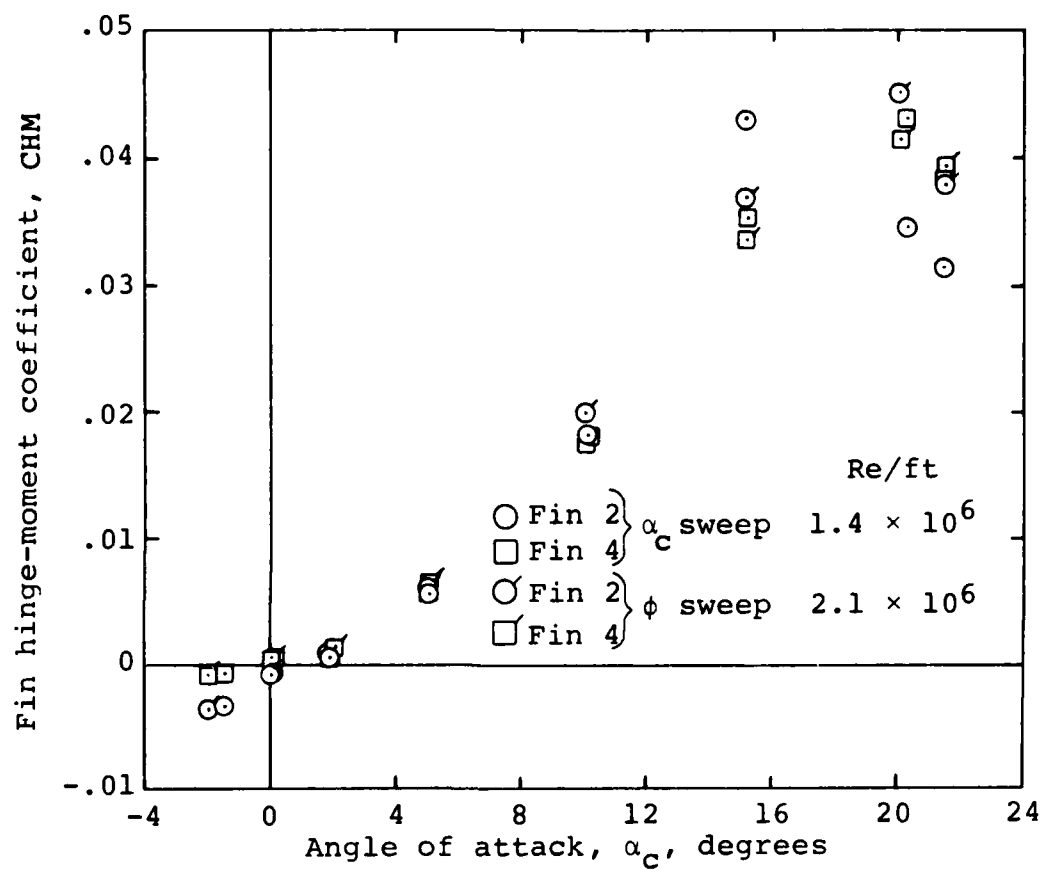
(a) $M_\infty = 0.8$

Figure 33.- Hinge moment acting on tail 51;
$\phi = 0°$, $\text{Æ} = 2.0$, $\lambda = 0.0$, $\delta = 0°$.

172
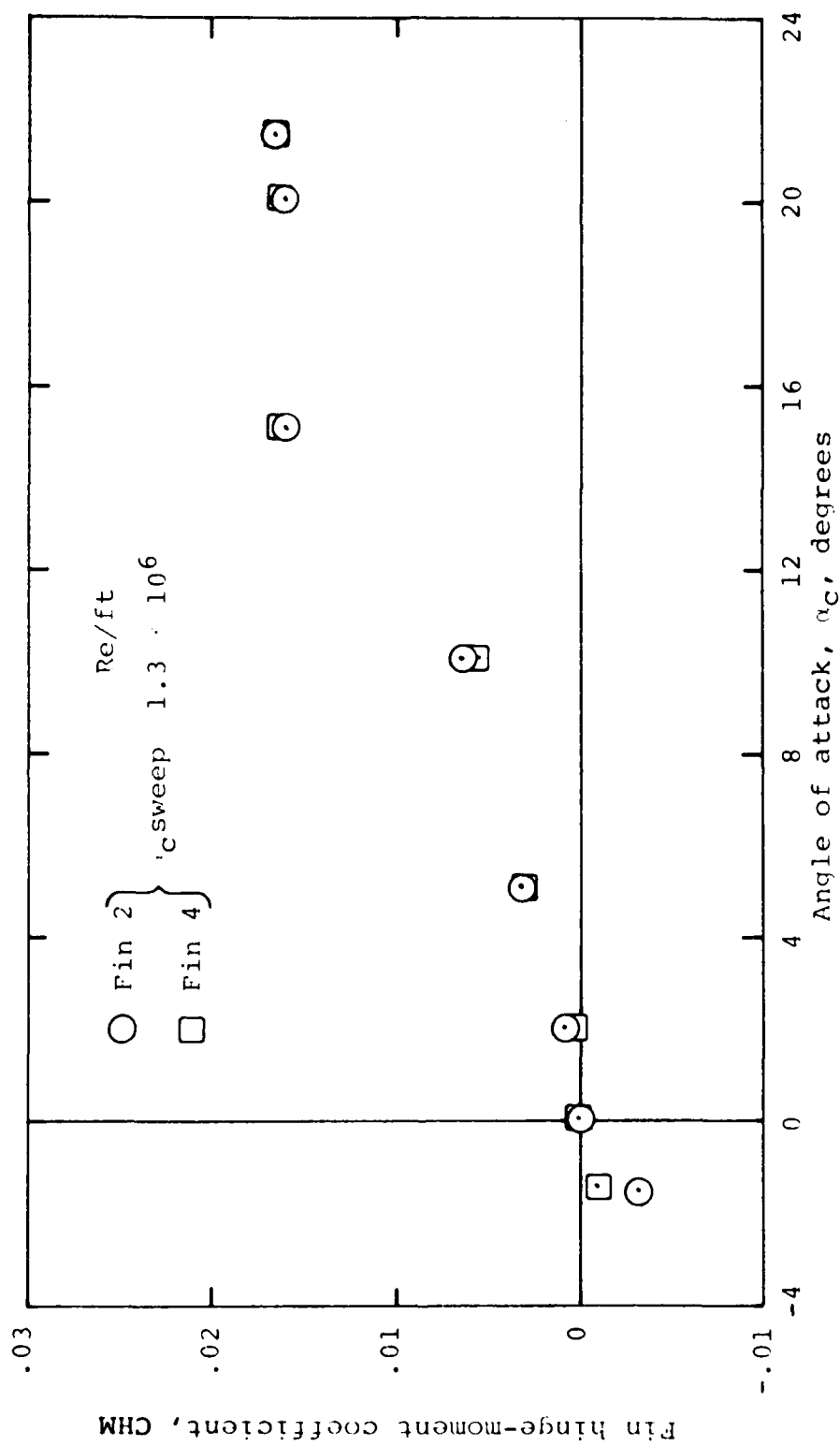
(b) M. = 0.9

Figure 33.- Continued.

173

Angle of attack, α_c, degrees
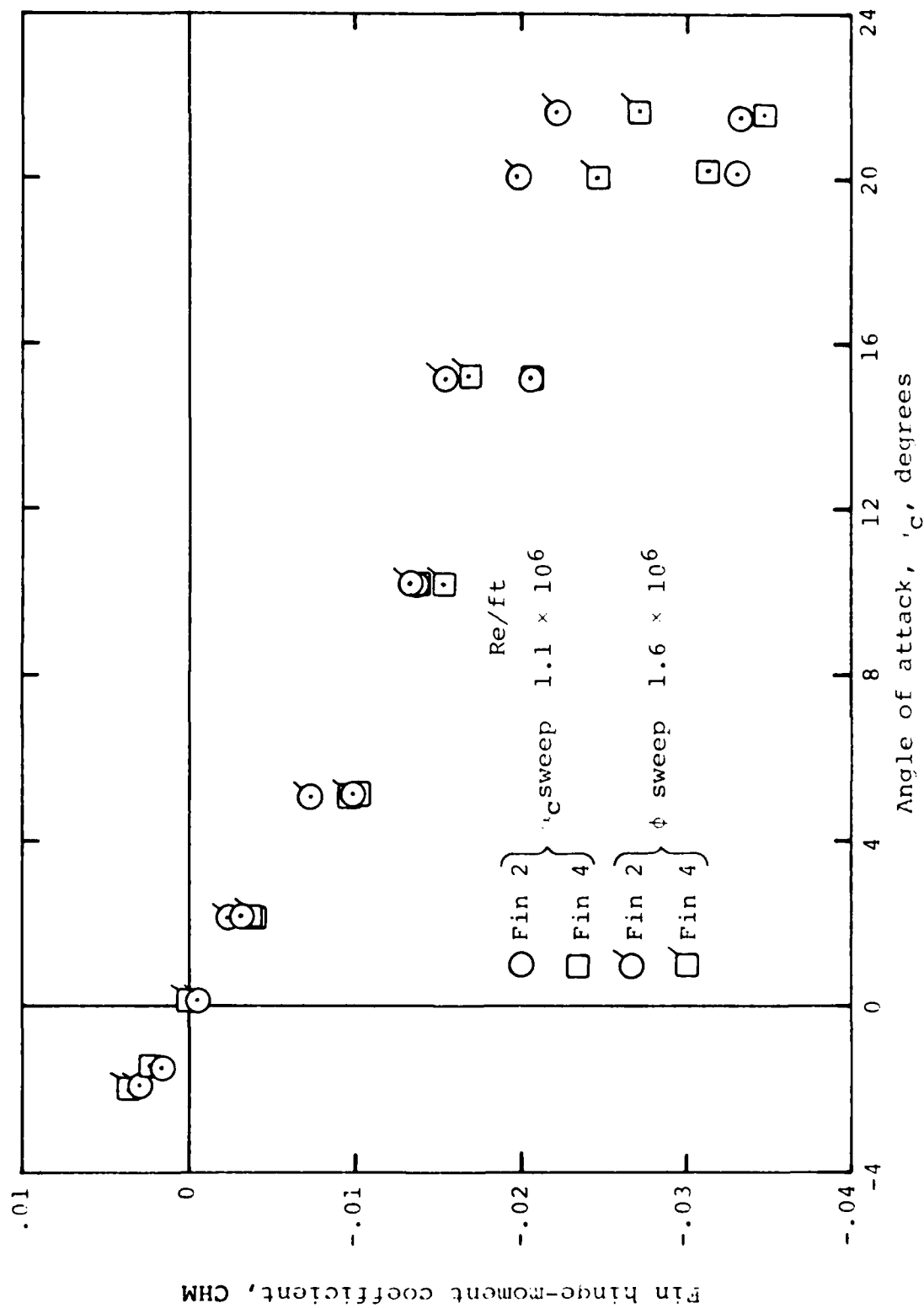
(c) $M_\infty = 1.2$

Figure 33.- Concluded.

Fin hinge-moment coefficient, CHM

Re/ft

α_c sweep 1.1×10^6

ϕ sweep 1.6×10^6

○ Fin 2
□ Fin 4
◐ Fin 2
◖ Fin 4
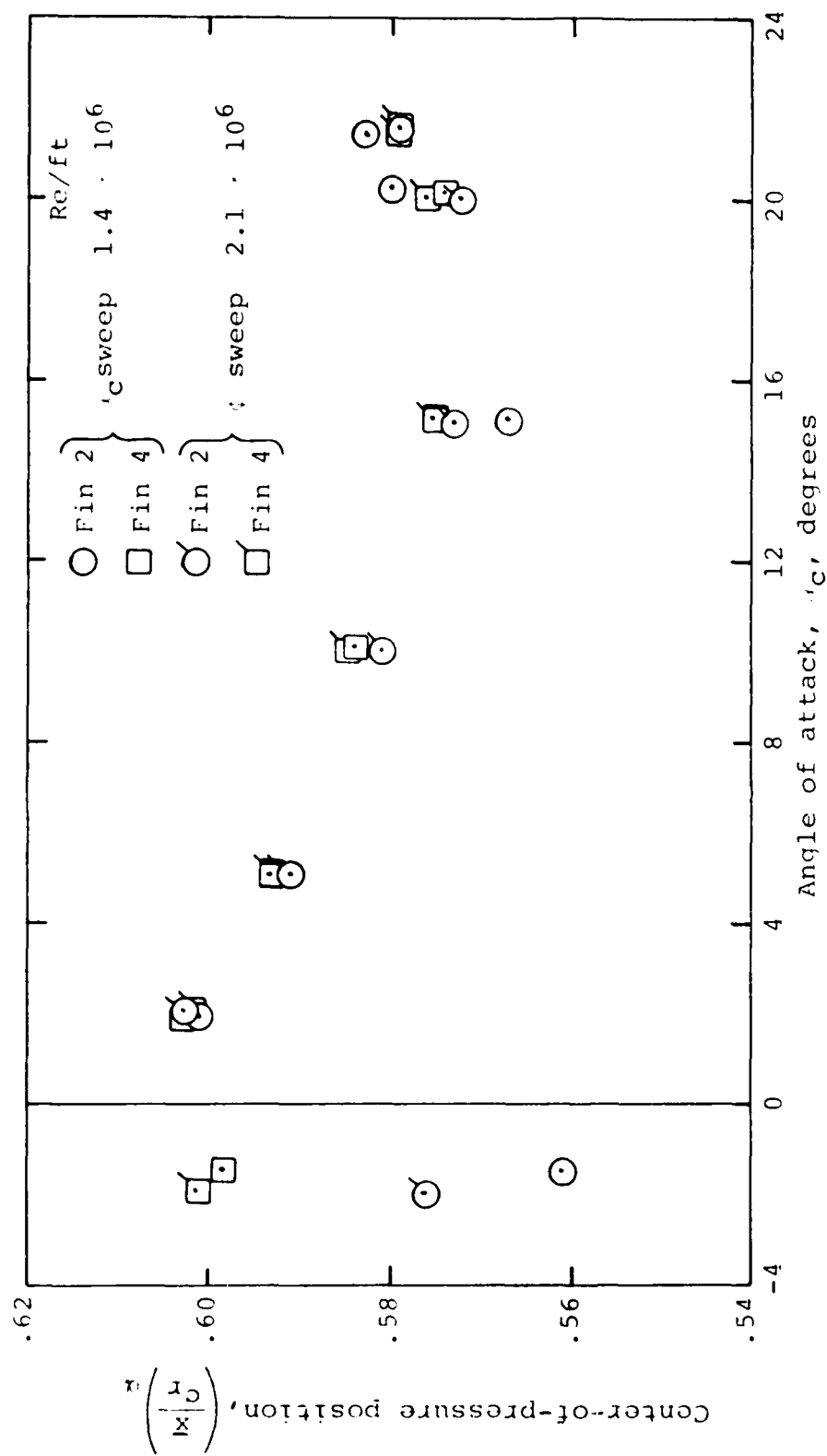
(a) $M_\infty = 0.8$

Figure 34.-- Longitudinal center of pressure of tail 51; $\beta = 0°$, $AR = 2.0$, $\lambda = 0$, $\delta = 0°$.
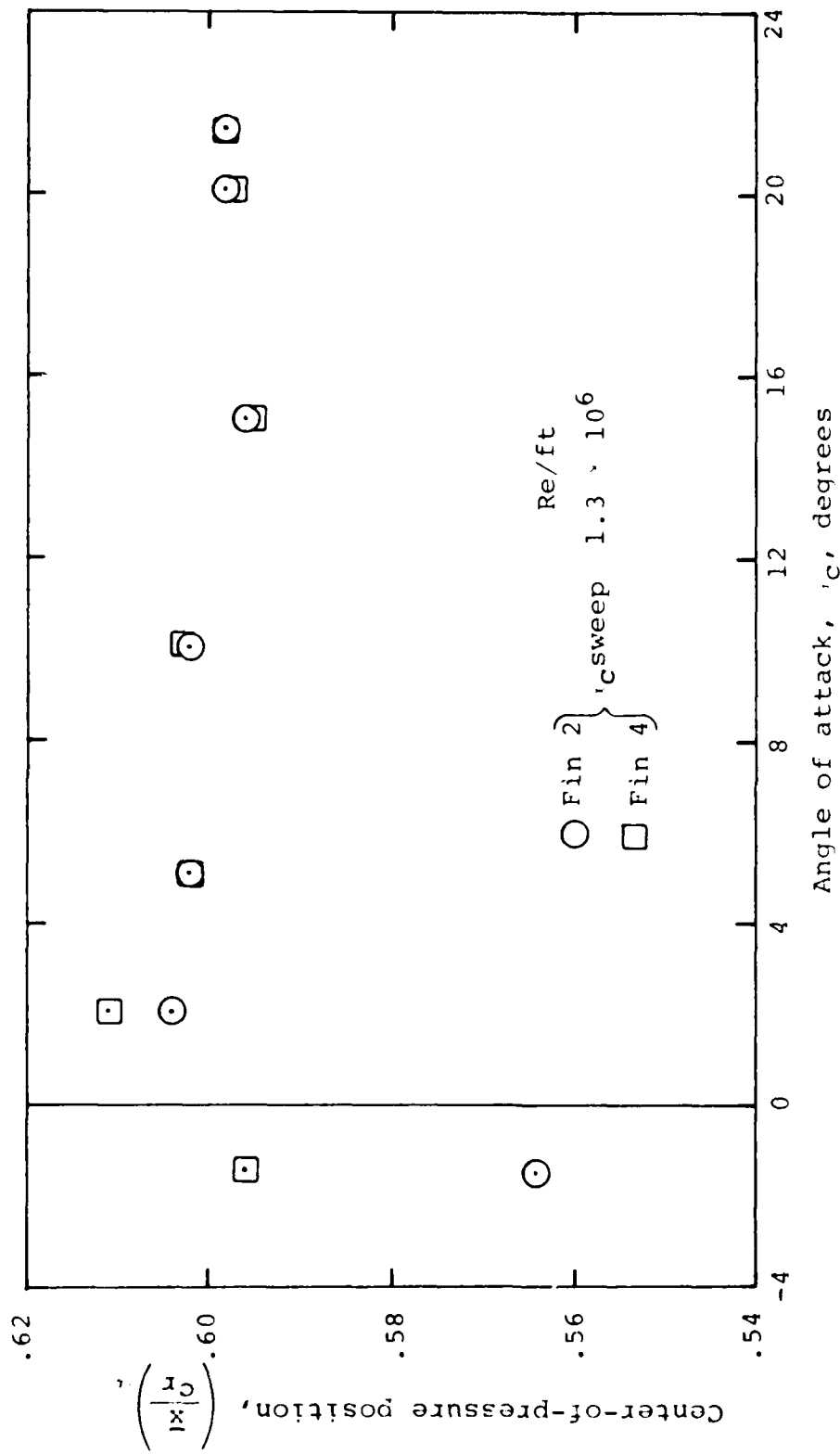
(b) $M_\infty = 0.9$

Figure 34.- Continued.

Re/ft

α_c sweep 1.1×10^6

ϕ sweep 1.6×10^6

○ Fin 2

□ Fin 4

⊘ Fin 2

◲ Fin 4

Angle of attack, α_c, degrees

Center-of-pressure position, $\left(\dfrac{x}{c_r}\right)$,
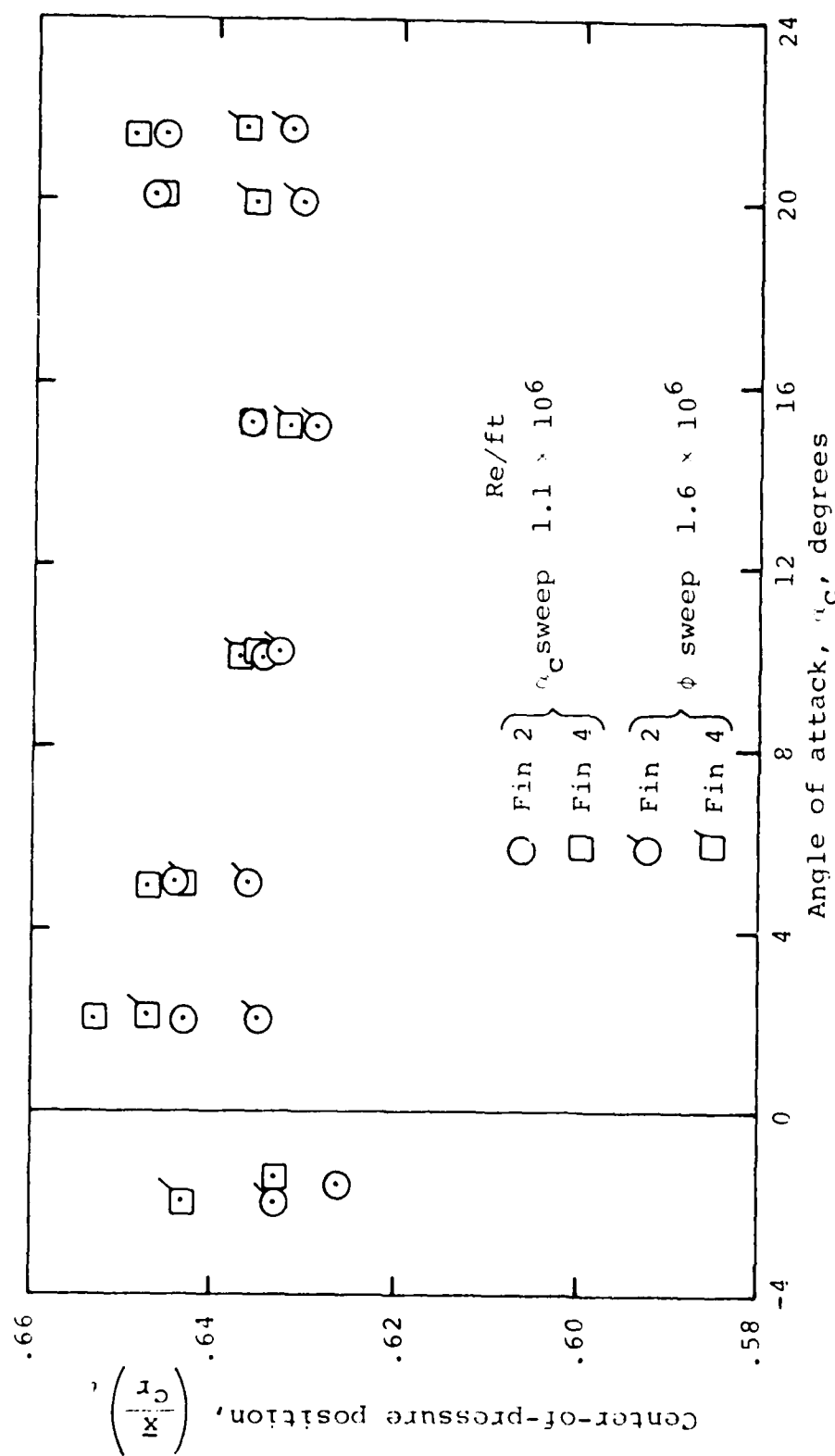
(c) $M_\infty = 1.2$

Figure 34.- Concluded.

177
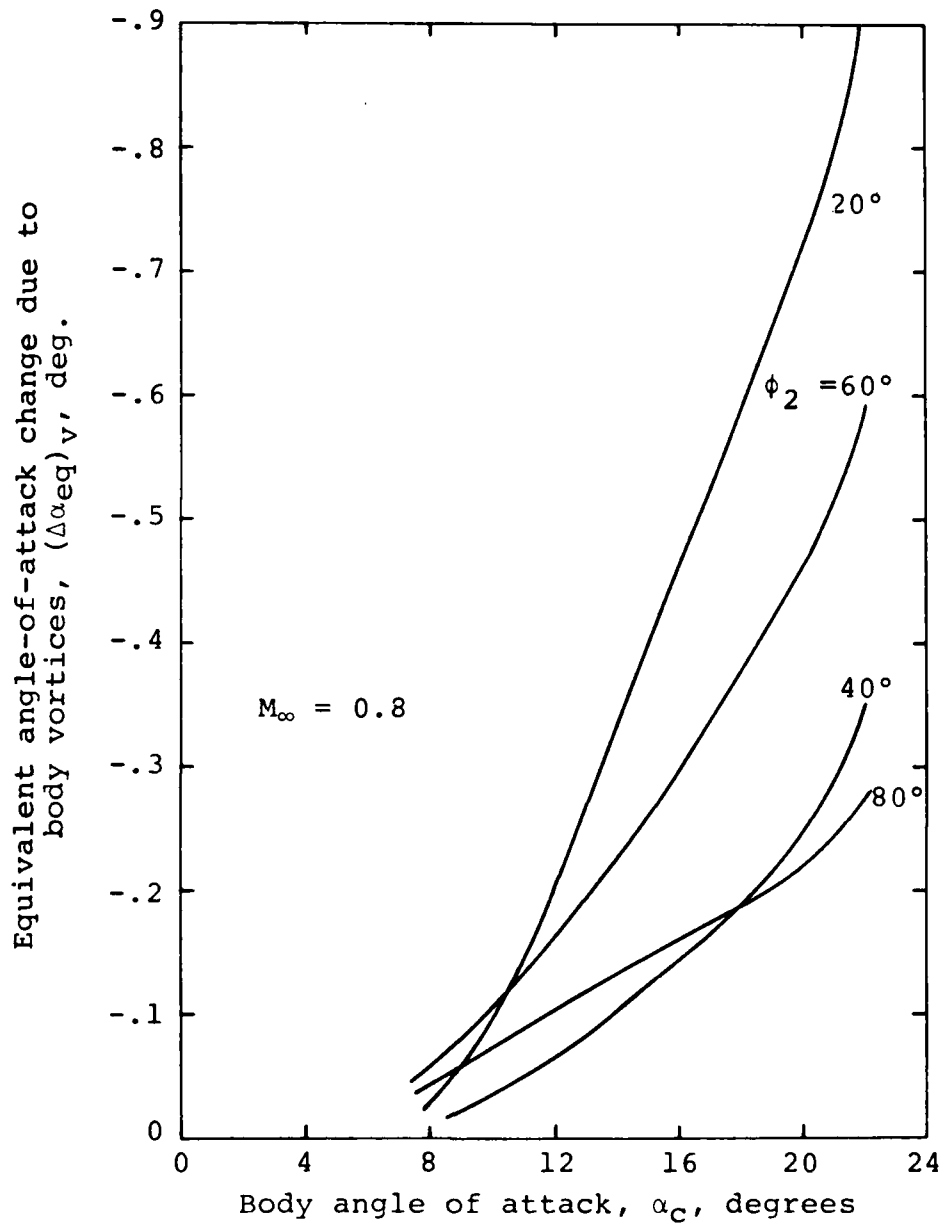
(a) $M_\infty = 0.8$, windward side

Figure 35.- Equivalent angle-of-attack change due
to body vortices at axial position of
fin T51 on triservice missile.

178
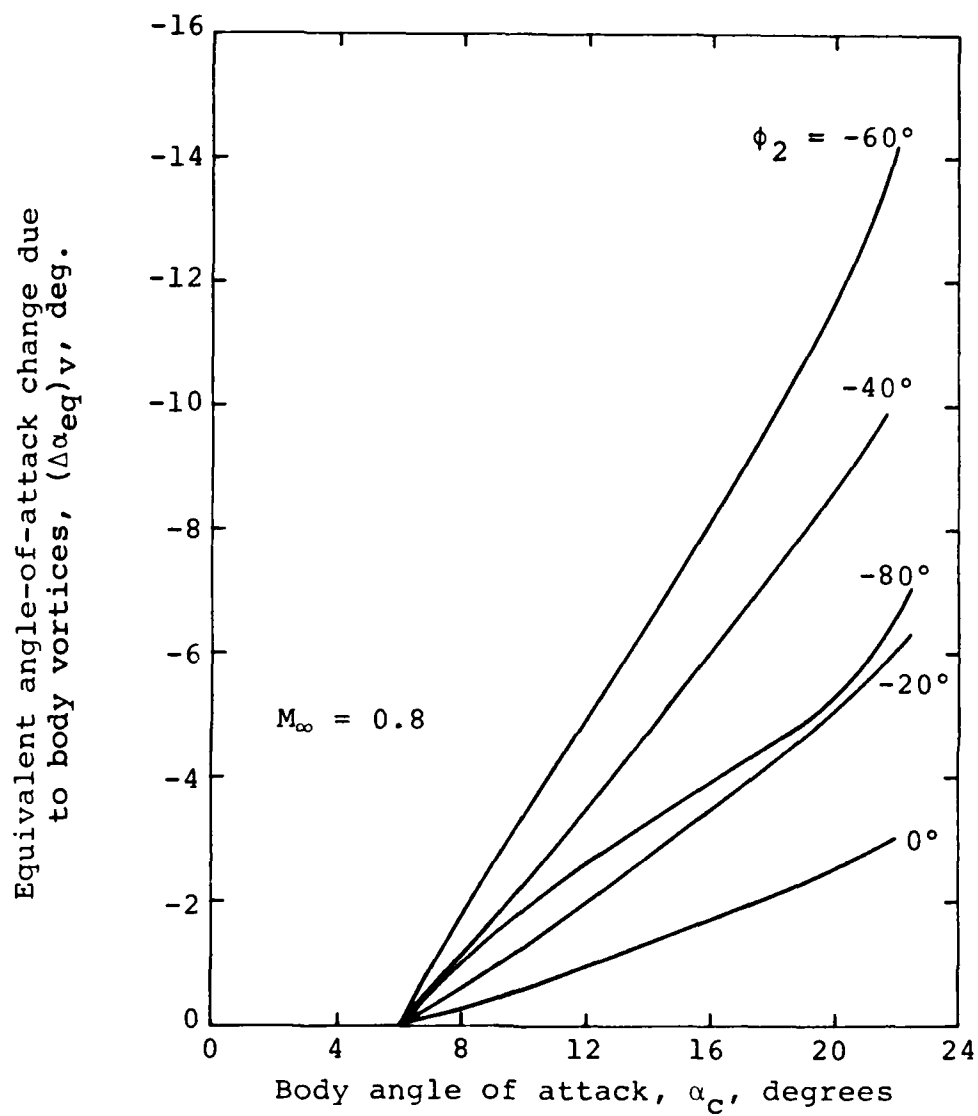
(b) $M_\infty = 0.8$; leeward side

Figure 35.- Continued.
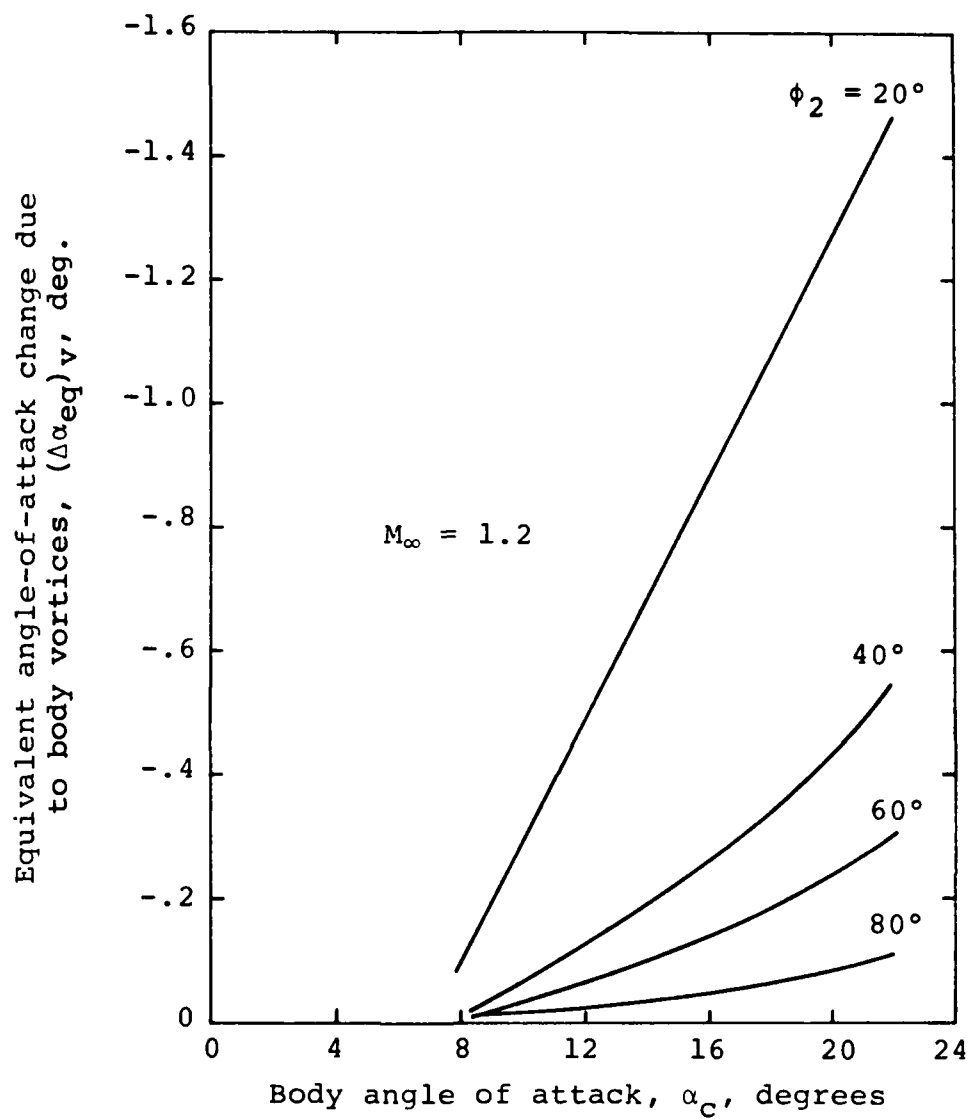
(c) $M_\infty = 1.2$; windward side

Figure 35.- Continued.

180
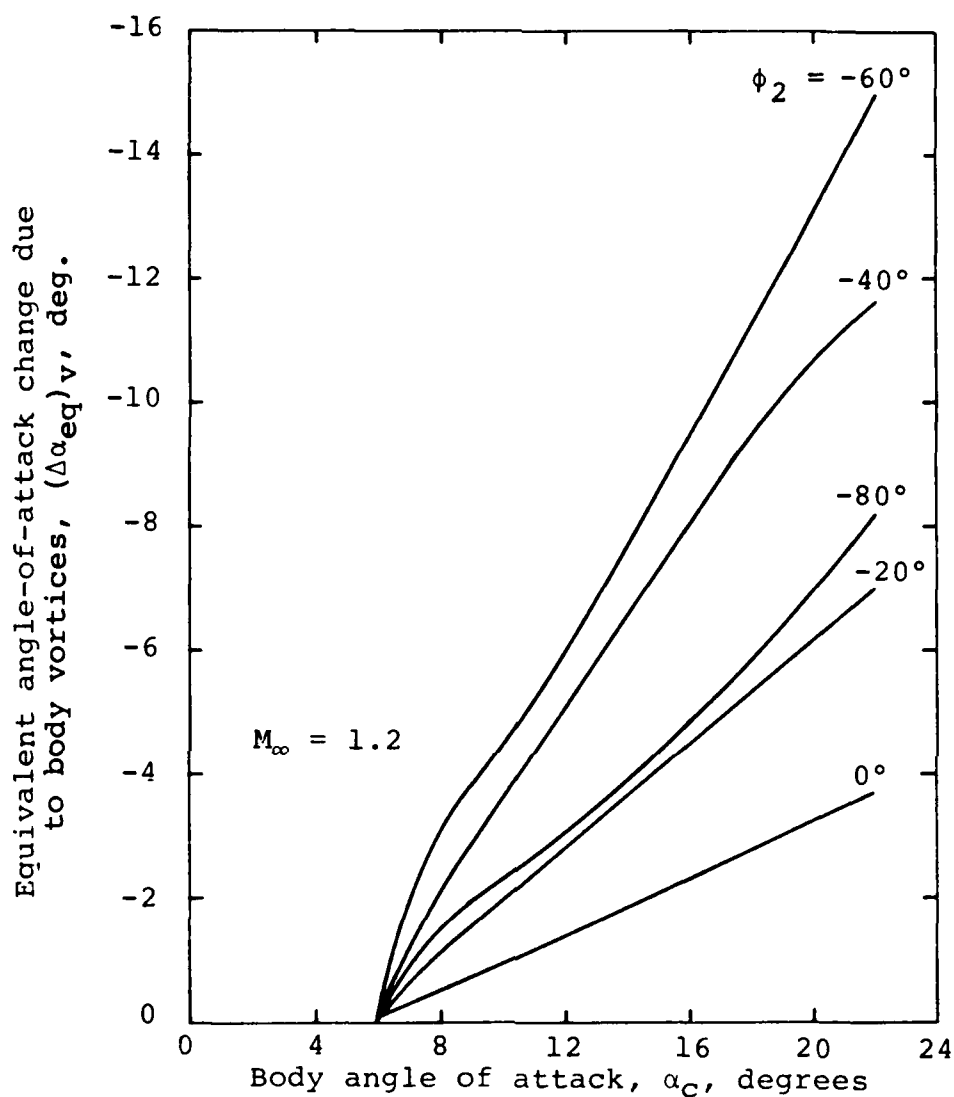
(d) $M_\infty = 1.2$; leeward side

Figure 35.- Concluded.
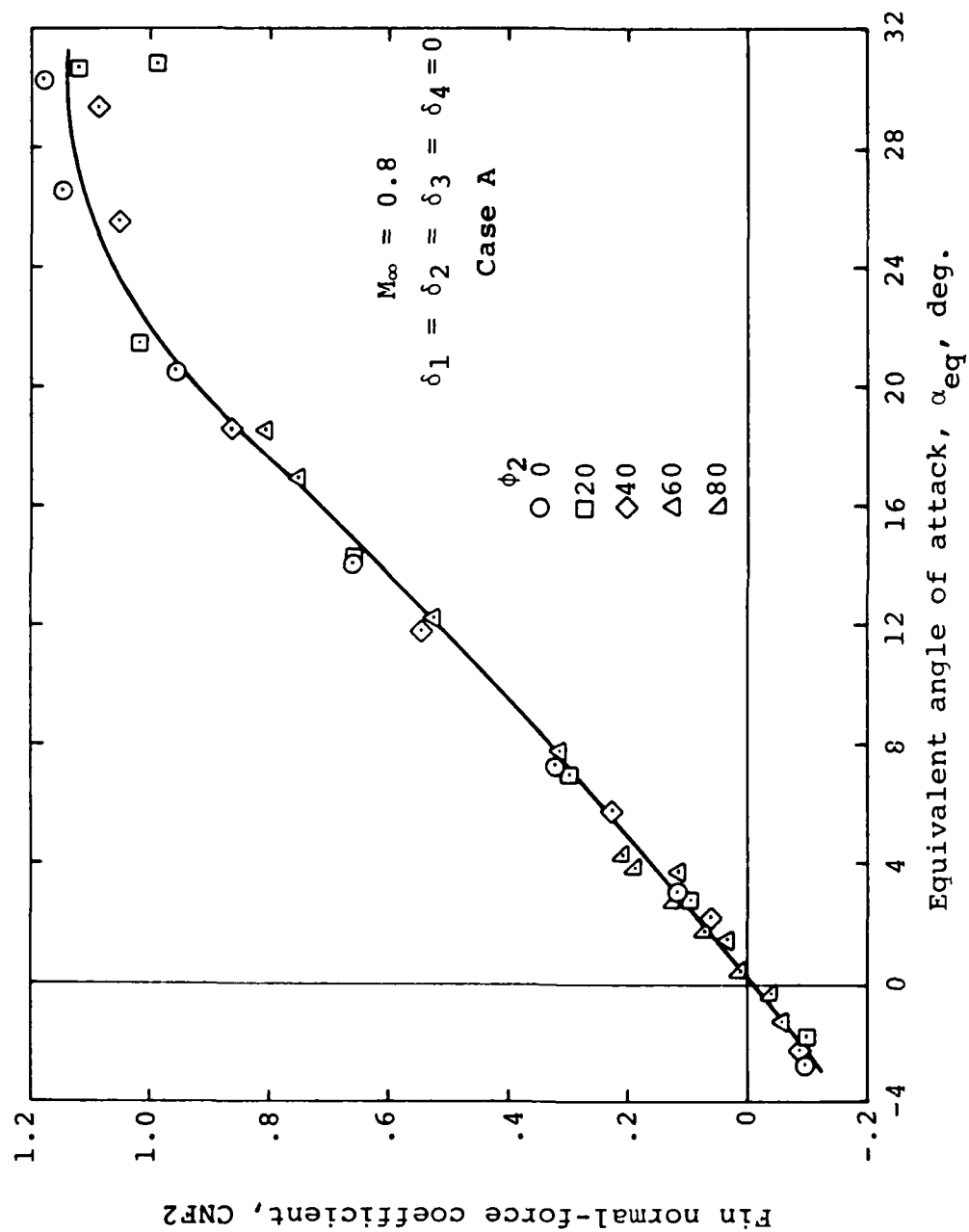
(a) $M_\infty = 0.8$

Figure 36.— Fin 2 normal-force correlation curve for case A, windward fins, $\delta_4 = 0$.
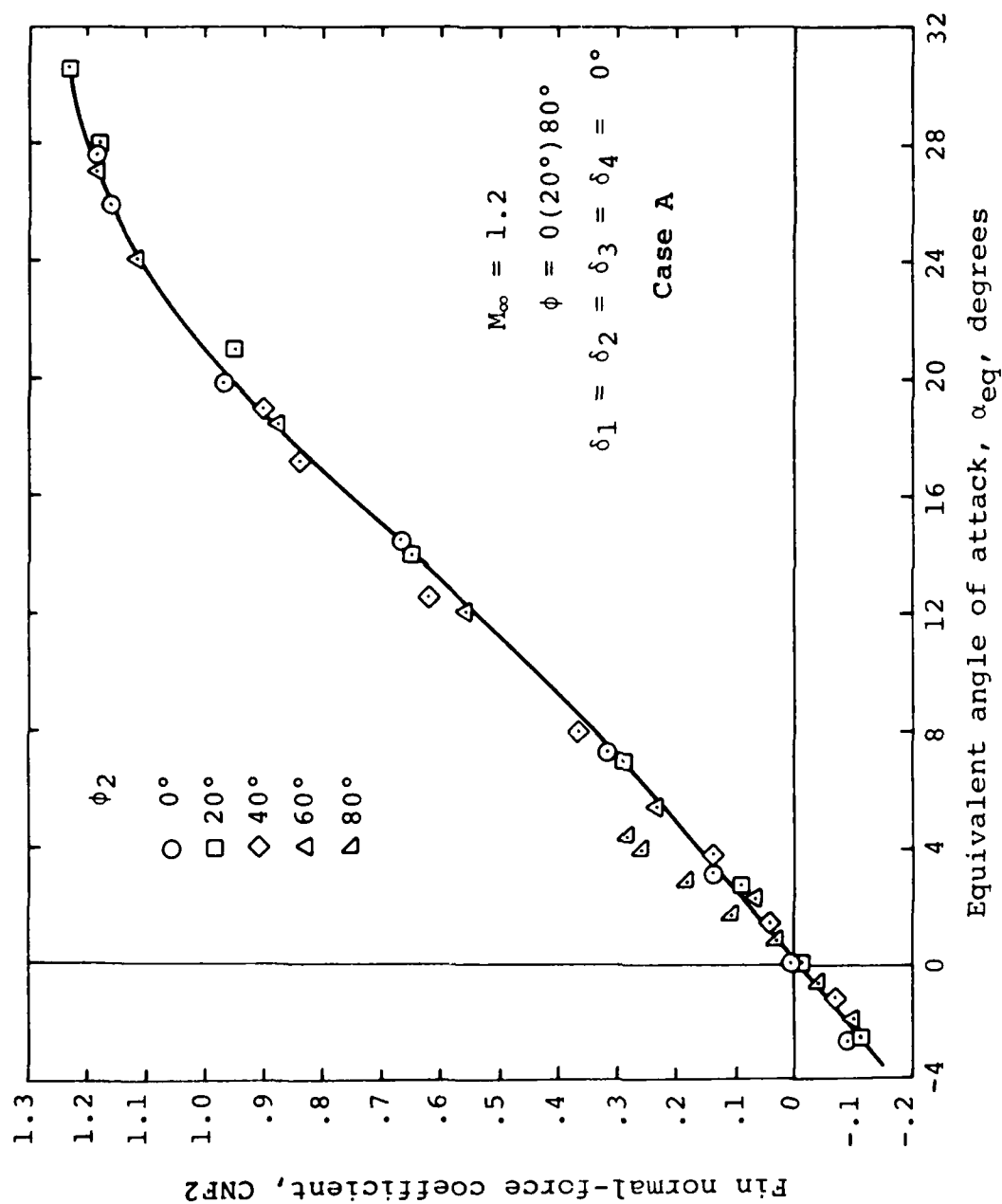
(b) $M_\infty = 1.2$

Figure 36.- Concluded.
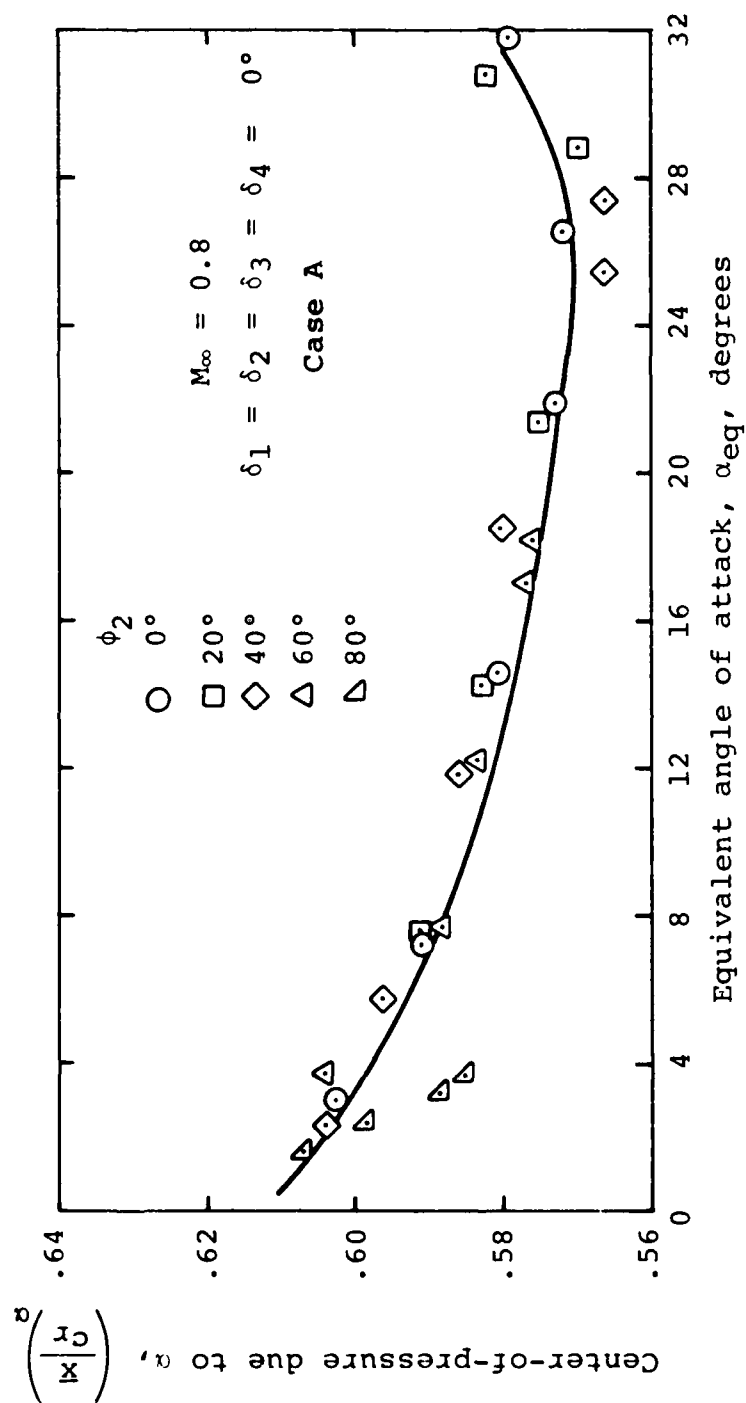
Figure 37.- Correlation curve for fin 2 center-of-pressure position due to angle-of-attack for case A, windward fins, $\delta = 0°$.

(a) $M_\infty = 0.8$

184

$M_\infty = 1.2$

$\delta_1 = \delta_2 = \delta_3 = \delta_4 = 0°$

Case A
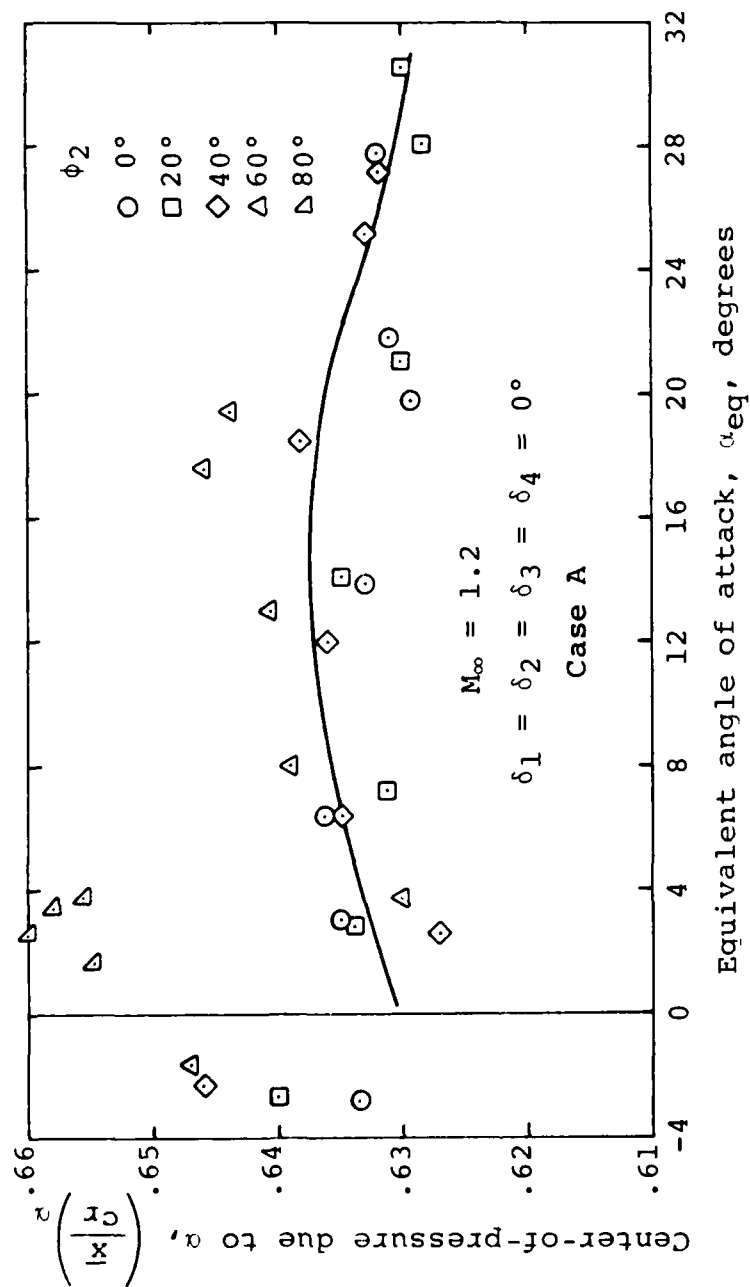
(b) $M_\infty = 1.2$

Figure 37.- Concluded.
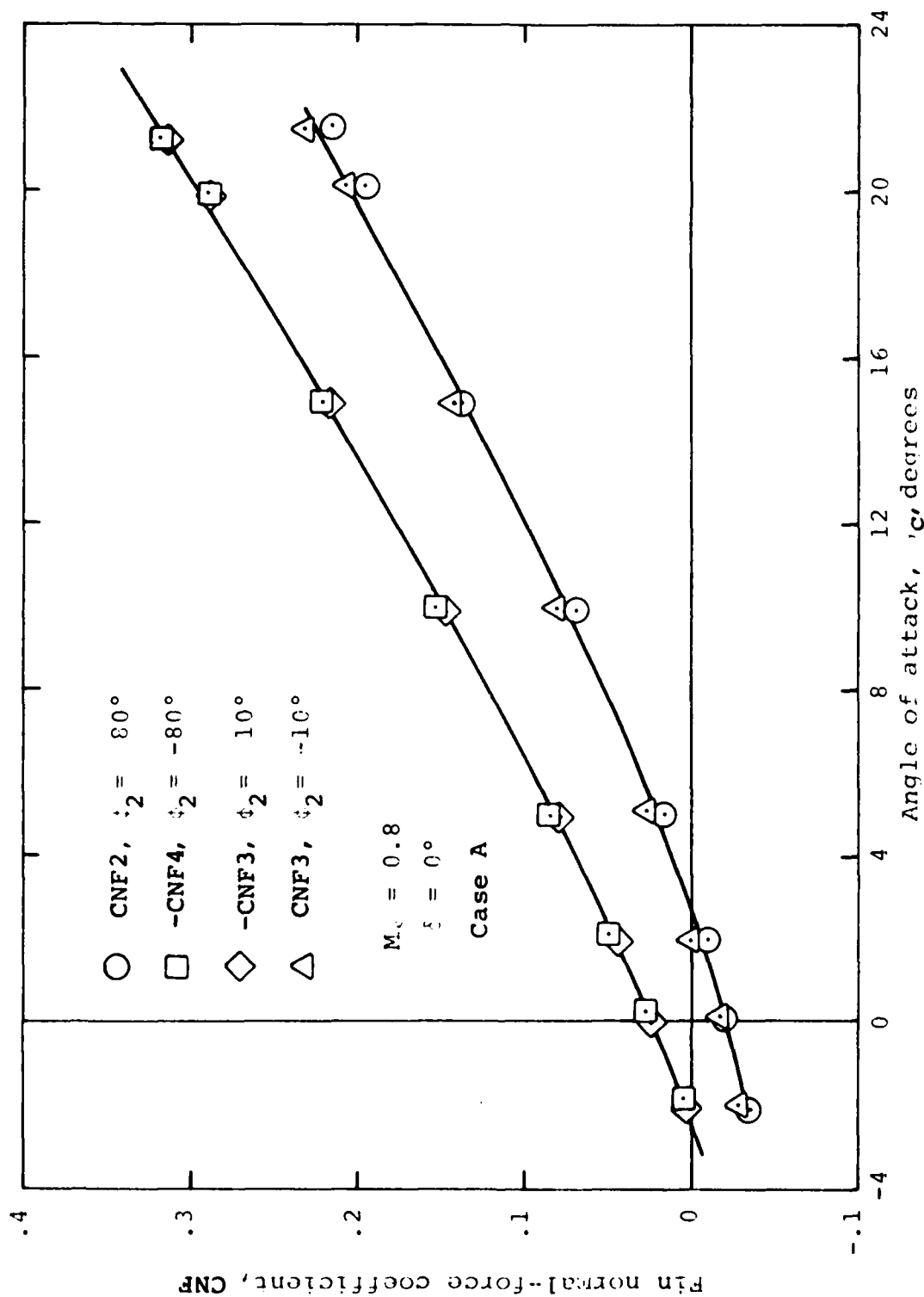
Figure 38.- Comparisons of fin normal-force coefficients which should be equal by symmetry considerations.
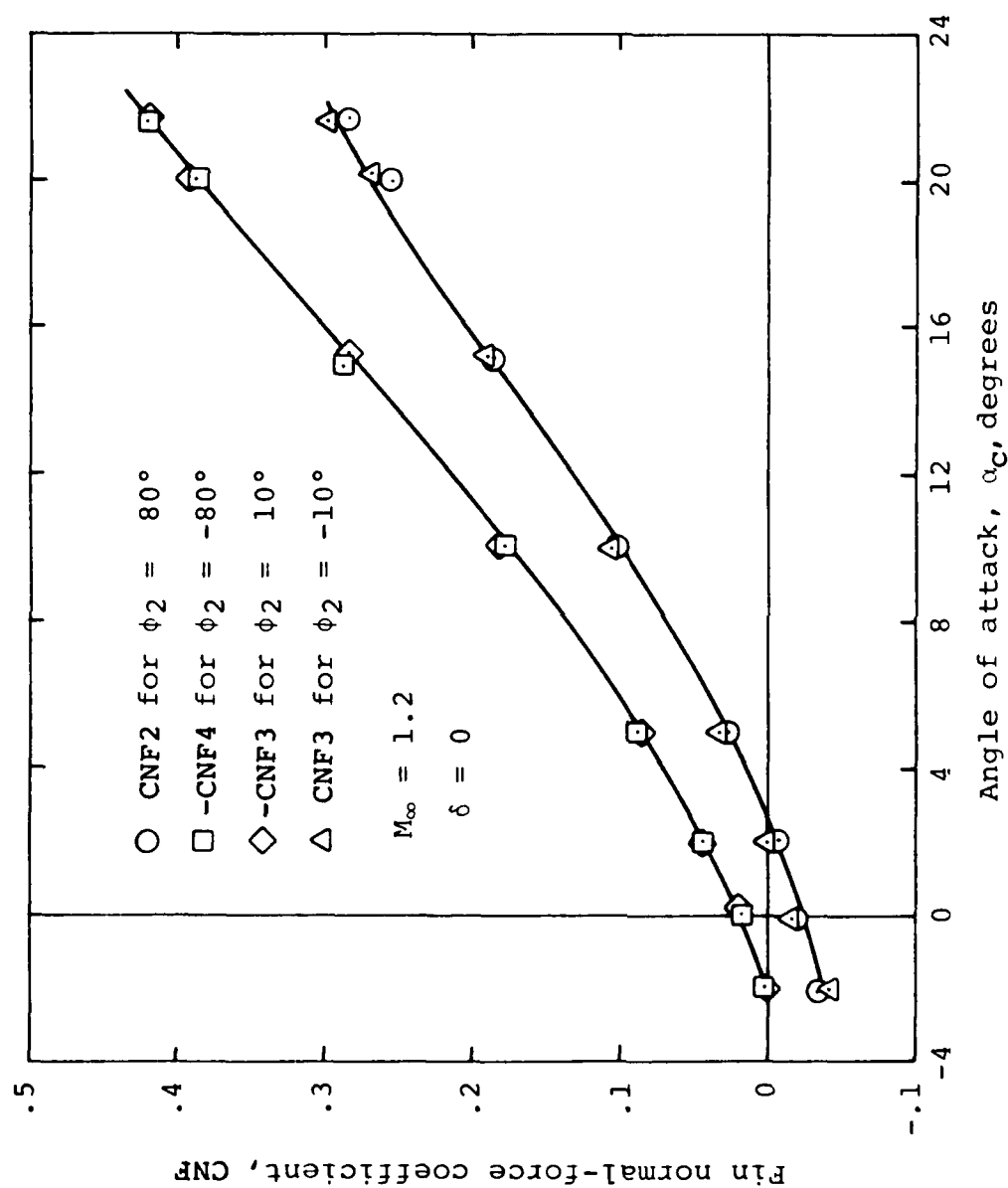
(a) $M_\infty = 0.8$

(b) $M_\infty = 1.2$

Figure 38.- Concluded.
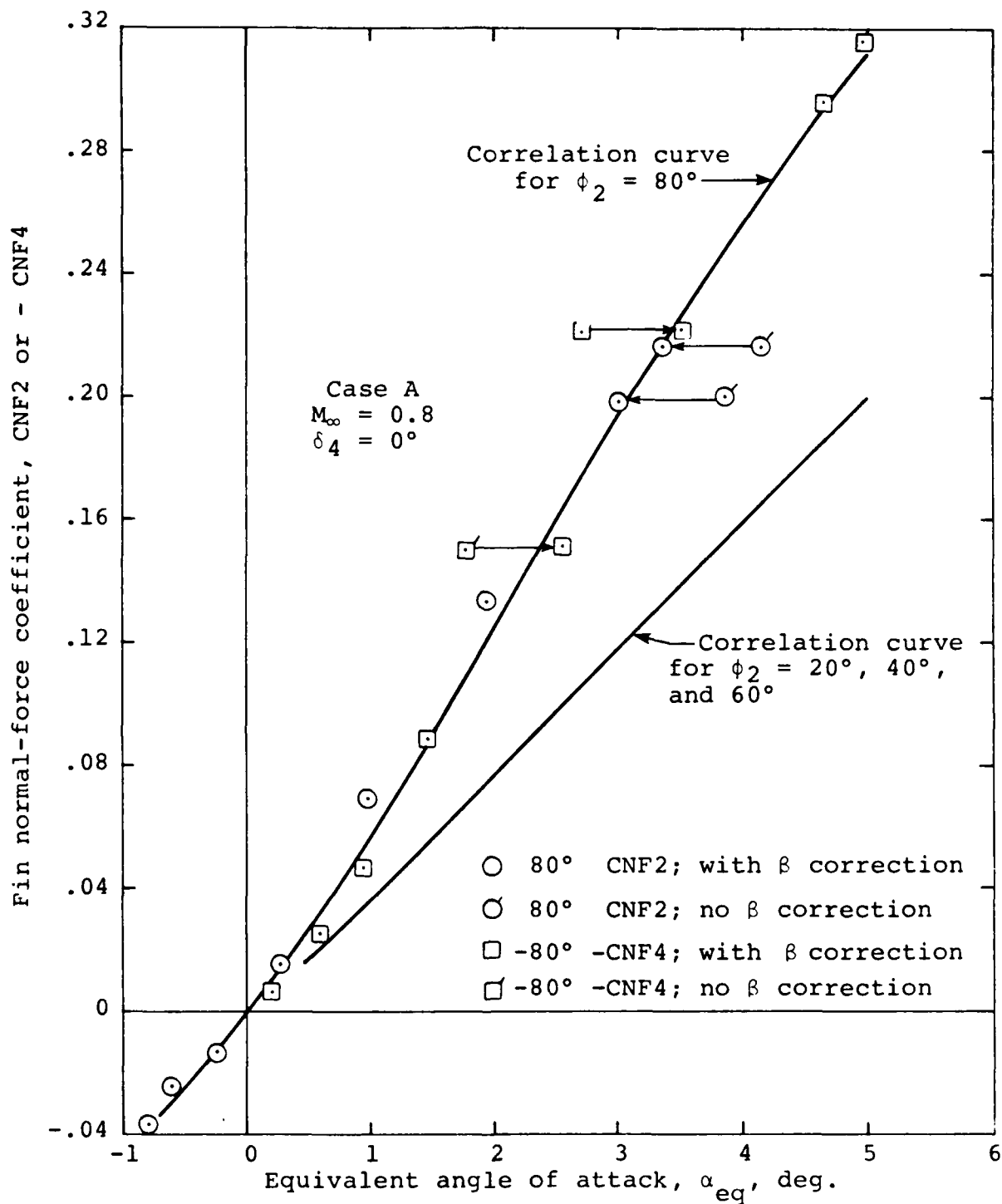
(a) $M_\infty = 0.8$

Figure 39.- Correction of normal-force correlation curve for
sidewash angle and comparison with predictions
on supersonic missile code NWCDM.

186
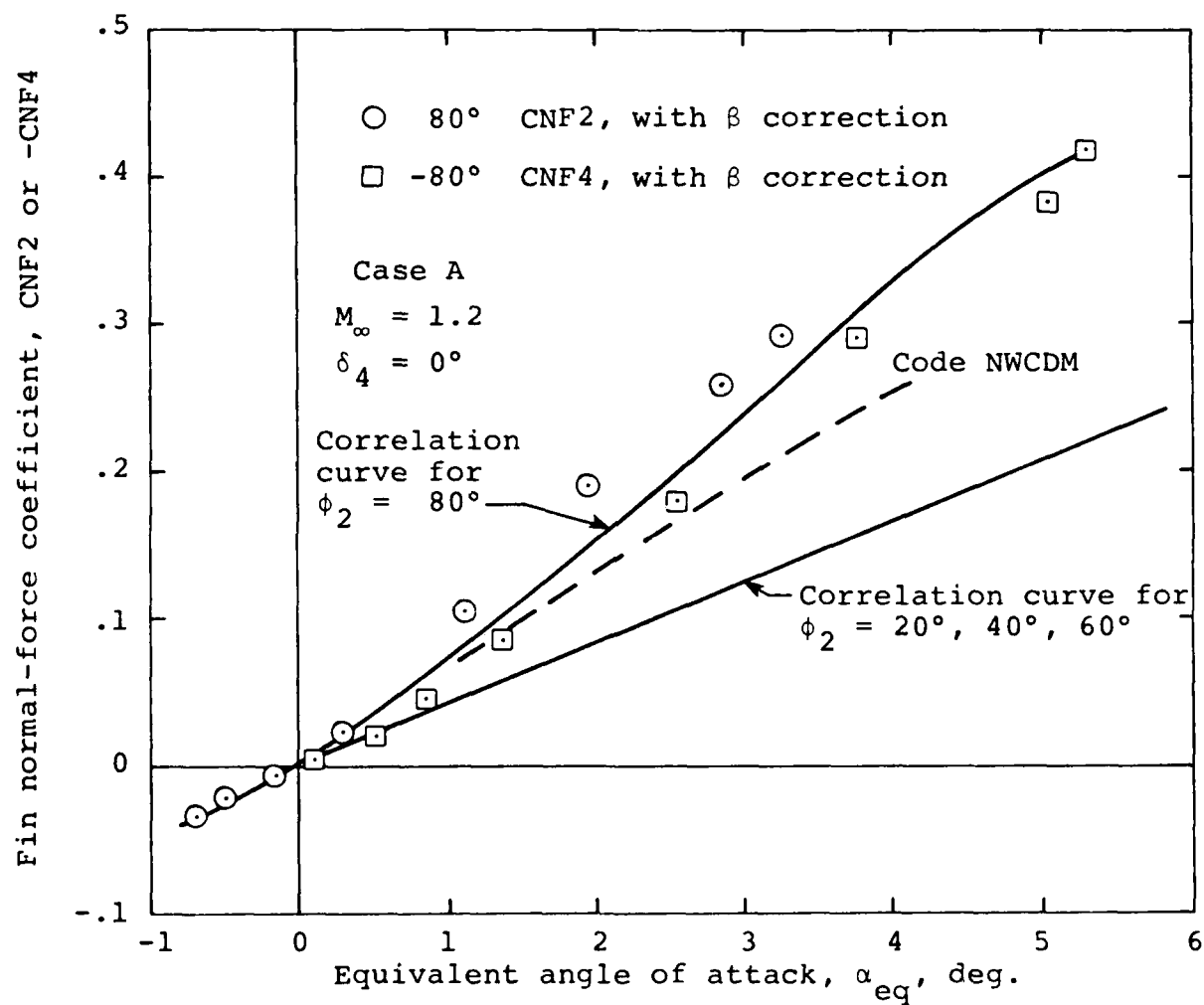
(b) $M_\infty = 1.2$

Figure 39.- Concluded.

189
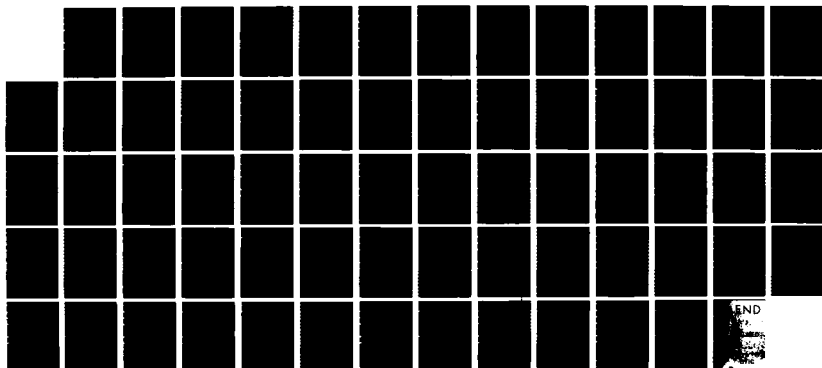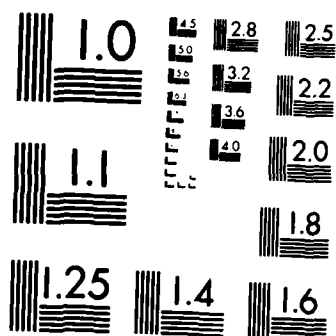
MICROCOPY RESOLUTION TEST CHART

NATIONAL BUREAU OF STANDARDS-1963-A
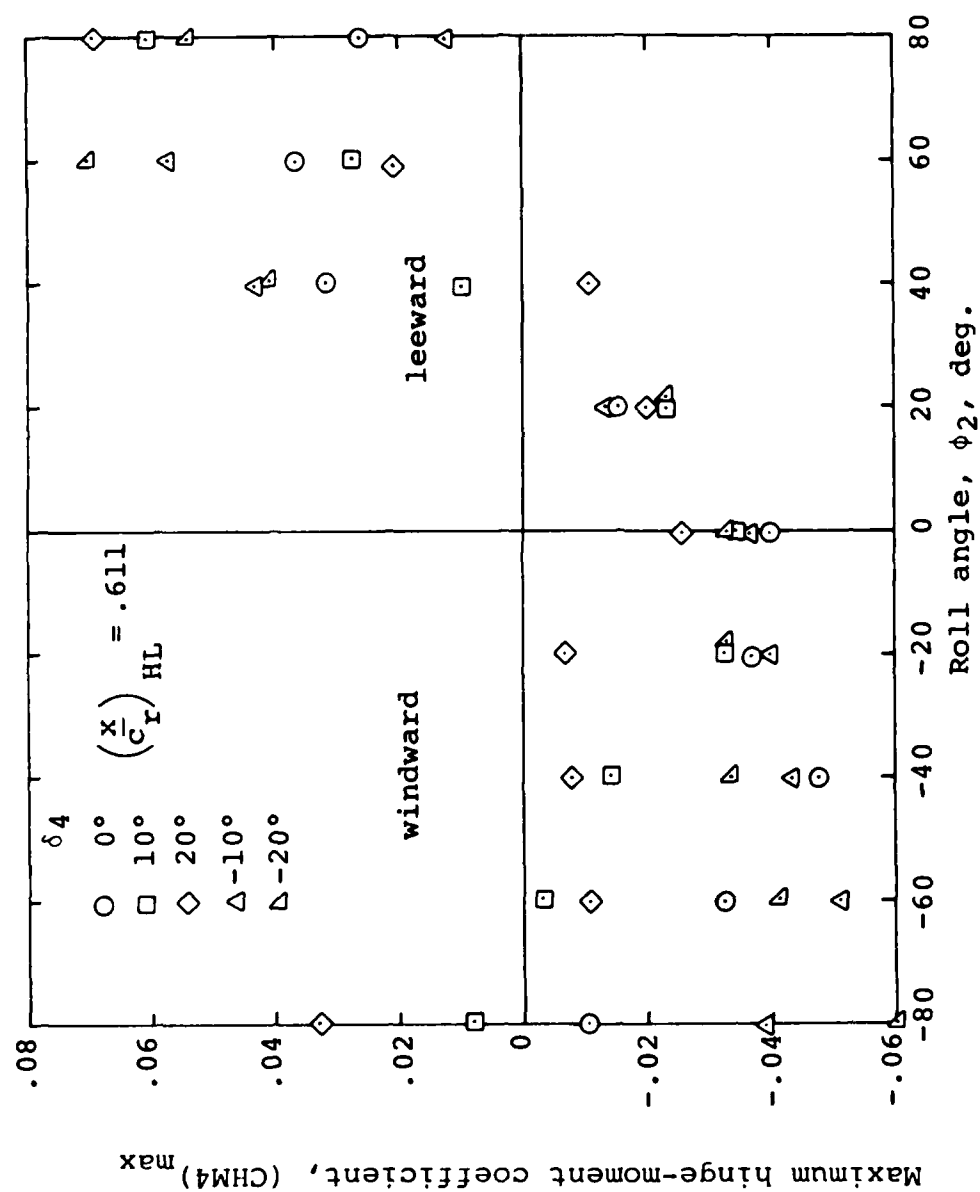
Figure 40.- Effect of roll angle and fin deflection angle on maximum
hinge-moment coefficient of fin 51 on triservice missile.

(a) $M_\infty = 0.8$

190
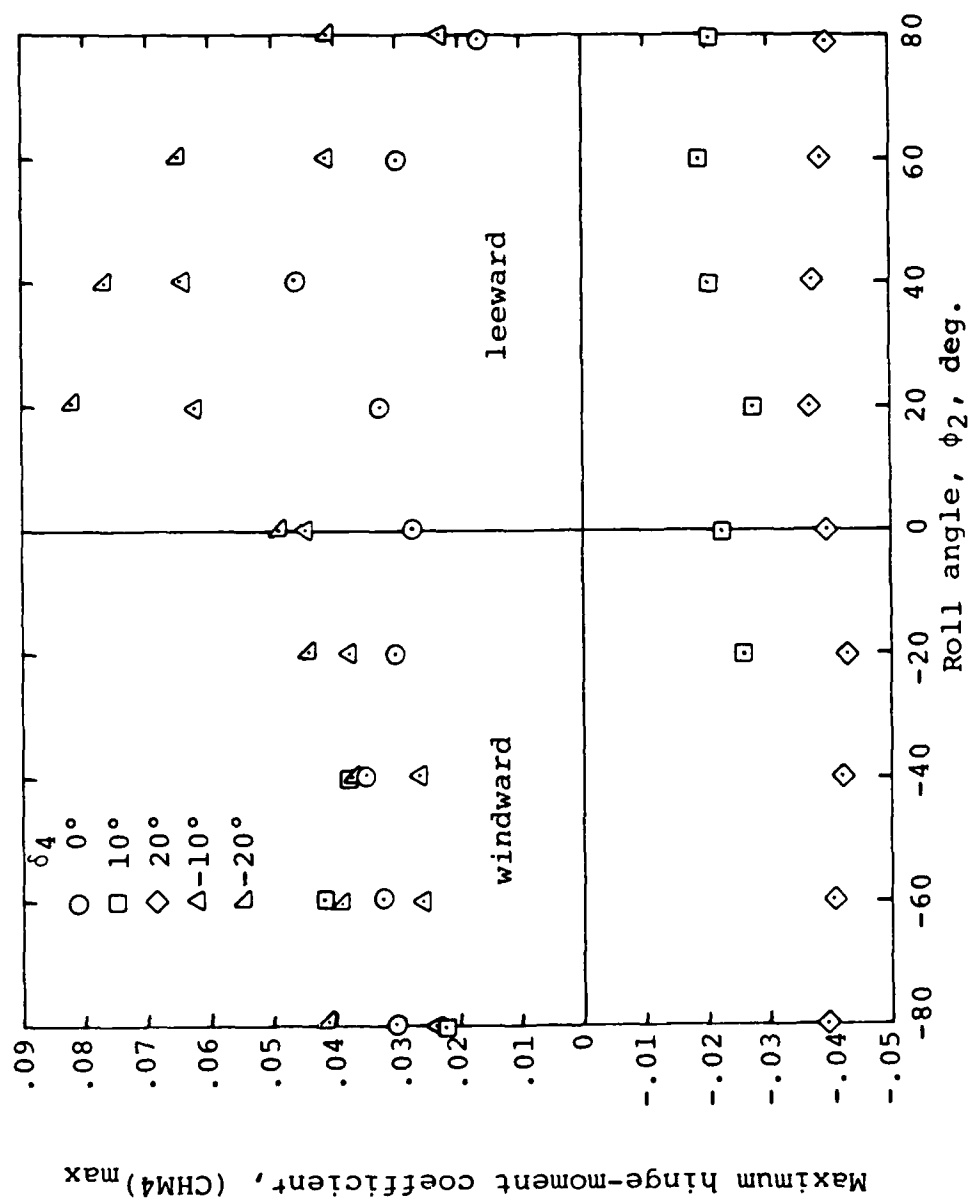
(b) $M_\infty = 1.2$

Figure 40.- Concluded.

191

(a) $M_\infty = 0.8$

Figure 41.- Fin normal-force correlation curve for case B; leeward fin, $\delta_4 = 0$.

192
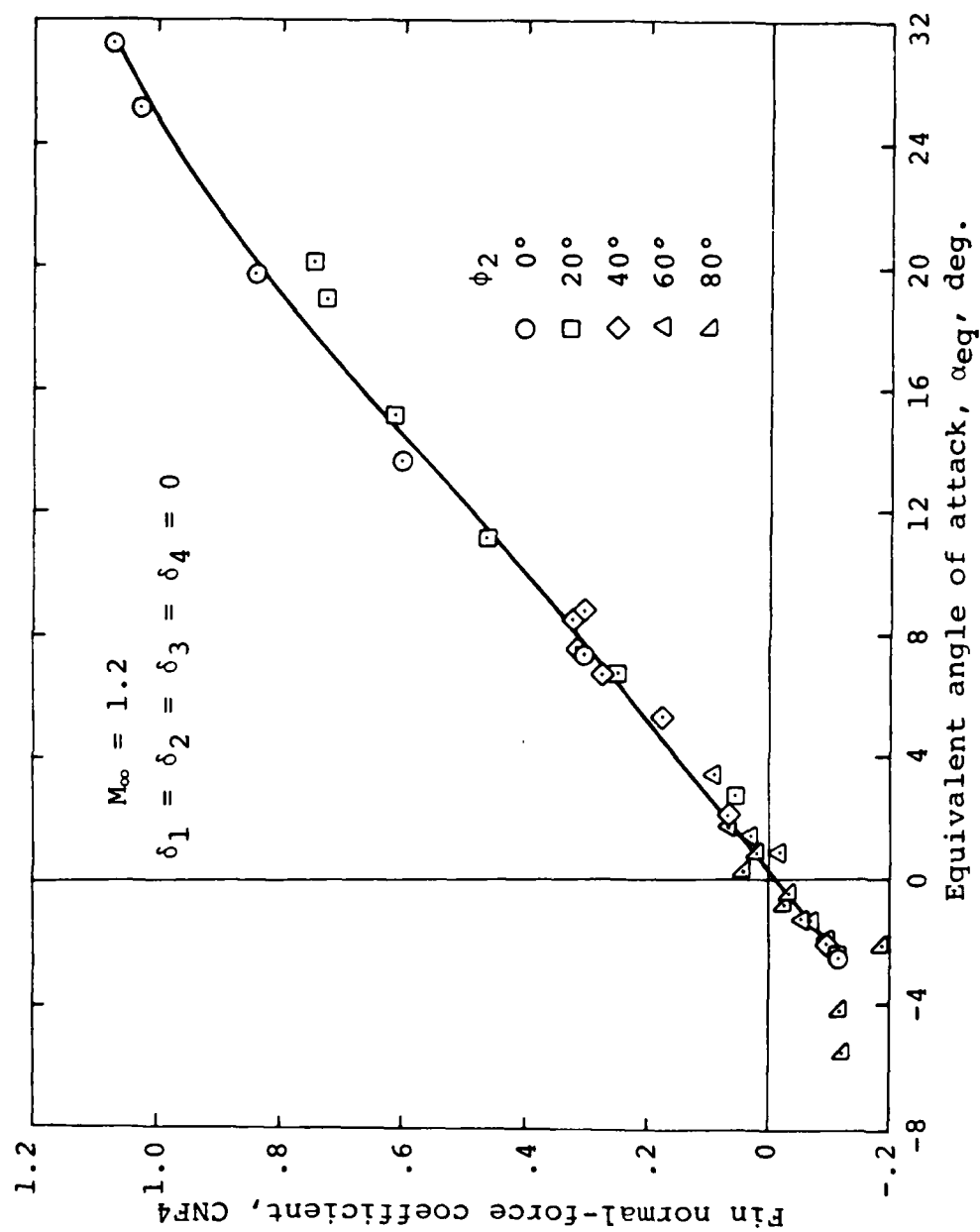
(b) $M_\infty = 1.2$

Figure 41.- Concluded.

193
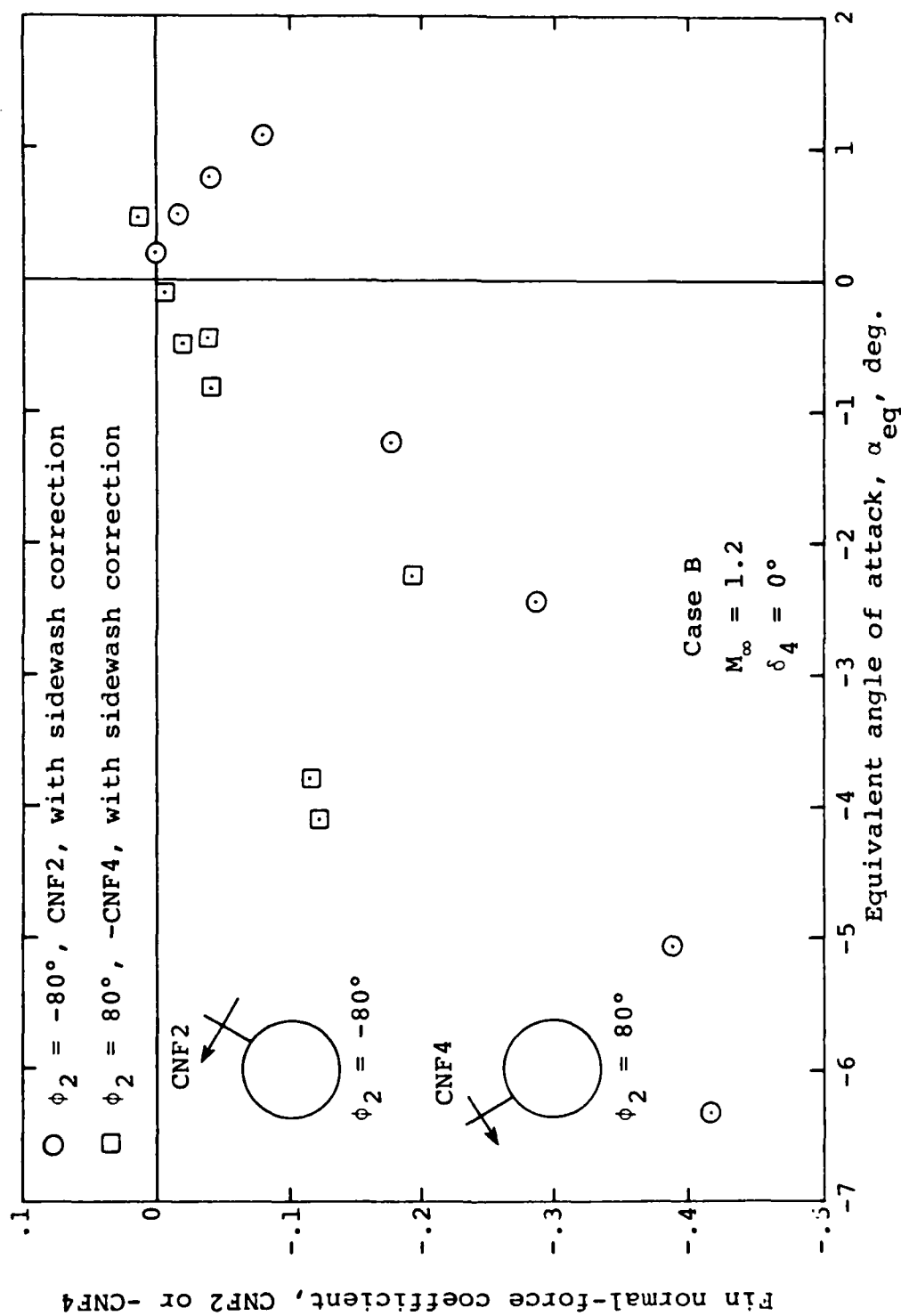
Figure 42.- Enlarged correlation curve to show behavior of CNF near leeward meridian.

(a) With sidewash correction
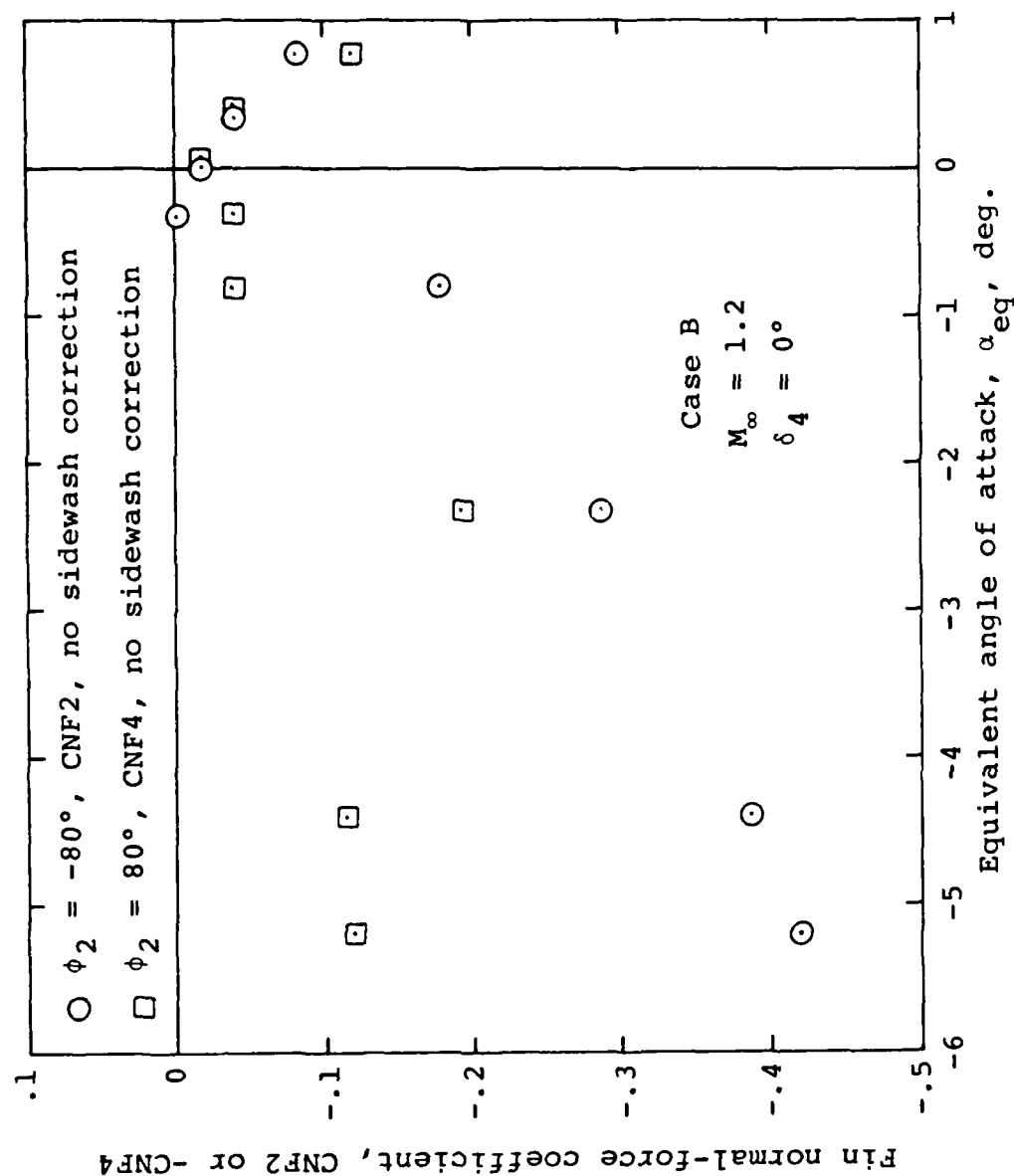
(b) No sidewash correction

Figure 42.– Concluded.

195
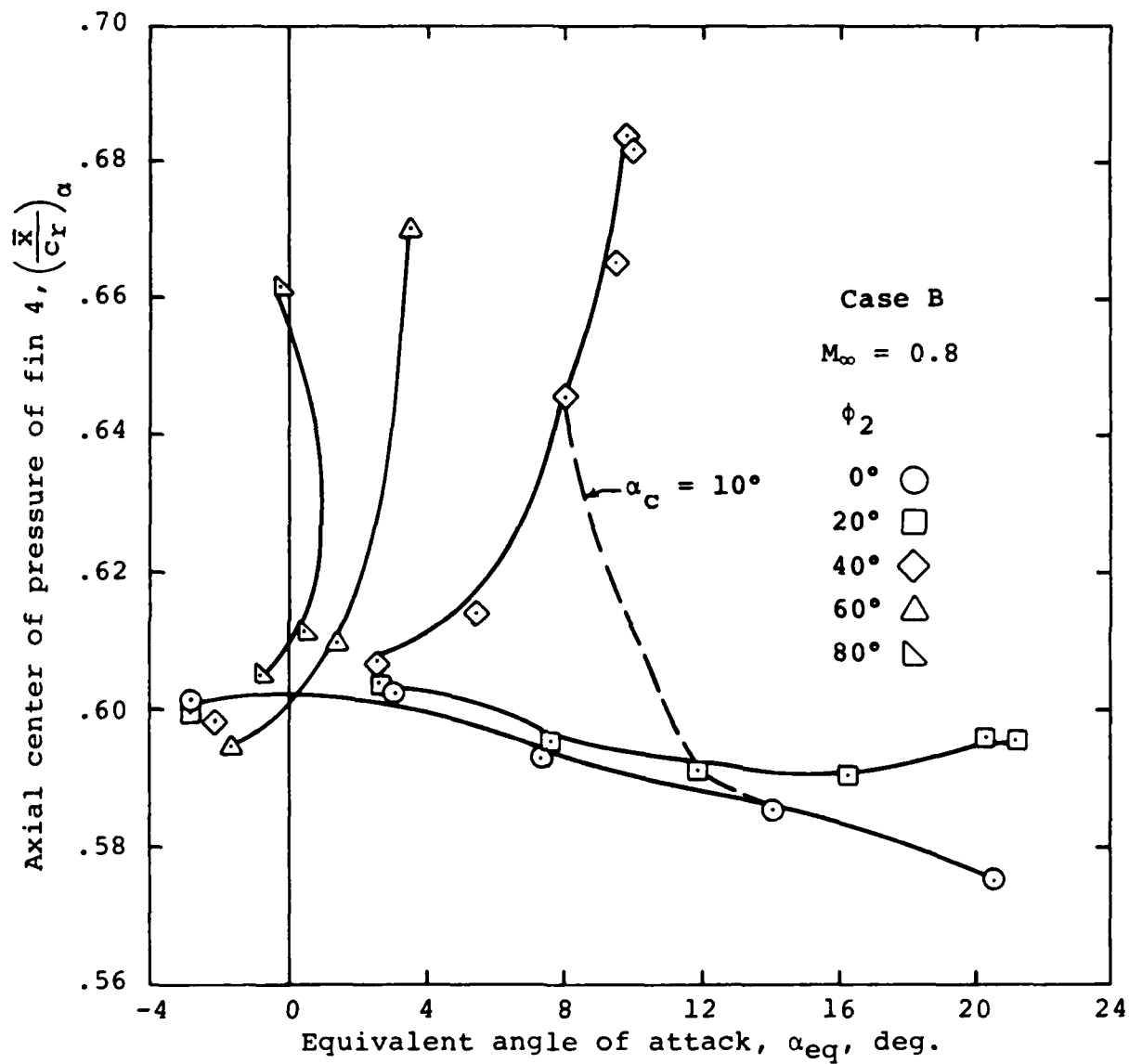
(a) $M_\infty = 0.8$

Figure 43.- Measured axial center-of-pressure position
of fin 4 on triservice missile.
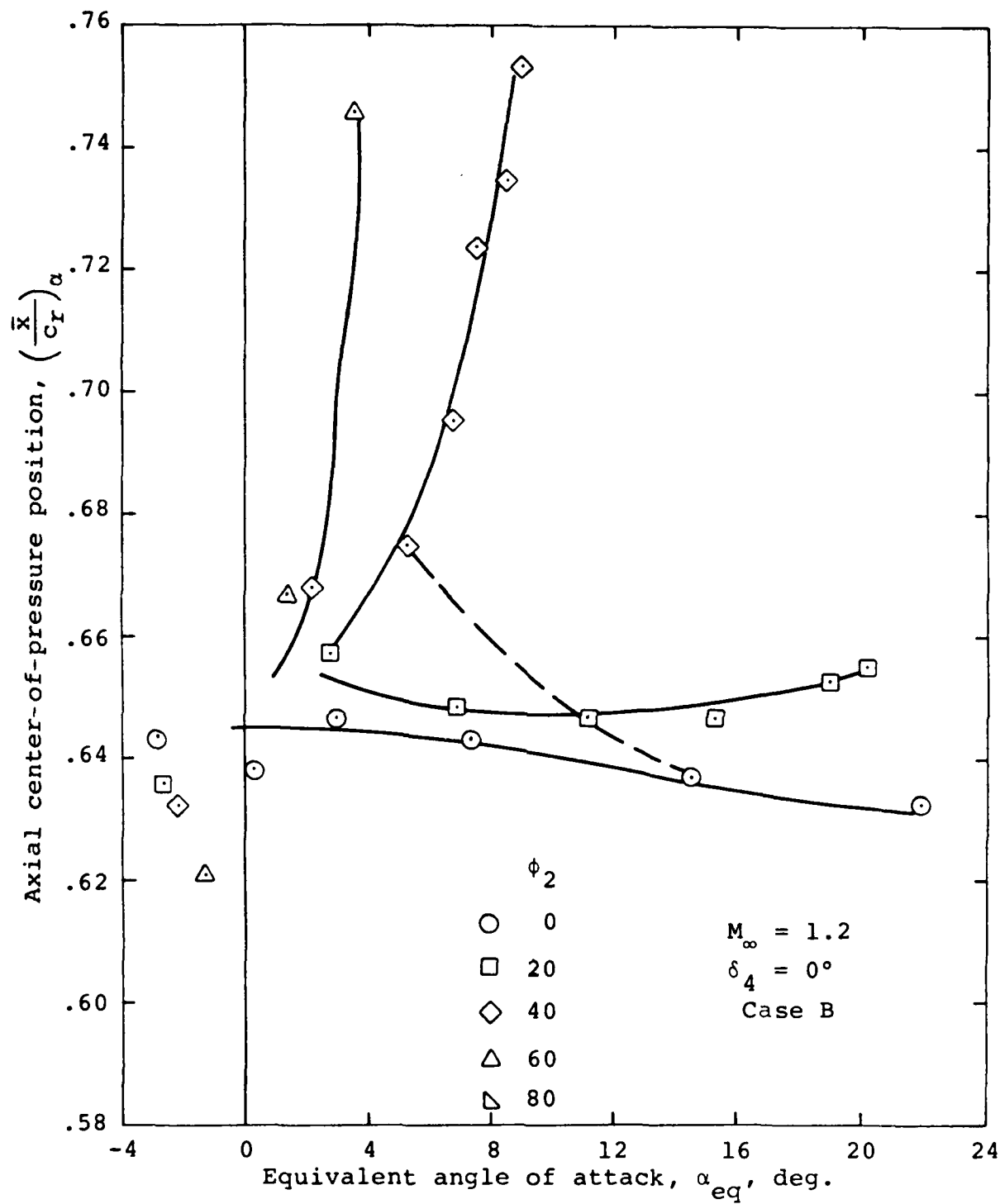
(b) $M_\infty = 1.2$

Figure 43.- Concluded.
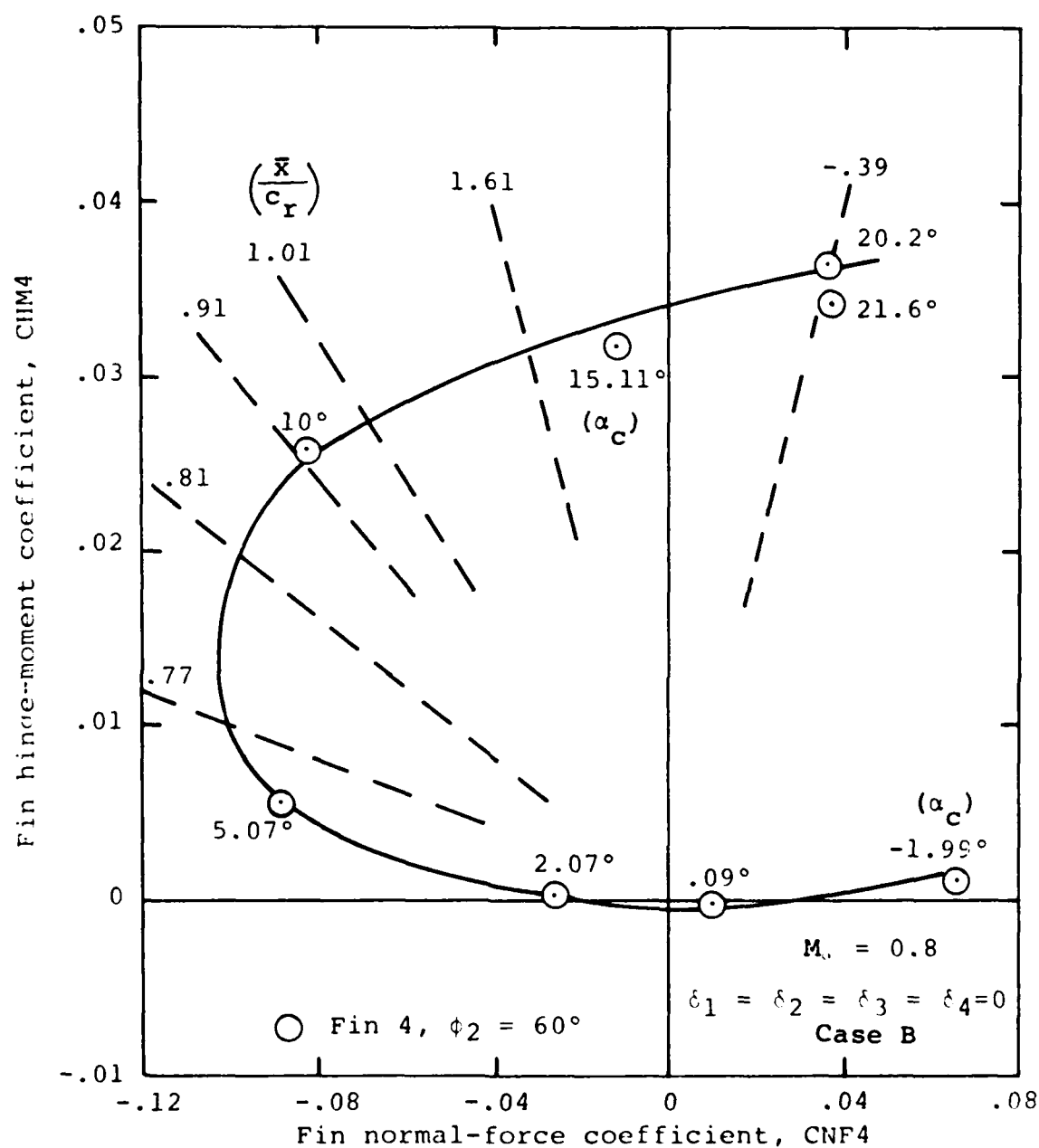
Figure 44.- Plot of CHM vs. CNF for fin 4 mounted on triservice missile, $M_\infty = 0.8$, $\phi_2 = 60°$.

198
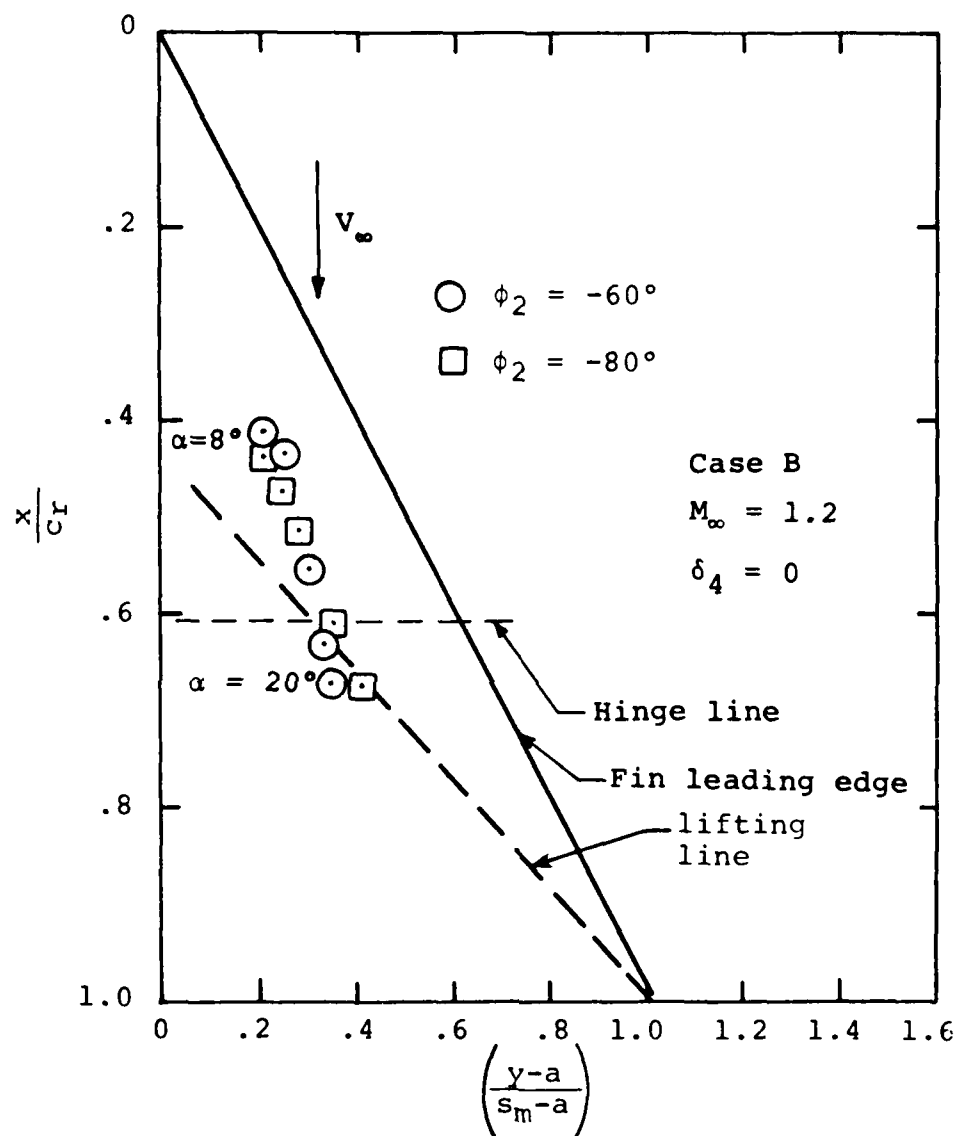
Figure 45.- Center of pressure of body vortex loading of T51
fin mounted on triservice missile as calculated
by a supersonic missile program.
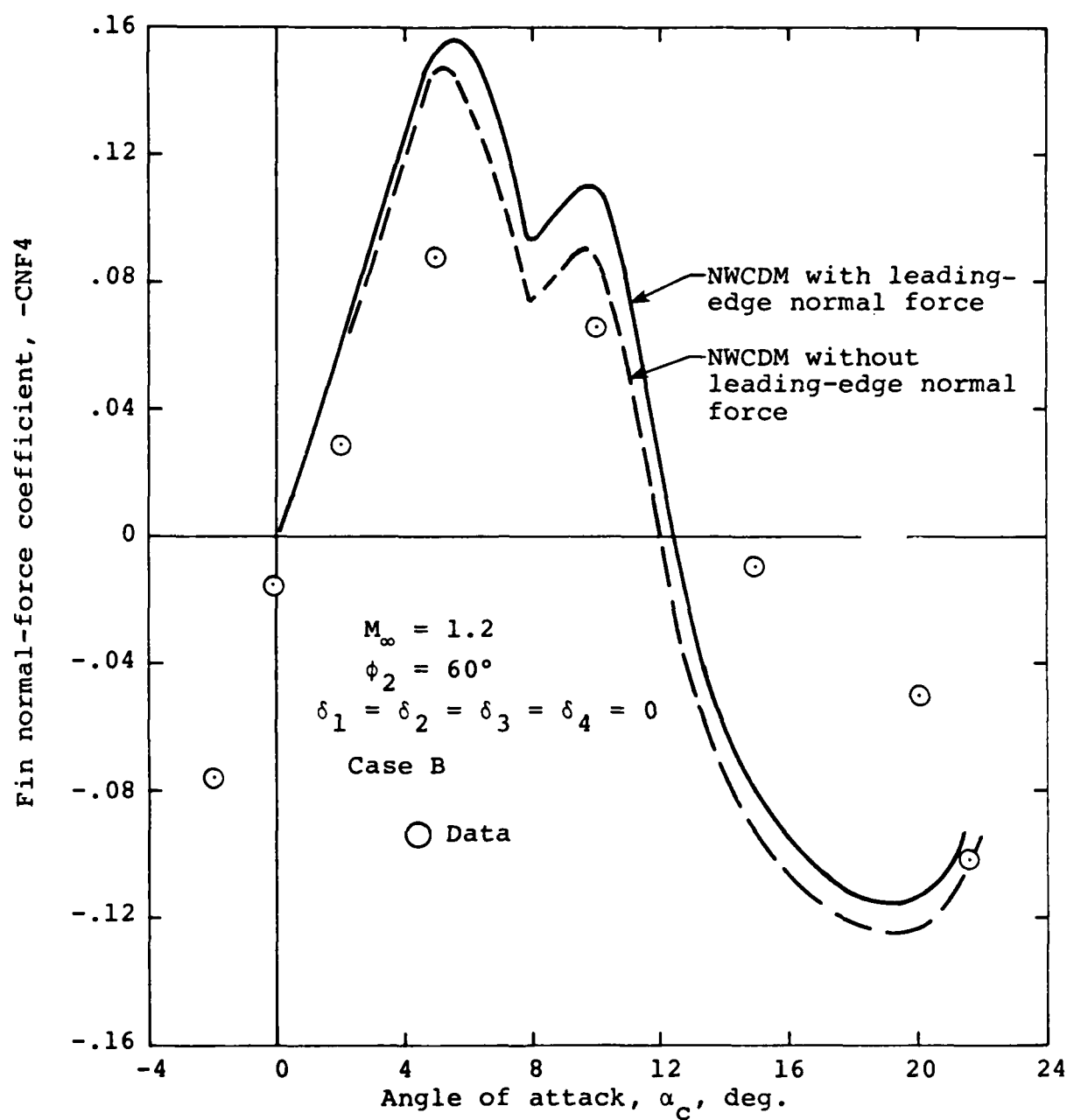
(a) Normal-force coefficient

Figure 46.- Comparison of fin measured characteristic with prediction of supersonic missile code NWCDM with strong vortex interference, $\phi_2 = 60°$, case B.

200
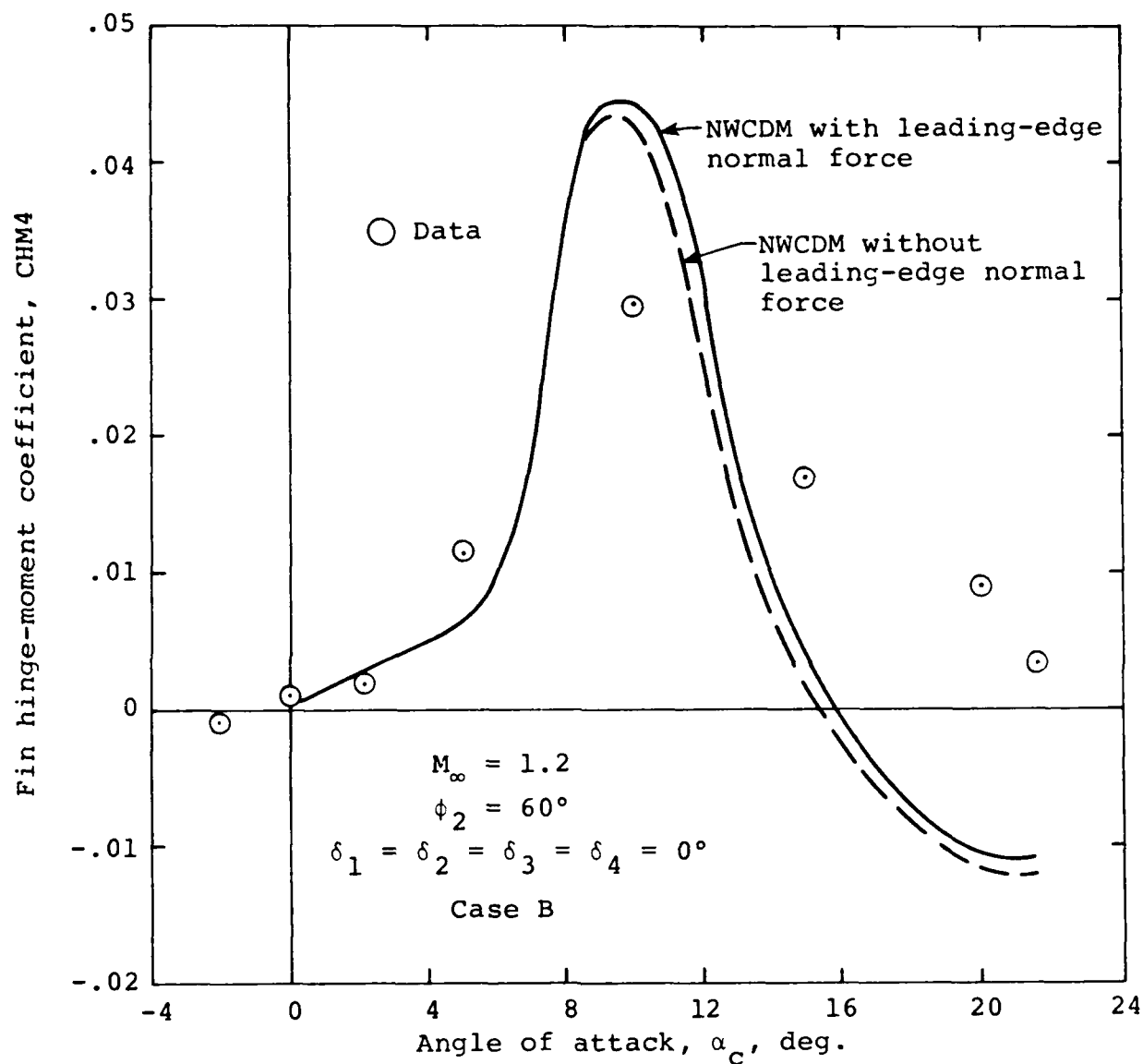
(b) Hinge-moment coefficient

Figure 46.- Concluded.

201
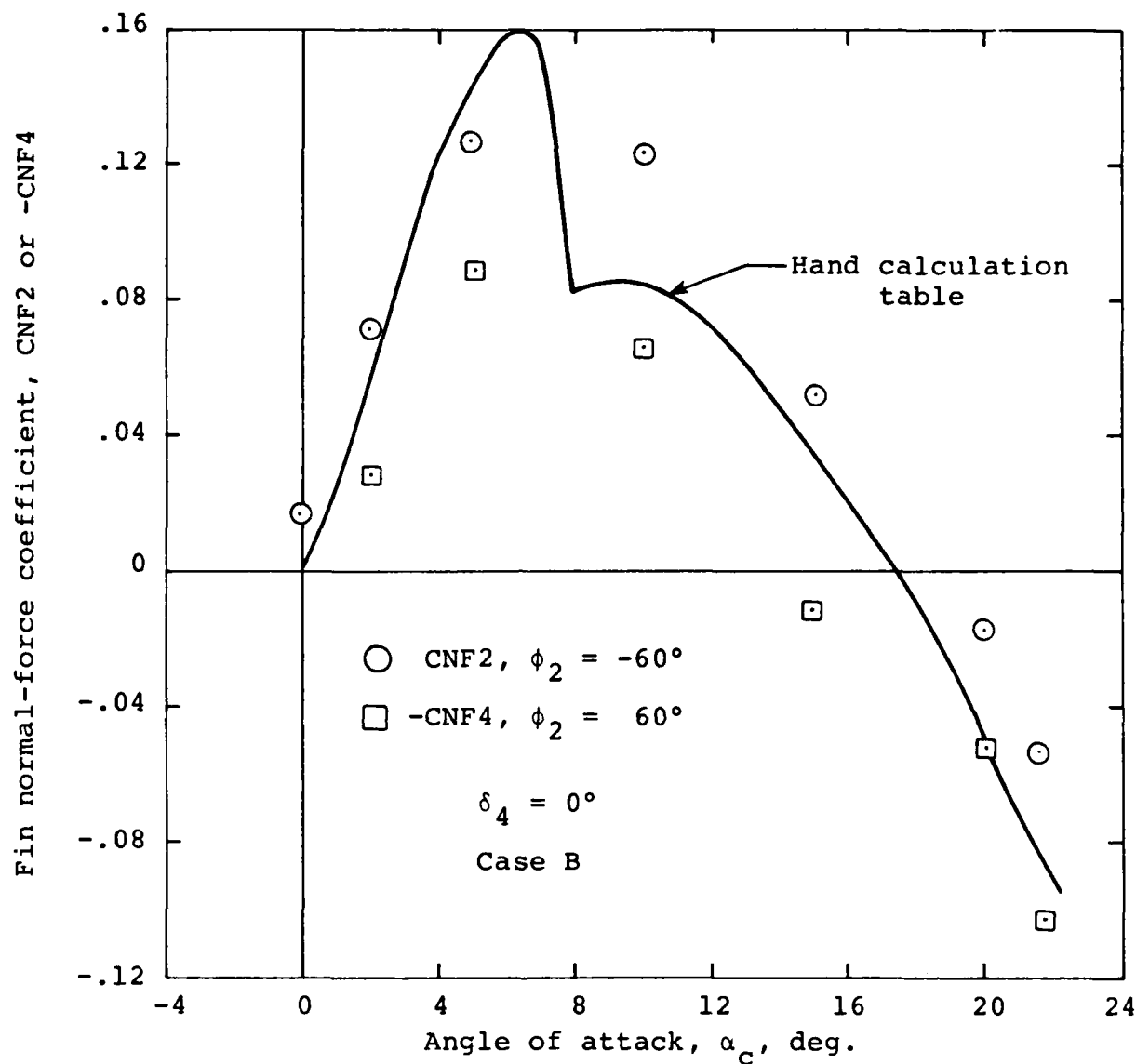
(a) Normal-force coefficient

Figure 47.- Prediction by hand calculation of CNF and CHM for fin 51 near body vortex; case B, $\phi_2 = 60°$.

202
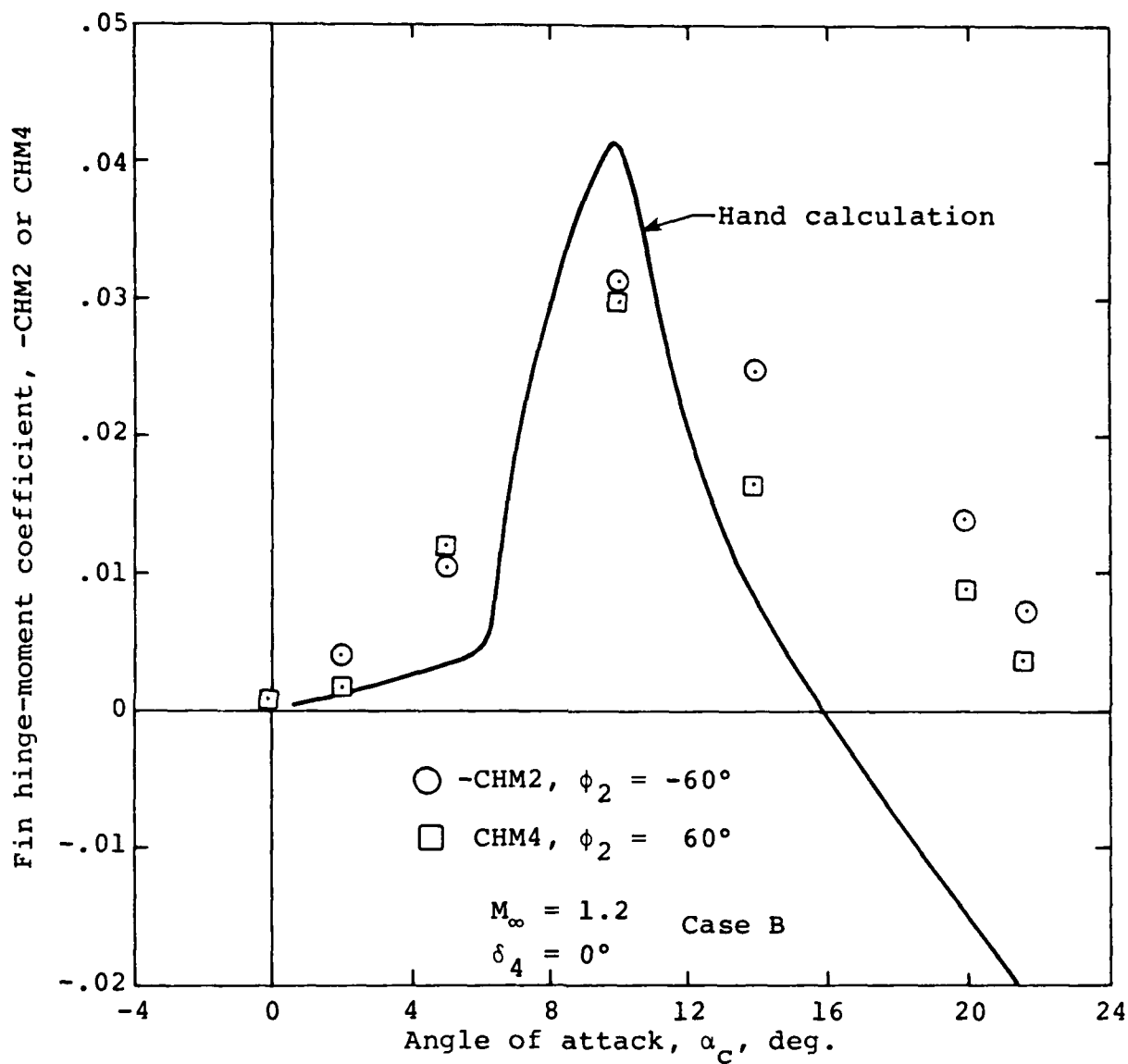
(b) Hinge-moment coefficient

Figure 47.- Concluded.
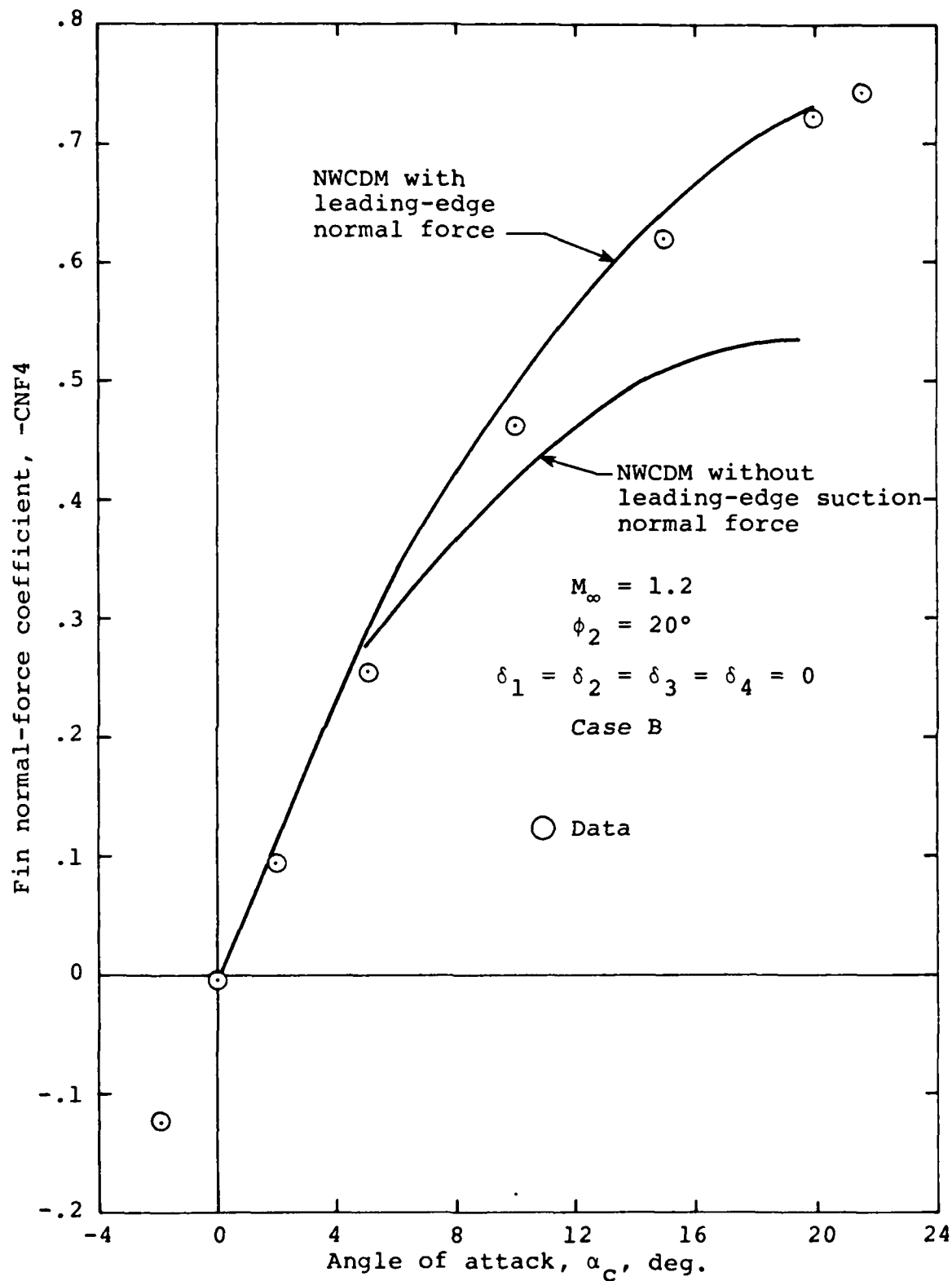
(a) Normal-force coefficient

Figure 48.- Comparison of fin measured characteristics with prediction of supersonic missile code NWCDM, case B.
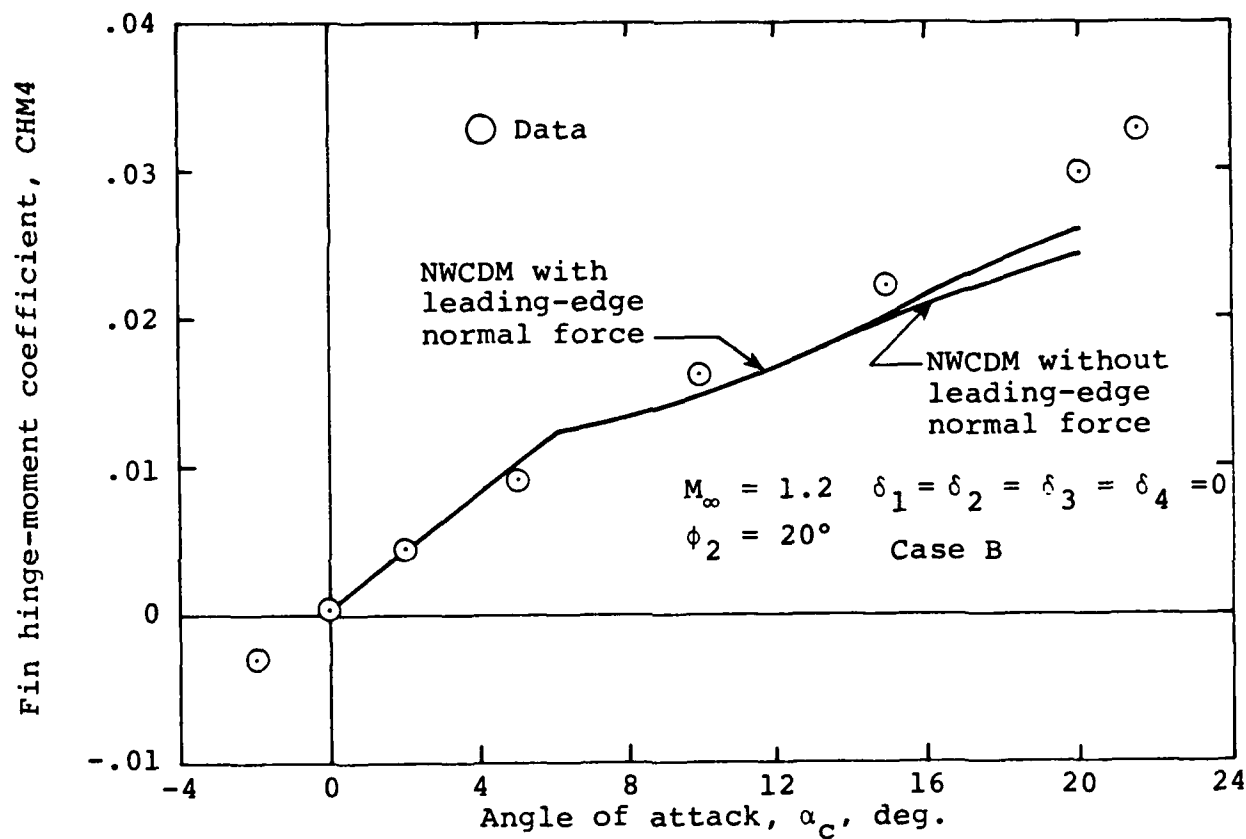
(b) Hinge-moment coefficient

Figure 48.- Continued.
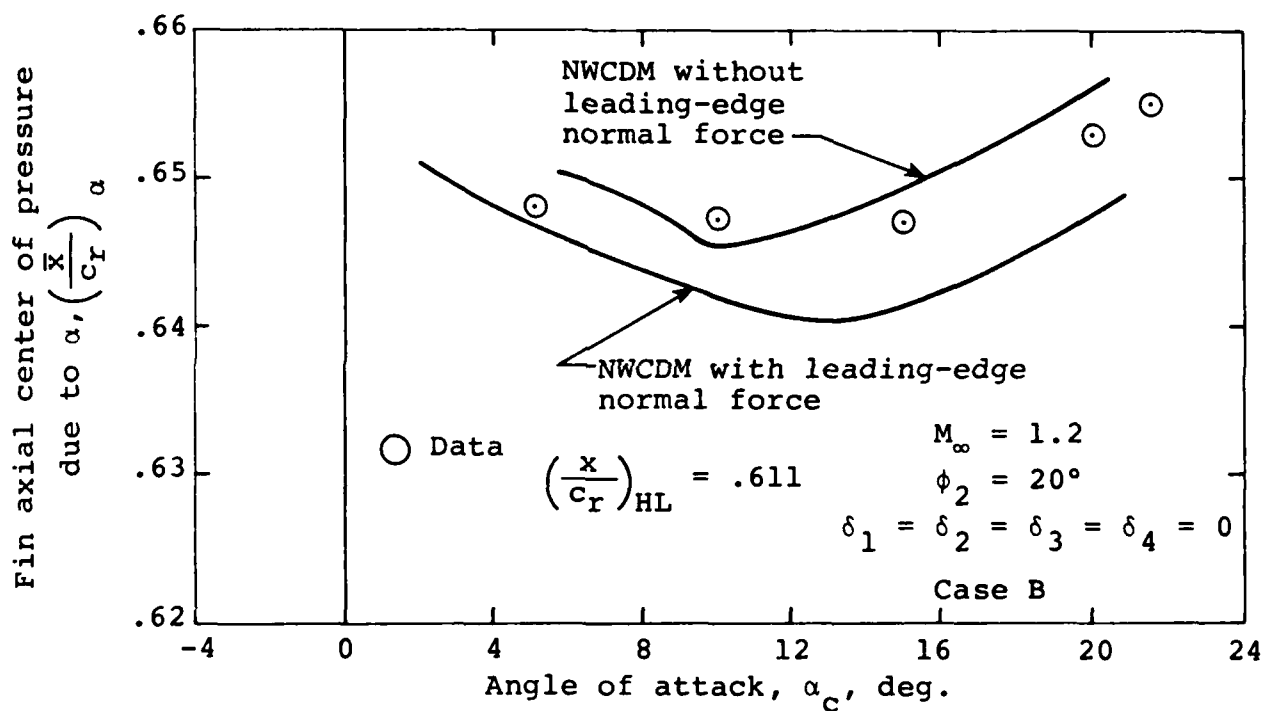
(c) Axial center-of-pressure position

Figure 48.- Concluded.
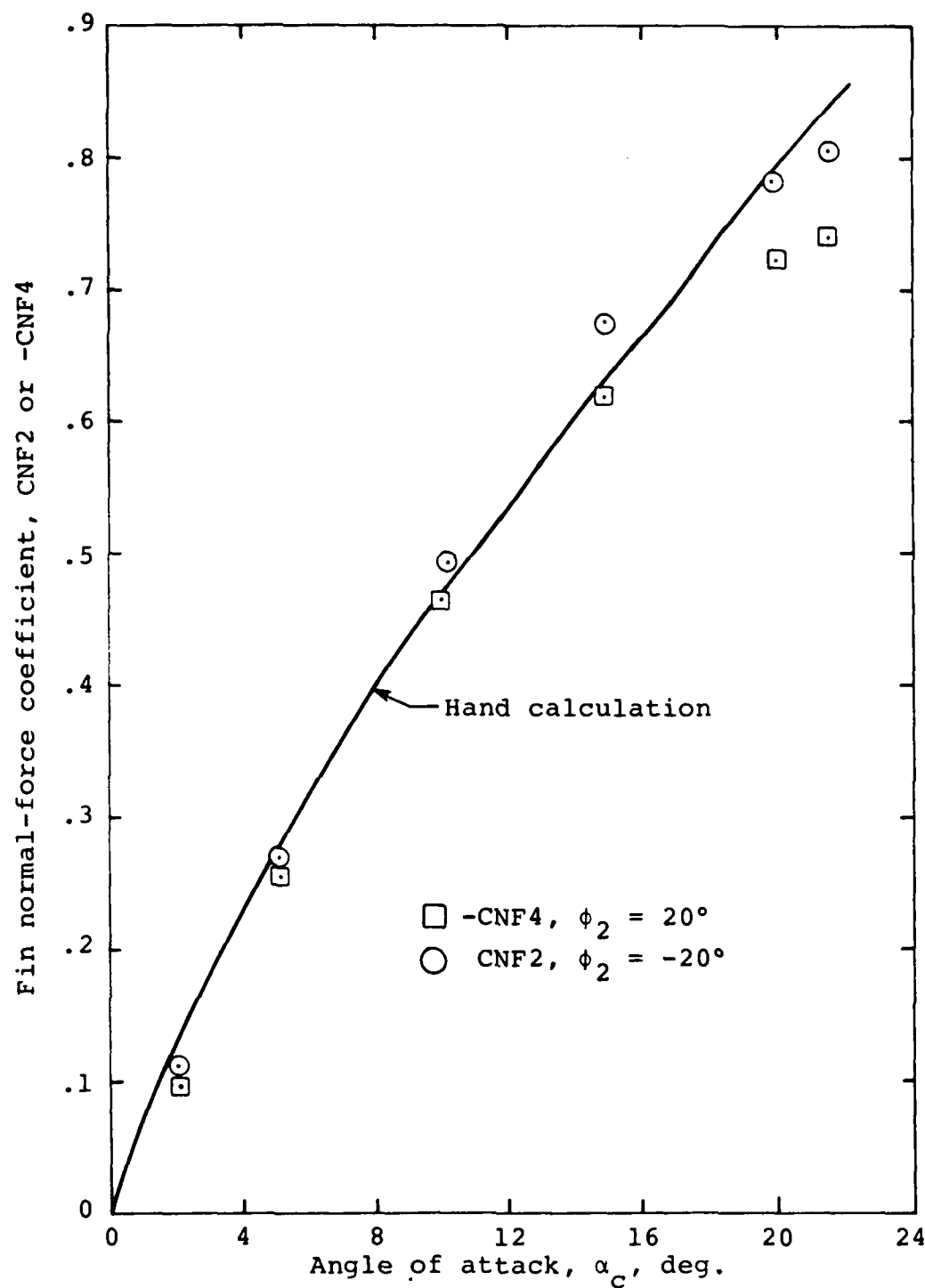
(a) Normal-force coefficient

Figure 49.- Prediction by hand calculation of CNF
and CHM for fin 51; $\phi_2 = 20°$, case B.
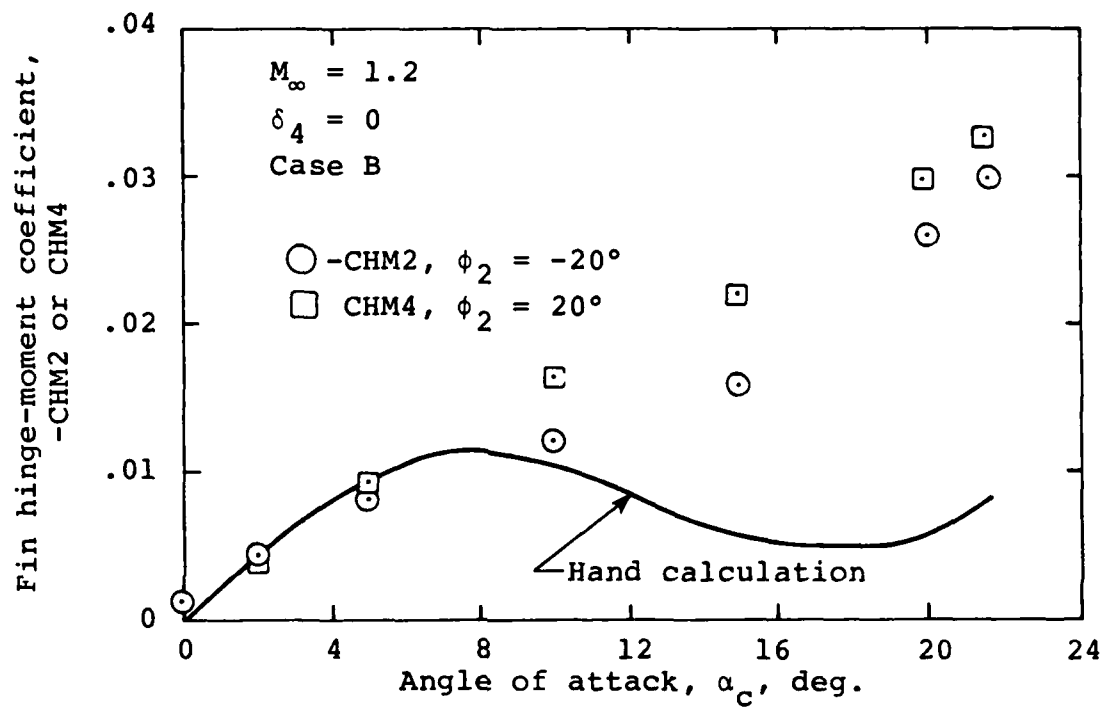
(b) Hinge-moment coefficient

Figure 49.- Concluded.
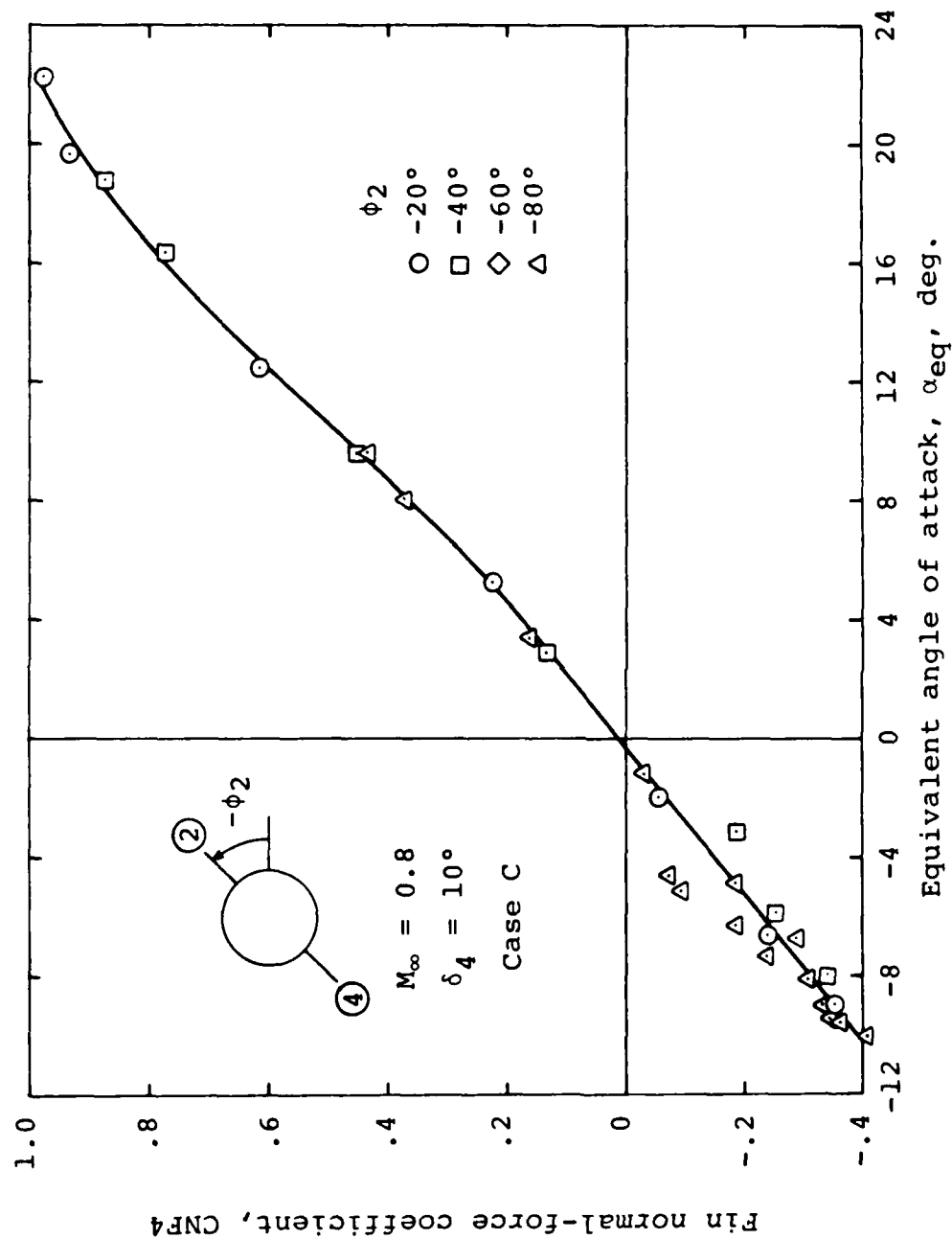
Figure 50.- Correlation curves of CNF4 vs. α_{eq} for fin 4 on triservice missile for various deflections; windward side, case C.
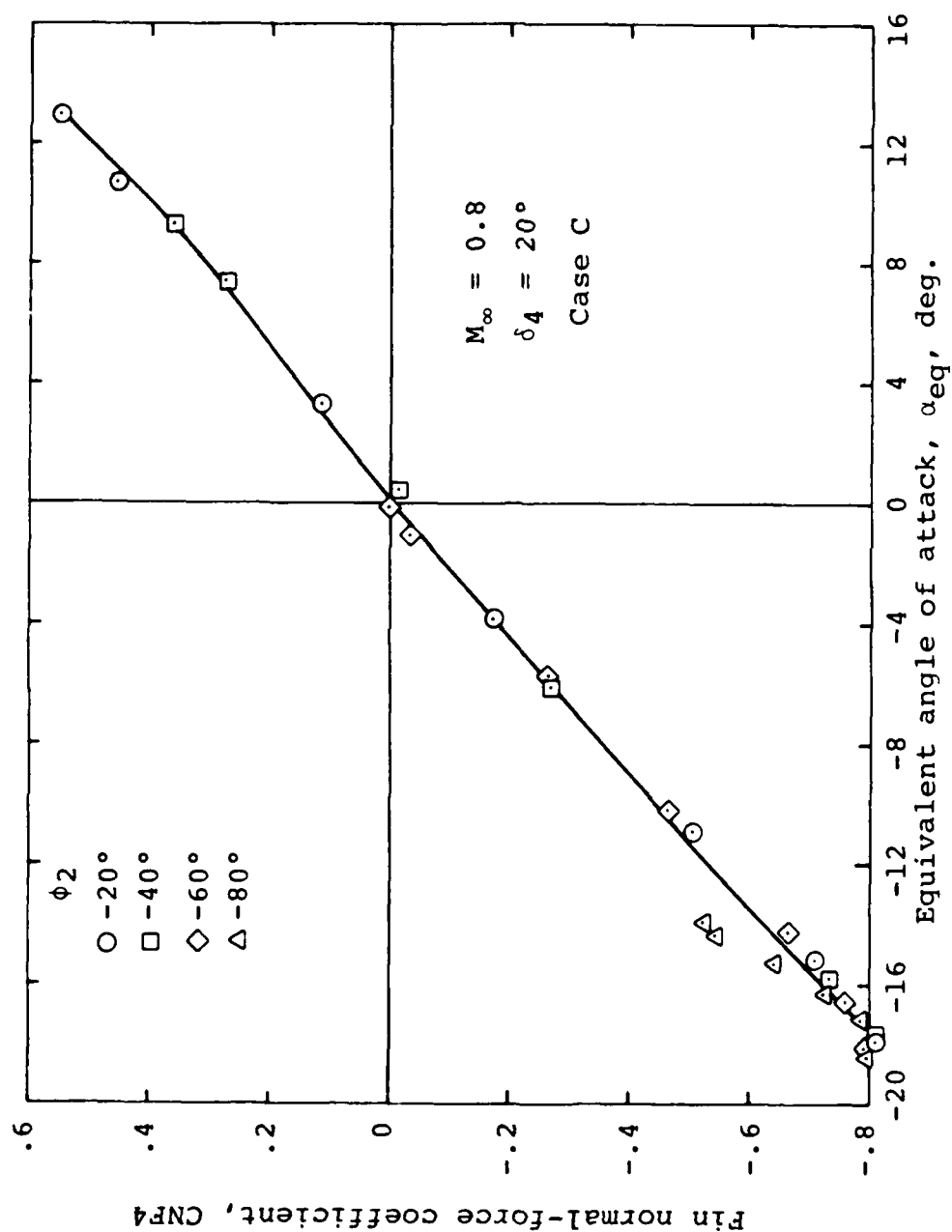
(a) $\delta_4 = 10°$

(b) $\delta_4 = 20°$

Figure 50.- Continued.

210
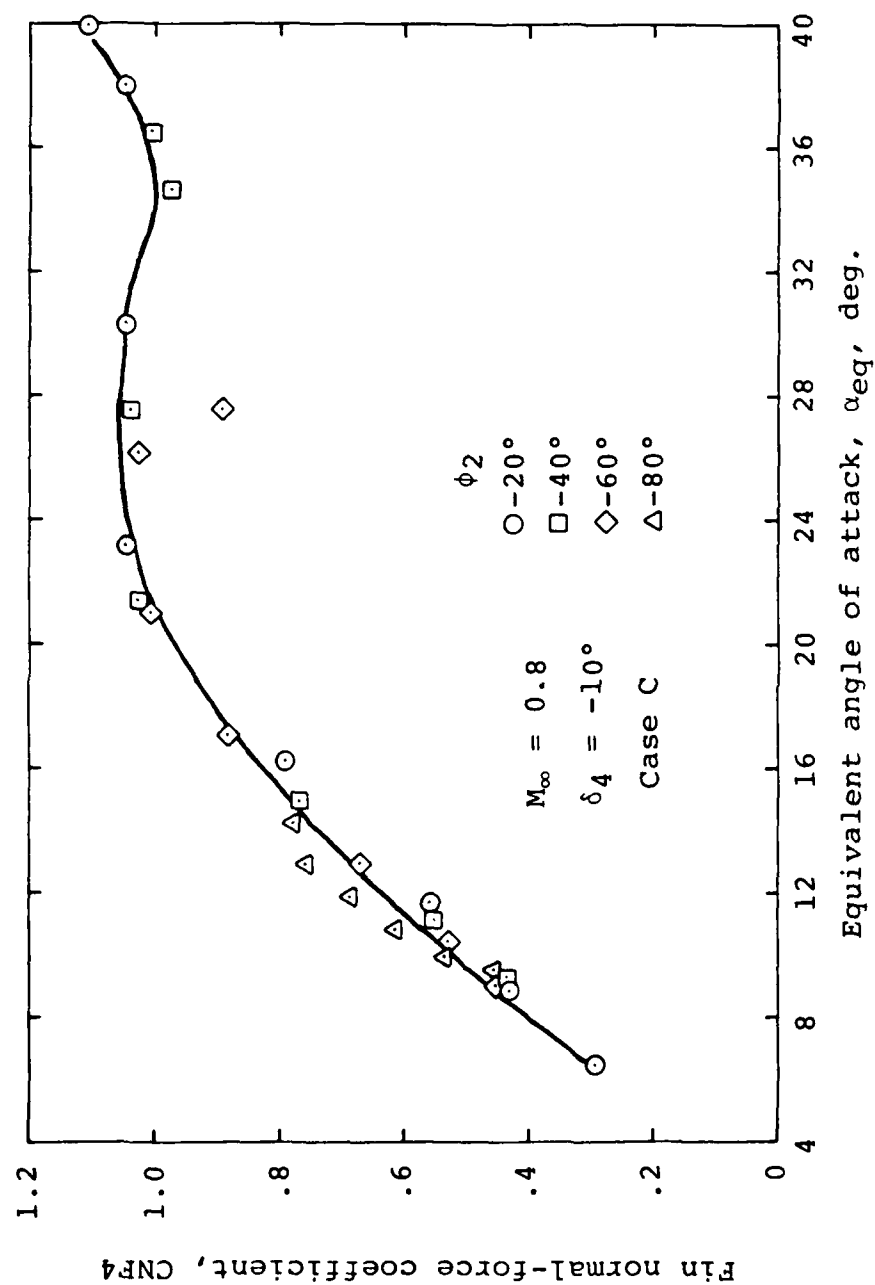
(c) $\delta_4 = -10°$

Figure 50.- Continued.
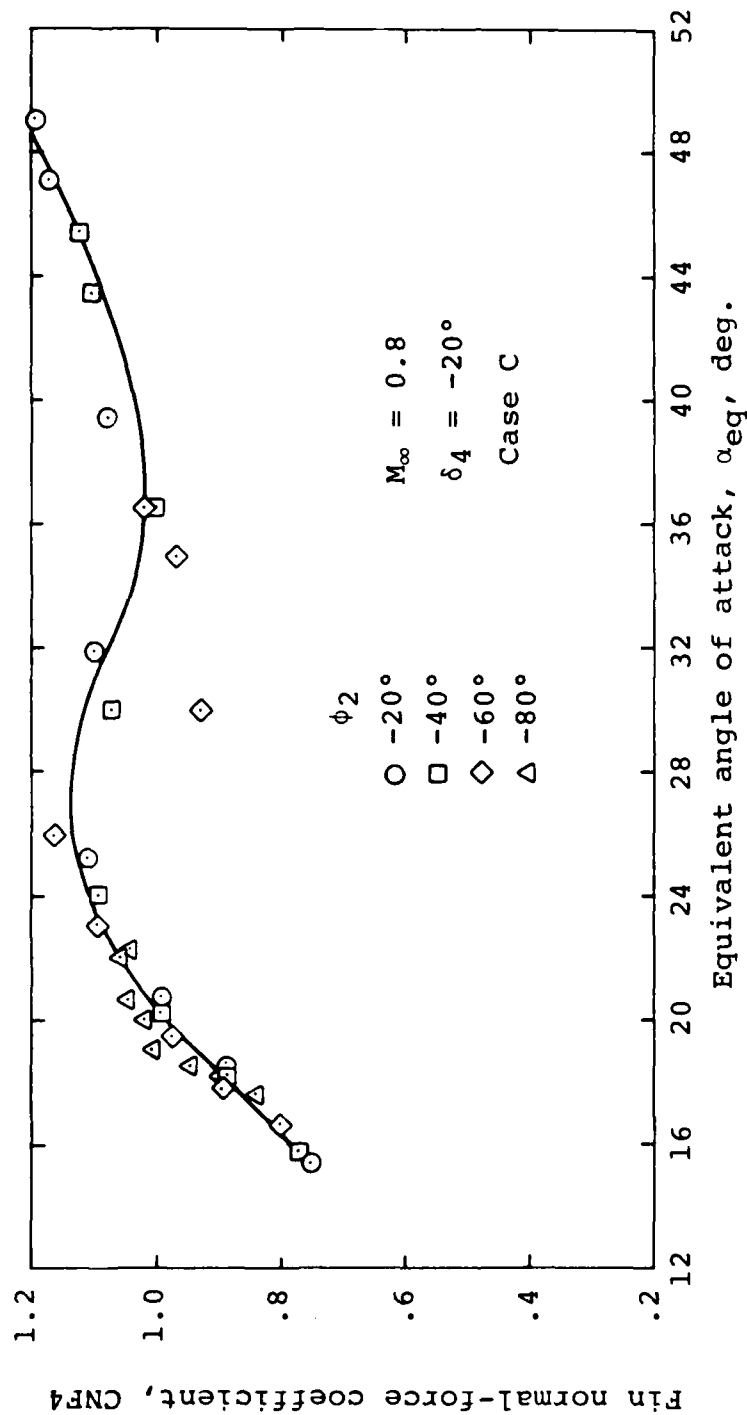
(d) $\delta_4 = -20°$

Figure 50.- Concluded.

212
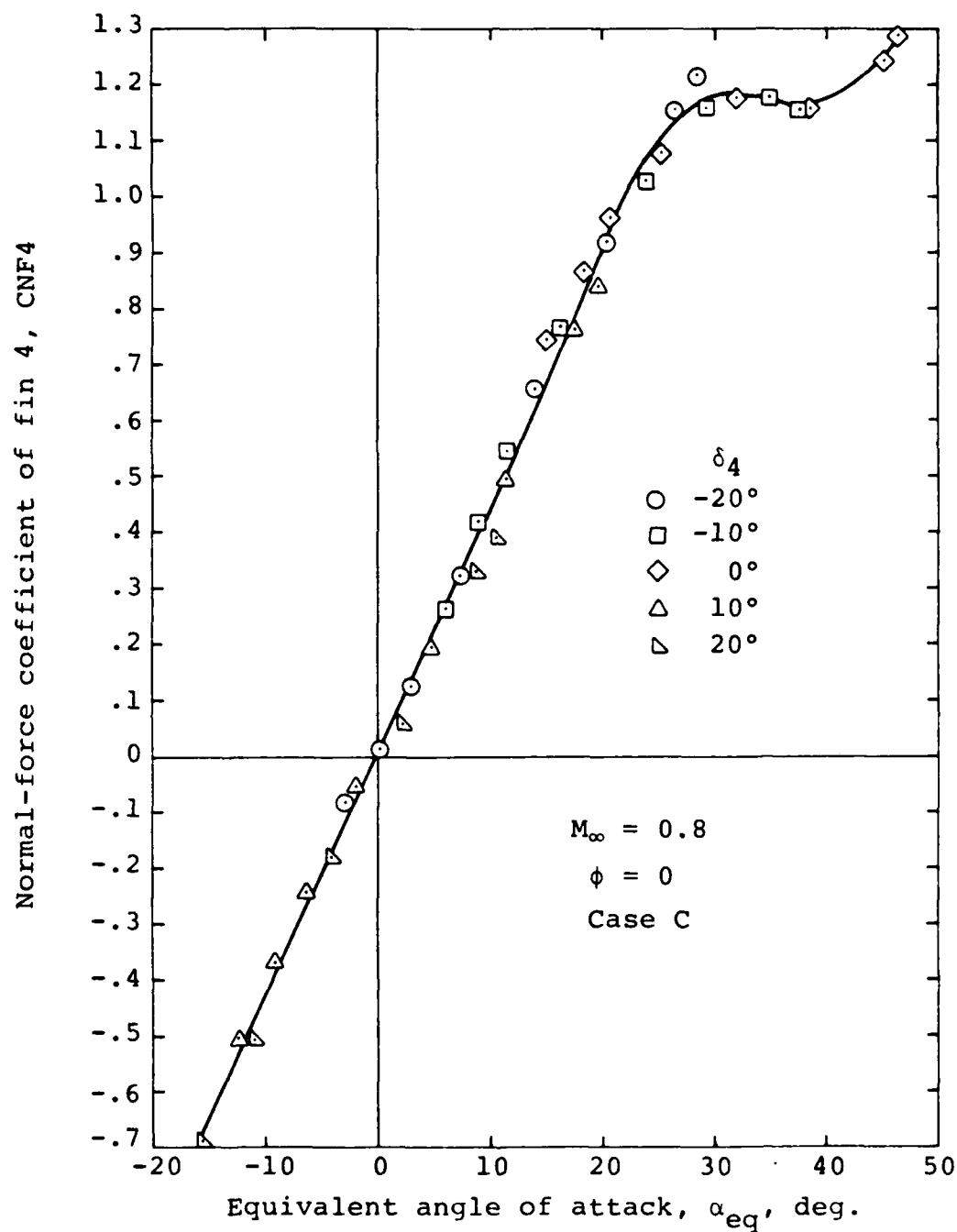
Figure 51.- Correlation of fin 4 normal-force coefficient
for $\phi = 0$ and various fin deflections; T51 fin.
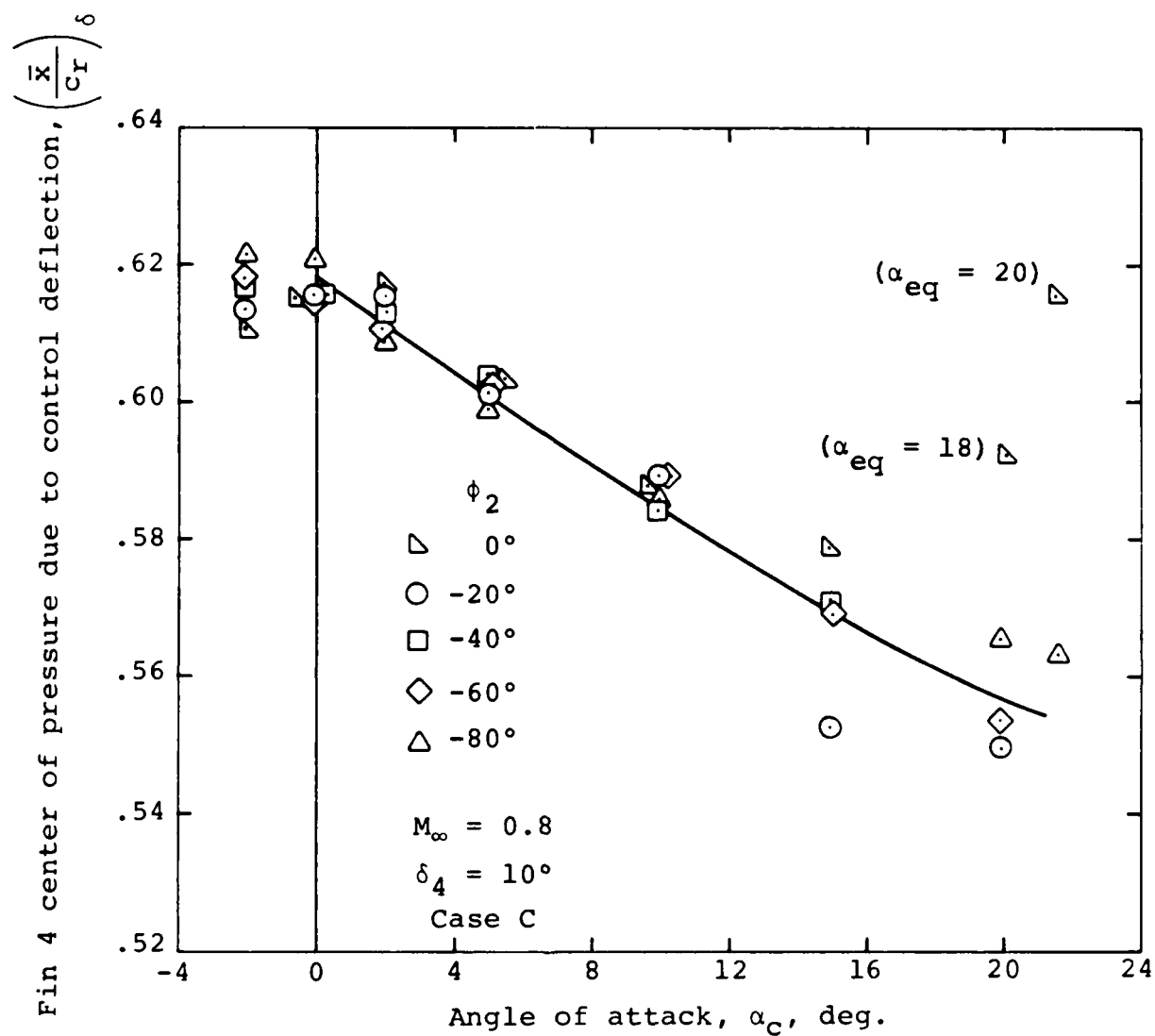
(a) $\delta_4 = 10°$

Figure 52.- Center of pressure due to control deflection for T51 fin mounted on triservice missile; $M_\infty = 0.8$, windward fin, case C.
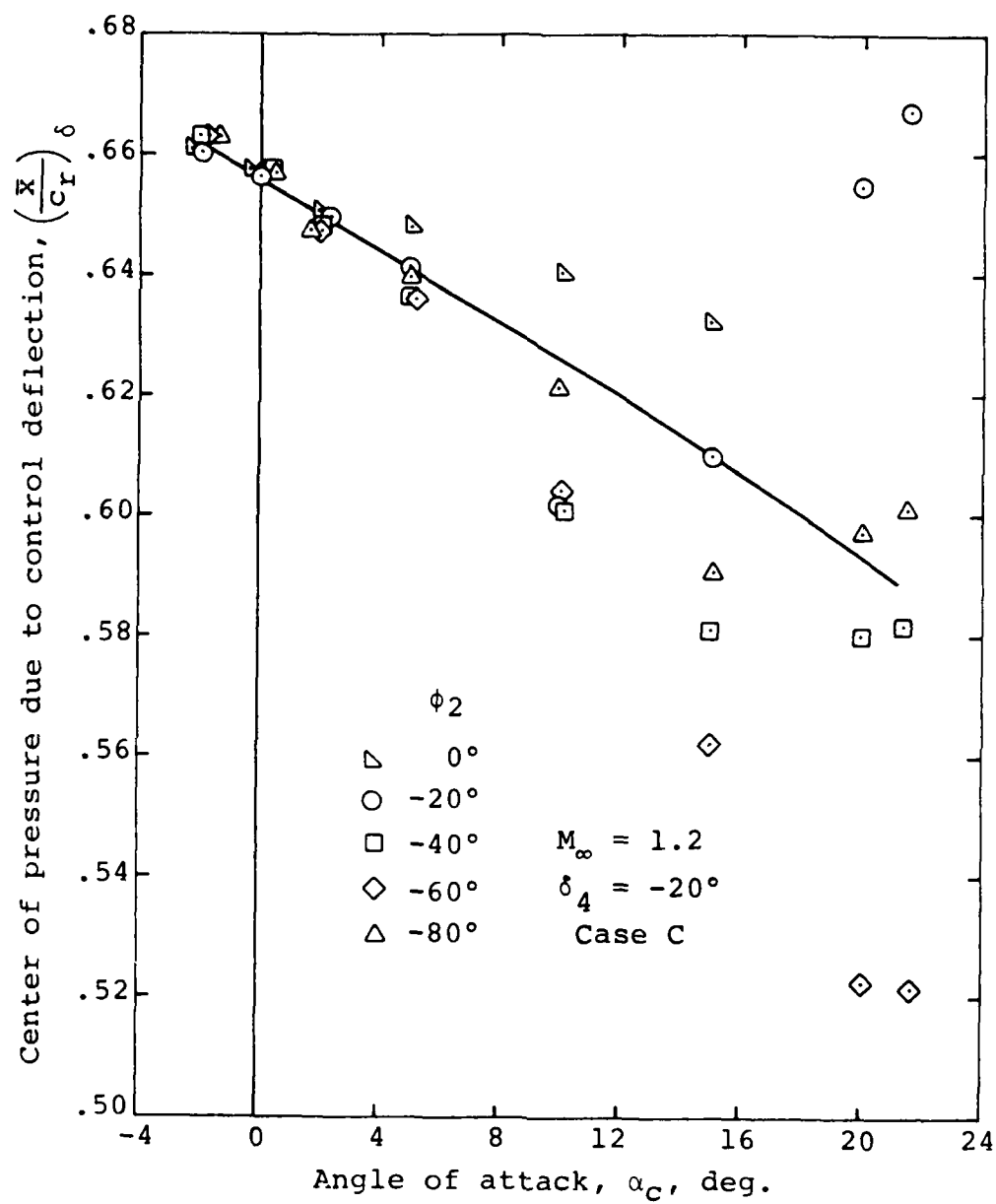
214
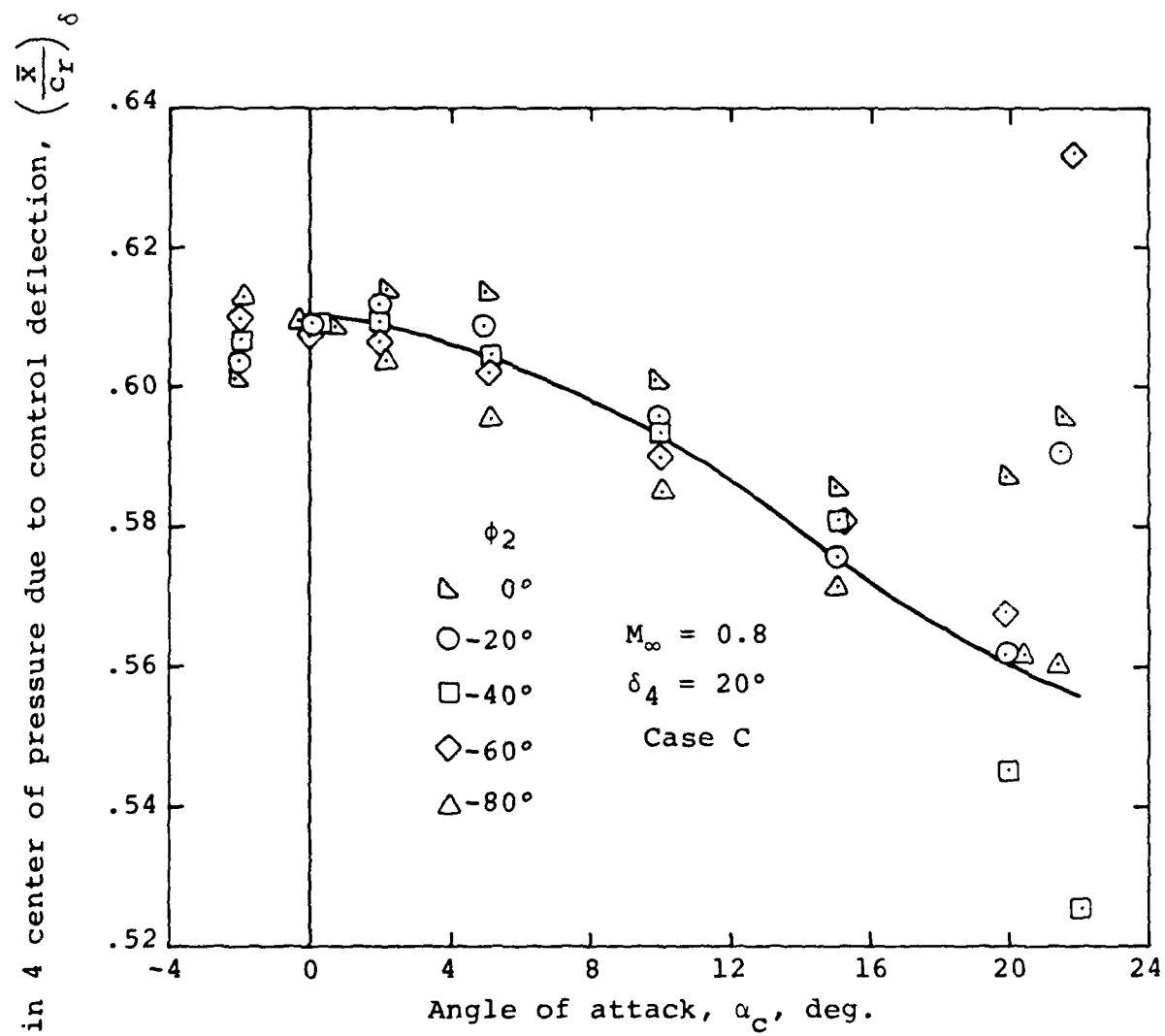
(b) $\delta_4 = 20°$

Figure 52.- Continued.
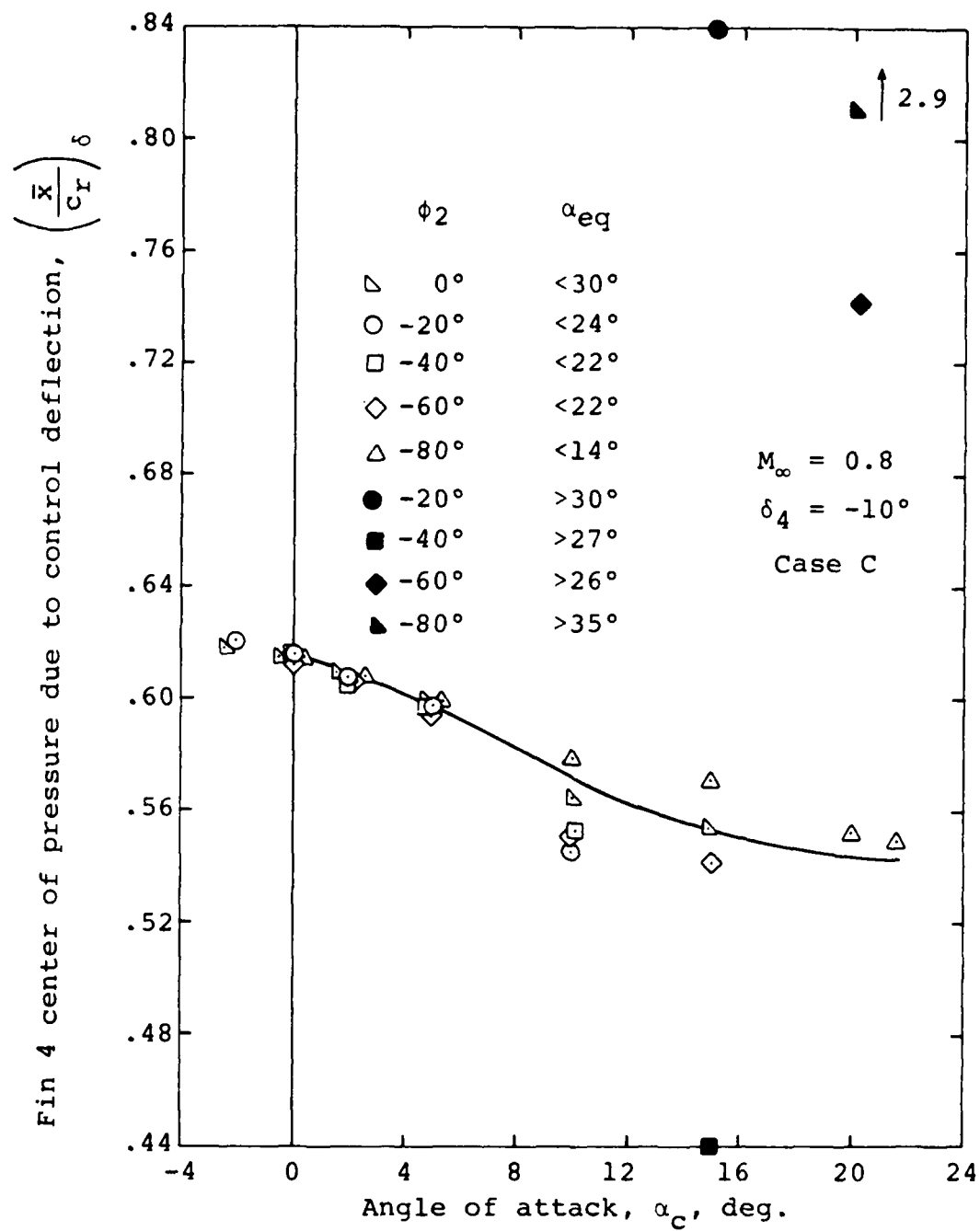
(c) $\delta_4 = -10°$

Figure 52.- Continued.
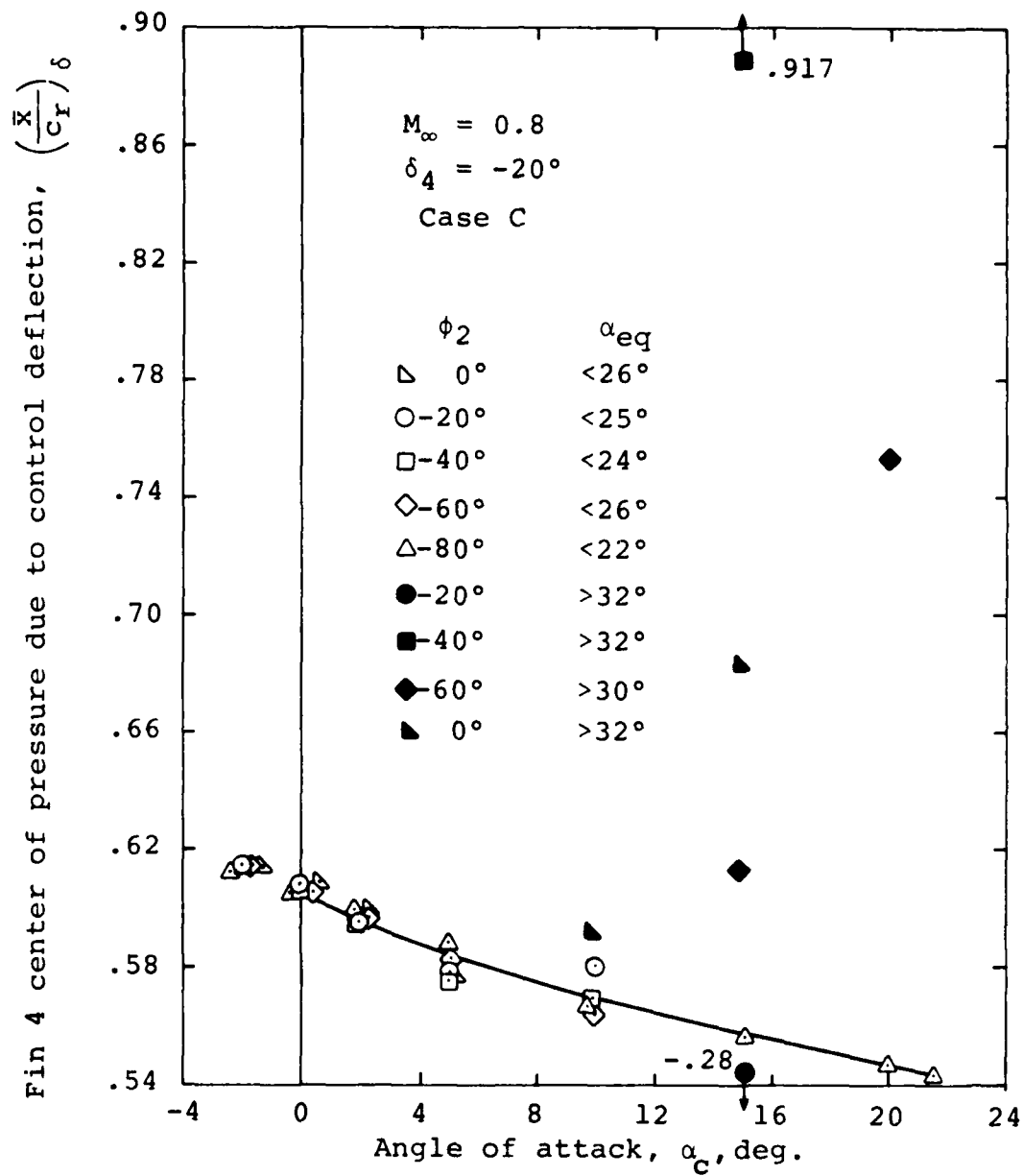
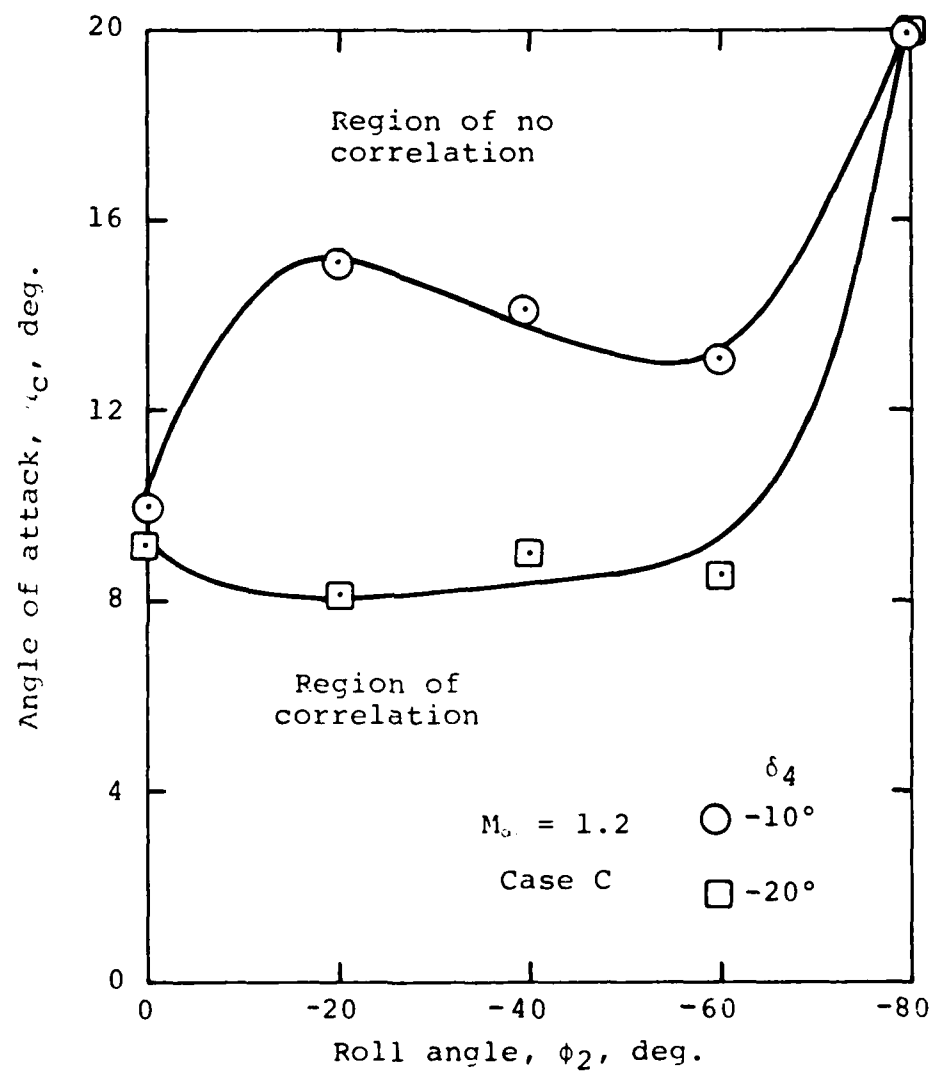(d) $\delta_4 = -20°$

Figure 52.- Concluded.
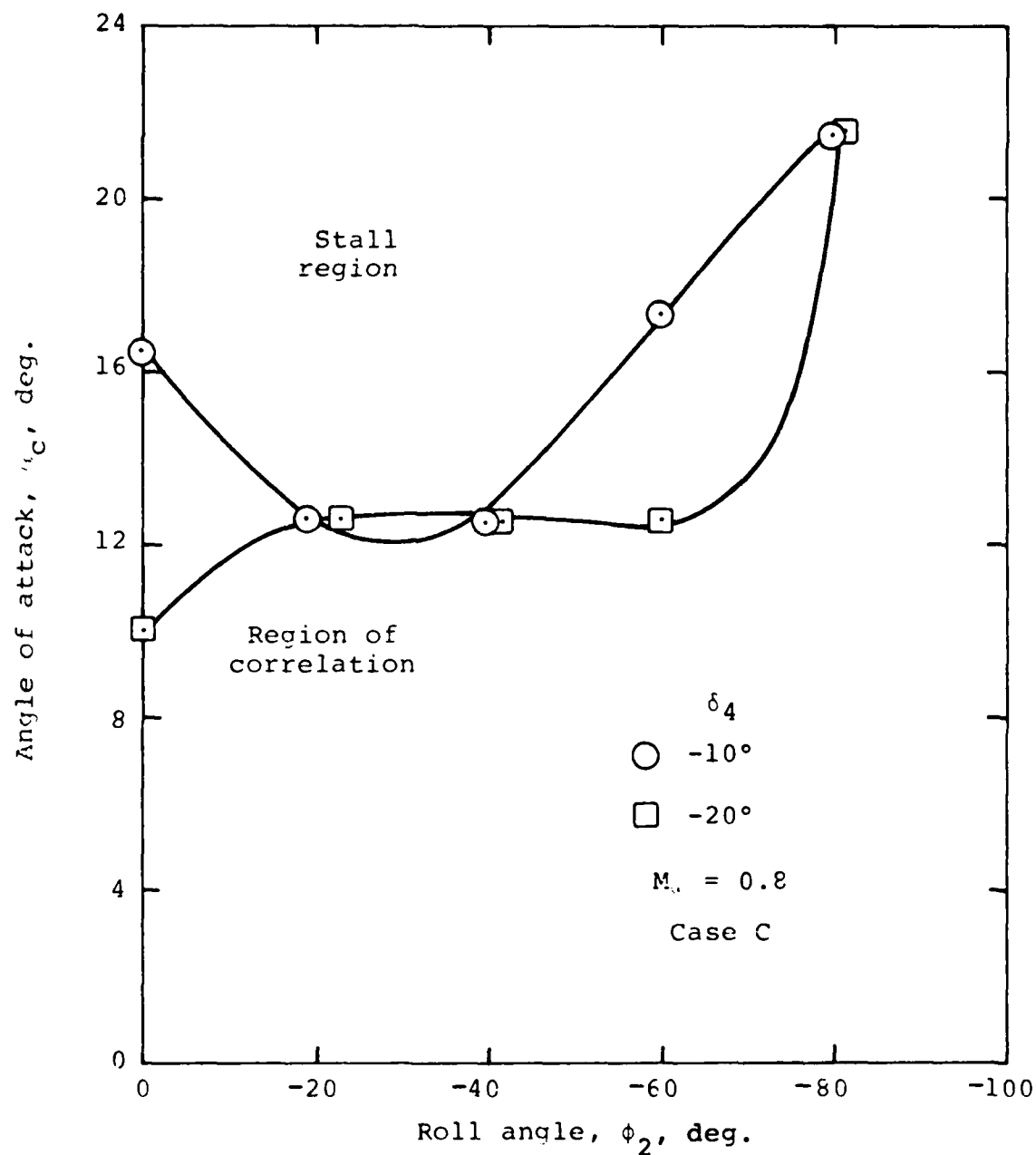
Figure 53.- Approximate limits of validity of correlation
curves for $(\bar{x}/c_r)_\delta$; $M_\infty = 0.8$, windward fin, case C.
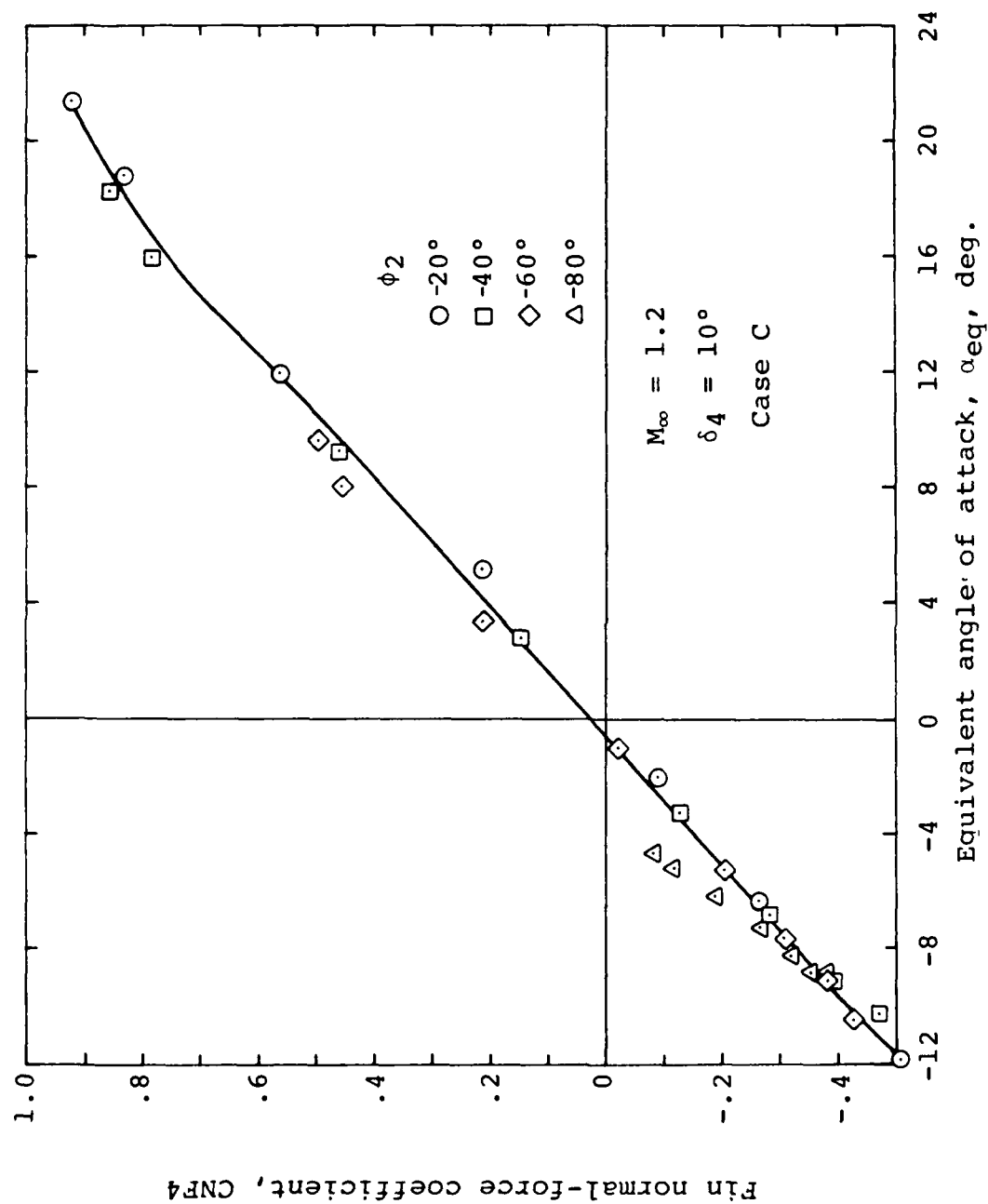
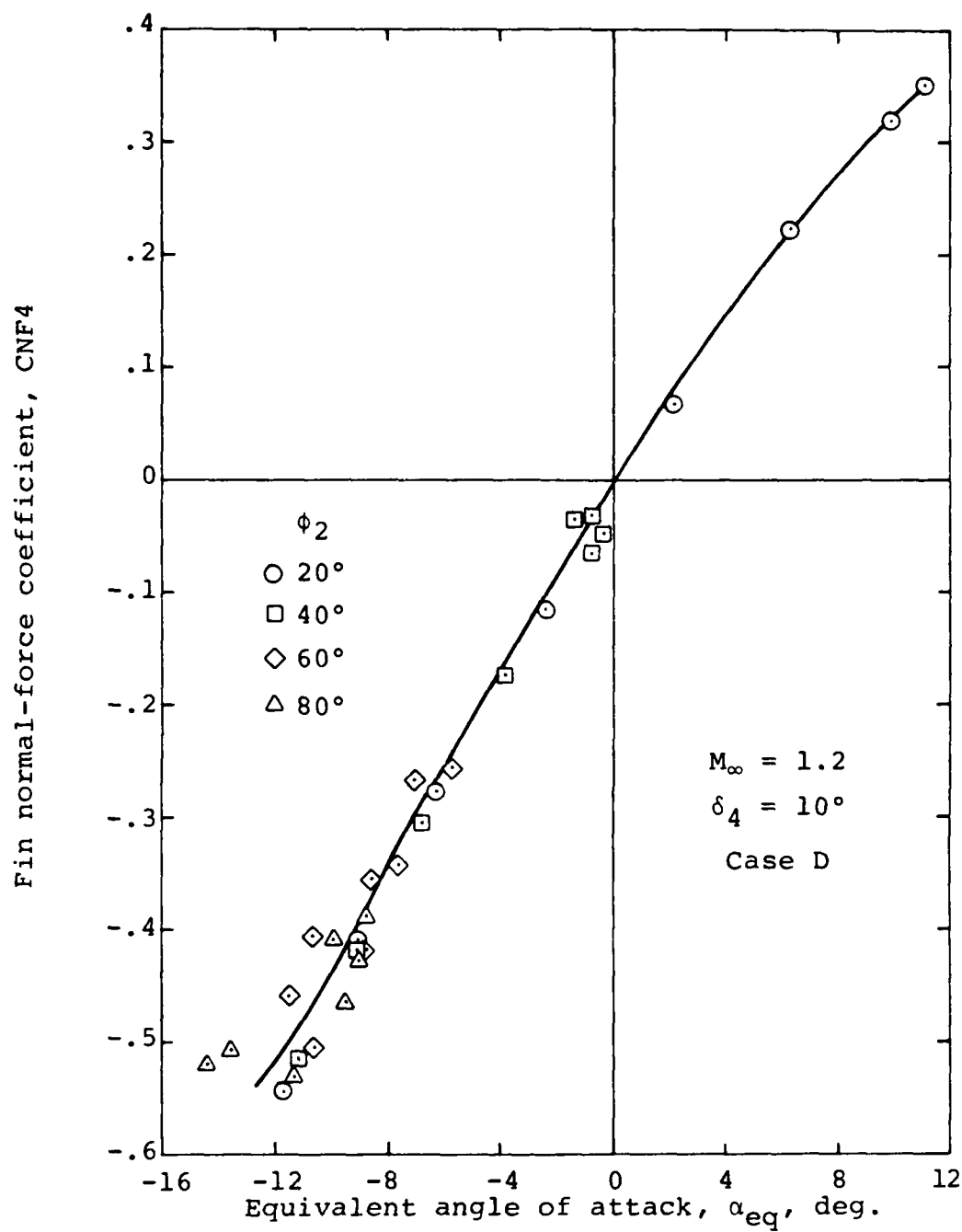Figure 54.- Correlation curves of CNF4 vs. α_{eq} for fin 4 on triservice missile for various deflections; windward side, case C.

(a) $\delta_4 = 10°$

219

(b) $\delta_4 = 20°$

Figure 54.- Continued.

$M_\infty = 1.2$

$\delta_4 = 10°$

Case C

ϕ_2

O -20°
□ -40°
◇ -60°
△ -80°

Equivalent angle of attack, α_{eq}, deg.
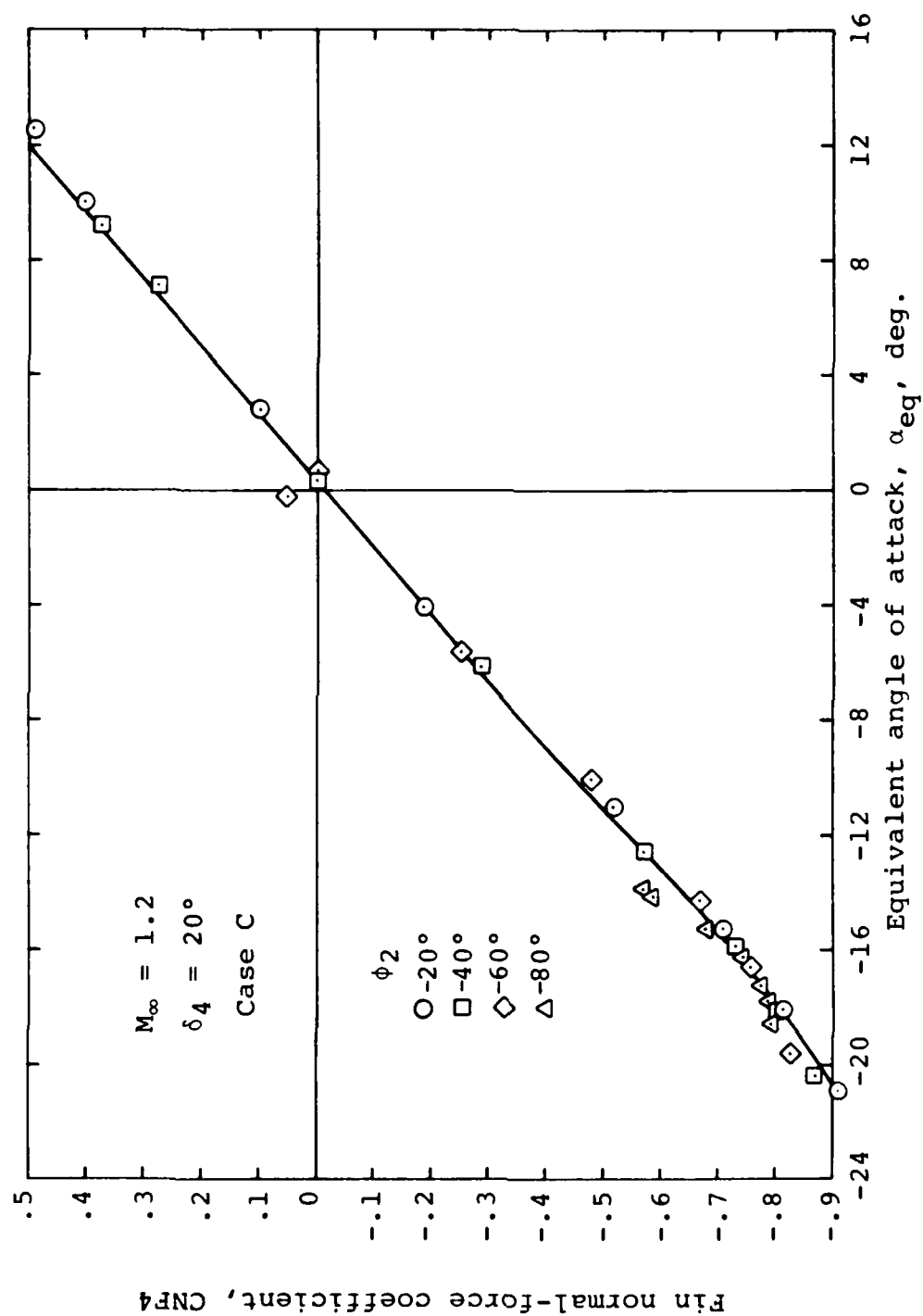
Fin normal-force coefficient, CNF4
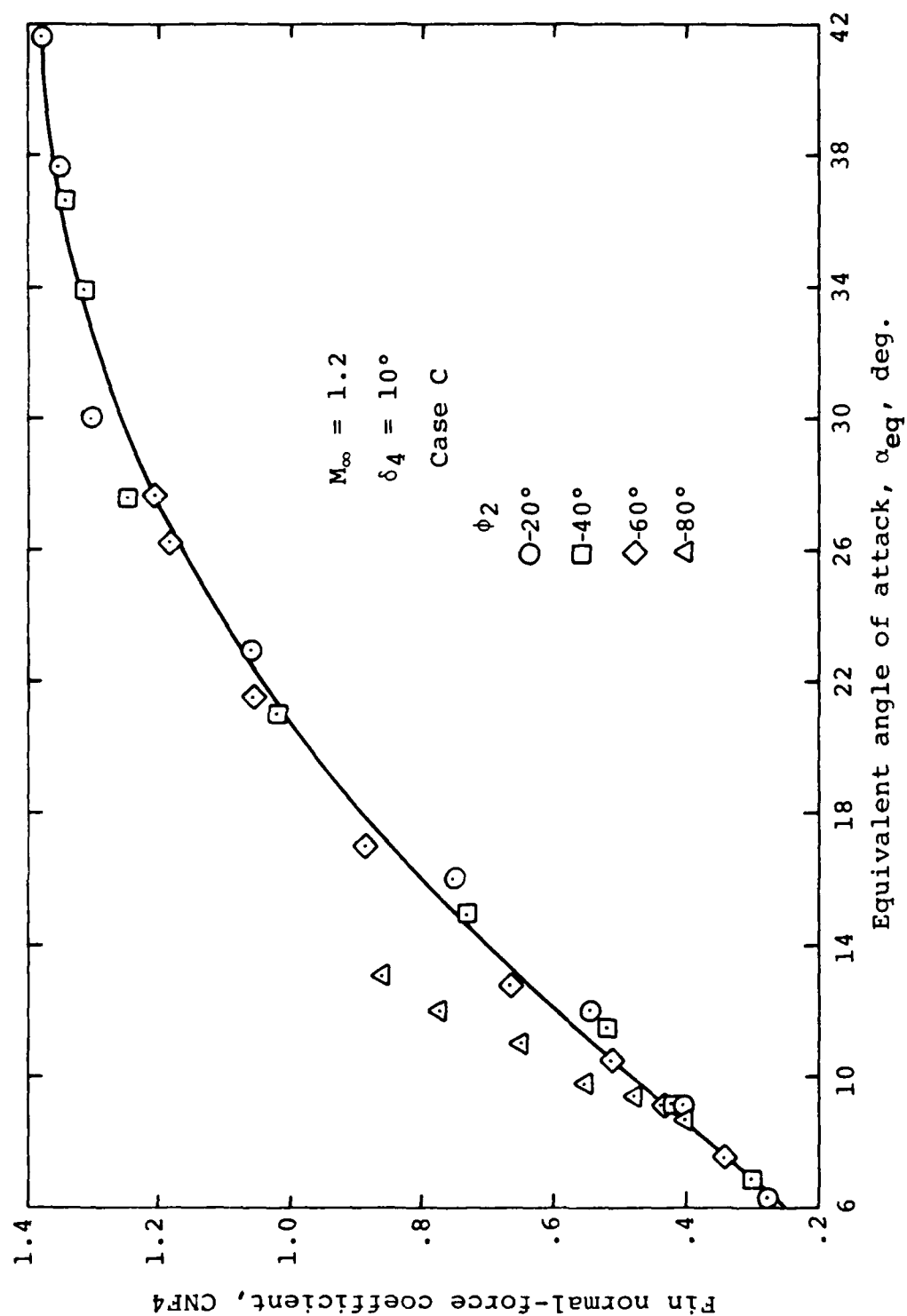
(c) $\delta_4 = -10°$

Figure 54.- Continued.
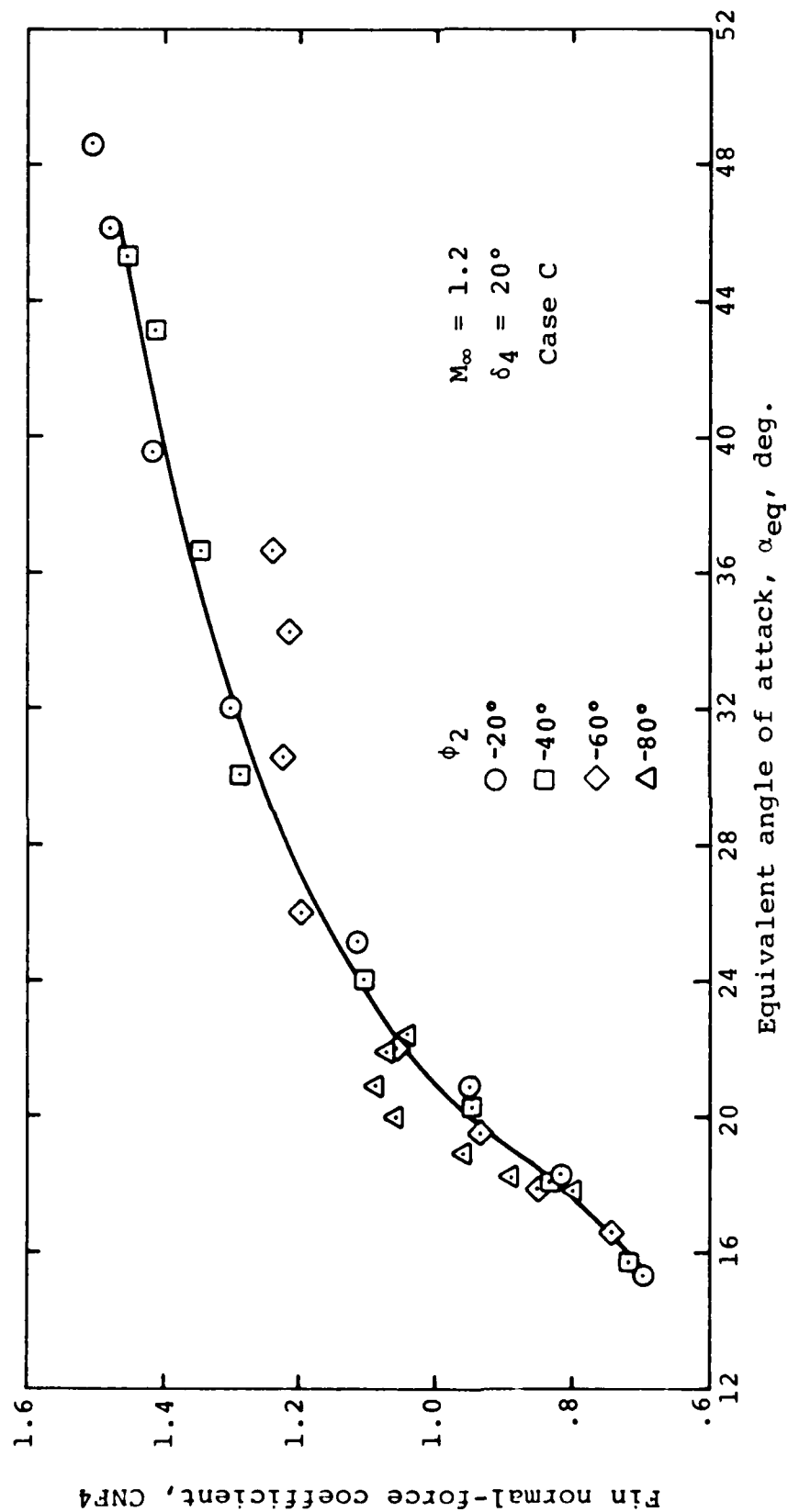
(d) $\delta_4 = -20°$

Figure 54.- Concluded.

222
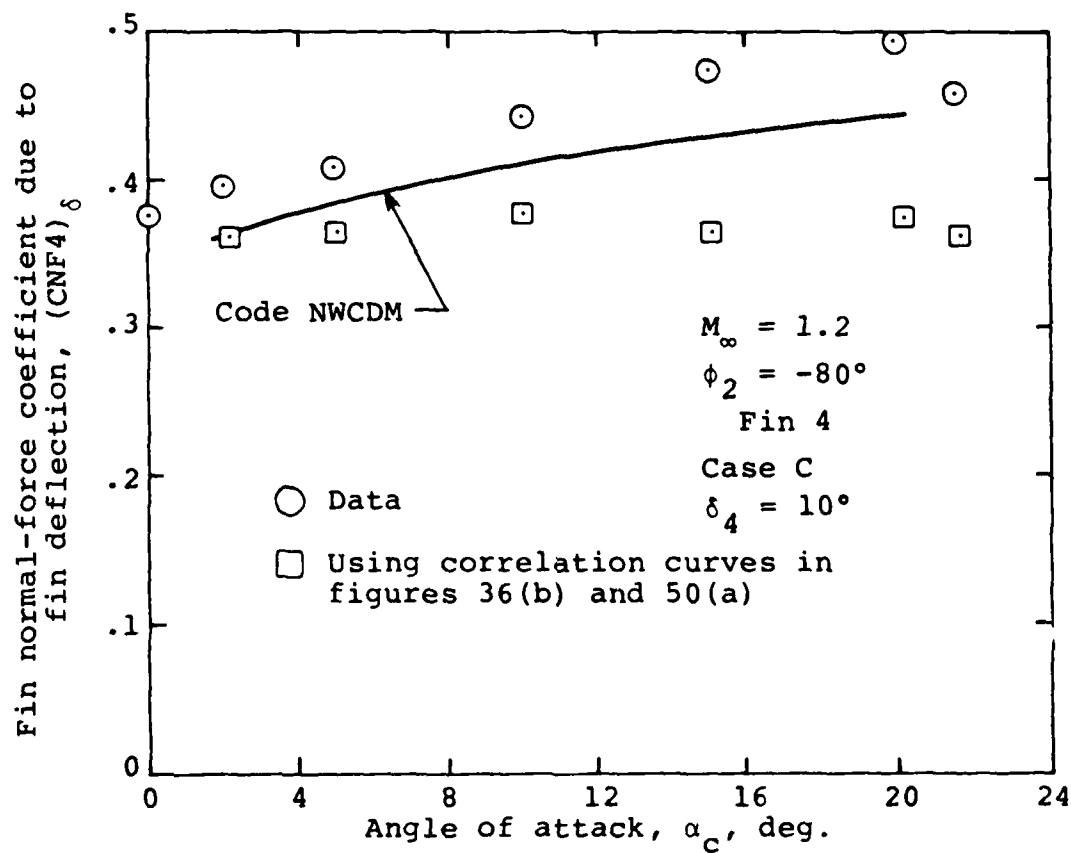
Figure 55.- Comparison of various methods for
obtaining CNF due to fin deflection.

223
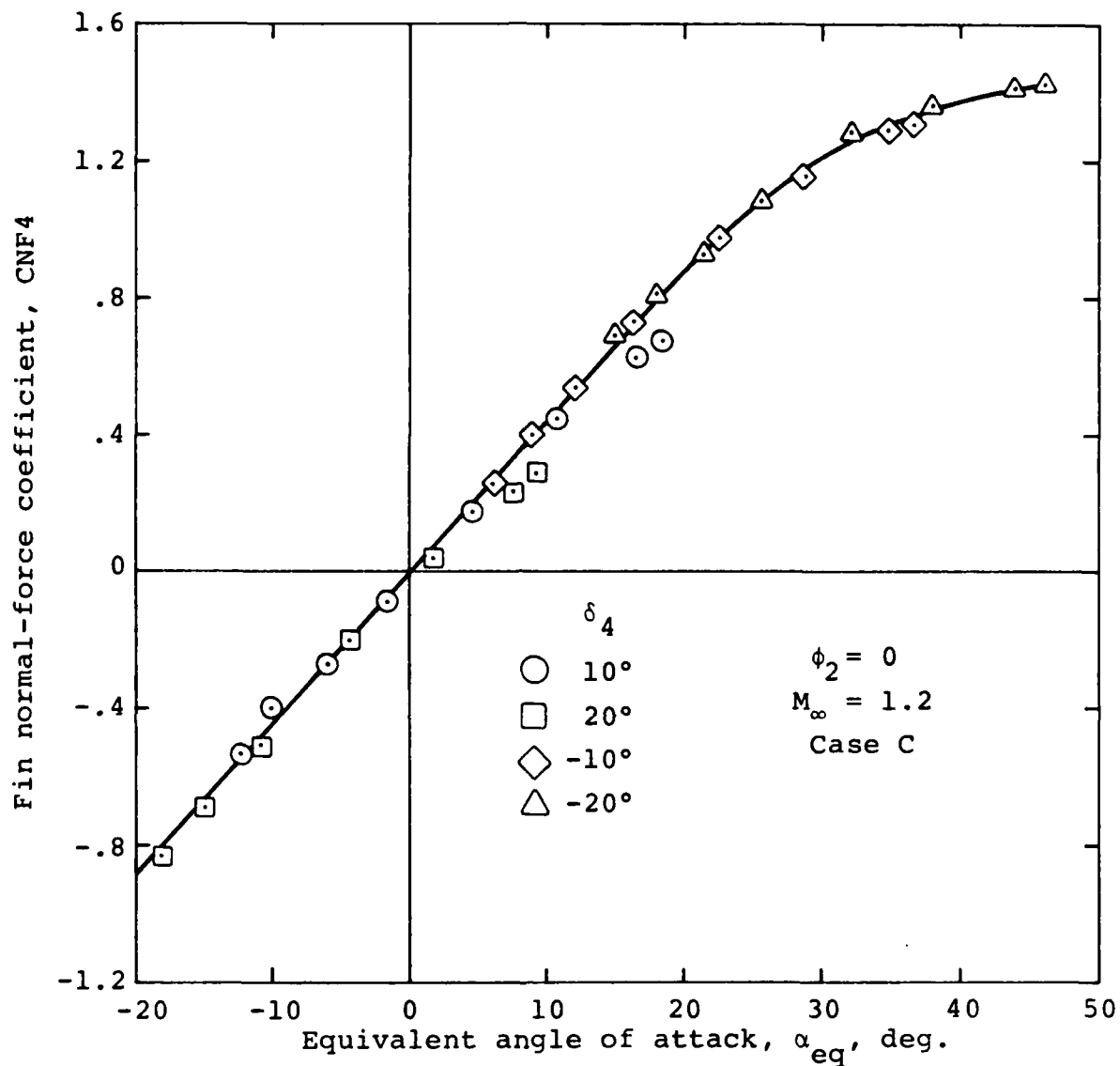
(a) Normal-force coefficient

Figure 56.- Correlation of fin 4 normal-force coefficient and center of pressure for $\phi_2 = 0$ and various fin deflections of T51 fin.

224
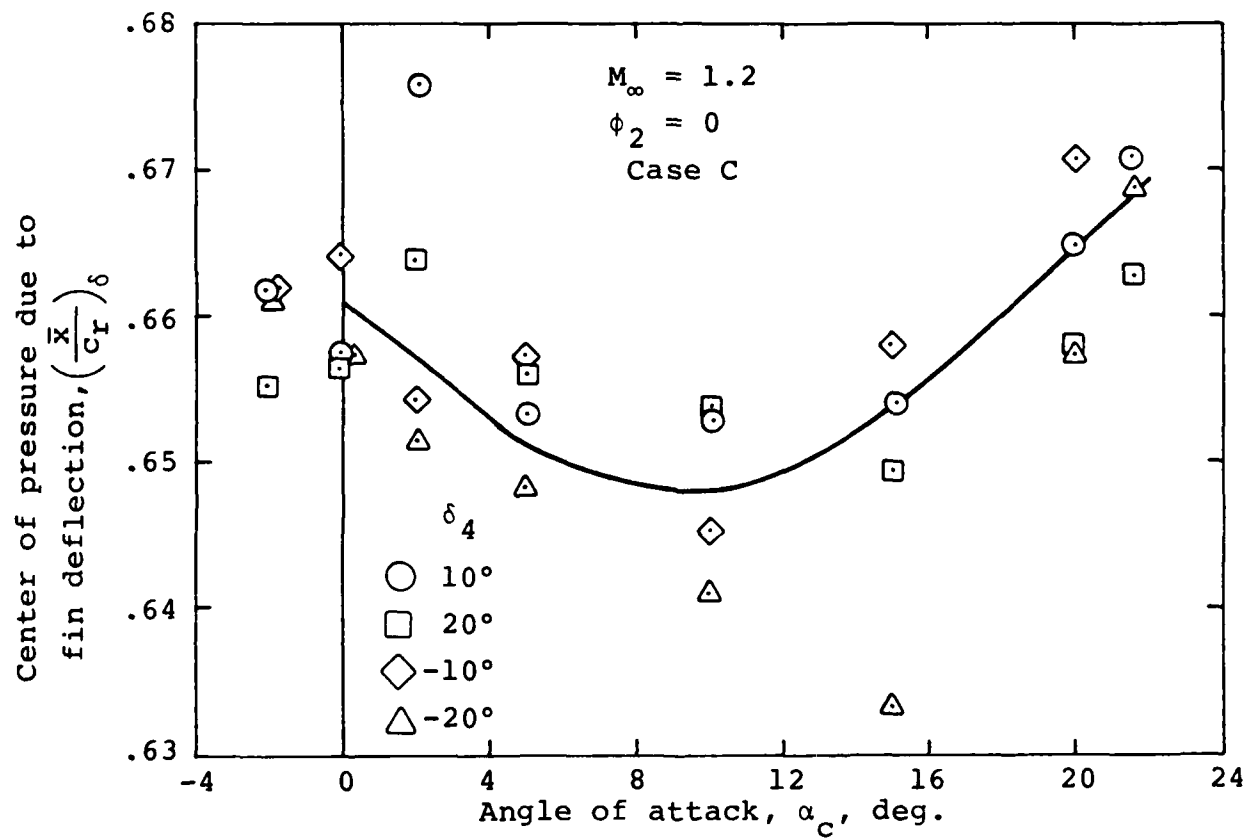
(b) Center of pressure due to fin deflection

Figure 56.- Concluded.
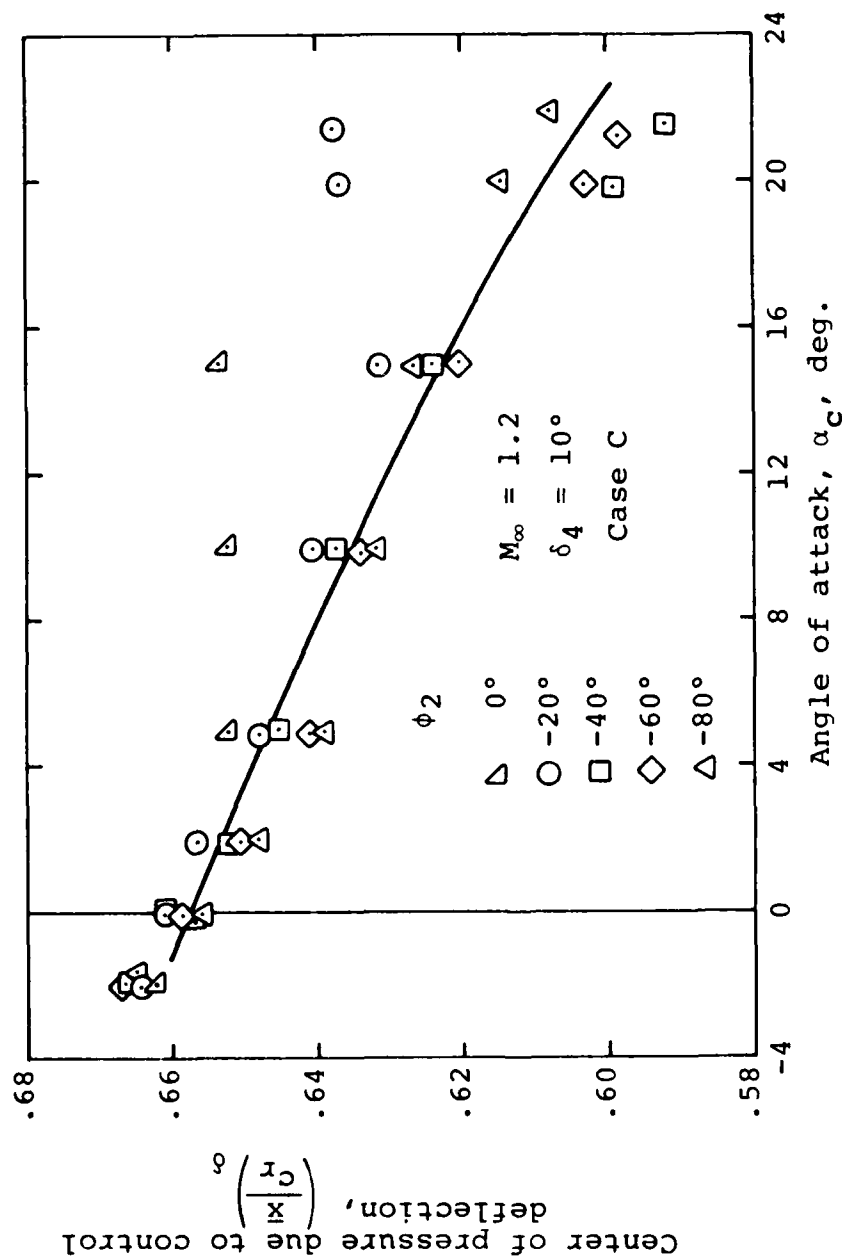
Figure 57.- Center of pressure due to control deflection for T51 fin mounted on triservice missile: $M_\infty = 1.2$, windward fin, case C.

(a) $\delta_4 = 10°$

226
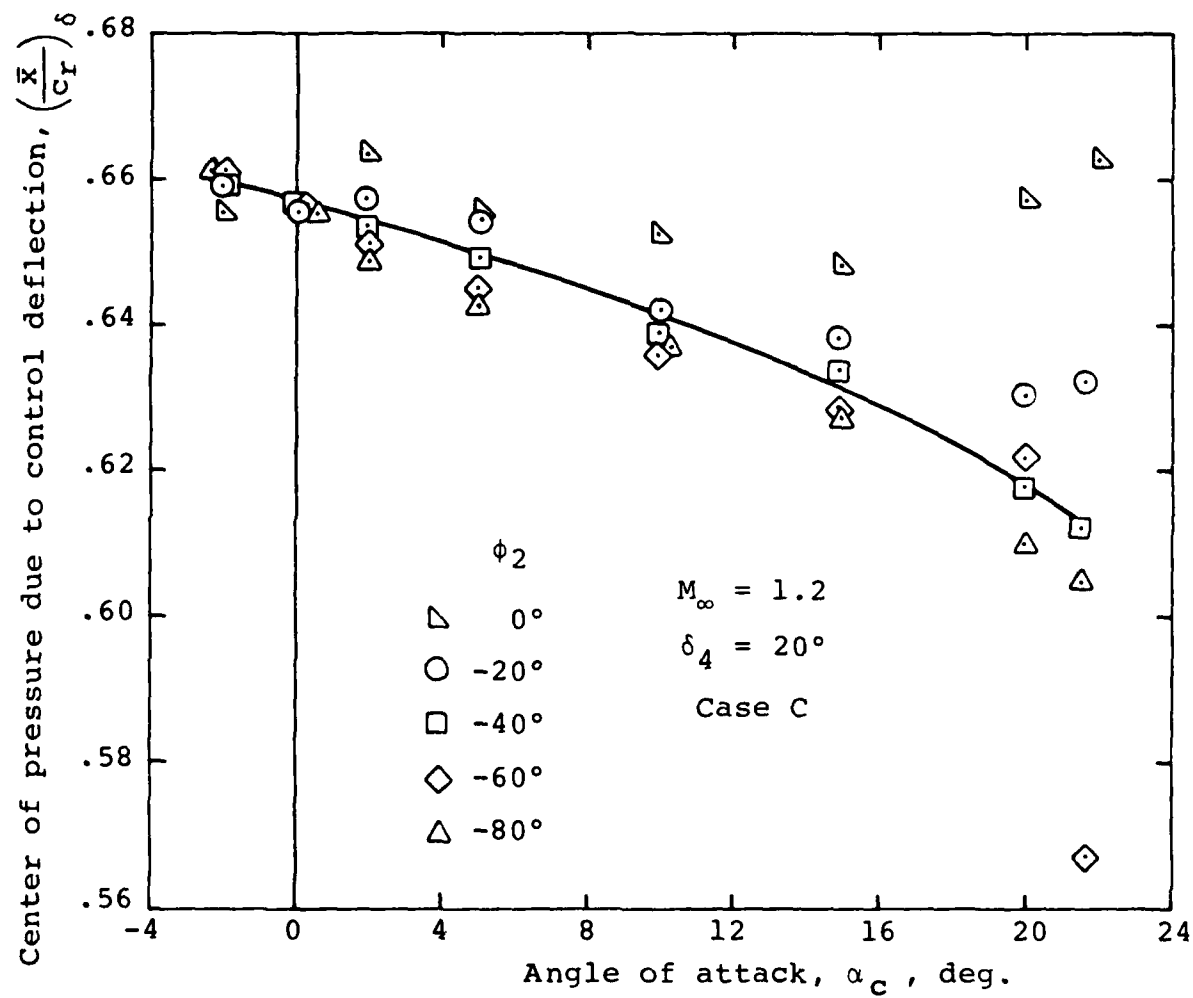
(b) $\delta_4 = 20°$

Figure 57.- Continued.
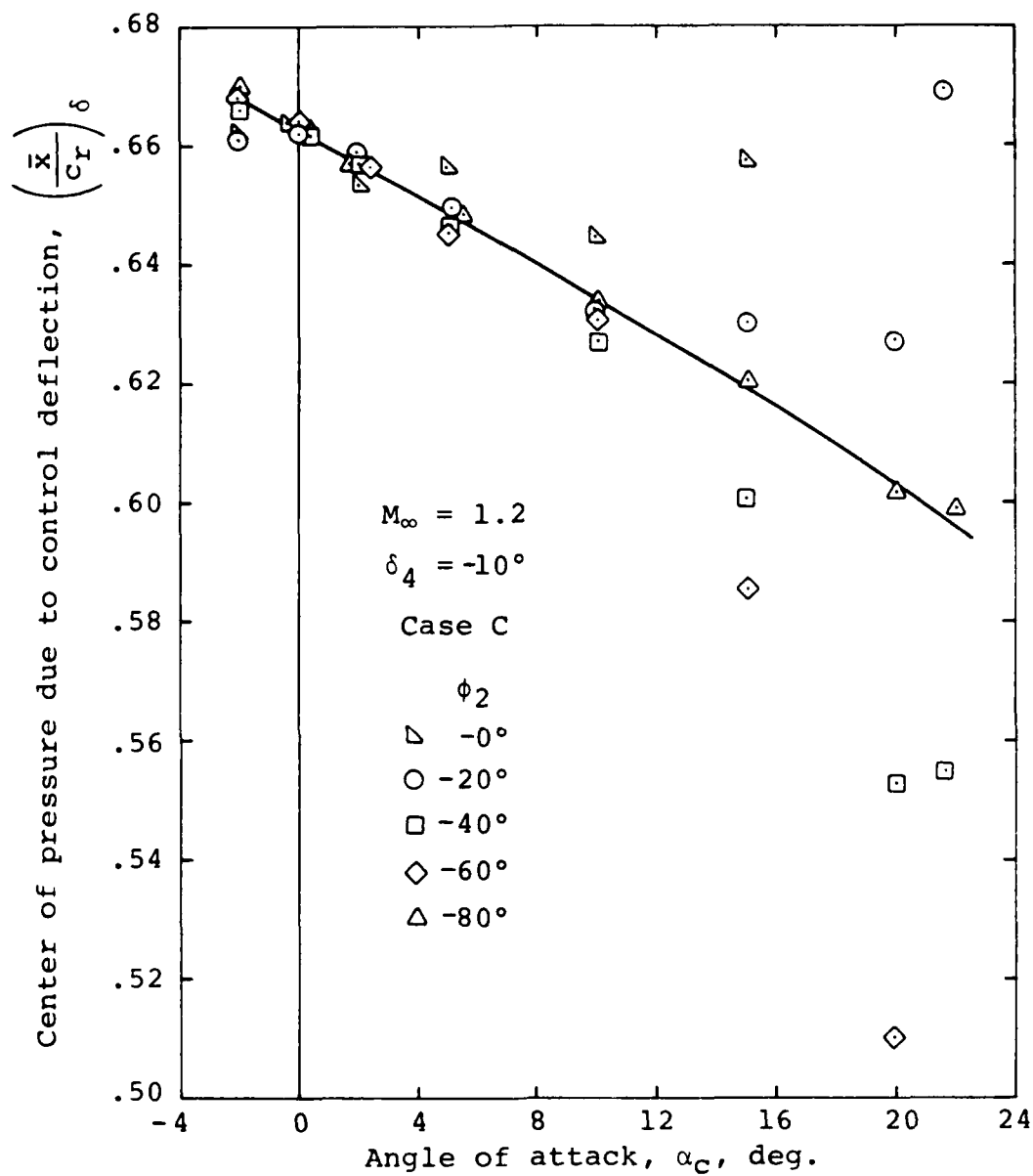
(c) $\delta_4 = -10°$

Figure 57.- Continued.

(d) $\delta_4 = -20°$

Figure 57.- Concluded.

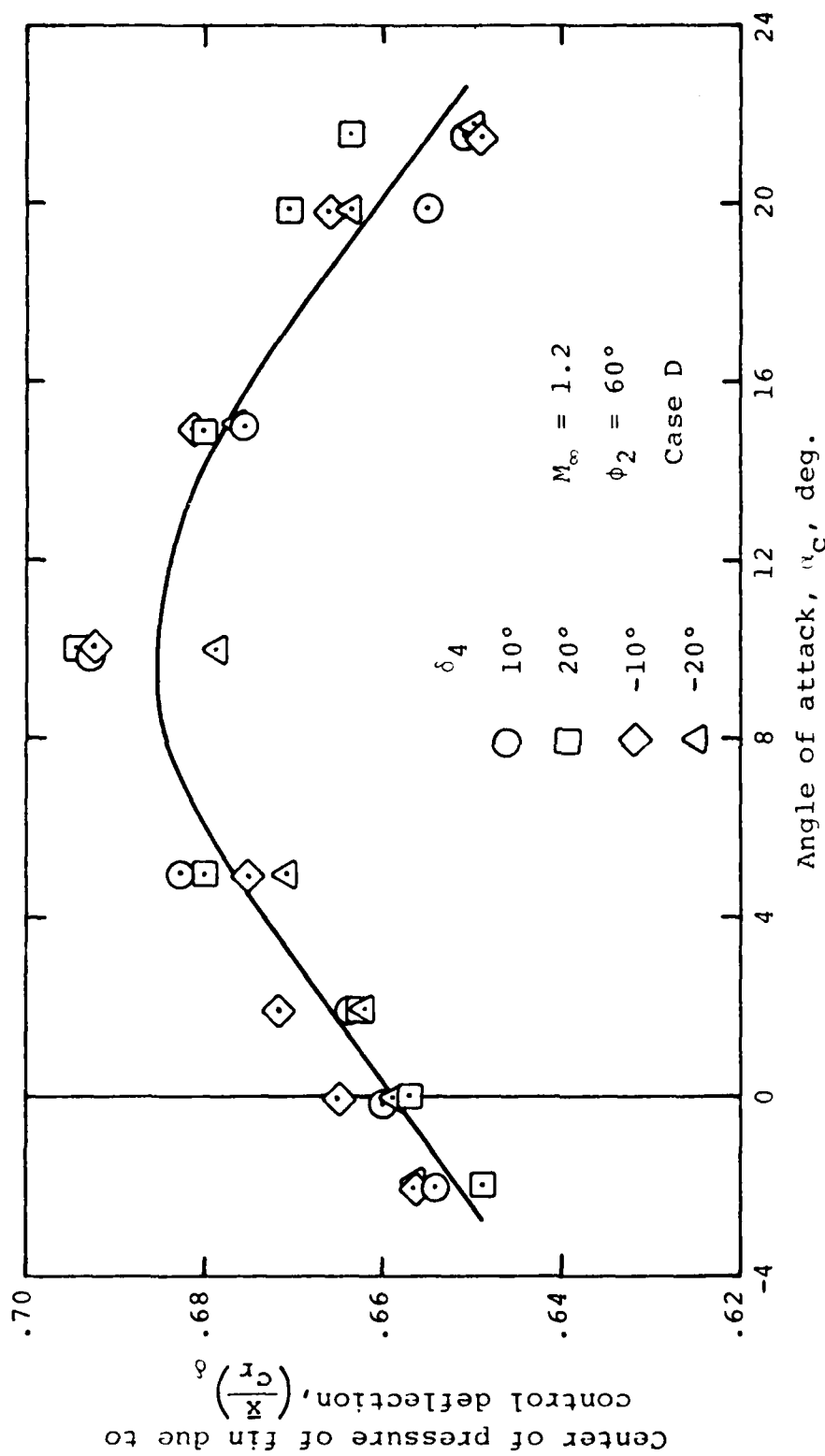Figure 58.- Approximate limits of validity of correlation curves for $(\bar{x}/c_r)_\delta$; $M_\alpha = 1.2$, windward fin, case C.
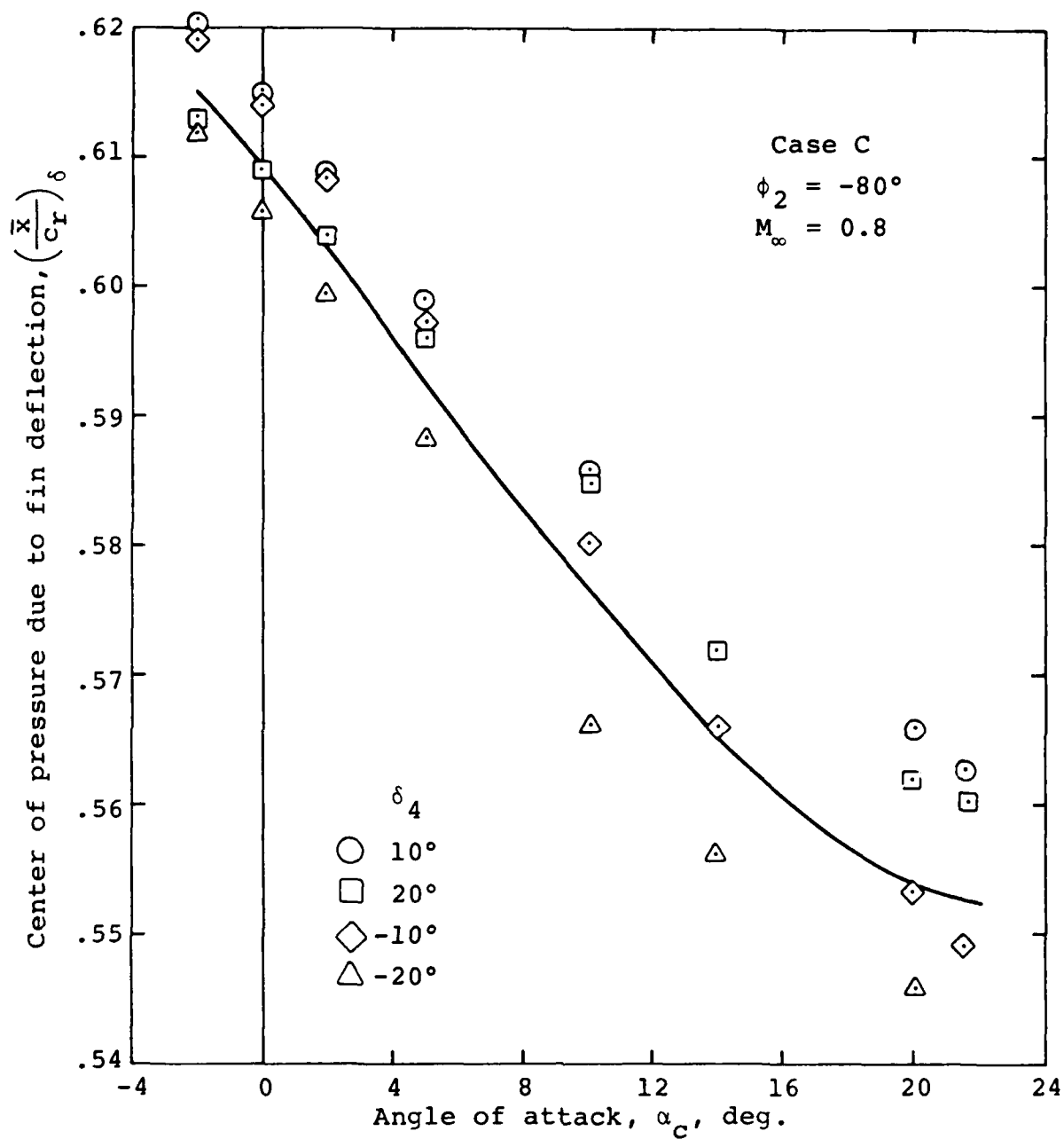
(a) $M_\infty = 0.8$

Figure 59.- Center of pressure due to control deflection for
fin 51 mounted on triservice missile correlated in an
alternate manner; windward fin, case C.

231
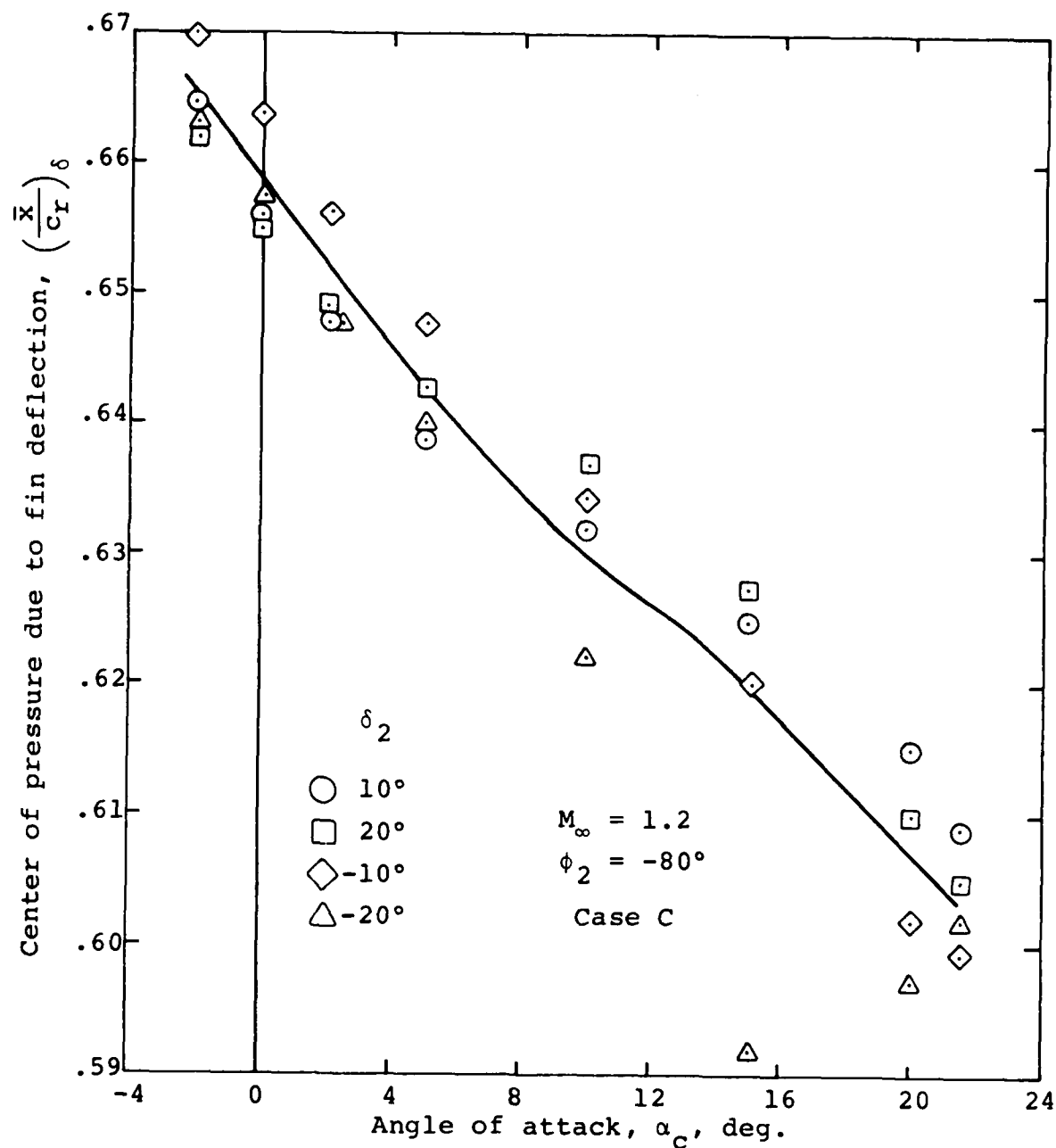
(b) $M_\infty = 1.2$

Figure 59.- Concluded.

232

(a) $\delta_4 = 10°$

Figure 60.- Correlation curves of CNF4 vs. α_{eq} for fin 4 on triservice missile for various deflections; $M_\infty = 1.2$, leeward fin, case D.

233
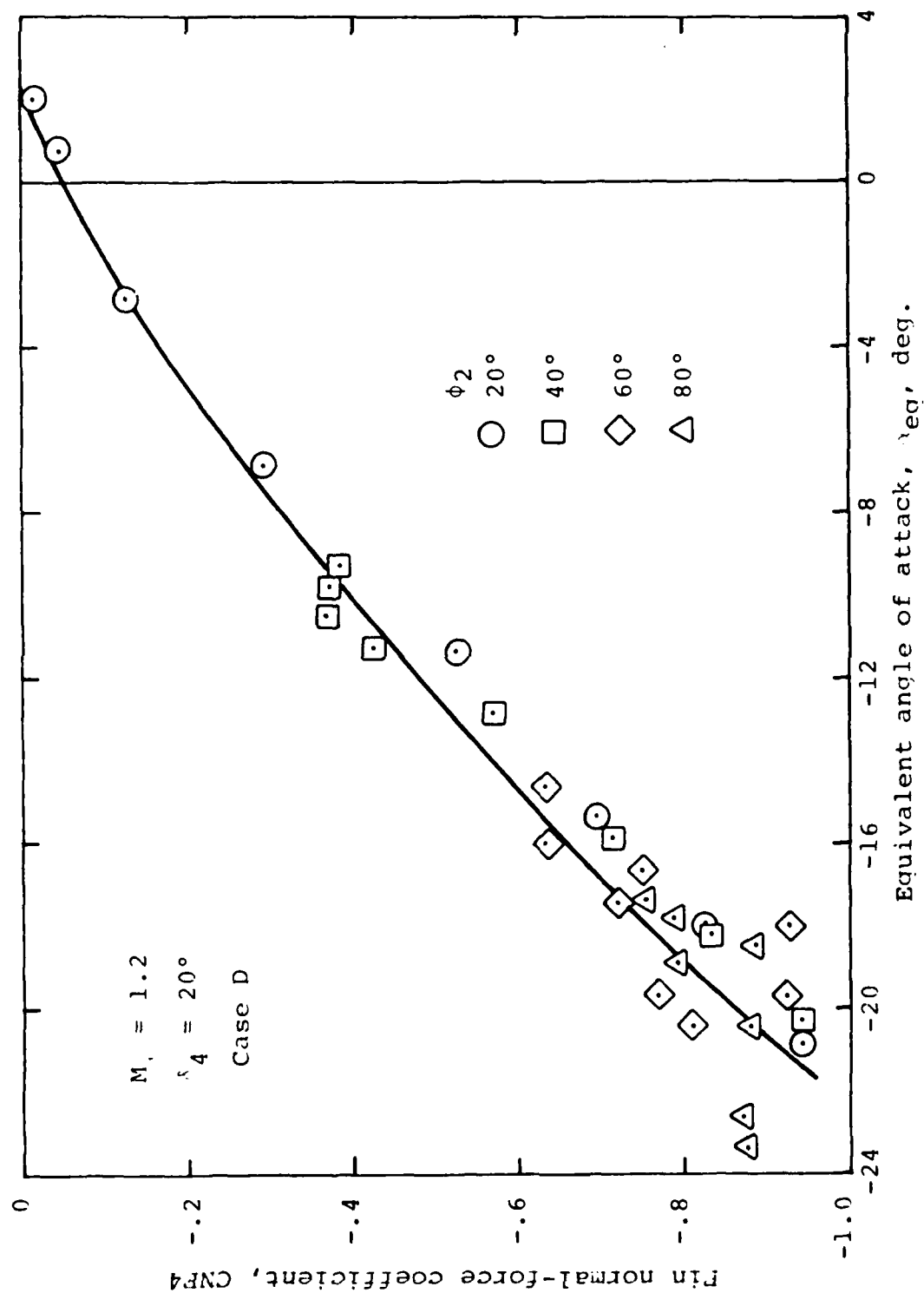
(b) $\delta_4 = 20°$

Figure 60. - Continued.
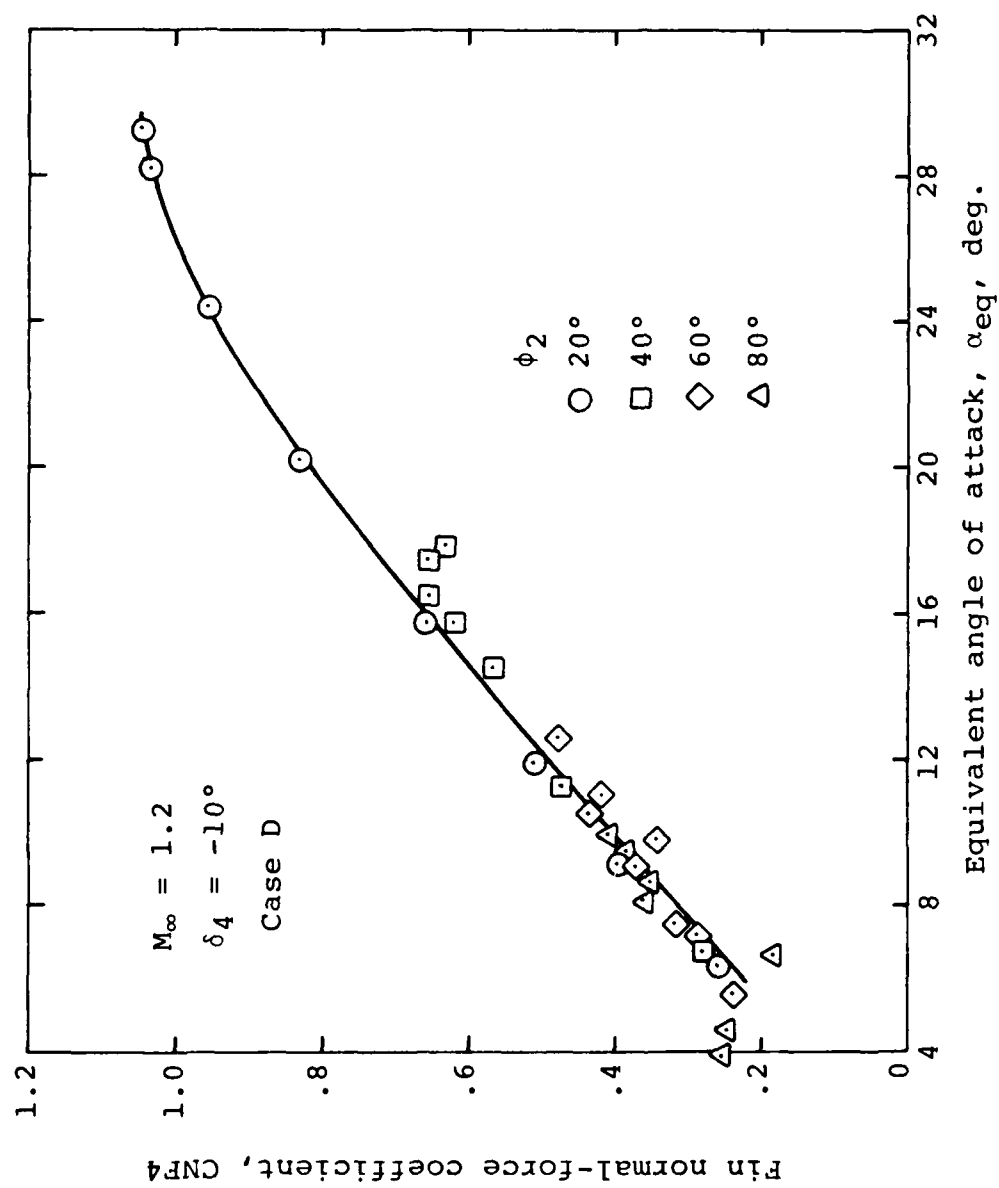
(c) $\delta_4 = -10°$

Figure 60.- Continued.

235
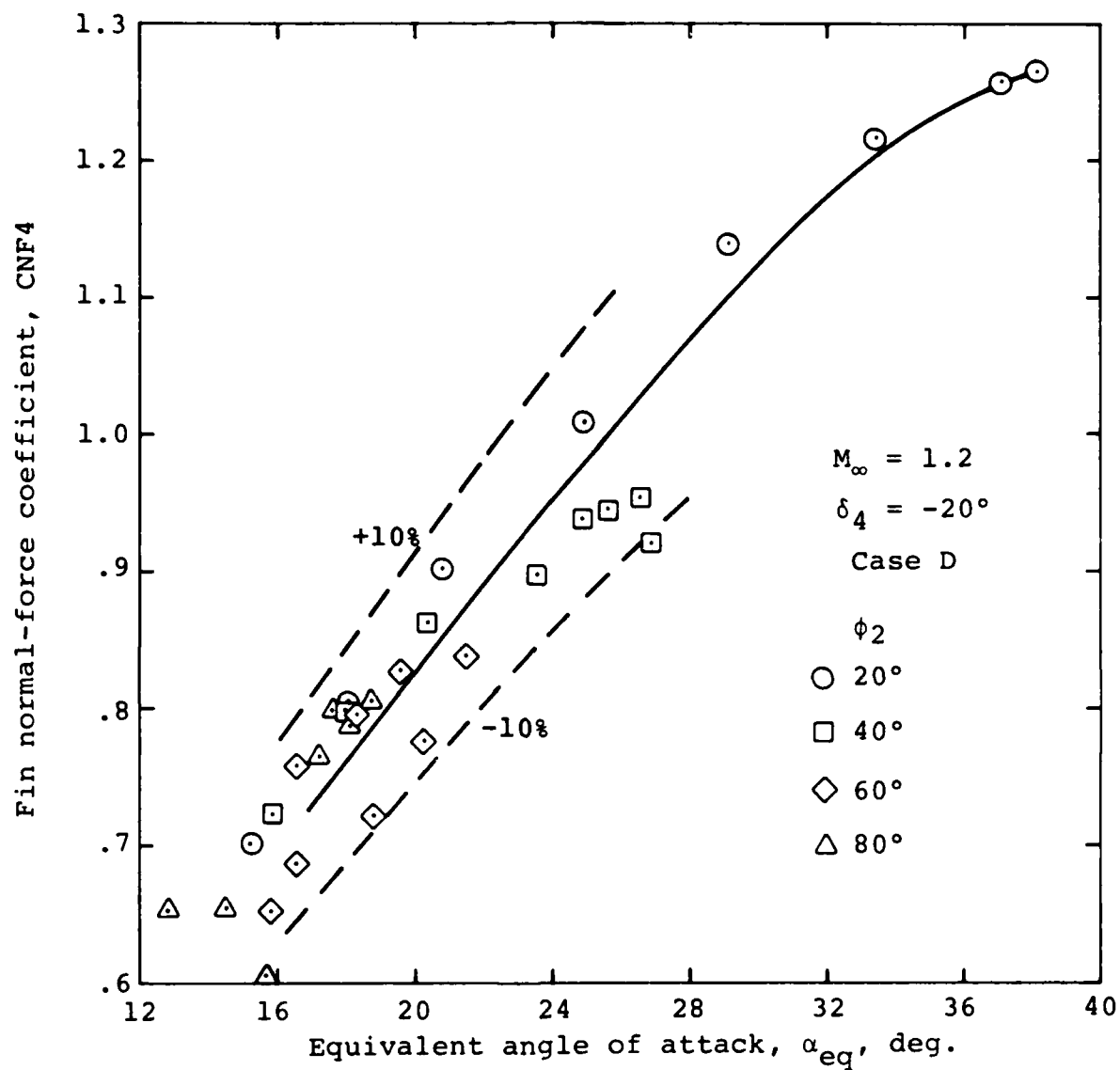
(d) $\delta_4 = -20°$

Figure 60.- Concluded.
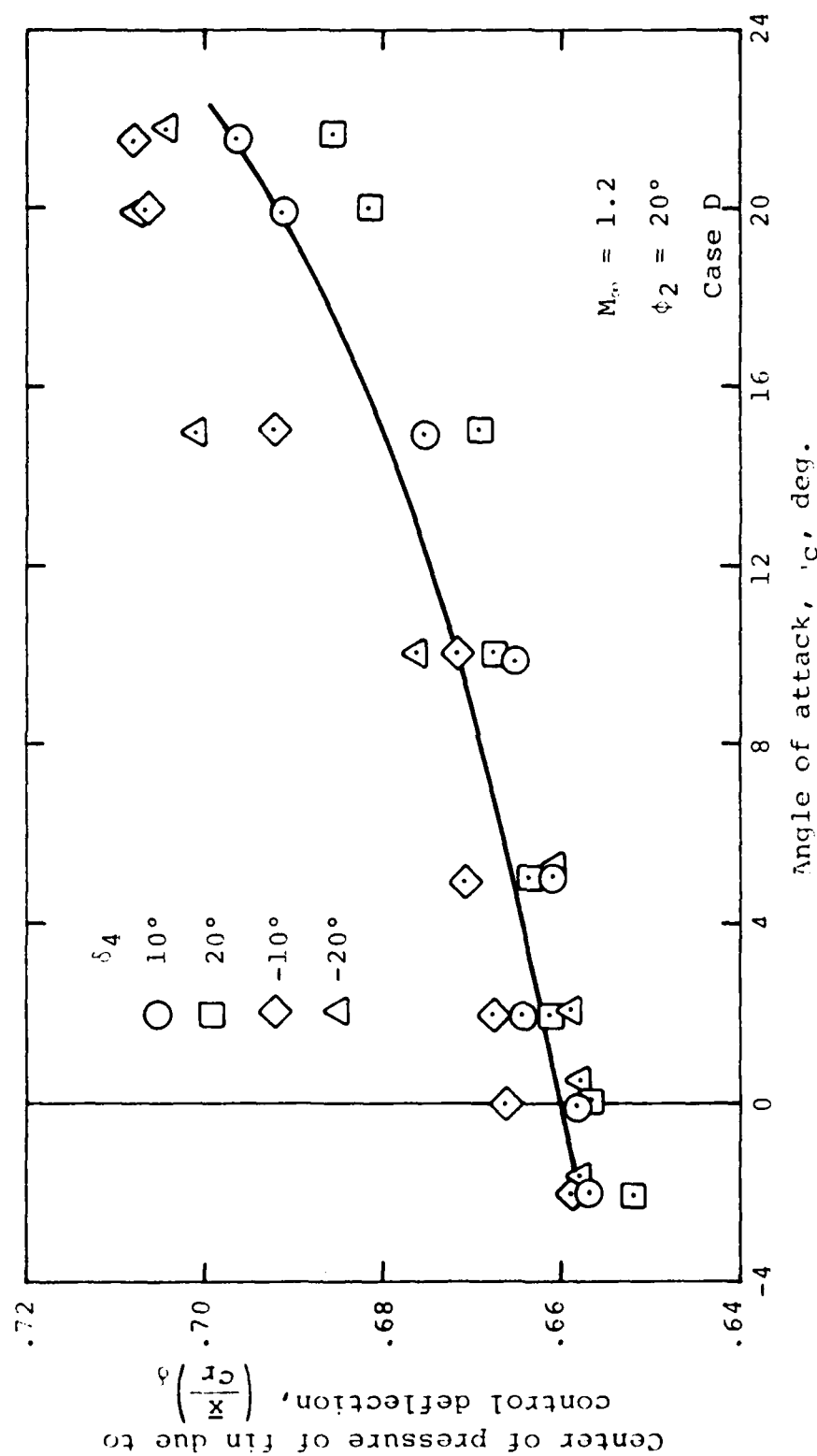
Figure 61.- Center of pressure due to control deflection for fin 51 mounted on triservice missile; $M_\infty = 1.2$, leeward fin, case D.
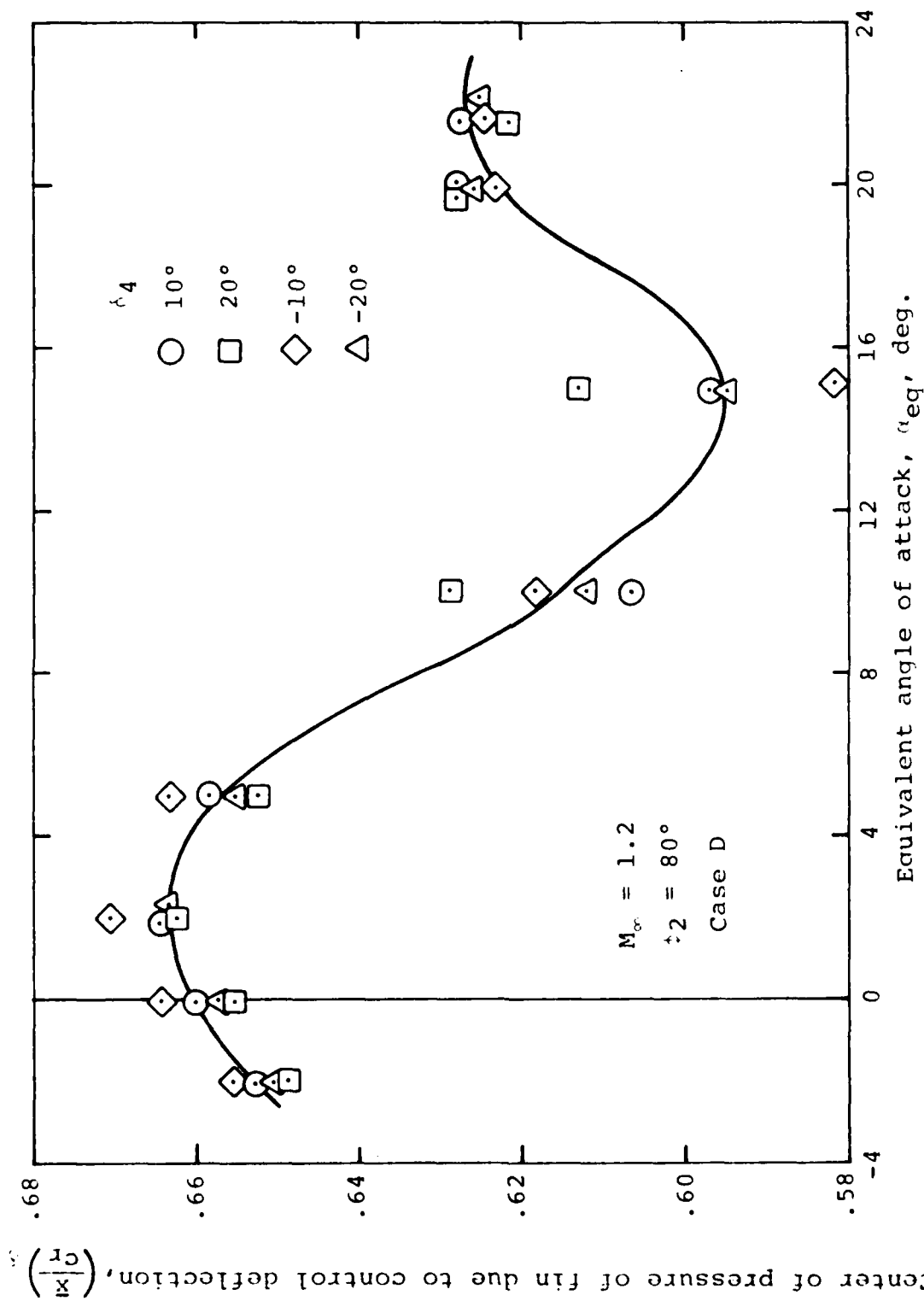
(a) $\phi_2 = 20°$

$M_\infty = 1.2$

$\phi_2 = 40°$

Case D
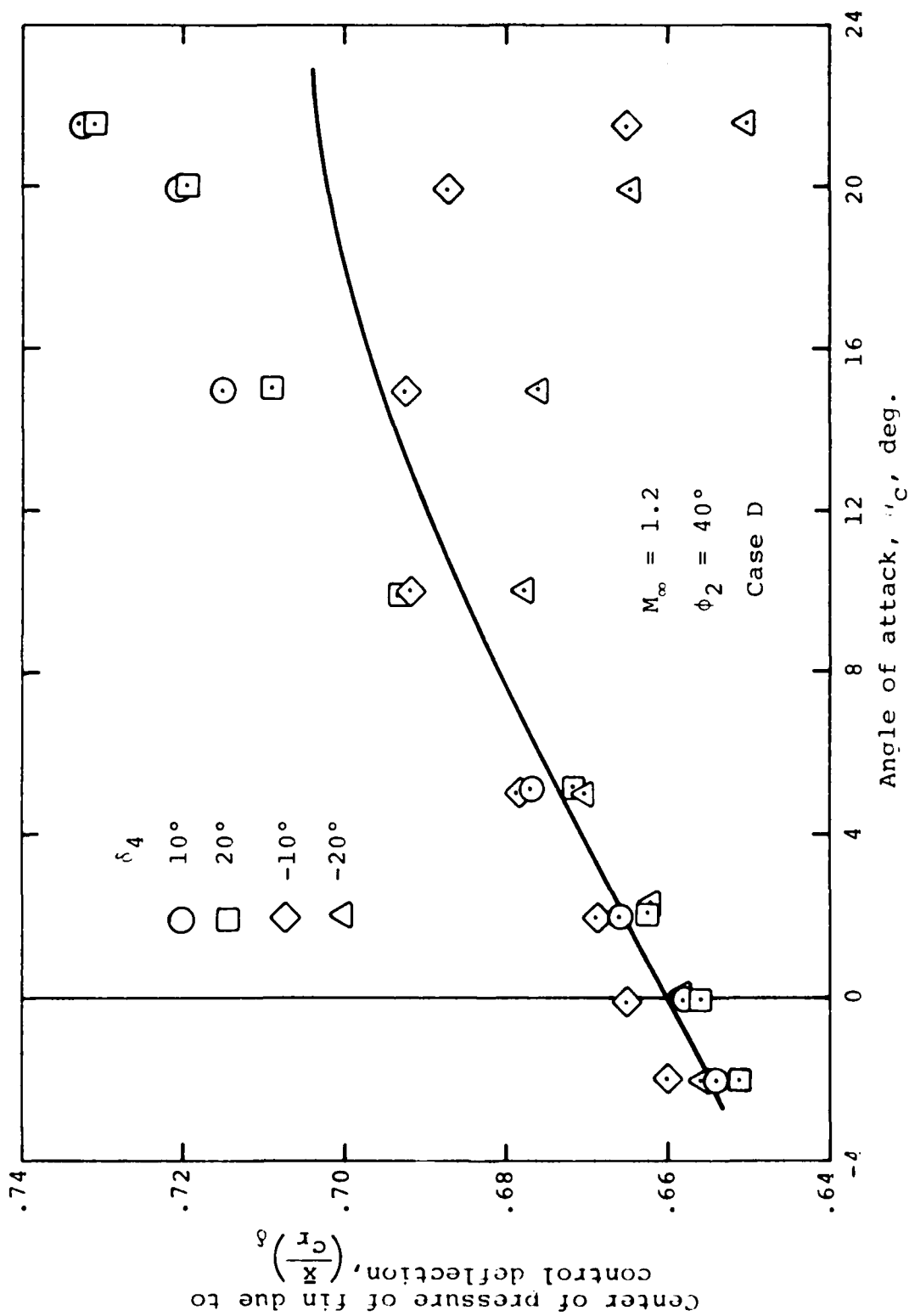
(b) $\phi_2 = 40°$

Figure 61.- Continued.

238

(c) $\phi_2 = 60°$

Figure 61.- Continued.

$M_\infty = 1.2$

$\phi_2 = 60°$

Case D

δ_4

○ 10°

□ 20°

◇ -10°

◁ -20°

Angle of attack, α_c, deg.

Center of pressure of fin due to control deflection, $\left(\dfrac{x}{c_r}\right)_\delta$

(d) $\phi_2 = 80°$

Figure 61.- Concluded.

Center of pressure of fin due to control deflection, $\left(\dfrac{x}{c_r}\right)$;

Equivalent angle of attack, α_{eq}, deg.

$M_\infty = 1.2$

$\phi_2 = 80°$

Case D
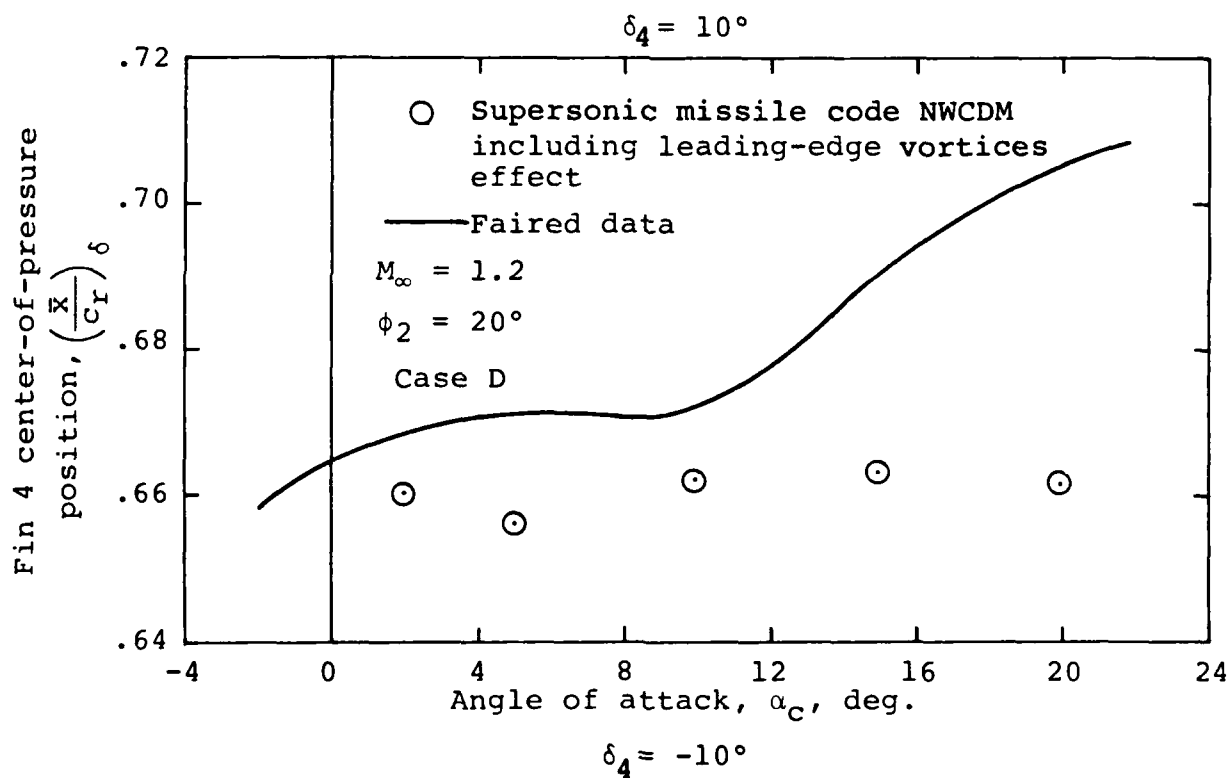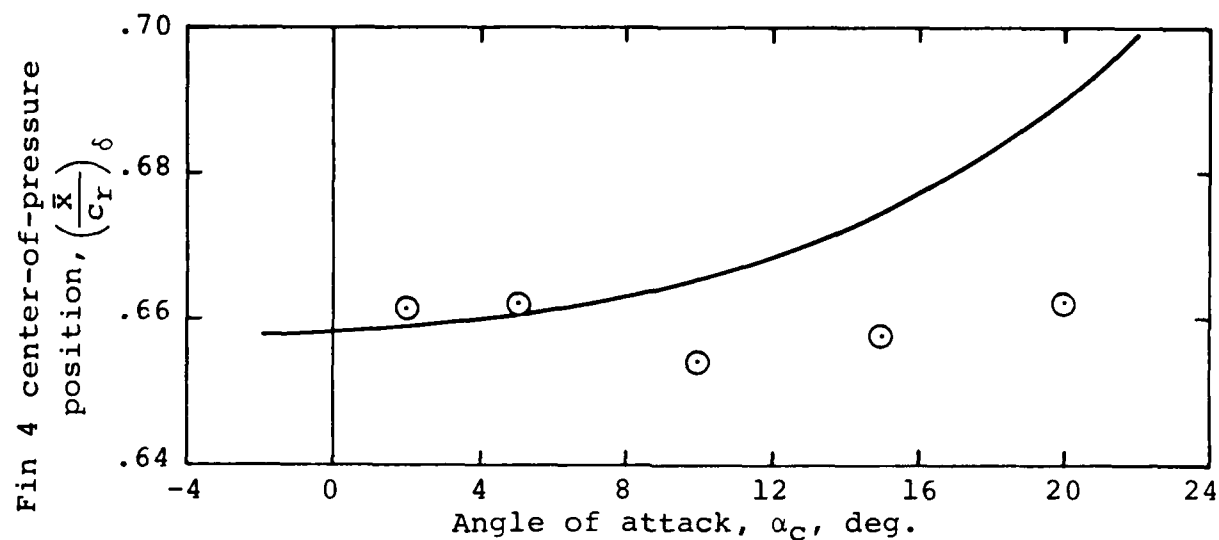
δ_4
10° ◯
20° □
-10° ◇
-20° △
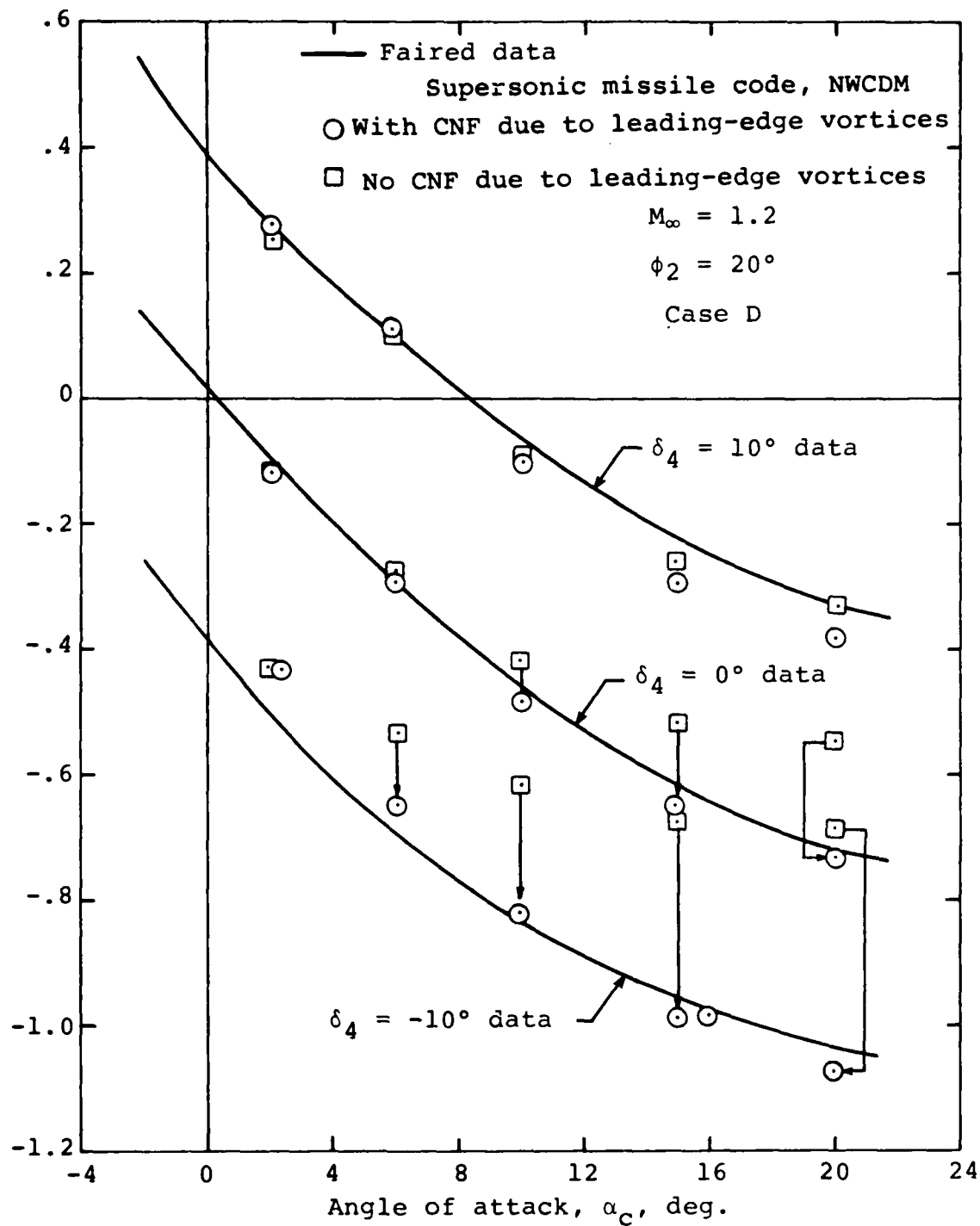
(a) Normal-force coefficient, CNF4

Figure 62.- Comparison of measured coefficients of fin 4 mounted
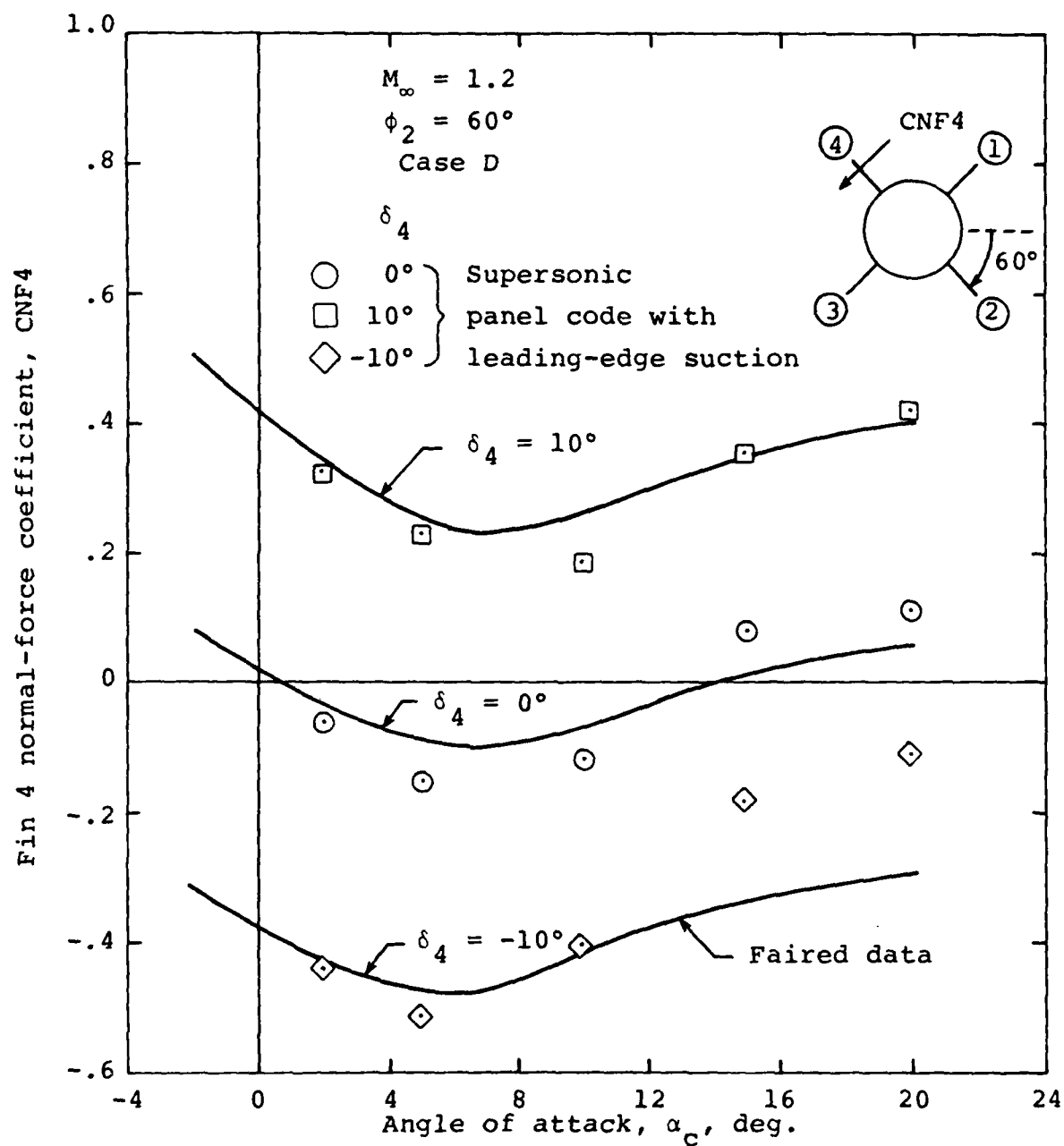on triservice missile with predictions of
supersonic missile code NWCDM.
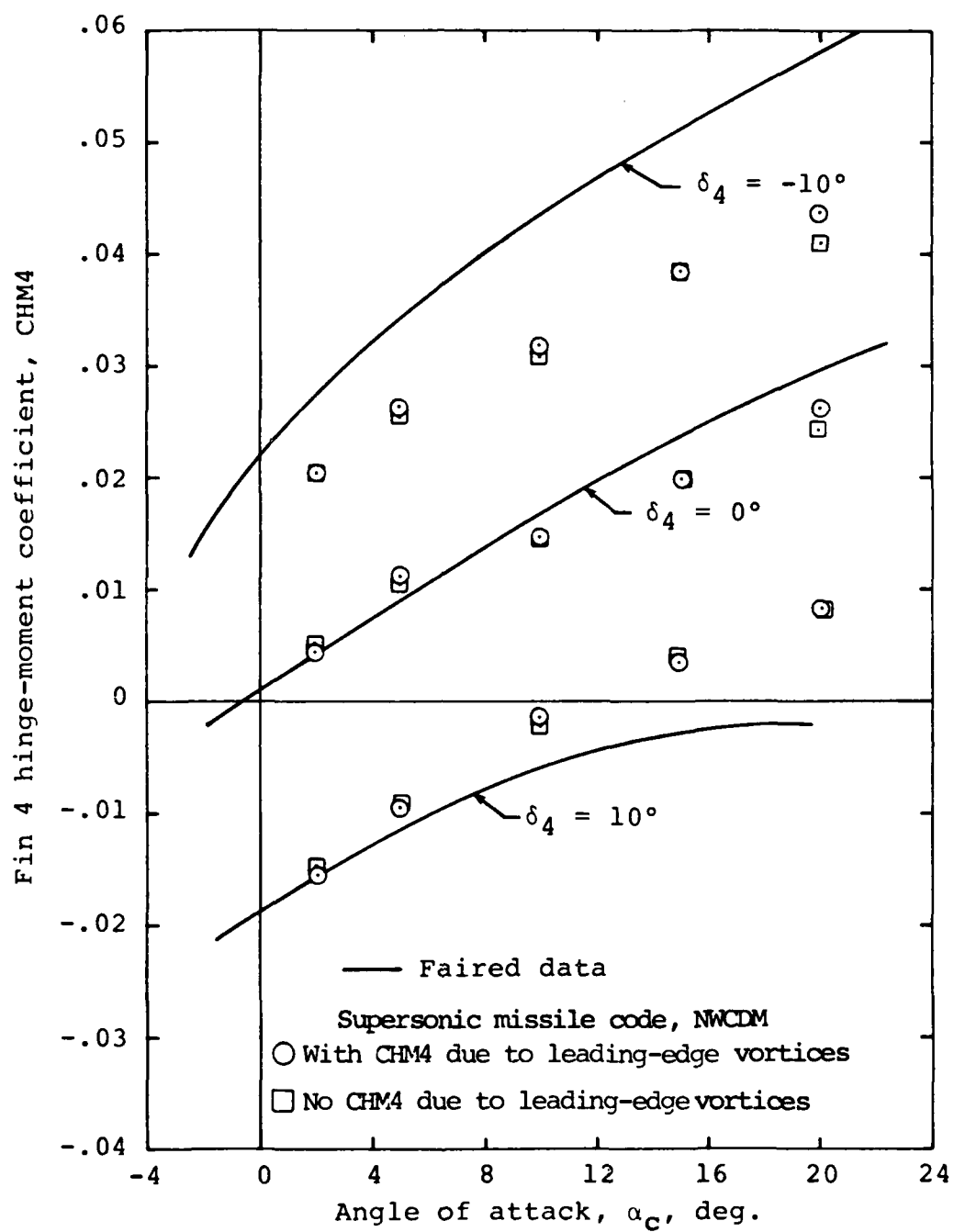
(b) Hinge-moment coefficient, CHM4
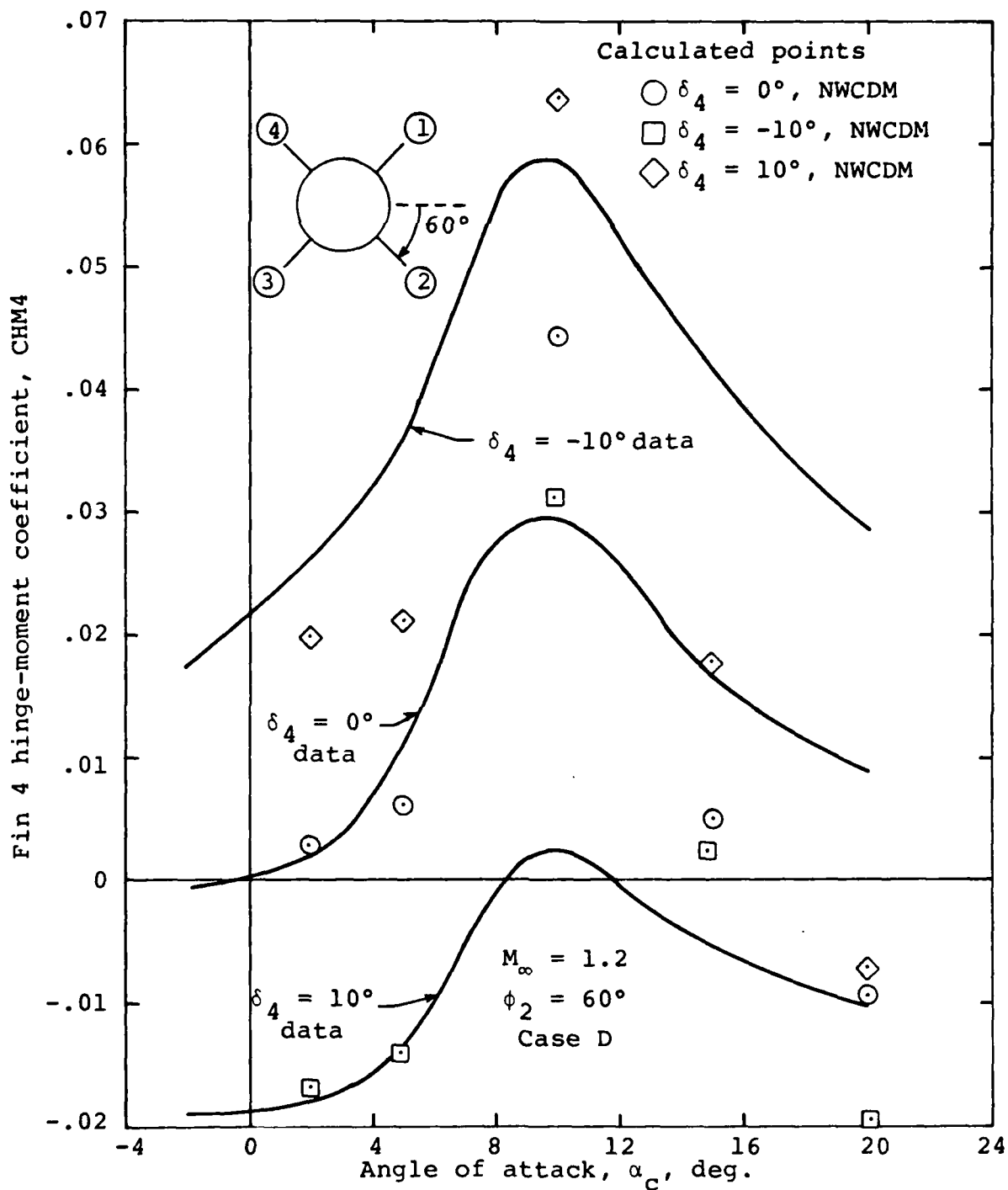
Figure 62.- Continued.

242

$\delta_4 = 10°$

$\delta_4 = -10°$

$\qquad\bigcirc\qquad$ Supersonic missile code NWCDM
including leading-edge vortices
effect

—— Faired data

$M_\infty = 1.2$

$\phi_2 = 20°$

Case D

(c) Center of pressure, $\left(\dfrac{\bar{x}}{c_r}\right)_\delta$
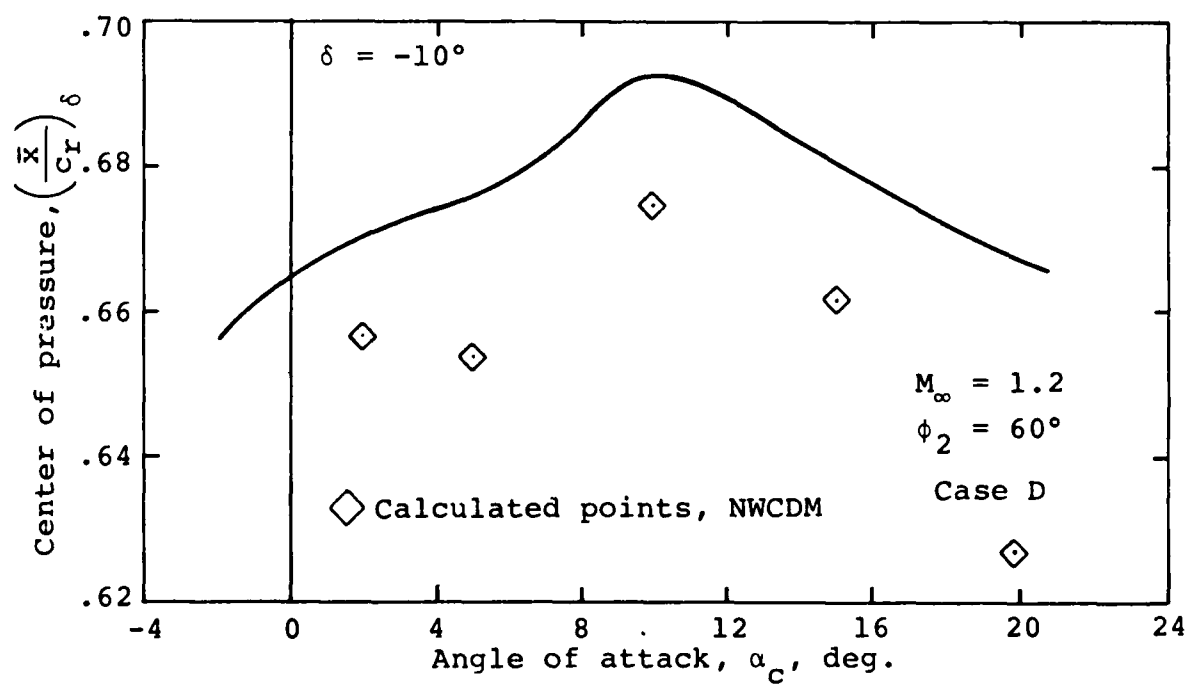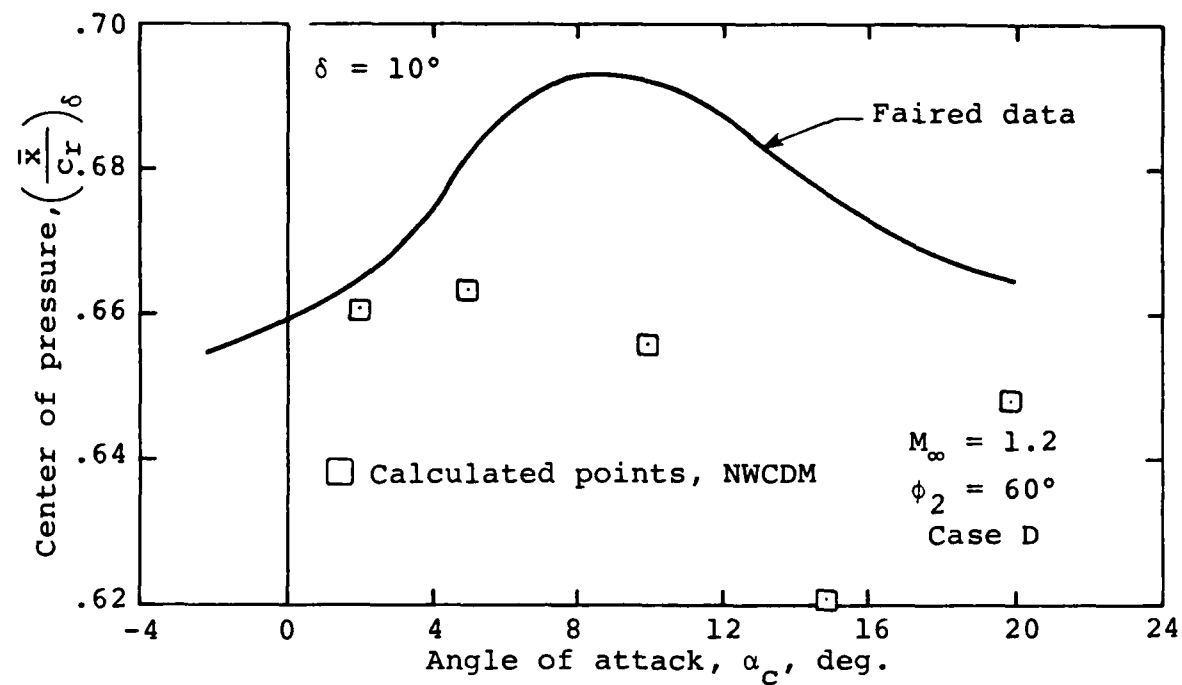
Figure 62.- Concluded.

(a) Normal-force coefficient, CNF4

Figure 63.- Comparisons of measured quantities for fin 4
mounted on triservice missile with predictions of
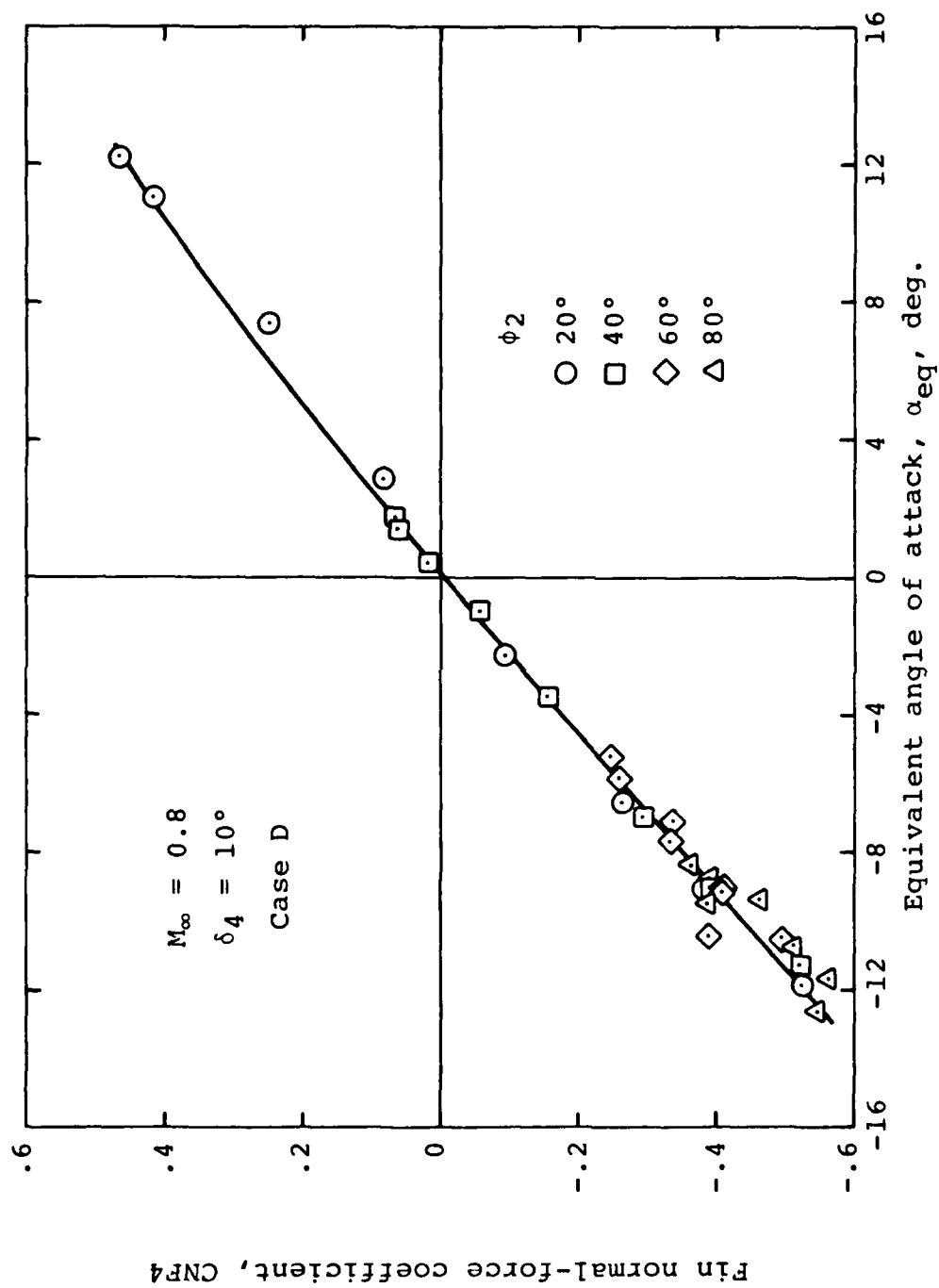code NWCDM; fin at vortex roll position.

244

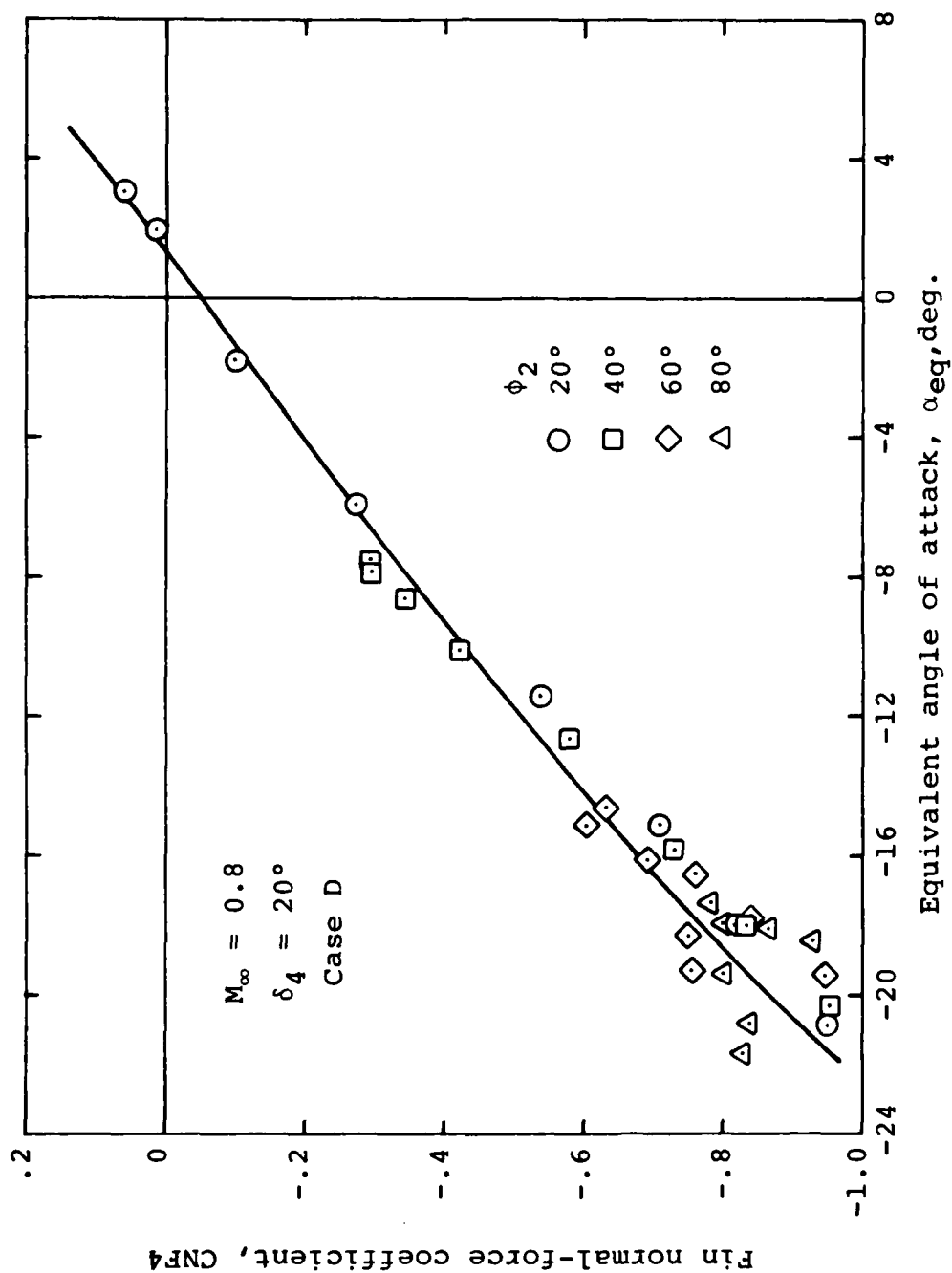(b) Hinge-moment coefficient, CHM4

Figure 63.- Continued.

(c) Center of pressure due to fin deflection

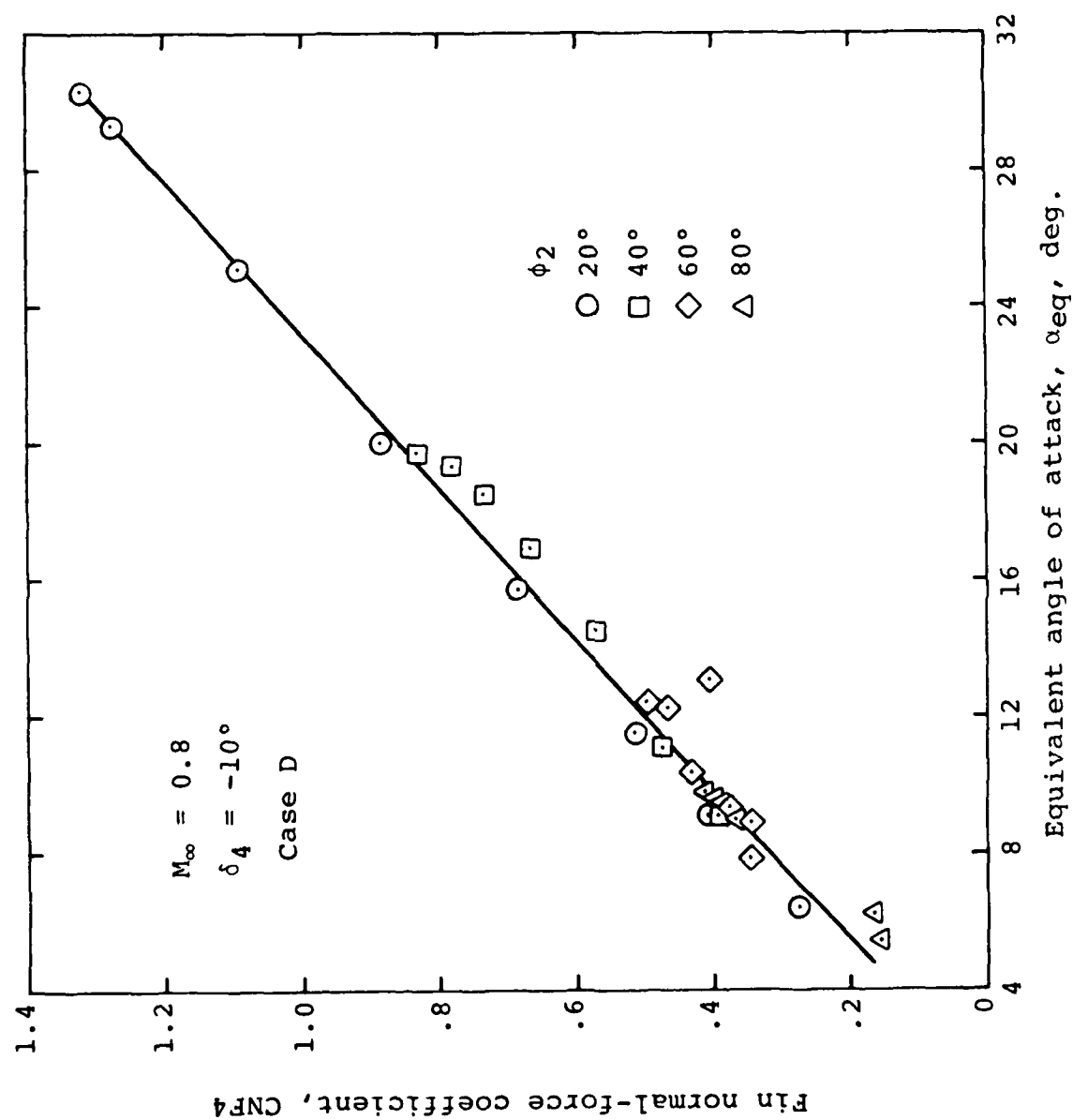Figure 63.- Concluded.

246

(a) $\delta_4 = 10°$

Figure 64.- Correlation curves of CNF4 vs. α_{eq} for fin 4 on triservice missile for various deflections; $M_\infty = 0.8$, leeward fin, case D.

(b) $\delta_4 = 20°$
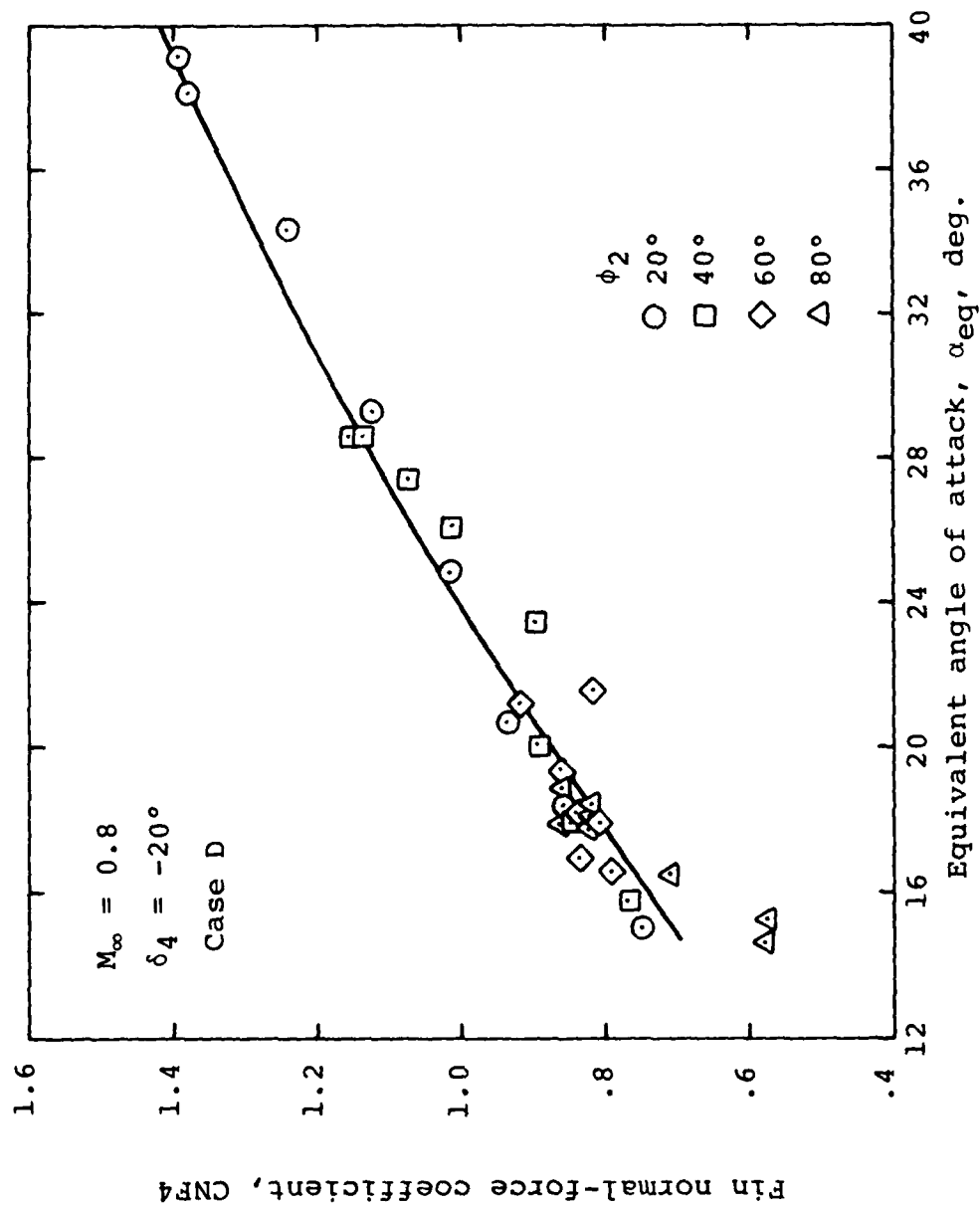
Figure 64.- Continued.

Fin normal-force coefficient, CNF4

Equivalent angle of attack, α_{eq}, deg.

$M_\infty = 0.8$

$\delta_4 = -10°$

Case D

ϕ_2
○ 20°
□ 40°
◇ 60°
△ 80°

(c) $\delta_4 = -10°$

Figure 64.- Continued.

249

(d) $\delta_4 = -20°$

Figure 64.- Concluded.

$M_\infty = 0.8$

$\delta_4 = -20°$

Case D

ϕ_2
○ 20°
□ 40°
◇ 60°
△ 80°

Equivalent angle of attack, α_{eq}, deg.

Fin normal-force coefficient, CNF4

250
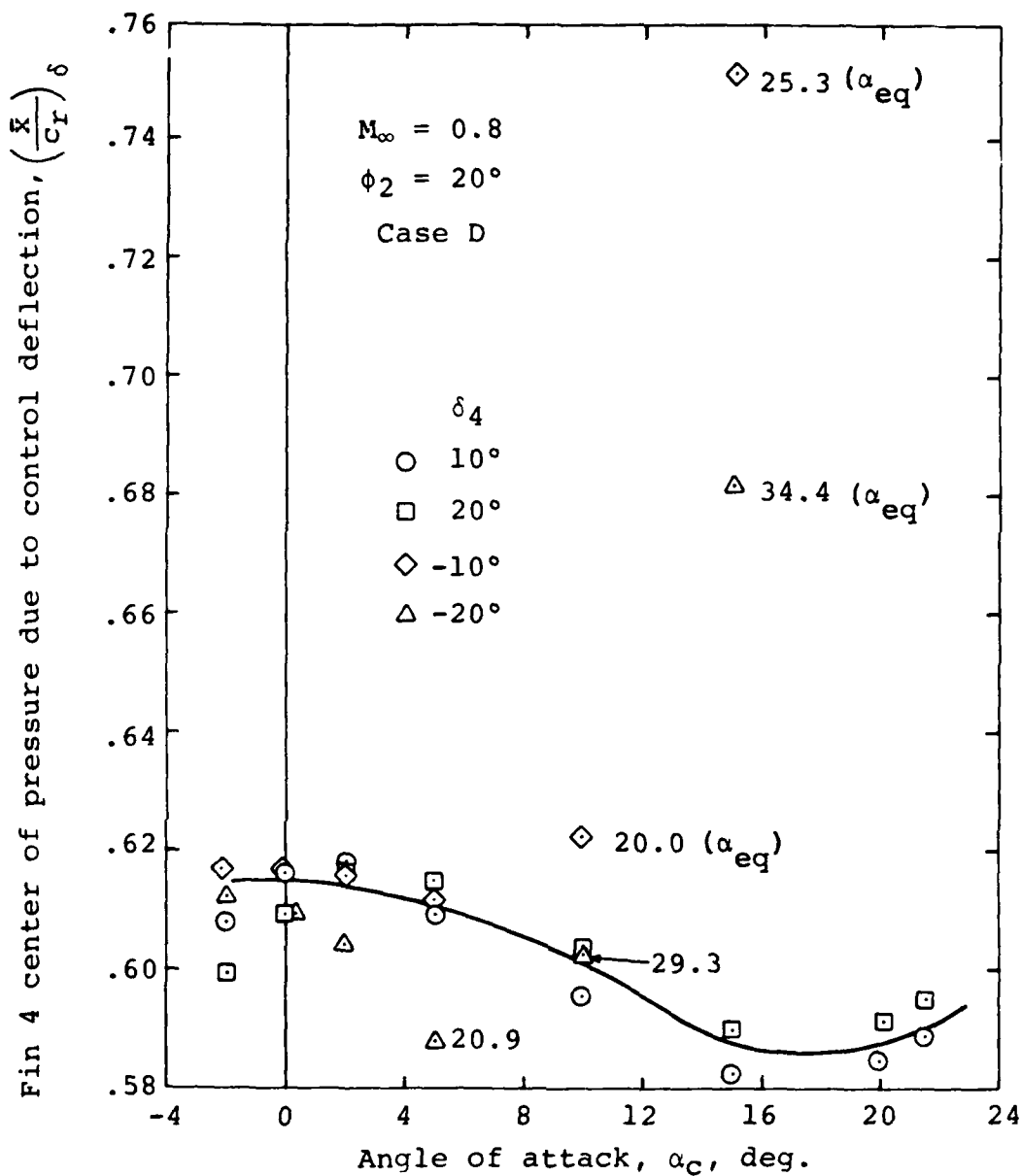
(a) $\phi_2 = 20°$

Figure 65.- Center of pressure due to control deflection for
fin 51 mounted on triservice missile;
$M_\infty = 0.8$, leeward fin, case D.

$M_\infty = 0.8$

$\phi_4 = 40°$

Case D

δ_4	
10°	◯
20°	□
-10°	◇
-20°	△

Angle of attack, α_c, deg.

Fin 4 center of pressure due to control deflection, $\left(\dfrac{x}{c_r}\right)_\delta$

(b) $\phi_2 = 40°$

Figure 65.- Continued.

$M_\infty = 0.8$

$\phi_2 = 60°$

Case D

δ_4

○	10°
□	20°
◇	-10°
△	-20°

Angle of attack, α_c, deg.

Fin 4 center of pressure due to fin deflection, $\left(\dfrac{x}{c_r}\right)_\delta$
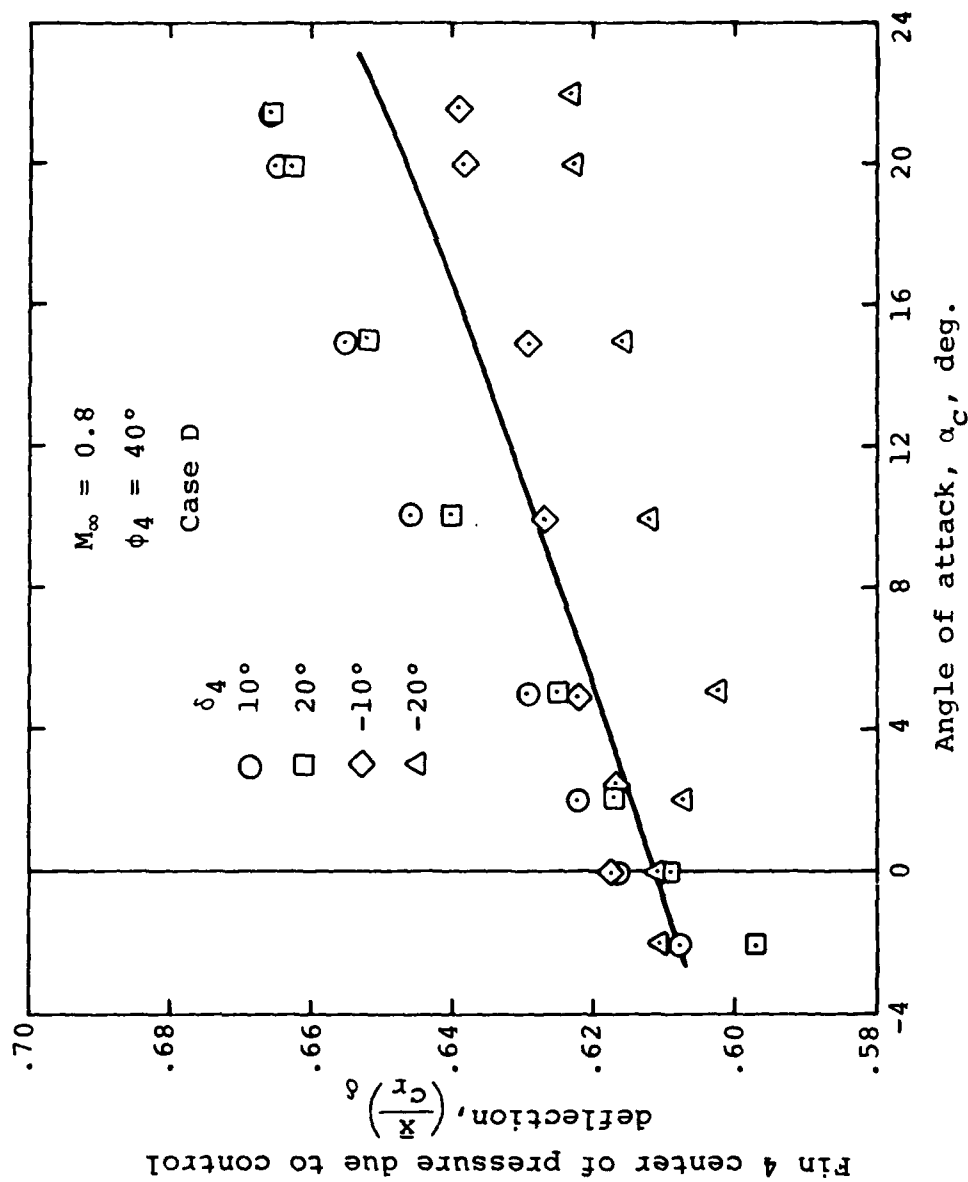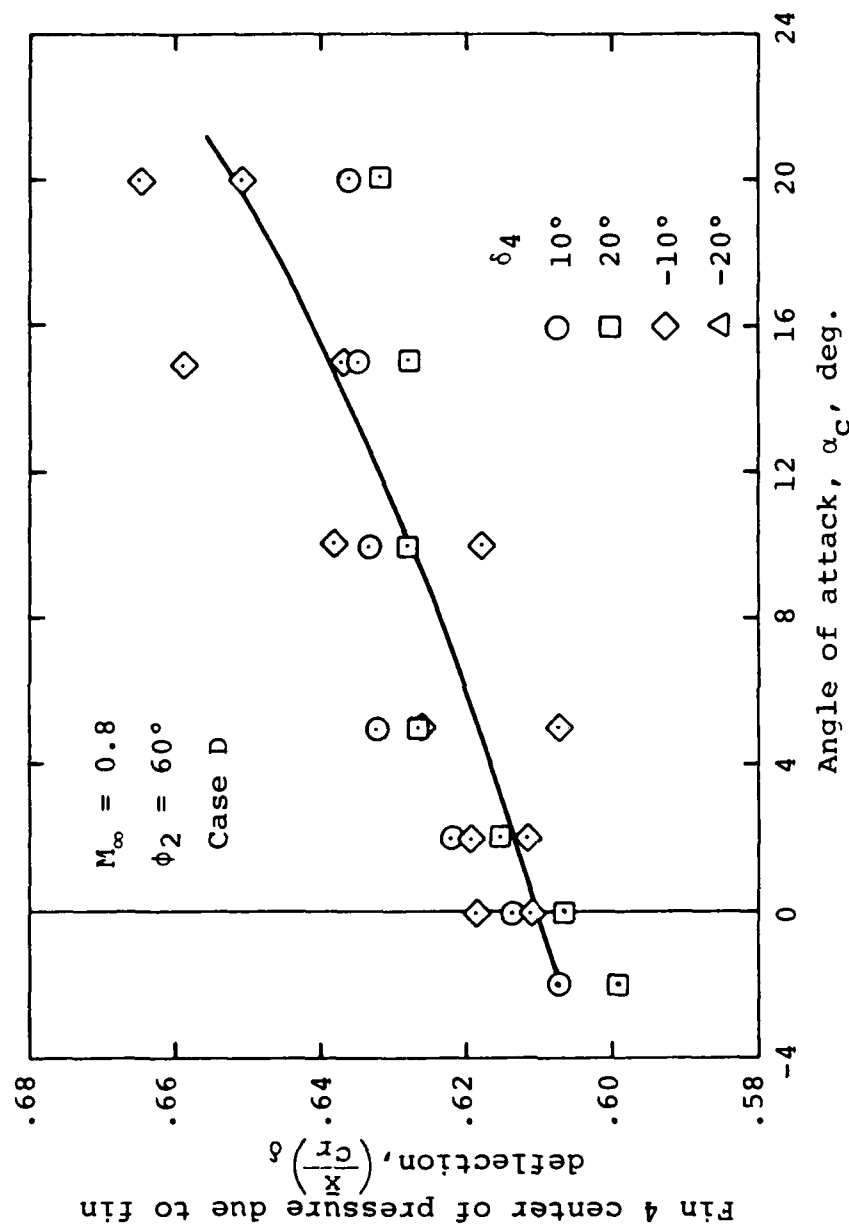
(c) $\phi_2 = 60°$

Figure 65.- Continued.
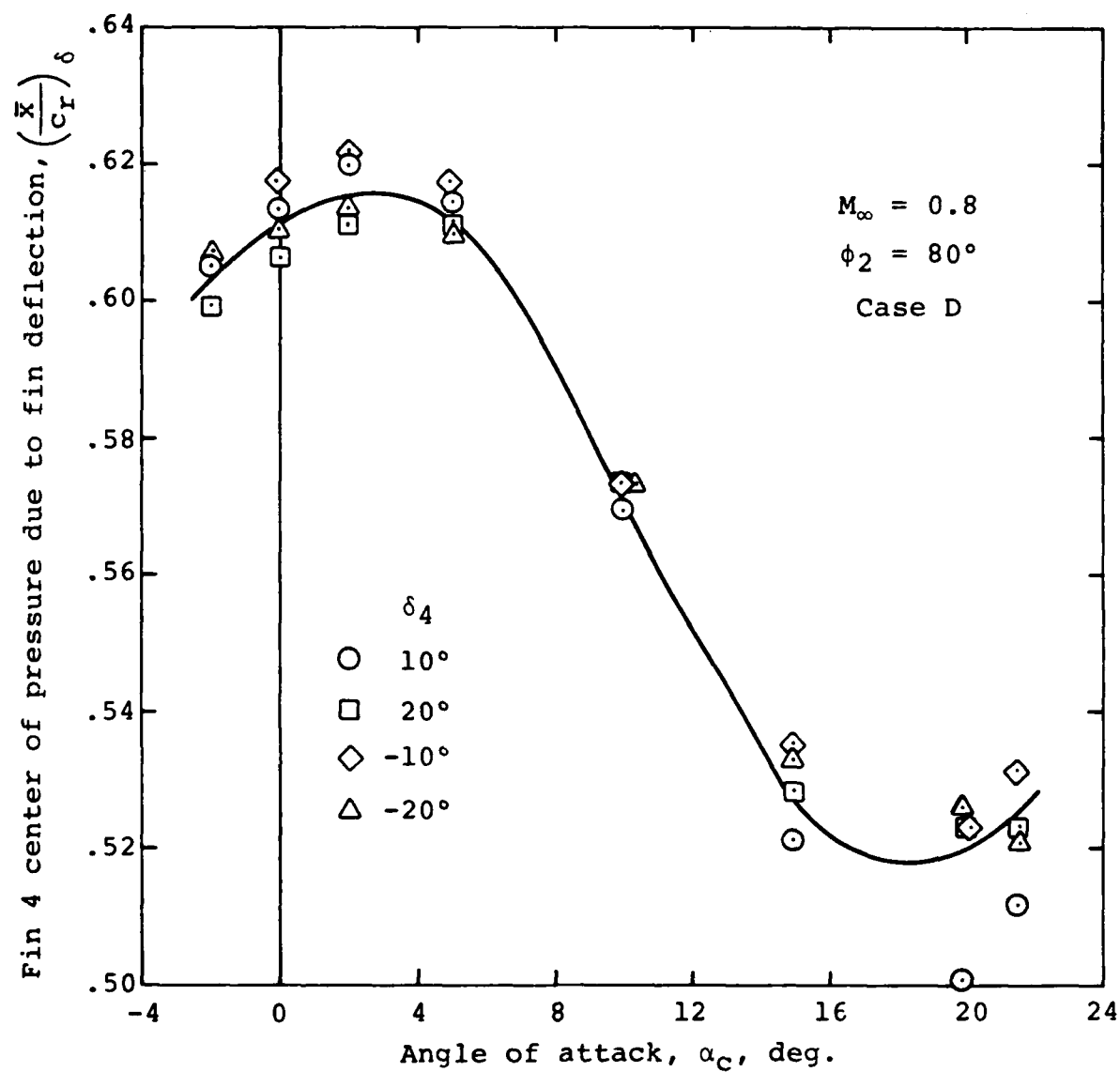
(d) $\phi_2 = 80°$

Figure 65.- Concluded.

DISTRIBUTION LIST

All addresses receive one copy unless otherwise specified.

Scientific Officer Code 432 Office of Naval Research 800 N. Quincy Street Arlington, VA 22217	1 copy
Commander DCASMA-SF 1250 Bayhill Drive San Bruno, CA 94066	1 copy
Attn: ACO DCRL-GFCA/84	
Director Naval Research Laboratory Attn: Code 2627 Washington, D.C. 20375	6 copies
Defense Technical Information Center Bldg. 5, Cameron Station Alexandria, VA 22314	12 copies
Office of Naval Research Western/Region Office 1030 E. Green Street Pasadena, CA 91106	1 copy
Mr. Vernon Hoehne Attn: AFWAL/FIGC Wright-Patterson AFB, OH 45433	15 copies

END

FILMED

12-84

DTIC